Experimental Study and Multi-scale Modelling of LCF Behaviour of Austenitic Steels Treated by SMAT

Jianqiang Zhou

▶ **To cite this version:**

Jianqiang Zhou. Experimental Study and Multi-scale Modelling of LCF Behaviour of Austenitic Steels Treated by SMAT. Materials and structures in mechanics [physics.class-ph]. Université de Technologie de Troyes, 2018. English. NNT : 2018TROY0018 . tel-03210910

HAL Id: tel-03210910

https://theses.hal.science/tel-03210910v1

Submitted on 28 Apr 2021

HAL is a multi-disciplinary open access archive for the deposit and dissemination of scientific research documents, whether they are published or not. The documents may come from teaching and research institutions in France or abroad, or from public or private research centers.

L'archive ouverte pluridisciplinaire **HAL**, est destinée au dépôt et à la diffusion de documents scientifiques de niveau recherche, publiés ou non, émanant des établissements d'enseignement et de recherche français ou étrangers, des laboratoires publics ou privés.

Thèse
de doctorat
de l'UTT

Jianqiang ZHOU

Experimental Study and Multi-scale Modelling of LCF Behaviour of Austenitic Steels Treated by SMAT

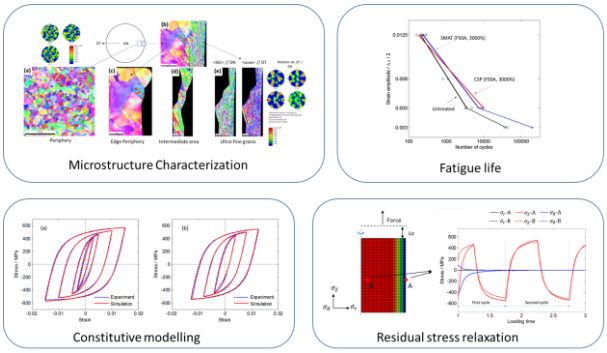

Spécialité :
Matériaux, Mécanique, Optique et Nanotechnologie

2018TROY0018 Année 2018

utt
UNIVERSITÉ DE TECHNOLOGIE
TROYES

THESE

pour l'obtention du grade de

DOCTEUR de l'UNIVERSITE DE TECHNOLOGIE DE TROYES

Spécialité : MATERIAUX, MECANIQUE, OPTIQUE ET NANOTECHNOLOGIE

présentée et soutenue par

Jianqiang ZHOU

le 28 juin 2018

Experimental Study and Multi-scale Modelling of LCF Behaviour of Austenitic Steels Treated by SMAT

JURY

M. G. HENAFF	PROFESSEUR DES UNIVERSITES	Président
M. L. DELANNAY	PROFESSEUR	Examinateur
M. X. FEAUGAS	PROFESSEUR DES UNIVERSITES	Rapporteur
Mme P. KANOUTE	INGENIEUR DE RECHERCHE ONERA	Examinateur
Mme D. RETRAINT	PROFESSEUR DES UNIVERSITES	Directrice de thèse
M. Z. SUN	ENSEIGNANT CHERCHEUR UTT	Directeur de thèse
M. L. TALEB	PROFESSEUR DES UNIVERSITES	Rapporteur

To my family, my teachers and my friends.

ACKNOWLEDGEMENTS

First and foremost, I would like to express my deepest gratitude to my supervisors, Dr. Zhidan Sun and Prof. Delphine Retraint, for their superior guidance, considerable support and encouragement throughout my PhD study at UTT. I would also like to extend my sincere thanks to Dr. Pascale Kanouté for her instructive advice and essential assistance of the theoretical studies in my thesis.

My sincere thanks should also go to the rest of the thesis committee members: Prof. Gilbert Hénaff, Prof. Xavier Feaugas, Prof. Lakhdar Taleb, as well as Prof. Laurent Delannay, for their patience to examine my work and giving insightful comments.

Moreover, I would like to express my special thanks to Prof. Hongqian Xue in NWPU for his kindly help and encouragement from my undergraduate study. He recommended me for this valuable opportunity of the PhD research.

I am greatly indebted to the colleagues in UTT, who gave me many help in technical support, experimental experiences, and valuable advices. They are Dr. Bruno Guelorget, Mr. François Weil, Prof. Manuel François, Prof. Xiaolu Gong, Dr. Yugang Li, Mr. Laurent Daniel, and other colleagues of LASMIS.

Besides, I would like to sincerely appreciate my friends in UTT for their company and help in both my work and daily life in France.

Last but not least, I would like to show my most sincere appreciation to my family, relatives, teachers and friends for supporting, encouraging and helping me throughout my life and career. Forever bless you!

Jianqiang Zhou

April 2018, at Troyes

Abstract

This work focuses on experimental analysis and multi-scale modelling of LCF behaviour of 316L steels treated by SMAT. The gradient microstructure features of a 316L steel treated by SMAT are characterized by EBSD, XRD and hardness tests. Grain size gradient, residual stress and plastic deformation are evaluated. The cyclic hardening/softening behaviour of the SMATed specimens and the evolution of the microstructures during cyclic loading are studied based on LCF tests and EBSD observations. A comparison between SMAT and conventional shot peening is performed by analysing the surface topography, residual stress fields, and work hardening profiles of the treated specimens as well as their effects on LCF life.

A modelling methodology of residual stress and work hardening is developed including constitutive modelling, reconstruction technique, and cyclic loading simulation. First, a macroscopic constitutive modelling of the cyclic plasticity behaviour of a 316L steel is performed. Then, a self-consistent modelling of the cyclic hardening/softening behaviour is developed. Afterwards, a new method for reconstructing residual stress and work hardening is proposed and applied to a SMATed structure. Both of the previous macroscopic and microscopic models are used to predict the cyclic behaviour of the SMATed material.

Keywords: SMAT, Austenitic stainless steel, Low cycle fatigue, Multi-scale modelling, Residual stresses, Work hardening.

Résumé

Ce travail de thèse est focalisé sur des caractérisations microstructurales, des essais de fatigue et une modélisation multi-échelle du comportement en fatigue oligocyclique d'aciers 316L nanocristallisés superficiellement par SMAT. Le gradient de taille de grains superficiel, les contraintes résiduelles et l'écrouissage générés sont évalués à l'aide de différentes techniques : EBSD, DRX et essais de dureté. Le durcissement/adoucissement cyclique des éprouvettes SMATées et l'évolution de la microstructure au cours du chargement cyclique sont ensuite étudiés grâce à des essais de fatigue et des observations par EBSD. Une comparaison entre le SMAT et le grenaillage conventionnel est réalisée en analysant la topographie de surface, les champs de contraintes résiduelles et les profils d'écrouissage générés. Les effets de ces deux traitements sur la durée de vie en fatigue oligocyclique sont également étudiés.

Une méthodologie de modélisation des contraintes résiduelles et de l'écrouissage est par ailleurs développée. Elle comporte une modélisation multi-échelle, la reconstruction des contraintes résiduelles et de l'écrouissage ainsi que la simulation du chargement cyclique. Une modélisation macroscopique de la plasticité cyclique de l'acier est d'abord réalisée. Une approche auto-cohérente du durcissement/adoucissement cyclique est ensuite développée. Enfin, une nouvelle méthode de reconstruction des contraintes résiduelles et de l'écrouissage est proposée et appliquée à une structure SMATée.

Mots clefs: Nanocristallisation superficielle, Acier inoxydable, Fatigue oligocyclique, Comportement cyclique, Modélisation multi-échelle, Contraintes résiduelles, Ecrouissage

CONTENTS

List of Tables

List of Figures

List of Abbreviations and Acronyms

CPFEM: Crystal plasticity finite element method;

CSP: Conventional shot peening;

EBSD: Electron backscatter diffraction;

FE: Finite element;

FEM: Finite element method;

FWHM: Full width at half-maximum;

GAM: Grain Average Misorientation;

GMF: Gradient microstructure feature;

GOS: Grain Orientation Spread;

HCF: High cycle fatigue;

KAM: Kernel average misorientation;

LCF: Low cycle fatigue;

RVE: Representative volume element;

SEM: Scanning electrical microscope;

SMAT: Surface mechanical attrition treatment;

SPD: Severe plastic deformation;

XRD: X-ray diffraction;

FCC: Face-centred cubic.

General introduction

Surface modification technology has been widely used in industry to improve in-service properties of materials through physical or chemical approaches. It is well documented that surface mechanical treatment techniques are able to generate a gradient microstructure in the near surface region of metallic materials, for example shot peening [1,2], SMAT [1] laser peening [3,4], deep-rolling [5,6]. During the process, a great number of crystallographic defects such as plastic slips could be activated. This can progressively lead to a thin ultrafine-grained or nanostructured layer at the surface of the treated metallic materials [1,2,6]. Underneath the grain-refined layer, there is an area named transition region characterized by the presence of a high strain hardening gradient and a high gradient of compressive residual stress. In the region far from the surface, the material is not affected, and the material characteristics such as grain size and dislocation density remain unchanged. These metallurgical parameters generated by surface mechanical treatment including ultra-fine grained layer, residual stress, work hardening, sometimes with phase transformation or twins together constitute a gradient microstructure feature in the near surface region of severe plastic deformed metallic materials.

In general, the mechanical properties of metallic materials with gradient microstructure features at the surface can be obviously changed with respect to their untreated counterparts. Ultra-fine grained austenitic stainless steel generated by SMAT and deep rolling manifests significant enhancement of mechanical properties such as tensile strength, fatigue limit, friction, or wear resistance [3,6–8]. Underneath the grain-refined layer is a transition region, where a high compressive residual stress field and work hardening gradient are generated due to SPD. A compressive residual stress field is able to improve fatigue life by increasing the resistance to crack initiation and reducing the crack propagation rate [9,10]. Furthermore, SPD may induce phase transformation which could lead to a significant strengthening of austenitic stainless steels processed by shot peening and deep-rolling [6,11].

The aim of this thesis is to study the LCF behaviour of 316L austenitic steels treated by SMAT through experimental analysis and Multi-scale modelling. A bibliographic study

of the research background is presented in Chapter 1 from the viewpoints of experimental characterization of microstructures, mechanical properties of the gradient microstructure feature, as well as multi-scale modelling approaches.

In Chapter 2, grain refinement, residual stress, and plastic deformation of a 316L austenitic stainless steel treated by SMAT are characterized using EBSD, XRD, hardness tests. The results show that cyclic stress amplitudes of SMATed specimens are significantly enhanced based on strain controlled LCF tests. The evolution of the microstructures during cyclic loading are also analysed through EBSD observations. The comparison between SMAT and CSP is performed in Chapter 3 by analysing surface topography, compressive residual stress, and work hardening of the treated specimens as well as their effects on LCF life.

In Chapter 4, the cyclic behaviour of the two studied 316L steels (316L-A in Chapter 3 and 316L-B in Chapter 2) highlighted by uniaxial strain controlled LCF tests is first analysed. Significant strain range memory effect can be observed for both the two steels according to the analysis. It is noted that the cyclic hardening/softening behaviour and the strain range memory effect can mainly be attributed to back stress. A set of constitutive relations is proposed in the combined kinematic/isotropic hardening framework to describe the cyclic behaviour of the 316L-A steel.

In order to model the cyclic behaviour of materials from more fundamental aspects, a self-consistent modelling is developed in Chapter 5. In this chapter, a crystal plasticity model is extended and coupled with a self-consistent model. For this purpose, a non-linear kinematic hardening rule is proposed at the slip system scale to model the cyclic hardening/softening behaviour induced by the back stress. The material parameters, which correspond to the cyclic behaviour of the 316L-A steel under a strain amplitude of ±1.25%, are determined by using an identification procedure developed in this work.

In Chapter 6, the LCF behaviour of the SMATed materials is studied through Multi-scale modelling. A new method of reconstruction of residual stress and work hardening is proposed and applied to a SMATed structure. Residual stress field and work hardening gradient are reconstructed for a SMATed cylindrical structure, based on XRD measurement, stress equilibrium relation, boundary conditions, as well as deformation history analysis. The reconstruction method is verified through self-equilibrium analysis with a FE model. The residual stress relaxation during cyclic loading and the strengthening effect due to SMAT are studied based on cyclic loading simulations using the FE model.

Chapter 1: Literature review

The as-generated gradient microstructure feature through surface mechanical treatments can have significant effects on mechanical properties of metallic material in service. Therefore, being able to thoroughly understand and precisely take into account gradient microstructure features is of great importance for material processing design and optimization. This thesis focuses on studying the fatigue behaviour of austenitic stainless steels treated by surface mechanical attrition treatment (SMAT) with experimental characterization and multi-scale modelling methods. This chapter reviews the state of the art on shot peening technologies, experimental characterization, and multiscale modelling approaches of the gradient microstructure features. At the end, the research objective, contents, and the structure of the thesis are outlined.

1.1 Introduction to shot peening technologies

1.1.1 Conventional shot peening and SMAT

Shot peening [2,4,12–14] is a mechanical surface treatment widely used to generate compressive residual stress and work hardening at the surface of metallic material so as to improve fatigue properties, reduce fretting, wear and stress corrosion cracking. Generally speaking, shot peening is based on high-speed impacts induced by spherical peening media with sufficient hardness to activate inhomogeneous plastic deformation at the surface of metallic materials. When a hard shot hits a structure or a part with a high kinematic energy and sufficient force, it can create a small dimple at the surface of the material. During this process, the surface will be indented under a tensile stress and simultaneously an opposite compressive stress can be induced beneath the dimple. If the value or the magnitude of the generated stress is higher than the yield strength of the material, a residual compressive stress will be retained due to inhomogeneous spring back and plastic deformation. After a great number of impacts, a stable distributed compressive residual stress field can be produced in the near surface region, and a tensile stress variation could be generated for the

sake of stress self-equilibrium through the structure. In addition, it is always inevitably coupled with work hardening/softening activities during the multi-impacts, and thus a work hardened (cold hardening) layer can be introduced and co-exists with the stress field. Both the residual stress and the work hardening could significantly influence the properties of materials.

Most of the failures in engineering materials such as fatigue fracture, wear or corrosion, are very sensitive to properties of the material surface, and in most cases, failures initiate at the surface and propagate to the interior. As mentioned above, the compressive residual stress and work hardening are able to affect crack initiation and propagation, and thus can play an important role in the fatigue properties of materials. Moreover, some other microscopic features, such as deformation-induced phase-transformation and twining, can also alter the local mechanical behaviour of metallic materials.

Conventional shot peening technologies propel the shot media mainly using air blast systems, centrifugal blast wheels or vapour blast machines. As varieties of the shot peening process, surface mechanical attrition treatment (SMAT), or ultrasonic Shot Peening technology, was developed by using high frequency ultrasonic devices to accelerate high quality spherical shot [1]. During SMAT, the shot irregularly strikes the surface of the part with high kinematic energy in an enclosed space. These strikes induce multi-directional severe plastic deformation at the surface of the material, and coarse grains can be refined down to the nanometre scale due to multi plastic slips. Fig. 1-1 illustrates schematic presentation of the conventional shot peening and SMAT.

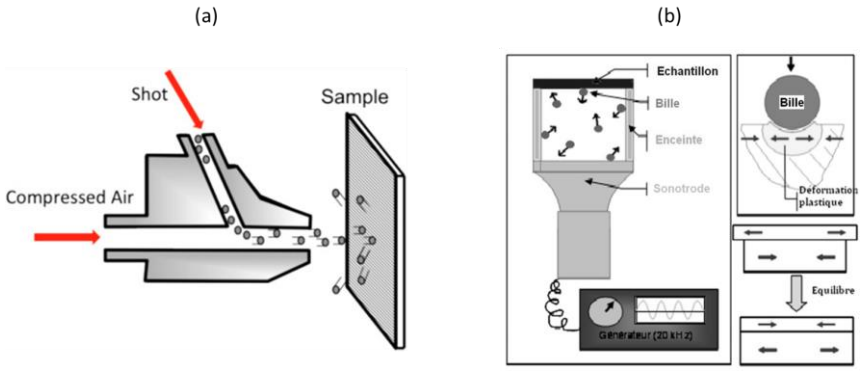

Fig. 1-1. Sketch of (a) conventional shot peening and (b) SMAT.

In addition to a high compressive residual stress field and a work hardening gradient in the near surface region, SMAT can also generate a nanostructured layer at the treated surface[1,15,16]. Metals with ultra-fine grains, especially at the nanometre-scale, possess enhanced mechanical properties compared to their conventional coarse-grained

polycrystalline counterparts, such as high strength, increased resistance to tribological and environmentally assisted damage [6–8,11,17–22], enhanced fatigue life. In addition, compared to the conventional shot peening technologies, SMAT can induce a low roughness and better surface properties for future thermo-chemical treatments, for example nitriding [23]. With these remarkable advantages, SMAT has attracted a considerable attention of the academia in recent years [1,5,8,11,18]. Besides the conventional shot peening and SMAT, other technologies which don't use shot media have also been developed, like laser shock peening for example, which can introduce a higher and deeper compressive residual stress field in the near surface region of materials [3,4,13]. This technology is based on shock wave by high power laser impulse and is out of the scope of the present work. It will thus not be further presented.

1.1.2 Nanostructured surface layer

Mechanically, the nanostructured surface layer can be generated by many surface mechanical treatment technologies, such as SMAT [24], severe shot peening [21,25], deep rolling [6], grinding [26]. All of these approaches are based on plastic deformation-induced grain refinement in the coarse polycrystalline regimes. At present, severe plastic deformation technique has gained a great interest in producing nanocrystalline materials [27–29]. Generally, several requirements should be meet in order to create nanostructures in bulk metallic materials [27], (1) prevailing high angle grain boundaries, thus a qualitative change in material properties can occur; (2) the processed material should have stable properties; (3) no mechanical damage and cracks should be generated during large plastic deformation.

SMAT has been proved as an effective method to achieve grain refinement down to nanometre scale at the surface of many metals and alloys [1,15,16,24]. Microstructure evolutions of pure Fe during SMAT [24] indicates that the grain refinement is caused by the formation of dense dislocation walls and dislocation tangles in original grains and in the refined cells (under further straining). The dense dislocation walls and dislocation tangles are transformed into subboundaries with small misorientations separating individual cells or subgrains. Afterwards, the subboundaries are changed to highly misoriented grain boundaries cells or subgrains. The subdivision takes place on a finer scale with increasing strain, and a stabilized grain size can be reached when dislocation multiplication rate is balanced by the annihilation rate so that the increase of strains could not reduce the subgrain size any longer [24]. In addition, under multi-directional peening during SMAT, the

dislocations not only interact with other dislocations in the current active slip systems, but also interact with inactive dislocations generated by previous deformation. Thus, the grains can be subdivided more effectively by the dislocation walls and dislocation tangles compared to other treatment technologies [24].

Materials with a nanocrystalline structure exhibit superior physical and chemical properties compared to their coarse-grained counterpart, for instance, low strain hardening [29], friction and wear [18,22,30], corrosion resistance [31,32], fatigue properties [6,8,21,33], and high yield strength [7,29] according to the well-known Hall–Petch relationship (Eq. (1-1)) [34,35].

$$\sigma_y = \sigma_0 + Ad^{1/2} \tag{1-1}$$

where σ_y is the yield stress, σ_0 is the lattice friction stress, A is the strengthening coefficient, d is the grain size. However, several studies imply that the nanostructured layer generated by SMAT can decrease the corrosion resistance due to the presence of microstrain, defect or cracks[36,37].

In terms of fatigue properties, it has been shown that the formation of nanostructures by SPD can lead to a significant increase in fatigue strength [6,8,21,38]. However, these improvements are mostly found under high cycle fatigue tests. Under strain-controlled low cycle fatigue with high strain amplitudes, the fatigue lifetime maybe decreased due to a deleterious effect of nanostructured grains on the resistance to fatigue crack growth [38]. Studies show that the key of enhanced fatigue properties lies in the potential of nanocrystals to suppress the crack initiation, since the scale of nano grains is below the critical persistent slip bands for failure initiation [33]. However, the crack propagation resistance of materials is degraded when the grain size is reduced.

In fact, many nanostructures generated by SPD are accompanied by an increased surface roughness and defects numbers, which would promote crack nucleation. In addition, fatigue-induced grain growth [39,40], residual stress and work hardening play important role in crack initiation and propagation as well. Therefore, it could be interesting but also challenging to thoroughly understand the fatigue behaviour of nanocrystalline materials.

1.1.3 Residual stress

Residual stress is usually defined as the stress, which remains in a mechanical part not actually subjected to any external loads. It is the result of the metallurgical and mechanical history of the part during its manufacture or treatment [41]. Residual stresses inside a

structure can modify the theoretical stress field, and thus have a positive or negative effect on the mechanical properties of materials. For example, on the one hand, the presence of compressive residual stresses in the surface layers can increase the fatigue strength and the resistance to stress-corrosion cracking. On the other hand, the tensile residual stresses could promote the stress corrosion of materials [41]. Residual stress can be introduced in mechanical parts during nearly all the manufacturing processes through mechanical, thermal or chemical approaches. Especially, some mechanical surface treatment technologies (e.g. shot peening, case hardening) are widely used to generate a compressive residual stress field in the region close to the surface of a structure to improve its fatigue properties. This is due to the fact that compressive residual stress can increase the surface resistance to crack initiation and reduce the crack propagation rate through modifying the stress field [4,8–10,42].

From length scale perspective, residual stresses are generally classified as Type I, II and III based on the length over which the stresses equilibrate [9], as shown in Fig. 1-2. Type I stresses self-equilibrate over macroscopic dimension of the component. It ignores the polycrystalline or multiphase nature of the material, and is often calculated using finite element tools. Type II residual stresses self-equilibrate over the dimension of several grains, and are the result of strain incompatibility between grains, created by the orientation dependent elastic and plastic anisotropy. Type III stresses exist over atomic dimensions and balance within a grain, for example, those caused by dislocations and point defects. [9,10].

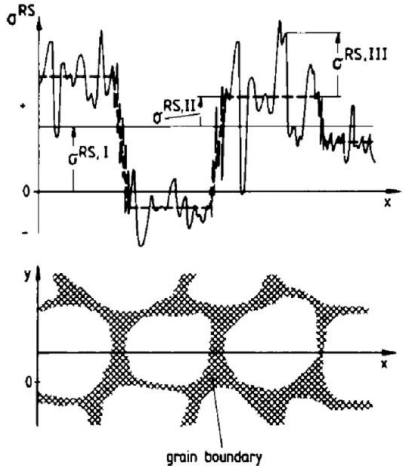

Fig. 1-2. Illustration of the Multi-scale nature of residual stresses in polycrystals [43,44].

In general, the Type I residual stresses, also named as macroscopic residual stresses, are widely used to increase the mechanical properties of materials in engineering fields. The Type II and III residual stresses, as inter- and intra-granular residual stresses, are mainly

studied to analyse materials from a physical viewpoint, such as slip bands and defects at the grain level [44,45]. Based on stress self-equilibrium relationship, when a compressive residual stress is generated in the near surface region by surface treatment technologies, there must be a residual stress field of tensile nature to ensure the equilibrium of the stress state of the whole structure. Similarly, microscopic tensile residual stresses could also be contained between or within grains, which are more prone to damage accumulation in the form of slip or twinning, subsequent formation of defects and micro-voids that lead to crack initiation and propagation during cyclic loading [44]. Therefore, a good understanding of all the three types of residual stresses and their effect on mechanical behaviour at different scales is crucial for the prediction and the optimization of mechanical properties of materials.

1.1.4 Work hardening

In addition to the generation of residual stress through inhomogeneous plastic deformation, there is inevitably the presence of work hardening in the material. Work hardening, also known as strain hardening, is a macroscopic phenomenological description of most metals which become strengthened when they are plastically deformed. At the microscopic scale, plastic deformation occurs through dislocation generation and movement within the crystal structure of materials. As dislocations develop, they can encounter and interact with other dislocations or crystalline defects, thereby producing resistance to further development [46].

Based on the dislocation storage and recovery mechanism, the work hardening process can be divided into four stages [47]. In the early stage of plastic deformation (Stage I), only easy glide occurs during single slip in single crystals with a low work hardening rate caused by storage of dislocation dipoles and multipoles on the primary slip system. After a certain strain level, single crystals exhibit a transition from a low hardening rate to a much larger rate due to the storage of dislocation tangles on multiple slip systems. This Stage II of hardening presents an approximately linear hardening behaviour with a relatively high work hardening rate and occurs in both single crystals and polycrystals. The stage III corresponds to a monotonic decrease of the work hardening rate with an increase of the flow stress, and a saturated stress is reached by the end of this stage when recovery balances dislocation storage. When the material is subjected to large strain, the fourth work hardening stage (Stage IV) intervenes with a further decrease of hardening rate without marked changes in the character of obstacles to dislocation movement. This stage is caused by the accumulation of dislocation debris, perhaps as a by-product of dynamic recovery [47].

Concerning the cyclic deformation response of polycrystals, hardening / softening behaviour is rather complex and dislocations tend to move in more planar ways during cyclic loading. The internal variables (e.g. effective stress, inter/intra-granular back stresses) can be related to several types of microstructures (e.g. short- and long-range interactions of dislocations), and dislocation density as well as configuration of dislocations cycle by cycle evolvement under different loading conditions [48–53]. In addition, phase transformation induced by stress or plastic deformation could also exhibit a macroscopic hardening effect of materials [8,54,55].

Up to now, many studies have confirmed the benefits of surface mechanical treatment in improving the fatigue properties of metallic materials. Most studies focus on the effect of residual stress and its working mechanism in service, whereas the effect of work hardening is often neglected due to its difficulty to be characterized and evaluated. In fact, work hardening generated by peening technologies can also influence the local stress-strain behaviour and microstructure of materials, and should have a considerable effect on crack initiation and propagation during cyclic loading. Hence, the contribution of work hardening in fatigue properties of material treated by peening technologies should be well considered in different applicative conditions.

1.2 Experimental study of shot peened and SMATed material

1.2.1 Gradient microstructure features

As a kind of ultrasonic peening technologies, SMAT is able to project spherical shots with a high energy to repeatedly strike the surface of materials. It allows introducing a large number of dislocations and/or deformation twins, which can lead to refined grains down to the nanometre scale at the surface[1,16,24]. Underneath the nanostructured layer, there is a mixed grain size region, where a mixture of ultra-fine grains and relatively large grains co-exist. In addition, the inhomogeneous plastic deformation can generate high compressive residual stresses and work hardened region close to the processed surface, while tensile residual stresses are simultaneously introduced beneath to equilibrate the stress field for the whole structure. As the effect of multi-impacts gradually decreases from the treated surface to the bulk of the treated part, the residual stresses and work hardening should also have a gradual variation trend in the near surface layer. These elements including the nanostructured layer, the mixed grain size region, the gradual variations of residual stresses, and work hardening together constitute the gradient microstructure features of SMATed

materials, as shown in Fig. 1-3. Besides, for some austenitic steels, martensitic transformation can also be induced during SMAT which increases the complexity of the gradient features [8,16].

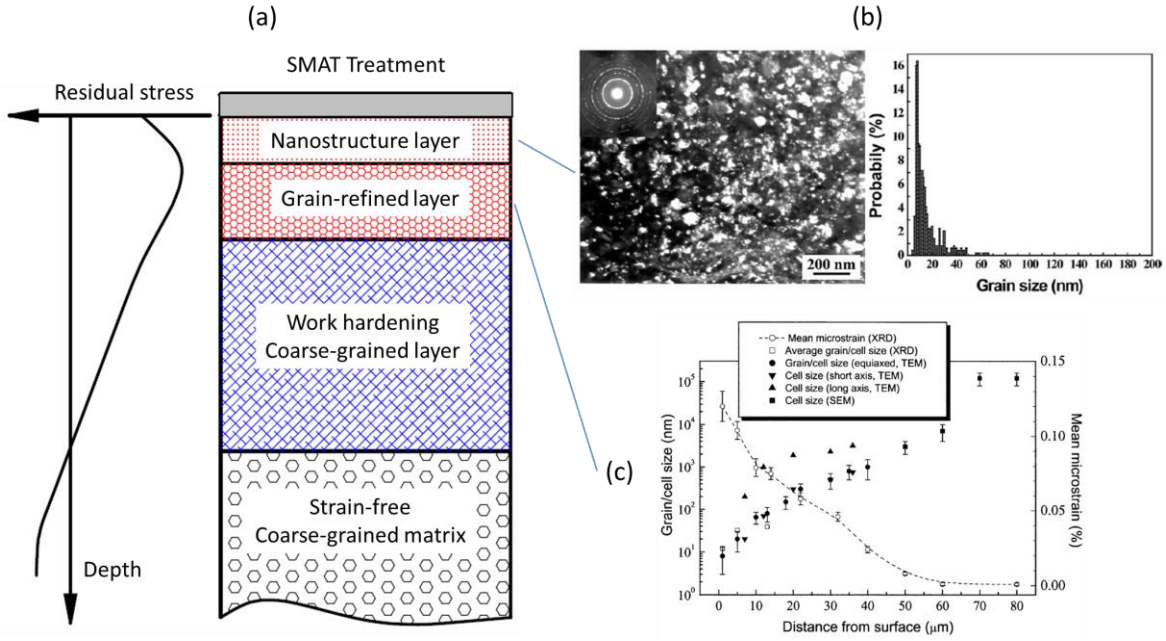

Fig. 1-3. Illustration of gradient microstructure features generated by SMAT. (a): schematic presentation of gradient microstructure; (b): typical TEM observations of ultrafine grains at the top surface for SMATed AISI 304 stainless steel [16] and (c): in depth variations of the grain/cell size and the mean microstrain from the treated surface of SMATed Fe sample [24].

In general, with SMAT, the coarse grains can be refined down to about 10 nm at the top treated surface, and the grain size increases with the depth in a thickness of about 50-60 μm for most metallic materials as a function of the treatment conditions, such as Fe [24], austenitic steel [7,8,16], low carbon steel [18], aluminium [56], titanium [57,58]. Underneath the nanostructured layer, the obvious plastic deformation affected microstructure can be highlighted through SEM, EBSD, TEM and XRD. This gradient features can be indirectly characterized by some microscopic mechanical testing techniques, for example nano-indentation [58,59], micro-hardness testing [1,17], micro-pillar compression [59,60].

1.2.2 Mechanical properties

1.2.2.1 Monotonic behaviour

As indicated in Section 1.2.1, the gradient microstructure features can be generated by SMAT, including nanostructured layer at the treated surface, mixed grain-refined layer, residual stress and work hardening fields in the near surface region. This typical

microstructural gradient can significantly affect the mechanical behaviour of SMATed materials. It is well known that the tensile strength of a material is strongly dependent on the grain size, according to Hall-Petch relationship (Eq. (1-1)). Therefore, the nanostructured layer generated by SMAT at the surface can exhibit very high tensile yield strength, as shown in Fig. 1-4.

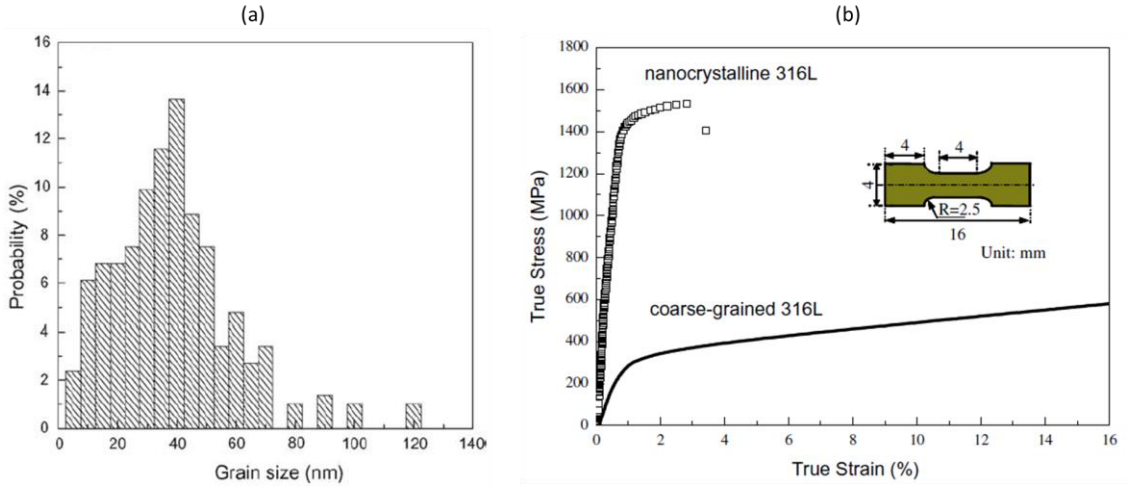

Fig. 1-4. (a) Grain size distribution in the region at about 6–8 μm beneath the polished top surface; (b): comparison of tensile true stress–strain curves for the nanocrystalline layer and the coarse-grain 316L samples [7].

Chen et al. [7] performed an uniaxial tensile test at room temperature for a 316L nanocrystalline (mean grain size: ~40 nm, Fig. 1-4a) dog bone-shaped specimen with a thickness of 15 μm using a microforce testing system. The result presented in Fig. 1-4b shows that the nanocrystalline layer exhibits a much higher yield strength and ultimate strength compared to its coarse-grain counterpart (average grain size: 20 μm). However, the elongation-to-failure of the nanocrystalline layer (about 3.4%) is significantly reduced due to its very low dislocation storage capacity inside the grains [7].

Underneath the grain-refined layer, the effects of residual stress and work hardening can also be indirectly identified by uniaxial tensile tests using progressive material removal method. Petit et al. [61] studied the tensile behaviour of the nanocrystalline and transition layer generated by SMAT. The tensile test samples were prepared by using mechanical polishing to remove the irrelevant part of the material, as shown in Fig. 1-5. The three experimental stress-strain curves, respectively corresponding to ‘nanocrystalline + transition layer’, ‘transition layer’ and ‘core material layer’, show an obvious gradient feature of the SMATed material. The tensile strength is significantly improved in the region

close to the treated surface, while the hardening rate and the ductility are reduced, which is consistent with the result presented in Fig. 1-4.

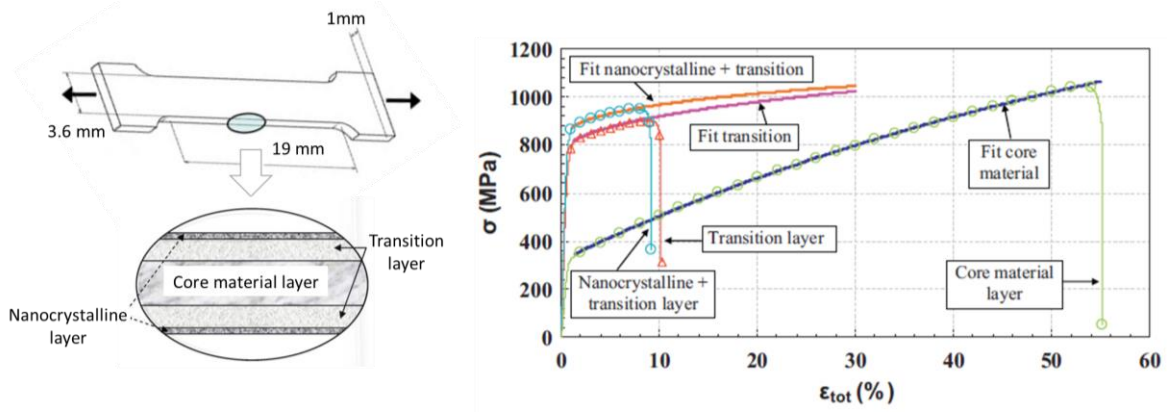

Fig. 1-5.True stress - strain curves and the fits for the transition layer, the core material and the nanocrystalline + transition layers of a SMATed 316L steel [61].

In addition to the micro uniaxial tensile test, the mechanical properties of the gradient microstructures generated by SMAT have also been widely evaluated by Nano-indentation and micro-indentation. Lu et al. [1] studied the properties of a SMATed Fe sample and its annealed state. The annealed in-depth hardness variation with respect to the treated surface was measured using Nano-indenter, as shown in Fig. 1-6. It shows that there is nearly no change in hardness profile after the sample was annealed at 593 K for 1 hour. In fact, this annealing permits the residual stresses in the region from the depth of 50 μm to 200 μm to relax. This result implies that the high hardness in the surface layer does not result from the residual stresses induced by the SMAT. In addition, after the recrystallization of the nanostructures and the formation of coarse grains due to annealing, the hardness close to the surface layer drops to that of the coarse-grained matrix, which indicates that the hardness increase induced by SMAT is mainly related to the grain refinement [1].

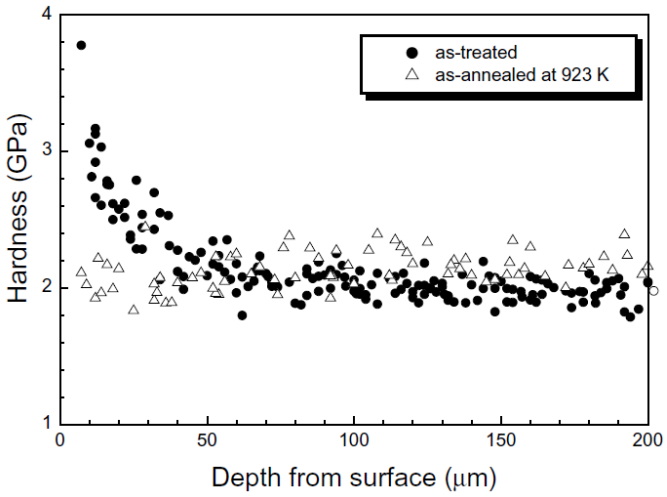

Fig. 1-6. In-depth variation of hardness from the treated surface for the SMATed Fe sample and for the SMATed-annealed (at 593K for 30 min) sample [1].

1.2.2.2 Fatigue properties

Compared to monotonic deformation, the mechanical behaviour of gradient microstructure features during cyclic loading is much more complex. Little previous work was conducted to study the cyclic hardening / softening behaviour of SMATed materials, and most studies are focused on the improvement of fatigue life due to SMAT. In fact, as indicated in Section 1.2.1, the nanocrystalline structure, residual stress and work hardening significantly influence the crack initiation and propagation during cyclic loading. Roland et al. [8] studied the effect of SMAT combined with subsequent annealing on fatigue life of a 316L stainless steel under high cycle fatigue, as illustrated in Fig. 1-7.

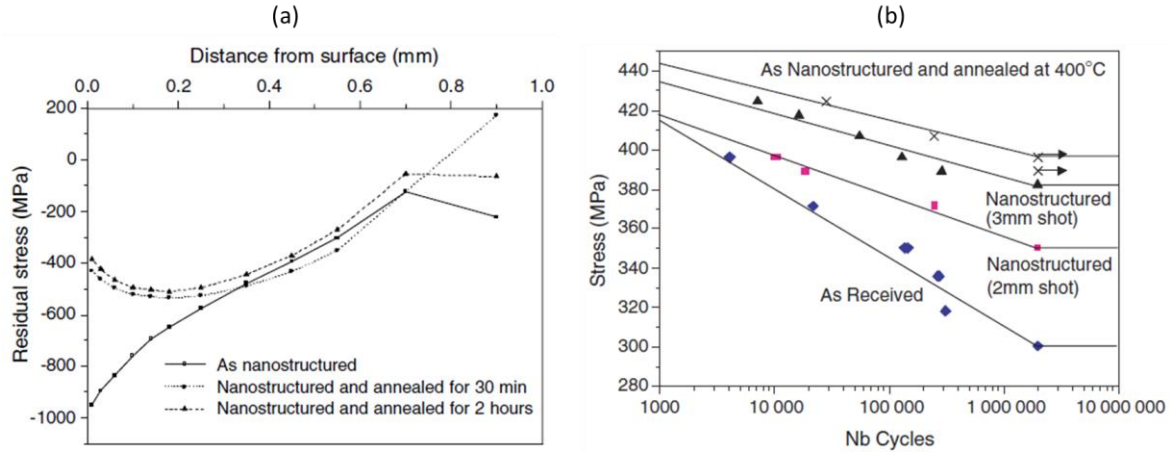

Fig. 1-7. (a): In-depth residual stress distribution after SMAT and subsequent annealing treatment (at 400 °C); (b) S/N curves of different conditioned samples [8].

It can be seen in Fig. 1-7a that SMAT generated a compressive residual stress field inside the structure with a very high value close to the treated surface. The subsequent annealing treatment lead to residual stresses relaxation by more than 50% in the near surface

due to the annihilation of dislocations induced by the annealing [8]. The S/N diagram for different treatment conditions shown in Fig. 1-7b implies a significant increase of fatigue strength of the nanostructured stainless steel compared to the untreated material. In addition, the fatigue strength of annealed samples is improved by approximately 5–6% compared with the nanostructured state. This phenomenon might be attributed to a suitable annealing treatment leading to an enhanced ductility, which could even further improve the LCF and HCF resistance of the material [8].

Sun et al. [62] studied the low cycle fatigue behaviour of a biomedical 316L steel treated by SMAT using strain controlled tension-compression fatigue tests with a strain amplitude ranging from ±0.3% to 1.25%. The obtained results show that the stress amplitude of the SMATed samples is significantly enhanced compared to the untreated ones, while the fatigue strength represented by the number of cycles to failure is not improved under high strain amplitudes [62]. In addition, other studies show that SMAT can also increase the fatigue life of titanium alloy [63], aluminium alloy [64,65] under low cycle fatigue tests. However, the fatigue life could be reduced when a longer treatment time duration is applied [65]. Moreover, SMATed samples could exhibit a different hardening / softening behaviour compared to the untreated ones during cyclic loading due to the gradient microstructure features [62,63].

In summary, it has been confirmed by experiments that the gradient microstructure features generated by SMAT can significantly improve the fatigue life of metallic materials under high cycle fatigue [8,33,66–68]. However, these benefits of SMAT under low cycle fatigue with high strain amplitudes seems still controversial [63–65]. In fact, the decrease of ductility of the generated nanocrystalline layer could induce a negative effect on the crack initiation and propagation. Moreover, the beneficial effect of compressive residual stresses could be much reduced due to their quick relaxation during cyclic loading with high strain/stress amplitudes. These different aspects will be discussed in the following sections.

1.2.3 Residual stress relaxation

Relaxation of residual stress can be occured during the service period due to thermal or mechanical loadings. The residual stress relaxation during fatigue has been widely investigated through various experimental approaches [42,69–77]. Results indicate that the residual stress relaxation increases with the maximum applied strain amplitude , and the residual stresses relaxation essentially occurs during the first cycle, followed by gradual relaxation during the fatigue lifetime [42]. The relaxation during the first cycle depends on

the monotonic yield strength of the material in tension and compression, while the relaxation during the subsequent cycles is related to the cyclic yield strength, thus dependent on the cyclic plastic strain amplitudes [42,78].

Dalaei et al. [42] investigated the residual stress stability of a shot peened micro alloyed steel under fully reversed strain-controlled push-pull fatigue tests at room temperature. The residual stress relaxation during the first and subsequent cycles under different strain amplitudes is illustrated in Fig. 1-8. It shows that the compressive residual stress in the near surface region was almost completely relaxed after the first cycle at $\Delta\varepsilon/2 = \pm 1\%$, while for $\Delta\varepsilon/2 = \pm 0.6\%$, the residual stress keeps one half of the initial values after the first cycle, and it remaines unchanged under a strain amplitude of ±0.25%. At the half fatigue lifetime, there still remains a certain amount of residual stress in the near surface region under strain amplitudes from ±0.25% to ±0.4%. Comparatively, all of compressive residual stress had been relaxed under stain amplitude of ±0.6%. Fig. 1-8 implies that the residual stress relaxation takes place mainly in the first several cycles, and then decreases gradually while the cyclic loading continues.

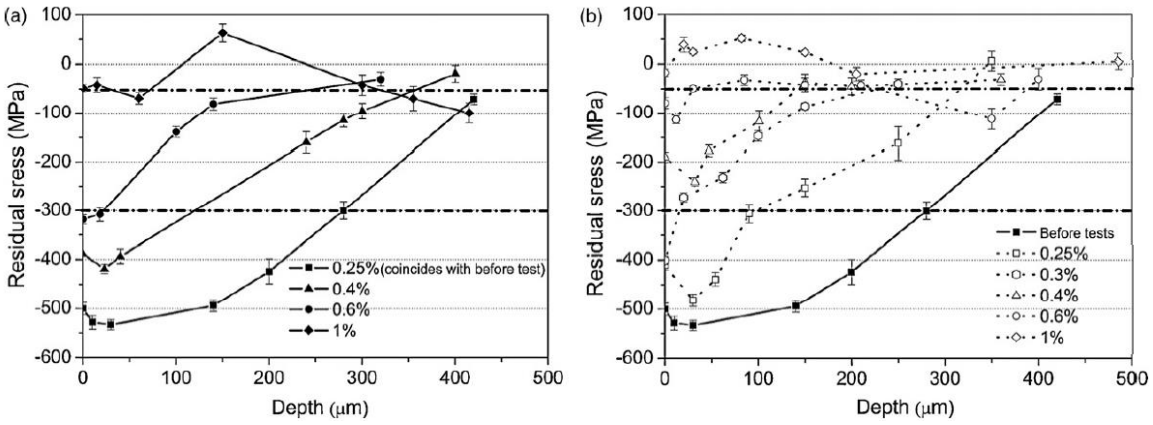

Fig. 1-8. Longitudinal residual stresses in depth variation obtained after different number of cycles (a) N= 1; and (b) N=Nf/2, under different strain amplitudes [42].

In addition, the stability of residual stress during fatigue loading is related to the surface treatment methods [78]. Nikitin and Besel [78] indicate that the near-surface residual stress, which is produced by consecutive deep rolling & annealing as well as high temperature deep rolling, presents more stable behaviour under strain-controlled low cycle fatigue at room temperature than is the one generated by conventional deep rolling. In order to accurately predict the fatigue behaviour of materials, the residual stress relaxation during cyclic loading is also estimated by finite element method through reconstructing an initial stress field inside the structure (e.g. [74,79–81]). This will be discussed in other next sections.

1.3 Multi-scale modelling of shot peened and SMATed materials

Section 1.2 reviewed the typical gradient microstructure features of SMATed materials and their mechanical properties characterized through different techniques. Modelling and numerical simulation are also very useful approaches which allow a better understanding of deformation mechanism, process optimization as well as life prediction of materials. As indicated in Section 1.1, the characteristics of a SMATed material include a thin nanocrystalline layer and a mixed grain-refined layer at the treated surface, along with residual stress and work hardening fields present down to deeper region. Given the complexity of these parameters, it would be a great challenge to precisely consider these characteristics in predicting and optimizing the mechanical properties of SMATed materials.

1.3.1 Introduction to multi-scale modelling

Plasticity is a multi-scale, multi-mechanism phenomenon manifested of irreversible microstructure rearrangement associated with line and point defects in crystals [82]. Metal plasticity is fundamentally associated with the nucleation and migration of dislocations in crystals and polycrystals as the underlying basis for microstructure rearrangement or evolution during plastic flow [82]. From the viewpoint of length scale, it can be characterized from atomistic scale to macroscopic continuum plasticity, as shown in Fig. 1-9.

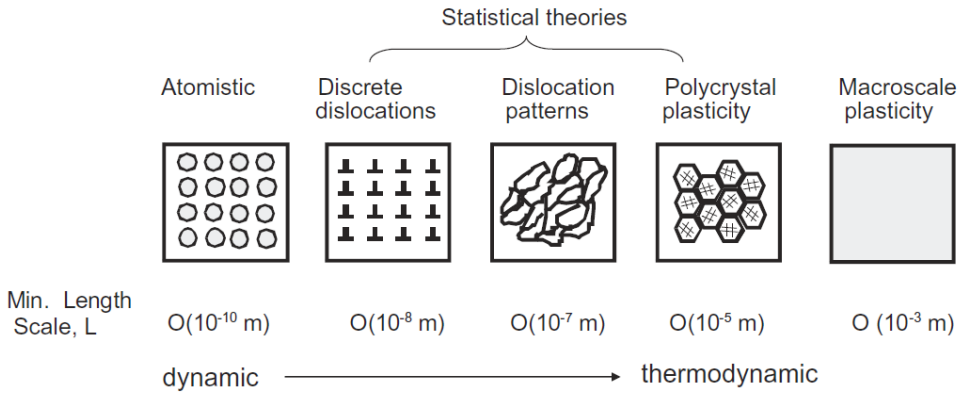

Fig. 1-9. Hierarchy of length scales in metal plasticity ranging from atomic (dislocation cores) to macroscopic scale [82].

At the macroscopic scale, the material can be considered as a homogeneous continuum body, and the elastic-plastic behaviour is studied in the continuum mechanics framework. In this case, phenomenological constitutive theories are mainly used to characterize the

stress-strain relationship of materials, involving yield law (e.g. Tresca, Von Mises, Hill), hardening rules, and so on. In general, the inelastic behaviour of a solid can be described in rate-independent plasticity or in viscoplasticity, and the relevant constitutive models have been successfully developed and used in industry, such as the rate-independent and rate-dependent nonlinear isotropic / kinematic hardening model [83], Johnson-Cook model [84]. In addition, the macroscopic constitutive model can couple other physical parameters, for example thermo-plasticity with the material parameters strongly dependent on the temperature [85].

However, macroscopic constitutive models are not sufficient to consider the deformation mechanisms of materials. This can be achieved by the micro-mechanical modelling methods at grain level. Crystal plasticity has been widely used to describe microscopic evolution of materials during plastic deformation, such as dislocation, disorientation, phase transformation, or twining [86]. These features can be quantitatively considered in the constitutive models based on the microscopic observations and measurements, and they can be effectively related to the macroscopic mechanical behaviour of polycrystals through for example finite element modelling [86] and self-consistent approaches [87–92].

In addition, more physically based modelling studies at small scales, for example discrete dislocation dynamics (DDD) and molecular dynamics (MD), have been proposed and are being developed to describe the deformation behaviour at dislocation and atomic scales. This aspect will not be further discussed in this thesis.

1.3.2 Simulation of shot peening process

Mechanical surface treatment such as shot peening is a complex multi-physics process, and it is thus very difficult to model it with analytical methods. Finite element simulations about shot peening have been performed in previous studies concerning grain refinement, residual stress distribution, work hardening variation, surface roughness, etc. [93–95,95–100].

1.3.2.1 Material constitutive model

Shot peening is a dynamic process, and strain rate plays important roles in residual stress distribution as well as induced plastic strains. Therefore, rate-dependent plasticity theory should be included in the constitutive model. Johnson-Cook model (Eq. (1-2)) [84] is widely used in shot peening simulation as it is able to effectively describe the rate-

dependent plasticity flow of materials with a simple form and few material parameters [93,94,101].

$$\sigma_y = [A + B(\overline{\varepsilon})^n]\left[1 + C\ln\left(\frac{\dot{\varepsilon}_p}{\dot{\varepsilon}_0}\right)\right]\left[1 + \left(\frac{T - T_{\text{room}}}{T_{\text{melt}} - T_{\text{room}}}\right)^m\right] \tag{1-2}$$

where, $\overline{\varepsilon}$ is the equivalent plastic strain, $\dot{\varepsilon}_p$ and $\dot{\varepsilon}_0$ are the applied and reference deformation rates; T, T_{room} and T_{melt} are respectively the applied, reference and melting temperatures; A, B, C, n and m are material parameters.

In addition, the combined kinematic/isotropic hardening model in its viscous form (Eq. (1-4)) can also be used to describe the rate-dependent plastic flow behaviour for shot peening simulation [95,100,102].

$$f = J_2(\boldsymbol{\sigma} - \boldsymbol{X}) - R - k \tag{1-3}$$

$$\dot{p} = \langle f/K \rangle^n \tag{1-4}$$

where, f is the yield function; $\dot{p}$ is the equivalent plastic strain rate; $\boldsymbol{\sigma}$, $\boldsymbol{X}$ are respectively Cauchy stress tensor and back stress tensor. The scalar R characterizes the isotropic hardening, and k represents the initial yield stress of material. K and n are material parameters. The McCauley brackets $\langle\cdot\rangle$ are used here to ensure that when $f < 0$, i.e. inside the elastic domain, $\dot{p}$ cancels out continuously [83].

Johnson-Cook model is widely used in shot peening simulation due to its simple form and easy implementation. The thermal effect can be effectively considered in this constitutive model through the temperature parameter T. In addition, some microstructure features such as grain size and dislocation can be incorporated into the constitutive equation to study the mechanism during shot peening (e.g. [93,94]). However, Johnson-Cook model is usually applied in the high strain rate regime (dynamic plasticity), and it may lead to a significant underestimation of stress in the low strain rate regime [83]. The parameters in Eq. (1-2) are usually identified through monotonic tensile curves, and they are unable to describe the complex cyclic plastic behaviour of materials. In comparison, the combined kinematic/isotropic hardening model is able to simulate the complex cyclic strain hardening behaviour of materials through non-linear kinematic hardening and isotropic hardening rules, eventually associated with strain range memory effect [103]. Nevertheless, the latter needs much more experiments and complex algorithms for identification. Besides, some other elastic-plastic constitutive relations are also used in shot peening simulations, such as power-law hardening model [99], Cowper-Symonds model [97,104], multi-linear elastic–

plastic model [105]. In addition, physically based constitutive model for example crystal plasticity is also used to study the microstructure evolution during shot peening [106–108]. However, there are few studies concerning the use of crystal plasticity models to model shot peening process.

As for the properties of shot, it is mostly considered as a rigid ball for the sake of simplification [98,102,105]. Furthermore, some authors used a simple elastic-plastic model to describe the behaviour of the shot in some conditions. For example, a bilinear elastoplastic model was used to describe the mechanical behaviour of a ceramic bead [109], and the deformable elastic-plastic steel ball was characterized by a linear interpolated relationship obtained from monotonic tensile tests [110].

1.3.2.2 Modelling of shot peening process

Using rate-dependent constitutive models, many studies have been performed to numerically investigate the shot peening process based on finite element method. The rapid development of computing capacity makes the simulation of multi-impacts possible, and it attracts great interests for deeply studying the shot peening process, including generation of residual stress, work hardening, grain refinement, surface damage, and so on.

Meguid et al. [111] carried out shot peening simulation with a large number of impacts to study the effect of rigid and deformable shots as well as the coverage and the peening intensity on the induced residual stress field and the plastically deformed zone. Frija et al. [98] integrated a damage law in the constitutive model to simulate the shot peening process with several rigid balls. The generated in-depth profiles of residual stress, the plastic deformation and the superficial damage have a good agreement with the experimental results. Klemenz et al. [102] analysed the topographies and residual stresses of a AISI 4140 plate after single and double impacts with finite element simulation and experimental measurement, and a good correlation was obtained. Mylonas et al. [105] investigated the effects of the shot type, velocity and impinging angle on the residual stress field, surface roughness, cold work and geometrical stress concentration factor of a AA7449-T7651 plate. Some other similar simulations were also performed [101,109,110].

Several simulation work focuses on surface nanocrystallization and grain refinement mechanism during severe shot peening. Bagherifard et al. [95] developed a finite element model of severe shot peening to study the treatment conditions that lead to surface nanocrystallization. The mechanical behaviour of material is described by a combined isotropic/kinematic hardening model, and the formation of the nanocrystalline structure is

estimated through the accumulated equivalent plastic strain [95]. Zhang [93] simulated the grain refinement during SMAT based on finite element modelling by using an empirical equation to describe the relationship between grain size and accumulated equivalent strain. The mechanical behaviour of the refined grains was considered by Hall-Petch equation (1-1), which was incorporated in the Johnson-Cook model to update the computation and simulation [93]. Hassani-Gangaraj et al. [94] studied the surface nanocrystallization during severe air blast peening process based on finite element method by linking the dislocation density evolution with the macroscopic Johnson-Cook equation through accumulated plastic strain. The grain refinement gradient in the surface layer was estimated by dislocation cell size. The result of simulation is in good agreement with the experimental results obtained by TEM / SEM [94].

In comparison, SMAT is a much more complex process due to multi-impacts with random angle. Zhang [93] studied the microstructure evolution during SMAT through finite element simulation. In this study, the effects of ball parameters (size, velocity, impact angle) and treatment conditions on residual stress and plastic deformation was numerically analysed [93]. Astaraee et al. [104] simulated the SMAT process by impinging the representative target of a plate using a sequence of shot in a random manner. The residual stress and the thickness of the plastically deformed layer obtained by the simulation are in a good agreement with the experimental measurements [104]. Moreover, Rousseau et al. [108] simulated the multi-impact during ultrasonic shot peening using crystal plasticity model and coupled with dislocation dynamics. The compressive residual stress, the evolution of dislocation density and disorientations inside grains were studied through single and multiple impacts [108].

In a word, the simulation of shot peening process has been widely studied in the framework of macroscopic continuum mechanics. Previous work is mainly focused on predicting residual stress and studying grain refinement. In order to thoroughly understand the deformation mechanism, simulation of shot peening and/or SMAT at microscopic scale, for example based on crystal plasticity and dislocation dynamics [108,112], should deserve more attentions.

1.3.3 Modelling of residual stress and work hardening

Prestress engineering has been developed for decades in order to increase the fatigue resistance of mechanical components, which consists in optimizing the residual stress field inside a structure [41]. The generation of residual stress due to severe plastic deformation is

often coupled with a work-hardened region, which could have a significant effect on the mechanical behaviour of material. Therefore, being able to precisely characterize and model the residual stress as well as the work hardening is of great importance.

1.3.3.1 Characterization of residual stress and work hardening

Accurate characterization of residual stress and work hardening through experimental approach is a crucial step for the subsequent modelling and prediction of mechanical properties of materials and structures. The residual stress can be evaluated through for example strain measuring technique, post-stress relaxation measurement, sectioning and material removal methods. In general, we divide them into the following destructive and non-destructive approaches [9,41]:

i. Destructive measurements. This approach is based on destroying the equilibrium relation in the mechanical component, and the residual stress is then evaluated from the relaxed state of the structure. In most cases, the residual stress is indirectly obtained by monitoring the change in strain [113]. This kind of approach is sensitive to the Type I residual stress, and thus only the macroscopic residual stress can be analysed through these destructive methods. The popular techniques are incremental hole drilling method [114], curvature and layer removal method [115] , crack-compliance method [116].

ii. Non-destructive measurements. For polycrystalline materials, the microscopic characteristics can be quantitatively identified by some physical approaches. For example, residual stress can be evaluated by measuring the lattice strain and studying the lattice spacing based on diffraction techniques, e.g. x-ray diffraction (XRD) and neutron diffraction [117]. XRD detects the residual strain at the surface of the material, and the neutron diffraction technique is able to perform the residual stress analysis within a volume of the sample. The peak shift of the diffraction wave is sensitive to the first two types of residual stress (Type I and II), whereas line broadening is sensitive to the second and third types (Type II and Type III) [9,41]. It is worth noting that the two diffraction techniques have been widely used to study the residual stress on both macroscopic and microscopic scales [117–122].

Moreover, High resolution EBSD also provides a powerful means to determine the lattice strain with resolutions ranging from sub-micron scale in back-scattered geometry to a few nanometres in cross-section [44]. Through High resolution EBSD , quantitative

residual elastic strain and stress at grain level can be evaluated, which is much beneficial for mechanism analysis of residual stress and deformation in a microscopic scale [123–126].

Besides the above mentioned techniques, the residual stress can also be indirectly evaluated by ultrasonic [127], indentation (e.g. [128,129]), photoelastic methods [130]. In comparison, the quantitative characterization of work hardening by experimental approaches is still in the stage of exploration. As indicated in Section 1.1.4, work hardening is just a macroscopic description of some mechanical phenomena during plastic deformation due to the microstructure evolutions, for example dislocation generation and annihilation, martensitic transformation, twining. These microscopic features change the deformation resistance, and affect the macroscopic stress-strain behaviour. Hardening/softening phenomenon can thus be observed during monotonic or cyclic plastic deformation.

In fact, decrease of crystalline size and increase of macrostrain during work hardening can induce a larger diffraction peak broadening [131]. Identification of dislocation density through the diffraction peak broadening obtained from XRD has been discussed in previous studies [132–135]. Some authors have qualitatively correlated the work hardening to plastic strain using the value of diffraction peak broadening through, for example the equivalent true plastic strain [131,136–139]. Prevéy [139] developed an empirical relationship between the amount of cold work and the diffraction peak width, as shown in Fig. 1-10a. The percentage of cold work was taken as the true plastic strain's absolute value of Rene 95 specimens in uniaxial compression and tension tests. It shows that the evaluated diffraction peak width fell in the same curve for the different deformation forms [139]. Afterwards, some authors used the diffraction peak width to qualitatively estimate the work hardening induced by shot peening. For instance, Li [43] evaluated the in-depth variation of equivalent plastic strain of a shot peened titanium alloy part by relating the diffraction peak width of the treated material and of the several uniaxial tensile tests, as shown in Fig. 1-10b.

(a)

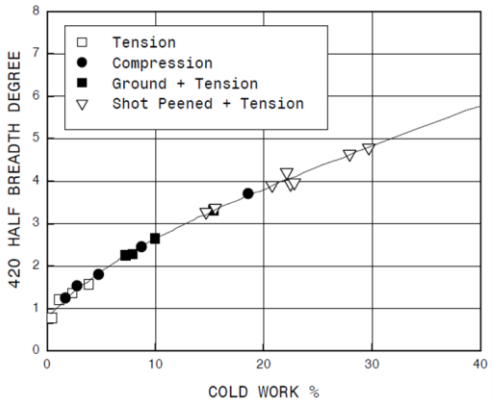

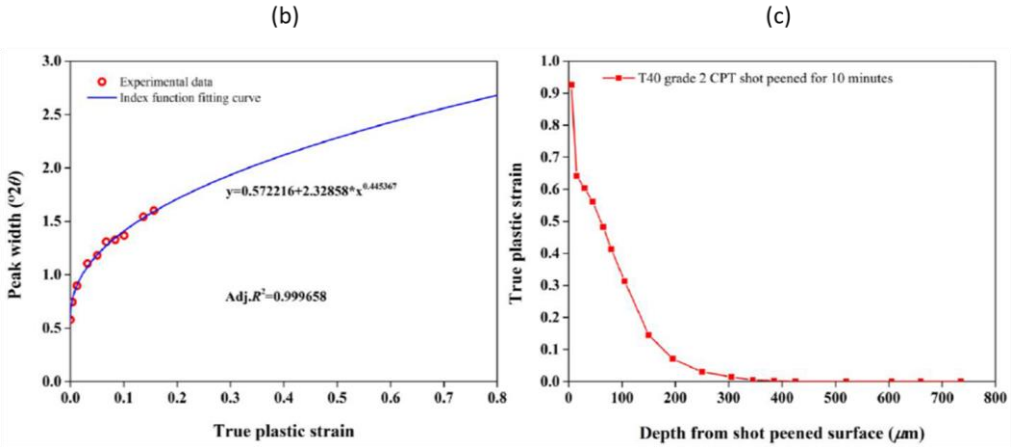

Fig. 1-10. Empirical relationship between the diffraction peak width with cold work (or plastic strain): (a) diffraction peak width to percentage of cold work for Rene 95 samples [139]; (b): diffraction peak width to true plastic strain and (c) true plastic strain distribution in a shot peened titanium alloy [43].

According to the qualitative relationship between plastic strain and diffraction peak width, the mechanical properties of materials can be well evaluated by taking into account the work hardening in the FE model, such as fatigue properties [136,140], Nano-indentation [137].

At the microscopic scale, work hardening can be quantitatively analysed based on dislocation theory with the help of microscopic observations, such as TEM, EBSD. [47,141–144]. It is very beneficial for the physically based modelling of plastic deformation [145,16,49,146]. Moreover, EBSD analysis provides possibilities for characterizing the microstructure evolution during plastic deformation. Grain misorientation, plastic slips and twins can be clearly observed and analysed through EBSD, which has been widely used to characterize the work hardening due to shot peening and other treatment technologies [147–149].

1.3.3.2 Reconstruction of residual stress and work hardening

Reconstruction of residual stress field and work hardening is of great importance to prescisely predict the mechanical behaviour of materials processed by shot peening. During the past decades, the reconstruction methods have been widely developed, and generally they includes the following several approaches: inverse eigenstrain [150–153], pre-deformation [154], boundary element method [155], definition of initial condition [77,137].

One of the popular approaches to reconstruct the residual stress field is based on the concept of permanent inelastic strain, also known as eigenstrain [156,150–152,157]. In this method, inelastic strains (eigenstrains) are the sources of deformation incompatibility and provide a powerful technique for the representation of residual stress [158]. Within a FE

framework, the arbitrary eigenstrain fields can be implemented by using pseudo-thermal strain, expressed in terms of optimized anisotropic thermal expansion coefficients which vary inside the structure, together with a uniform temperature change [152,153,157–161]. The eigenstrain approach has been successfully used to predict the inelastic strain and reconstruct the residual stress field generated in various applications, for example shot peening [156,152,162,157,163,151,160], laser peening [158,159,161,164,165], welding [151,166], for structures with more or less complex geometrical shapes. In addition, the formulation of the eigenstrain approach ensures strain compatibility, global stress equilibrium, and necessitates appropriate boundary conditions [157,158]. Besides the eigenstrain method, similar work has also been conducted to reconstruct the residual stress field for example using inverse approach [167,168], pre-deformation [80,154], and boundary element method [155].

In general, linear elastic or elastic perfectly plastic behaviour is used to describe the mechanical behaviour of materials while predicting inelastic strain and reconstructing the residual stress field through the eigenstrain method [150,151,157–160,162,169]. Thereby, the hardening behaviour of materials is not considered in this method. In practice, the generation of residual stress through inhomogeneous plastic deformation is inevitably accompanied by plastic flow and hardening/softening activities of materials. As a result, subsequent analysis performed in the literature with only the introduced residual stress taken into account could not completely reflect the true mechanical behaviour of materials [170,136,160].

In the literature, history-dependent hardening was taken into account in some work. For example, Song et al. [160] incorporated a combined kinematic/isotropic hardening model in the FE model after the reconstruction of a residual stress field through eigenstrain method. In their work, the initial kinematic hardening was related to the eigenstrain (plastic strain) through a simple linear relation. Musinski and McDowell [152] employed a combined kinematic/isotropic hardening model to determine the quasi-thermal expansion eigenstrain distribution of a shot peened sample. Then this eigenstrain distribution was used to reconstruct the residual stress within a crystal plasticity framework. Li et al. [137] described the work hardening effect of a shot peened sample based on a Ludwik type isotropic hardening expression, and only the accumulated plastic strain was included in the constitutive model. Smith et al. [77] used a multilinear kinematic model to describe the plastic constitutive behaviour of the material, and the multi-kinematic hardenings of the shot peened material were determined through maximum equivalent stress and maximum

deviatoric residual stress. In all the work mentioned above, the accumulated effect (accumulated plastic strain) and the deformation history of shot peening were not separately taken into account. In fact, the accumulated plastic strain and the plastic strain tensor are generally associated with the isotropic and the kinematic hardening effects. They both play important roles in mechanical behaviour of a material. Moreover, not only the residual stress should be self-equilibrated for the whole structure, but also the work hardening should maintain an equilibrium condition due to the constitutive relation of a material. Simultaneously taking into account both these equilibrium conditions should be crucial for reconstructing the residual stress and work hardening fields.

1.3.4 Cyclic plasticity modelling of 316L

Fatigue is one of the most frequent failure modes of materials in service. In general, inelastic strain is used to predict the fatigue behaviour of material for structures optimization and design. Being able to precisely characterize the cyclic plasticity behaviour is always of great importance to understand the mechanical behaviour of a material and to perform life prediction as well as optimization for a structure. During the last decades, many cyclic constitutive modelling methods have been developed based on the macroscopic phenomenological continuum plasticity theory and microscopic quasi-physically or physically based crystal plasticity theory.

1.3.4.1 Cyclic modelling through macroscopic continuum plasticity theory

Armstrong and Frederick (AF rule) [171] introduced a recall term in Prager [172]'s linear kinematic hardening formulation to describe the dynamic recovery effect. Chaboche et al. [103] gave a better description of transient hardening evolution and ratcheting effect by superposing several back stresses, each of which obeying the AF rule [103,173]. In order to govern the ratcheting response, a threshold was used in the dynamic recovery terms of one or several nonlinear kinematic hardening (AF) rules [174]. Ohno and Wang [175] introduced a critical state for the dynamic recovery of the decomposed AF rules to improve the description of ratcheting effect. These developed nonlinear kinematic hardening rules were henceforth extended and widely discussed in cyclic plasticity modelling studies [83,176–178].

Strain range memory effect can be observed for some polycrystalline materials, such as 316L steels [103,179], 304L steels [180–182], BLY160 steel [183], polycrystalline copper [184]. In order to describe the strain range memory effect, Chaboche et al. [103] introduced a new internal state variable related to a memory surface in plastic strain space.

This memory surface can evolve due to plastic strain history, and thus keep the memory of previous largest plastic strain. The initial proposed rule of strain range memory was generalised by Ohno [185] as the cyclic non-hardening range approach. Further development was performed to describe the evolution of the memory surface by introducing a memory evanescence term [186], which allows to consider the different rates of the memory surface evolution. This approach was subsequently adopted in some cyclic modelling studies [186,184,180,187,188,183]. The memory variable is generally considered through asymptotic isotropic hardening constants [103,187,186,83,189,183,190,191], or sometimes through kinematic hardening based on the developed AF rules [192,180,193,194]. For example, Kang et al. [192] described the strain range dependent hardening and non-saturating hardening through a kinematic hardening rule extended from Ohno and Wang [175]'s multilinear kinematic hardening model. Krishna et al. [180] considered the memory effect in both the isotropic hardening constants and the several kinematic hardening components. Zhu et al. [194] incorporated the radius of the memory surface in the developed dynamic coefficients of the AF rules respectively for long-range, middle-range and short range back stresses in order to improve the description of the transient Bauschinger effect.

The strain range memory effect is strongly related to the cyclic hardening/softening behaviour. The memory evanescence term proposed by Nouaihas et al. [186] can be used to describe the cyclic softening which follows the cyclic hardening. This approach was further evaluated and used by Krishna et al. [180] in modelling the cyclic hardening/softening of a 304 stainless steel through considering the simultaneous evolution of isotropic hardening and kinematic hardening. Yaguchi et Takahashi [195] introduced a softening index surface in the Ohno–Wang model [175] with the assumption that the magnitude of back stresses vary with the progress of cyclic deformation. A logistic function was incorporated in the asymptotic values of the kinematic hardening and isotropic hardening parameters by Xu et al. [183] to trace the softening evolution for a low yield point BLY160 steel. Ahmed et al. [193] described the cyclic hardening/softening response of Haynes 230 based on the method of Krishna et al. [180], and both the isotropic effect and the radius of memory surface were considered through the dynamic recovery terms of AF rules. Zhu et al. [190] used three isotropic hardening variables to describe the cyclic hardening-softening-hardening behaviour of a 316L austenitic steel, with each variable having a critical value of accumulated plastic strain to distinguish the three stages.

In terms of cyclic behaviour under low cycle fatigue (LCF), 316L austenitic stainless steels have been extensively investigated due to their wide applications. The cyclic plasticity modelling of 316L steels including hardening, ratcheting response, and strain range memory effect, etc., has been largely studied under uniaxial loading [103,196,174,197,49,190] and multiaxial or non-proportional loading [198–201]. However, most of the previous studies were focused on the description of the hardening/softening and the subsequent saturation stages under high strain/stress amplitudes. In fact, a material may undergo more complex cyclic behaviour in the LCF regime, especially under low load amplitudes. On the one hand, the loading-unloading transition occurs when the plastic modulus drastically changes; on the other hand, after the initial hardening and the saturation stages, a large range of softening can occur before fracture, sometimes followed by a significant secondary hardening [202,190,203]. Therefore, an accurate modelling of the cyclic behaviour of materials in the LCF regime could be more sophisticated.

Furthermore, the cyclic behaviour and pre-hardening effect (or memory effect) of 316L steels have been thoroughly studied based on microstructure analysis and Cottrell [204]'s stress partitioning method [205,52,53,49,179,206]. It was highlighted that the strain range memory effect of 316L steels during uniaxial cyclic loading is mainly due to back stress [179]. From the microscopic viewpoint, back stress and effective stress are respectively associated with the long range and short range dislocation interactions. A constitutive model based on the evolution of back stress and effective stress is preferably recommended to better describe the microstructural evolution during cyclic deformation.

1.3.4.2 Cyclic modelling through physically based constitutive model

Section 1.3.4.1 discussed the cyclic plasticity modelling work in the framework of continuum plasticity theory. In fact, polycrystalline materials can undergo complex microstructural evolutions during cyclic loadings. The phenomenological constitutive models are unable to describe the evolution of microstructure and to describe the deformation mechanism at a microscopic scale. A preferable approach is to describe the cyclic behaviour of polycrystalline materials in a microscopic scale according to the deformation mechanism. In general, the movement of dislocations constitutes the main physical basis for plastic deformation over a wide range of loading conditions [207,208]. A series of physically based modelling methods has been developed over the last decades by incorporating the evolution of plastic slips or dislocation densities into the constitutive models, for example crystal plasticity.

The crystal plasticity model is able to relate the mesoscale mechanical behaviour to the micro-scale material properties. It is thus beneficial to take into account crystal plasticity model in the finite element framework. On the one hand, the stress equilibrium condition and strain compatibility can be automatically satisfied by the FE model. On the other hand, crystal plasticity finite element method (CPFEM) offers good flexibility by considering various constitutive formulations for plastic flow and hardening in the scale of slip system. The constitutive laws in slip system scale have been widely developed from the empirical viscoplastic rules [209,210] to physically based multi-scale models of plasticity, including a variety of size-dependent effects and interface mechanisms [86]. Moreover, other complex mechanism can also be studied based on CPFEM for example martensite formation, twining, and heterogeneous elements. In terms of cyclic loading simulation, CPFEM has been widely used to describe the cyclic plasticity behaviour of polycrystalline materials by using various multi-scale constitutive laws for different materials, for example 316L [211], 304L [212], inconel 718 superalloy [213], IN 100 [214], or Ti–6Al–4V [215].

In addition to CPFEM, the scale-transition law (or interaction law) from a single crystal grain to the macroscopic polycrystalline aggregate can be realized through self-consistent method. Self-consistent method describes the overall response of a polycrystal by taking into account the mechanical properties of single grains and the interaction of each grain with its surroundings. Early studies originated by Sachs [216] in 1928 and developed later by Tayler [217] in 1938. Afterwards, a set of transition laws was successively developed by Lin [218] in 1957, Kröner [88] in 1958, Hill [219] in 1965. A modified version was proposed by Berveiller and Zaoui [89] in 1979 through simplifying the interaction law of Hill [220] to characterize the elasto-plastic behaviour of an aggregate as isotropic. Cailletaud and Pilvin [221,222] modified the interaction law of Berveiller and Zaoui by adding a term in the transition rule, which takes into account the intergranular kinematic hardening. In addition, some other interaction laws were developed for polycrystalline materials with small and/or large deformation [90,221,223–226]. Studies indicate that the developed interaction laws and coupled with the constitutive laws in slip system scale can well predict cyclic plasticity behaviour of polycrystalline materials [91,92,227–230].

However, few studies were performed to predict the cyclic hardening/softening and the strain range memory effect of polycrystalline materials using crystal plasticity model. Evrard et al. [229] described the cyclic hardening/softening behaviour of an austenitic-ferritic stainless steel using a dislocation based constitutive model coupled with self-consistent method. In their work, the cyclic softening is represented by dislocation structure

evolution within ferritic grains [229]. Cruzado et al. [213] simulated the cyclic hardening/softening behaviour of inconel 718 superalloy based on CPFEM by introducing two terms to characterize the critical resolved shear stress. These two terms, respectively determine the monotonic deformation and cyclic softening. Moreover, Pham et al. [49] developed dislocation-based constitutive model to describe the cyclic behaviour of a 316L steel based on internal variables. In their work, cyclic hardening/softening was mainly represented through the evolution of intergranular back stress and intragranular back stress, which are respectively determined by the movement of dislocations [49].

1.4 Scope of the thesis

Over the last decades, it has been shown that SMAT is able to generate a nanostructured layer at the treated surface and a high and deep compressive residual stress field in the near surface region. These typical features are beneficial for the resistance to crack initiation and crack propagation. Fatigue studies have indicated that SMAT can significantly improve the fatigue properties in stress-controlled loading tests and in HCF regime. However, the effect of SMAT on fatigue properties in LCF regime is sometimes contradictory. On the one hand, the compressive residual stress could be quickly relaxed during the first several cycles under high loading amplitudes. On the other hand, the nanostructured layer presents a lower ductility, and could have a negative effect on crack initiation and propagation. In addition, the effect of work hardening on fatigue lifetime is still unclear. Furthermore, due to the complex microstructures of the SMATed materials, it should be a great challenge to precisely predict their mechanical behaviour through numerical simulation.

This thesis focuses on experimental analysis and multi-scale modelling of LCF behaviour of an austenitic steel (316L SS) treated by SMAT. Experimental characterization, constitutive modelling of cyclic plasticity, reconstruction of residual stress and work hardening, and multi-scale modelling study of LCF behaviour together constitute this thesis. The manuscript is organized through the following five parts:

1) The gradient microstructure features of an austenitic stainless steel (316L) treated by SMAT is characterized using EBSD and XRD in Chapter 2. LCF behaviour in terms of macroscopic hardening/softening effect and microstructure evolution of the SMATed material under fatigue loading are analysed based on the uniaxial strain-controlled tension-compression fatigue tests.

2) A comparison between SMAT and conventional shot peening is performed by analysing the surface topography, residual stress, work hardening, etc. in Chapter 3. The effects of these characteristics on fatigue life in LCF regime are also investigated.
3) Experimental analysis and constitutive modelling of cyclic behaviour of the studied materials are performed in Chapter 4. A cyclic constitutive model is developed and implemented to describe the cyclic behaviour of a 316L steel including the cyclic hardening/softening and the strain range memory effect.
4) In Chapter 5, a single crystal plasticity model is adapted and coupled with the self-consistent method to describe the cyclic hardening/softening behaviour of a 316L steel. An identification procedure is proposed in order to better describe the evolution of the back stress and the isotropic hardening during cyclic loading.
5) A new method of reconstruction of residual stress and work hardening is presented and applied to a SMATed structure. A multi-scale modelling method is also discussed and included in the reconstruction process. Moreover, the effects of residual stress and work hardening on mechanical behaviour of the studied material are investigated through cyclic loading simulation of the SMATed structure.

Finally, Chapter 7 provides a summary and gives conclusions of this work. Potential directions for future work are presented as well.

Chapter 2: Experimental study of LCF behaviour of a 316L steel treated by SMAT

As indicated in Chapter 1, the nanocrystallization mechanism and microstructure evolution during SMAT have been deeply investigated through both experimental characterization and modelling methods. However, the LCF behaviour of materials treated by SMAT is not extensively studied. Mechanical behaviour of the gradient microstructure features in LCF regime should deserve more attentions, including the nanostructured layer, the transition layer, and the work hardened region. This type of study concerning the SMAT affected region constitutes important elements not only in terms of mechanical properties characterization and deformation mechanism analysis, but also in terms of modelling and numerical simulation. In this chapter, LCF behaviour of a 316L stainless steel treated by SMAT is studied based on the analysis of macroscopic cyclic behaviour in relation to microscopic mechanisms. The gradient microstructure, residual stress and work hardening in the near surface region of the SMATed material are firstly evaluated through EBSD, XRD. Afterwards, mechanical behaviour of the SMATed materials and the evolution of microstructure during cyclic loading are investigated to thoroughly understand the cyclic deformation mechanism of the SMATed material.

2.1 Material and experimental procedure

The material investigated in this work is a 316L ASTM F138 stainless steel, and its chemical composition is shown in Tab. 2-1. The studied steel was in the overquenched state in order to get a homogeneous austenitic phase.

Tab. 2-1. Nominal chemical composition (wt.%) of the studied 316L stainless steels.

Fe	C	Mn	Si	P	S	Cr
48.4	0.013	1.7	0.26	0.017	0.003	17.37
Ni	Mo	Cu	N	Ti	V	
14.52	2.8	0.08	0.088	<0.005	0.07	

For SMAT and fatigue tests, cylindrical dumbbell shaped specimens were machined from the material in form of bar. The specimen has a gauge length of 12 mm with a diameter of 6 mm, as shown in Fig. 2-1.

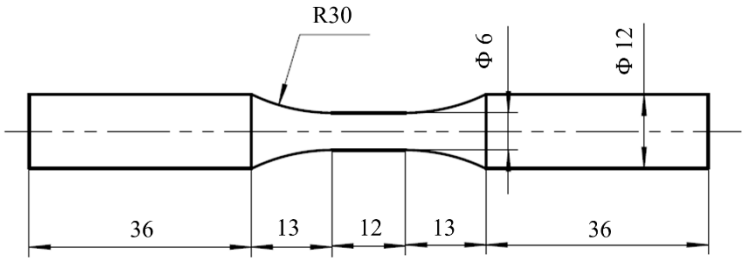

Fig. 2-1. Shape and dimensions of the cylindrical specimen used for low cycle fatigue tests.

The cross-section of the specimen was chemically attacked and then observed using digital optical microscopy. The microstructure is presented in Fig. 2-2. It shows that the as-received material has an initial grain size of about 10-20 µm.

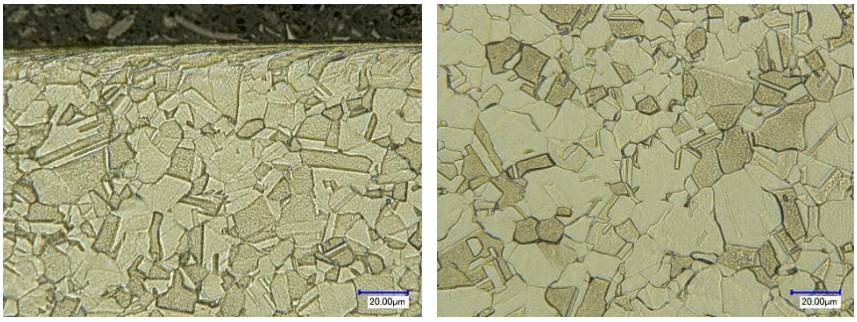

Fig. 2-2. Microstructure of the cross-section of the 316L specimen located in the surface (left) and center (right) region.

SMAT is based on the vibration of spherical shots boosted by a high frequency (20 kHz) ultrasonic generator. The cylindrical specimen is installed in an enclosed space, and rotating around the centre axis to ensure uniform peening over the surface, as shown in Fig. 2-3. In this work, a mass of 20 g of steel shots with 3 mm of diameter is enclosed in the chamber. The distance between the surface of the sonotrode and the specimen is 12 mm. When the ultrasonic generator vibrates under a given power, the shots are projected at high speed to impact the surface of the specimen repeatedly during the desired duration. The entire gauge length of the fatigue specimens can thus be covered by the strike.

Two SMAT conditions, respectively named SMAT Less High (SLH) and SMAT Very High (SVH) are considered. SLH corresponds to a treatment of 30 minutes with a generator power of 30%. For SVH, a treatment of 15 minutes was first performed with a generator power of 30%, followed by a treatment of 5 minutes with a generator power of 50%. Detailed treatment information is given in Tab. 2-2.

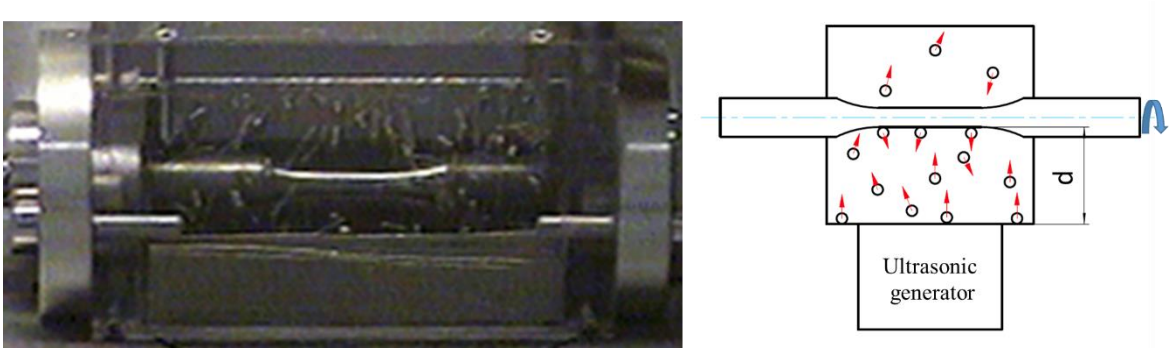

Fig. 2-3. Presentation of SMAT treatment for a cylindrical specimen.

Tab. 2-2. SMAT conditions for the 316L steel.

Sample	SLH	SVH		
Generator power	27%	27%	&	50%
Duration	30 minutes	15 minutes		5 minutes
Shot	Material: 100 Cr 6, diameter: 3 mm			
Distance (d)	12 mm			

2.2 Characterization of gradient microstructure features

2.2.1 Metallurgical state of the SMATed material

The mechanisms of grain refinement due to SMAT for a 316L stainless steel have been studied using Transmission Electron Microscopy (TEM) by Roland et al. [8,231,232]. It was shown that at low strain level, the microstructure is characterized by high density of mechanical twins and dislocation arrays. With the increase of strain during SMAT, twin-twin interactions occur, which is able to subdivide the original austenitic grains into smaller blocks and, ultimately, leads to the formation of nanocrystallites (range from 50 to 400 nm) involving the mechanisms such as boundary sliding and rotation of crystalline domains. Consequently, SMAT generates a grain size gradient and microstructural defects through the mechanically affected region below the surface of the material.

In order to investigate the metallurgical states of the SMATed material, EBSD observations on transverse cross-section were performed for SLH and SVH specimens. The experimental data were obtained using a scanning electron microscope FEG-SEM SUPRA 55 VP operating at 20 kV equipped with the OIM^{TM} software system. For EBSD observation, the central part of the fatigue specimens was successively cut, molded, mechanically ground, polished to a mirror-like finish and then polished with an OPS solution.

Fig. 2-4 illustrates the gradient distribution mapping obtained by EBSD in the near surface region for the specimens SVH and SLH. It can be seen that the impingement of flying shot at high strain rate generated an obvious gradient microstructure in the near surface region. A large amount of multi-slips can be observed close to the surface, especially for the SVH specimen. In addition, compared to SLH specimen, the grains and grain boundaries become bleared from the treated surface to a depth of about 100 μm. This must be due to the higher impact intensity during SMAT that activates very severe plastic deformation in the near surface region, and induced a great number of plastic slips and misorientations of grains.

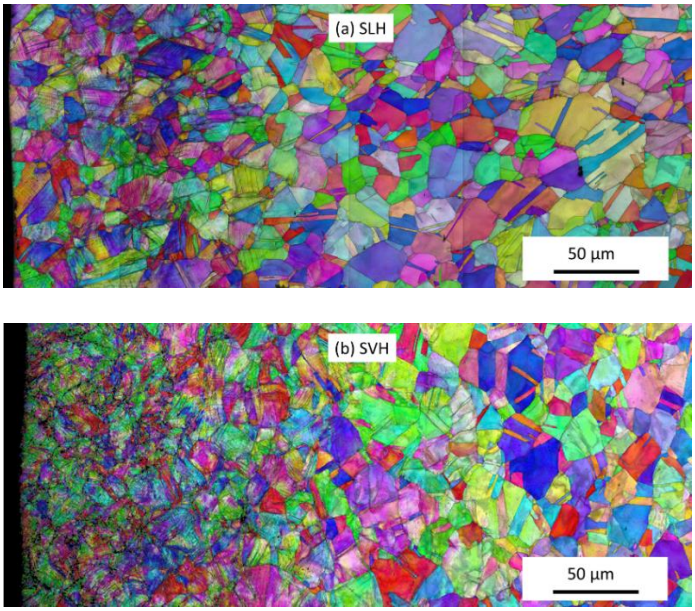

Fig. 2-4. Gradient distribution of metallurical observation by EBSD : (a) SLH; (b) SVH.

The plastic deformation extent in the near surface region of SVH and SLH specimens can also be indicated by Kernel Average Misorientation (KAM) values [233]. In KAM, the mean misorientation between each measurement point and its neighbours is calculated, excluding any high angle boundaries (In this case a 3x3 kernel was used, including 8 neighbours for each point and HAGBs were defined by misorientations >15°). The KAM values were measured and calculated in different regions from the treated surface to the inner core of the specimens SVH and SLH, as shown in Fig. 2-5. The average misorientation decreases nearly linearly from the treated surface to the interior of both the SVH specimen and the SLH specimen, which confirms that the plastic deformation extent decreases linearly from the treated surface to the interior of the specimen. In addition, the KAM values of the SVH specimen is about twice over than that of the SLH specimen, which must be induced by severe plastic deformation due to the 5 minutes of higher treatment intensity. This

phenomenon is consistent with the distribution of plastic slips density illustrated in Fig. 2-4, and they both present a plastic deformation gradient in the near surface region of the SMATed specimens.

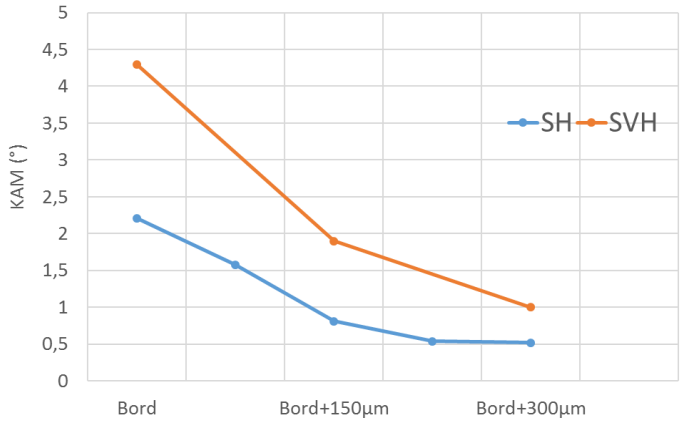

Fig. 2-5. In-depth variation of KAM values for SLH and SVH specimens.

Moreover, The SMAT affected region presents a significant increase of hardness and strength [1,7,61]. Fig. 2-6 plots hardness variation of SLH and SVH specimens as a function of depth from the treated surface, as determined by using a Vickers microhardness tester, with a load of 0.025 kg. It can be seen that there is a significant increase of hardness in the SMAT affected region. Close to the treated surface, hardness reaches a value as high as 400 $HV_{0.025}$ which is about twice that in the coarse-grained region (center region of the specimen). The hardness begins to be constant between 0.5 mm and 2 mm below the treated surface. This signifies that the depth within which the material is plastically affected by SMAT is more than 500 µm. Fig. 2-6 also indicates that higher is the treatment intensity, higher is the hardness increase.

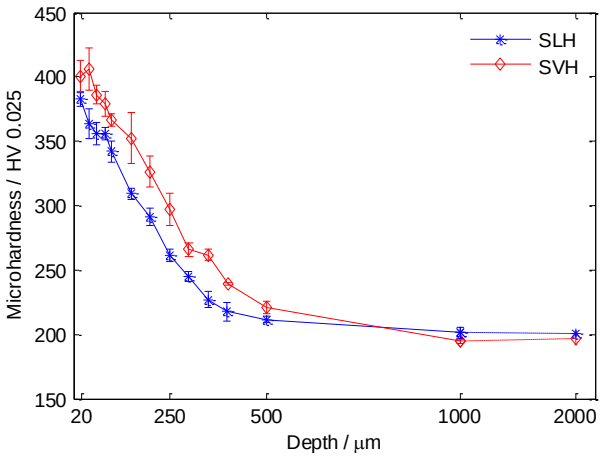

Fig. 2-6. Hardness variation as function of the depth from the treated surface for SLH and SVH specimens.

The hardness increase induced by SMAT is generally due to the compressive residual stress and the work hardening, as shown in Fig. 2-4 and Fig. 2-5. In the case of austenitic stainless steel, another possibility is that austenitic phase can be partially transformed into martensitic phase due to SPD with a high strain rate [8,234]. Presence of martensitic phase induced by SMAT can increase the hardness of the affected region. However, for the 316L steel studied in this work, no martensitic phase was detected based on the XRD analysis (this will be discussed in Section 2.2.3). This result is consistent with the observations presented in the literature [23].

2.2.2 Surface nanocrystallization

In Section 2.2.1, the gradient features in the near surface region of SMATed materials are presented. Moreover, SMAT can generate a superficial nanocrystalline layer at the treated surface due to multi-directional severe plastic deformation [1,235]. Fig. 2-7 shows detailed microstructure observed using EBSD for the SVH specimen. Typical microstructure at a periphery region (the scan step size is 0.1µm) on the transverse cross-section of the specimen after SMAT is illustrated in Fig. 2-7a. It can be seen that this periphery region is not affected by SMAT because the grains do not look deformed and no plastic slip traces can be observed. A large fraction of twins can be detected in this region and the average grain size is about 10 µm. The associated pole figure shows a random orientation distribution. No texture is thus presented in this periphery region.

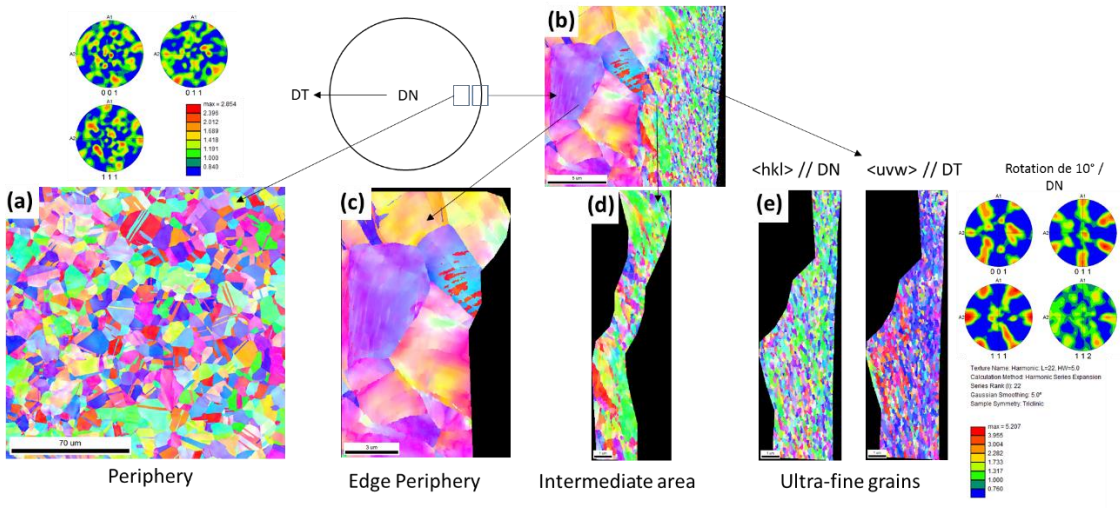

Fig. 2-7. EBSD observations performed on the cross-section of the SVH specimen: (a) typical microstructure observed in a periphery region, and (b) mechanically affected region showing three different areas: (c) edge periphery area, (d) intermediate area, and (e) ultra-fine grain area.

Fig. 2-7b shows a region mechanically affected by SMAT with the presence of a gradient microstructure. The used scan step size is 25 nm. Very similar result has been

obtained in [236] for a 316L steel treated by SMAT. In this mechanically affected region, different microstructural features can be clearly observed. In the edge periphery area (Fig. 2-7c), the grain size is apparently not changed by SMAT. However, the colour in each grain is no longer uniform compared to untreated material. As a matter of fact, the grains in this area are subdivided by plastic slips. These plastic slips occurring in different slip systems are caused by the multi-directional impacts of the shot during SMAT. In this area, original grains are just split by plastic slips and no new grains are present. This observation is consistent with the mechanisms highlighted by [231,232] using TEM, as indicated above. In the intermediate area (Fig. 2-7d), a mixture of ultra-fine grain and relatively large grains that were originally present can be noticed. In this area, the impact intensity is actually higher than in the edge periphery area so that new smaller grains are formed while the size of other grains is not affected by the treatment.

Concerning the ultra-fine grain shown in Fig. 2-7e, they must be formed during SMAT as they are rather equiaxed. The grain size ranges from 50 nm to 300 nm (Fig. 2-8a). The thickness of this ultra-fine grain area is about 5 μm. According to the pole figure associated to this area, the ultra-fine grains are oriented with a large fraction of <111> axes parallel to the sample radius (SR) and a major <110> axis parallel to the sample revolution axis (SRA). The formation of this texture is due to the SMAT as no further mechanical load has been applied. Almost no twin can be distinguished in this area according to the micrograph shown in Fig. 2-7e. This can be confirmed by Fig. 2-8a where the curves of area fraction versus grain diameter are quantitatively presented. It can be seen that the curve of ultra-fine grain area including twins and the curve excluding twins are nearly the same, which means that there is almost no twin in this area or the quantity is very small. However, as previously shown in Fig. 2-7a, in the SMAT non-affected region (i.e. periphery region), many twins are present. This observation can be confirmed by Fig. 2-8b which shows that a high fraction of twins (represented by Σ3) is actually present. As a matter of fact, the SMAT non-affected region represents the initial state of the material without SMAT treatment. Based on the fact that no twins can be distinguished in the ultra-fine grain area (small grain area), it can be concluded that small grains present in the ultra-fine grain area are actually newly formed due to the grain refinement effect of SMAT when the treatment intensity is high.

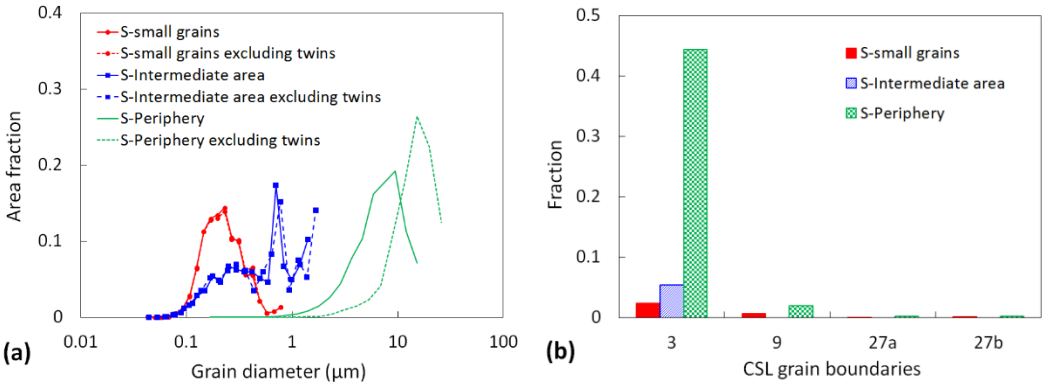

Fig. 2-8. Grain diameter and grain bounday analysis for SVH specimen (S): (a) Distribution of grain diameter evaluated in different areas with and without twins taken into account, and (b) fraction of $\Sigma 3^n$ CSL (Coincidence Site Lattice) grain boundaries for different areas. Note that $\Sigma 3$ represents twin boundaries.

Fig. 2-9 shows the grain orientation spread (GOS) of the SVH specimen in the near surface region from about 20 μm of the treated surface. GOS characterizes the mean intragranular misorientation, i.e. the misorientation within a grain. It can be found that SMAT generate a gradient distribution of the intragranular misorientation from the treated surface to the centre of the specimen. For the ultra-fine grains in Fig. 2-9b, they are less misoriented because they are actually well formed by multi-slips due to SMAT (Fig. 2-20). In addition, texture was observed and the grain shapes remained equiaxed in this area after SMAT, which suggests that grain-boundary sliding must also have contributed to the deformation, besides the plastic slips shown in Fig. 2-7b.

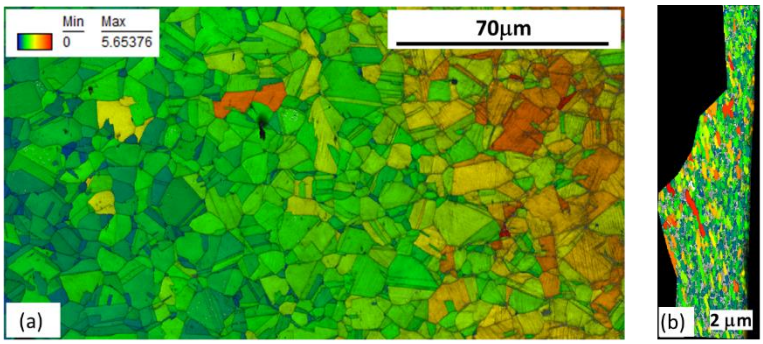

Fig. 2-9. (a) GOS map from about 20 μm of the treated surface (right side of the map) for the SVH specimen; (b) GOS map of the ultra-fine grain area (top surface, see Fig. 2-7e).

2.2.3 XRD patterns analysis

2.2.3.1 Martensitic transformation

Besides the grain refinement and work hardening, some studies indicate that austenitic phase could be partially transformed into martensitic phase due to SPD with a high strain rate during SMAT [8,234,235]. The phase transformation, residual stress and work

hardening of SVH specimen are evaluated through XRD by using a Cr-Kα radiation. Iterative electrolytic polishing (See Appendix A) was used to remove the material from surface of the specimen, and subsequent XRD patterns were recorded between the angle from 60° to 140° at 30 kV and 30 mA current, with a step size 0.02 and a scan speed of 1.5°/min. Fig. 2-10 illustrates the diffraction patterns of the SVH specimen measured in different depth. Three major diffraction peaks of $\gamma(111)$, $\gamma(200)$ and $\gamma(220)$ in the 60°-140° range confirm the presence of the austenite FCC phase. In addition, all the diffraction patterns in Fig. 2-10 indicate that no martensitic transformation occurred during SMAT. This is contrary to the previous studies [8,234,235], in which strain-induced martensitic transformation was detected during severe plastic deformation. The difference should be considered due to the chemical components of the studied material.

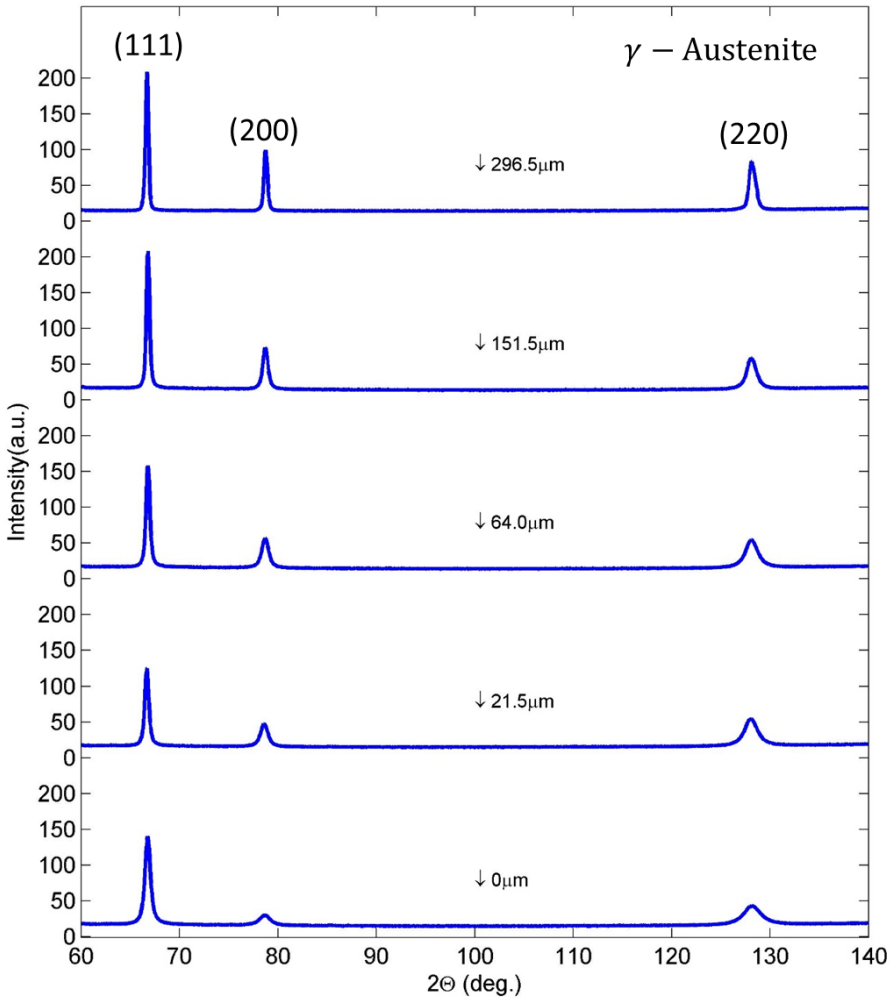

Fig. 2-10. X-ray diffraction patterns measured in different layers of the SVH specimen.

In addition, the layer with a larger depth presents higher intensity of diffraction peaks and lower width of the waves. This phenomenon indicates that there is a significant in-depth

variation of lattice deformation and dislocation defects in the SMAT affected region, as has been discussed in the above. Moreover, a small displacement of the peaks in the 2θ axis can be observed, which implies that a residual stress field was generated inside the structure during SMAT.

2.2.3.2 Residual stress

In-depth variation of residual stress were evaluated as well by following the Theta-2Theta analysis in each polished layers using classical $\sin^2\psi$ method [113]. The X-ray diffraction peak was determined through centre of gravity method. In order to obtain the largest peak shift possible for a given lattice deformation, the diffraction peak was chosen at the highest angle possible, and thus the 2θ range of 125°-133° was considered with the ψ angle ranging from -55° to 60°.

In the case of a cylindrical sample, a set of axial and circumferential stresses (σ_z^m and σ_θ^m) can be obtained by removing the outer surface layer step by step (Fig. 2-11). When a periphery volume of material is removed by electrolytic polishing, the cylindrical sample will have a new self-equilibrium state, which is characterized by a change of residual stress field more or less pronounced depending on the thickness of the removed layer. Therefore, the measured stresses using XRD are the ones after re-equilibrium, and they do not represent the true residual stresses inside the sample as generated by SMAT. In addition, the radial residual stress is also difficult to be directly evaluated due to release of the stress during iterative removal of the outer material.

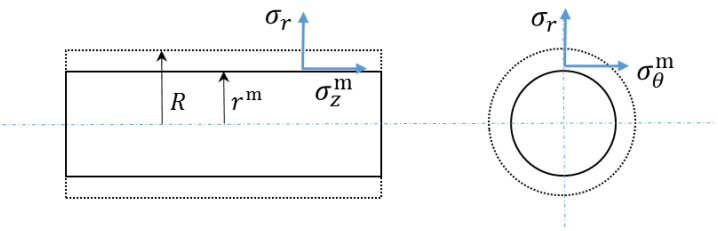

Fig. 2-11. Description of XRD measurements with an iterative material removal method on a cylindrical sample.

Based on the self-equilibrium and stress coupling relationship in a cylindrical coordinate system, the residual stresses present in the treated sample ($\sigma_r^{\mathrm{rs}}, \sigma_\theta^{\mathrm{rs}}, \sigma_z^{\mathrm{rs}}$) can be corrected from the measured stresses ($\sigma_\theta^{\mathrm{m}}, \sigma_z^{\mathrm{m}}$) using the following equations [113]:

$$\sigma_r^{\mathrm{rs}}(r^{\mathrm{m}}) = -\int_{r^{\mathrm{m}}}^{R} \sigma_\theta^{\mathrm{m}} \frac{d_r}{r} \qquad (2\text{-}1)$$

$$\sigma_\theta^{\mathrm{rs}}(r^{\mathrm{m}}) = \sigma_\theta^{\mathrm{m}}(r^{\mathrm{m}}) + \sigma_r^{\mathrm{rs}}(r^{\mathrm{m}}) \tag{2-2}$$

$$\sigma_z^{\mathrm{rs}}(r^{\mathrm{m}}) = \sigma_z^{\mathrm{m}}(r^{\mathrm{m}}) - 2\int_{r^{\mathrm{m}}}^{R} \sigma_z^{\mathrm{m}} \frac{d_r}{r} \tag{2-3}$$

Fig. 2-12a illustrates in-depth variation of the as-measured axial and circumferential stresses in the near surface region of a SVH specimen while the three corrected true residual stresses (radial, circumferential, axial) are presented in Fig. 2-12b. A significant difference between the as-measured stresses and the corrected true stresses can be noticed, especially for the axial stress in the region far from the treated surface. In addition, the radial residual stress that is experimentally inaccessible by using XRD was calculated based on the stress self-equilibrium and stress coupling relationship (Eq. (2-1)).

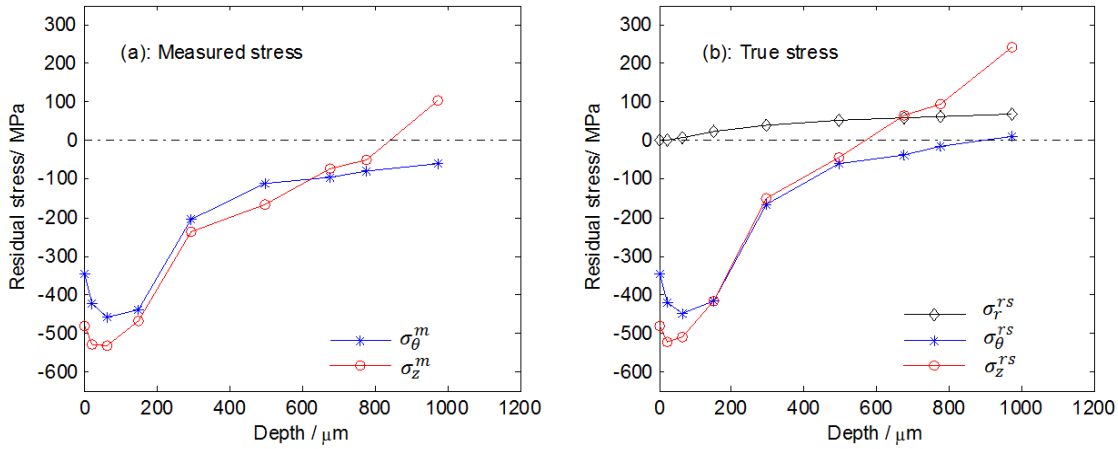

Fig. 2-12. In-depth variation of residual stress of SVH specimen: (a) measured stresses; (b) true stresses.

Comparing to the microstructure observation (Fig. 2-4), the compressive residual stress can reach to a depth of about 550μm, which is consistent with the micro-hardness result in Fig. 2-6. In addition, the axial residual stress is higher than the circumferential residual stress in the near surface region, and it goes from compressive in a smaller depth of the surface region to tensile in the interior. This should be due to the equilibrium relationship of the cylindrical structure.

2.2.3.3 FWHM analysis

Besides the peak shift of XRD patterns, diffraction peak broadening contains important information about the microscopic characteristics of a material as well. The diffraction peak broadening is related to the grain distortion, dislocation density and the type II and III residual stresses. Some material properties have been identified successfully based on the Full width at half-maximum (FWHM) value. For example, it can be correlated qualitatively

to the induced plastic deformation for a shot peened part, as discussed in Section 1.3.3. Fig. 2-13 illustrates the in-depth variation of FWHM value for the SVH specimen, which is measured by diffraction peak with the highest 2θ value in Fig. 2-10. A linear decrease of the FWHM value in the near surface region can be observed in both the axial and the circumferential directions, just like the micro-hardness variation in Fig. 2-6. Moreover, the two solid curves in Fig. 2-13a and Fig. 2-13 b indicate that the plastically affected region can reach to a depth of around 600 µm from the treated surface.

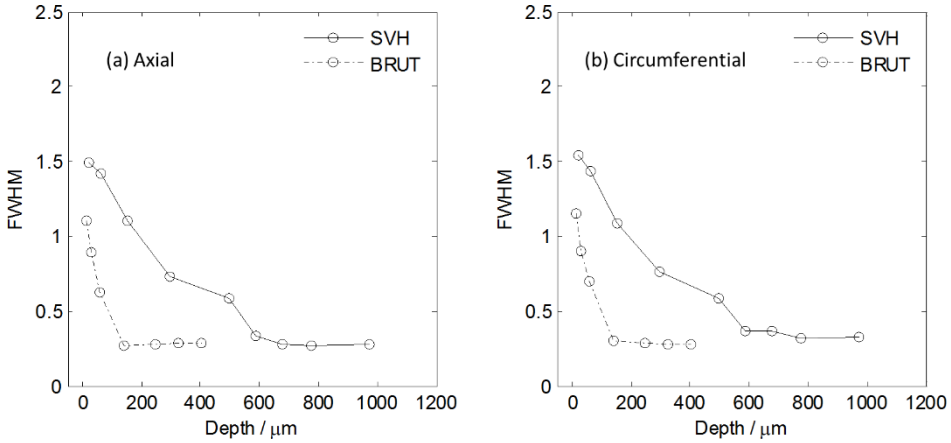

Fig. 2-13. In-depth variation of FWHM value measured on the SVH specimen.

2.3 LCF analysis of the SMATed material

The gradient microstructure features of the SMATed specimen are discussed in the above Section 2.2. These features should have a significant effect on the mechanical behaviour of the material. In this section, the macroscopic cyclic behaviour of SMATed material is studied under strain-controlled LCF tests. LCF tests were carried out on untreated (UNT) and SMATed (SLH and SVH) specimens at room temperature using a servo-hydraulic machine. Uniaxial tension-compression fatigue tests were performed under total strain control with a load ratio $R_\varepsilon = -1$. An extensometer with a gauge length of 10 mm was used to control the total strain with a strain rate of $4 \times 10^{-3} s^{-1}$. Three strain amplitudes (±0.5%, ±0.8% and ±1.25%) are considered for studying the cyclic behavior of the SLH and SVH specimens.

2.3.1 Cyclic stress amplitude

Cyclic stress amplitude evolution during fatigue loading gives a good illustration of the cyclic behaviour of a material regarding softening or hardening phenomenon. Fig. 2-14 shows cyclic stress amplitude as a function of number of cycles for different material states

with strain amplitudes of ±0.5%, ±0.8% and ±1.25%, respectively. Globally it can be observed that SMAT significantly enhanced the mechanical strength and change the cyclic hardening/softening behaviour of the specimens. From Fig. 2-14, it can be seen that higher imposed strain gives larger cyclic stress amplitude. For a given strain amplitude, the cyclic stress amplitude of the SMATed specimens is higher than that of the untreated ones. Furthermore, higher SMAT intensity leads to higher stress amplitude.

The increase of stress amplitude of SVH and SLH specimens with respect to untreated ones is due to the SMAT affected region, which can enhance the global mechanical strength of the SMATed specimens, as the increase of hardness in the near surface region (Fig. 2-6). On the one hand, strain hardening can improve the mechanical strength due to dislocation entanglement which can impede further permanent deformation of material. On the other hand, the generated nanocrystalline layer has higher yield strength according to Hall-Petch relationship. However, the last one might have a small contribution to global mechanical behaviour of specimens because of its very thin thickness (5 µm) compared to the thickness of the work hardened region (about 600 µm according to the microhardness and FWHM curves) and the diameter of specimens (6 mm).

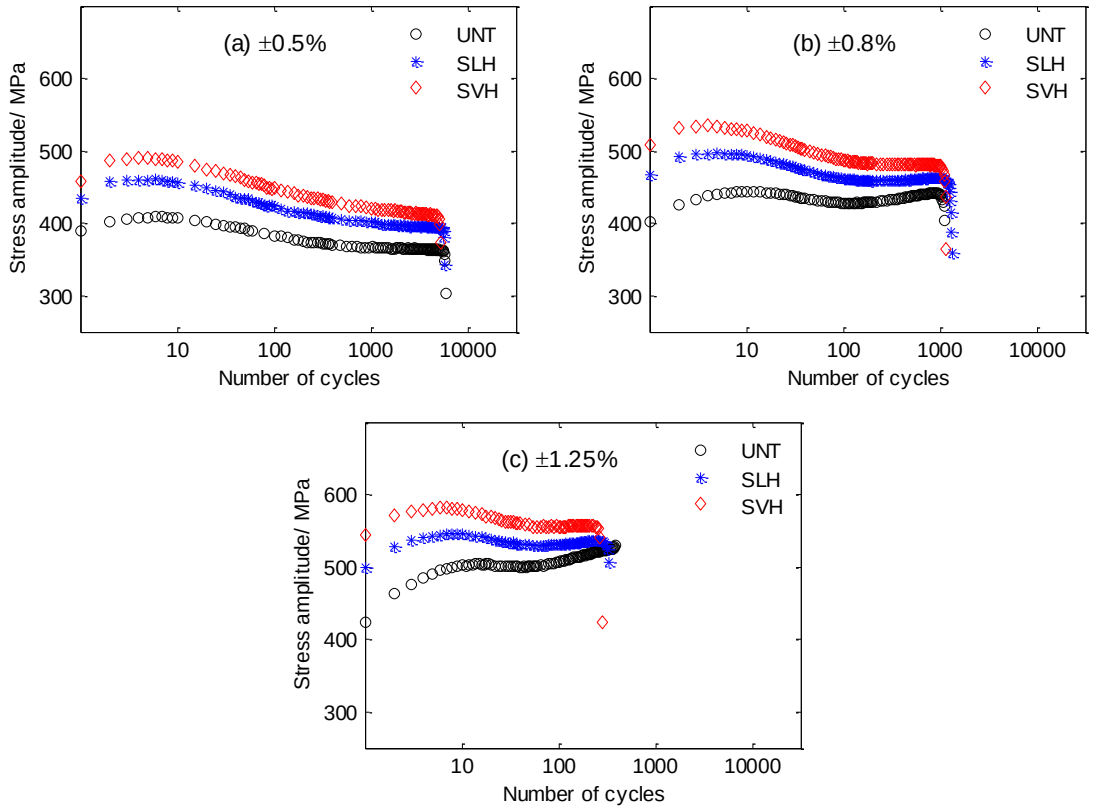

Fig. 2-14. Cyclic stress amplitude curves for different material states under strain amplitudes of: (a) ±0.5%, (b) ±0.8%, and (c) ±1.25%.

2.3.2 Hysteresis loops

LCF hysteresis loop illustrates the relationship between strain and stress, and characterizes more specifically the plastic cyclic deformation behaviour of a material. Fig. 2-15 illustrates the comparison of hysteresis loops among UNT, SLH and SVH specimens under $\Delta\varepsilon/2 = \pm 1.25\%$. In Fig. 2-15a, hysteresis loops of SVH and SLH specimens have larger height and smaller width (which represents plastic strain range) than that of the untreated specimen. It signifies that SVH and SLH specimens exhibit higher stress amplitude and lower plastic strain during the second cycle. As cyclic loading continues, the difference between these hysteresis loops gradually decreases (Fig. 2-15b), and they are nearly superposed by the end of fatigue tests (Fig. 2-15c). This phenomenon indicates that SMAT mainly affects the cyclic behaviour of the early stage of LCF, and its effect is reduced during cyclic loading.

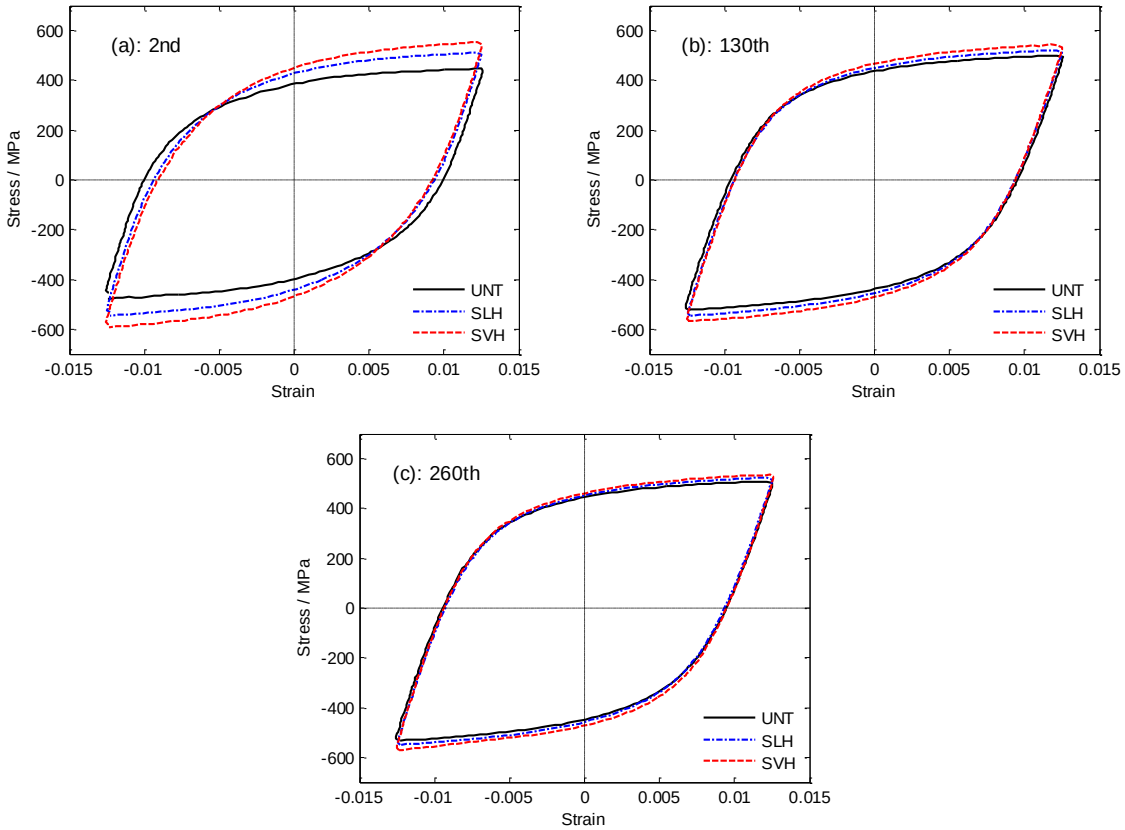

Fig. 2-15. Hysteresis loops with $\Delta\varepsilon/2 = \pm 1.25\%$ for: (a) 2nd cycle, (b) 130th cycle, and (c) 260th cycle.

Under cyclic loading with high strain amplitude, new plastic slips can be activated, which could lead to the restructuring of the dislocations introduced by SMAT in the work hardened area. As cyclic loading goes on, dislocation structure in the work hardened area induced by SMAT could tend to be similar to that in the untreated material. Accompanied with these dislocation activities, most of the compressive residual stress introduced by

SMAT will be relaxed, especially during the first several cycles under high strain amplitude [42], and the remained compressive residual stress may not be high enough to significantly influence the whole cyclic behaviour of the fatigue specimen at the subsequent stage of fatigue. Effect of the residual stress will be further discussed in the following chapters.

2.3.3 Cyclic hardening/softening

Most engineering materials exhibit cyclic hardening/softening to some extent during cyclic plastic deformation. Each stress-strain hysteresis loop has a definite geometry, with a loop width that is double of plastic strain amplitude, and stress amplitude is proportional to elastic strain amplitude. Therefore, hysteresis loop geometry can be expressed by the ratio of plastic strain amplitude and elastic strain amplitude which is named as strain ratio SR [237]:

$$SR = \Delta\varepsilon^p / \Delta\varepsilon^e \tag{2-4}$$

Hardening factor H can thus be expressed as the ratio of strain ratio SR at saturated cycle SR_s and the strain ratio at first cycle SR_1 [237]:

$$H = SR_s / SR_1 \tag{2-5}$$

According to Eq. (2-5), it can be stated that $H < 1$ means cyclic hardening and $H > 1$ means cyclic softening with respect to the initial state. Based on Eq. (2-5), Fig. 2-16 gives the hardening factor H variation as a function of number of cycles for different material states with strain amplitude of ±0.5%, ±0.8%, and ±1.25%, respectively. The slope of curve stands for hardening/softening rate in the cycle. It can be seen that under lower strain amplitude (±0.5%), although the cyclic hardening rate is smaller in the initial hardening stage, the maximum stress amplitude is reached earlier, and a longer softening phase occurs after the short period of initial hardening (Fig. 2-16). Under strain amplitudes of ±0.8% and ±1.25%, untreated specimens undergo more obvious hardening than SLH and SVH specimens. In addition, secondary hardening can be observed after a period of softening. This phenomenon is more significant for untreated specimens than for SLH and SVH ones. Moreover, SLH specimens undergo a slight secondary hardening, while the stress amplitude of SVH specimens are nearly stabilized (Fig. 2-16c).

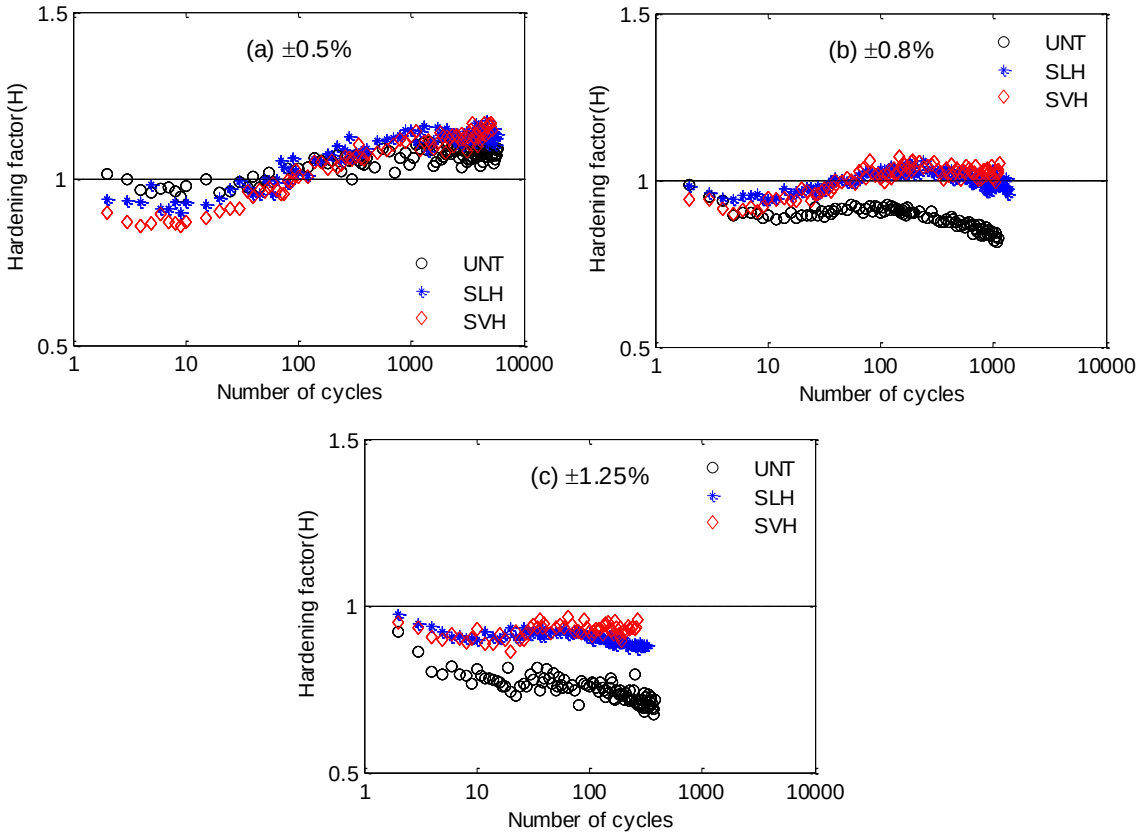

Fig. 2-16. Hardening factor variation curves for different material states under strain amplitudes: (a) ±0.5%, (b) ±0.8%, and (c) ±1.25%.

It is well documented that the mechanical behaviour of metastable austenitic stainless steels during static and cyclic loadings can be influenced by the martensitic transformation [238,239]. Furthermore, it is postulated that secondary cyclic hardening at room temperature might be due to the formation of martensite in austenitic stainless steel [240,241]. However, according to XRD measurements carried out in this work, as shown in Fig. 2-17, no martensitic phase was detected on UNT and SVH specimens after fatigue tests, which is consistent with the results presented in [242]. In this case, the presence of secondary hardening in 316 L is probably related to the formation of specific dislocation structures involving activation of secondary slip systems.

Hardness variation of SLH and SVH specimens after fatigue tests was evaluated, and Fig. 2-18 illustrates the result under strain amplitude $\Delta\varepsilon/2 = \pm 0.8\%$. It can be seen that after LCF, compared with the states without fatigue loading, the hardness in the SMAT affected region of SVH and SLH specimens decreases about 50 $HV_{0.025}$, whereas the centre region of SMATed specimens increases from 200 $HV_{0.025}$ to about 220 $HV_{0.025}$. This signifies that SMAT affected region is softened, while untreated material is hardened with respect to their initial states, which is consistent with the assumption indicated above that the dislocation structures in the work hardened area generated by SMAT and in the untreated bulk material

tend to be similar under the effect of cyclic loading. In addition, the residual stress relaxation during cyclic loading should also contribute to the decrease of the hardness.

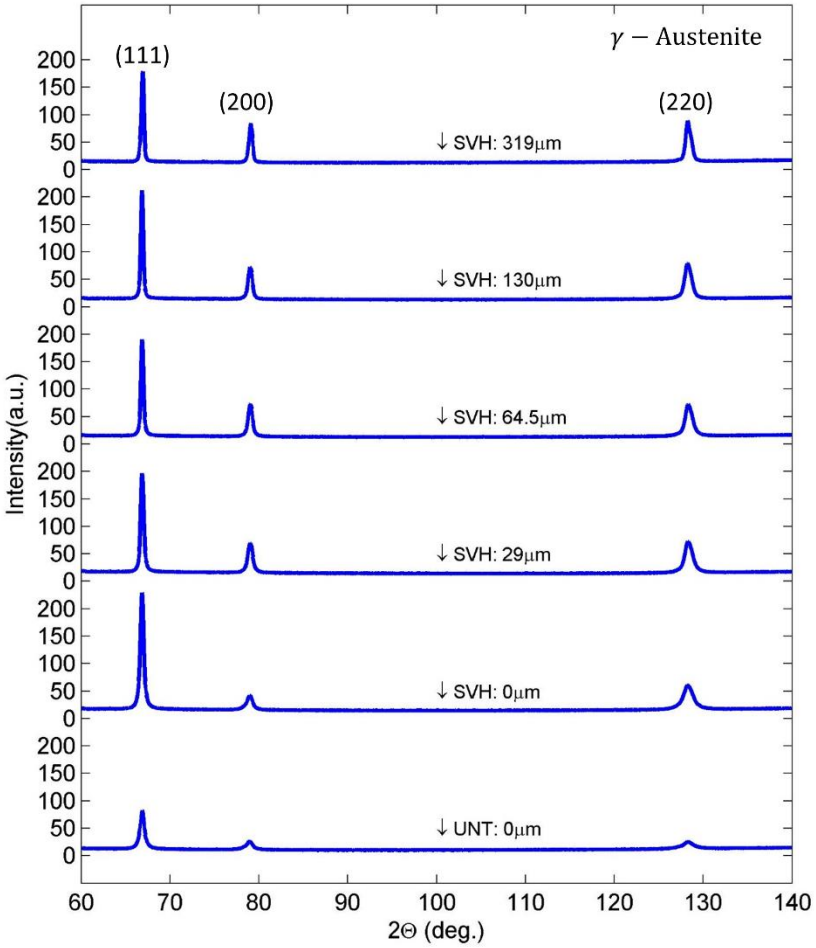

Fig. 2-17. X-ray diffraction patterns obtained for different layers of the SVH specimens and at the surface of UNT specimen after fatigue tests under strain amplitude of ±1.25%.

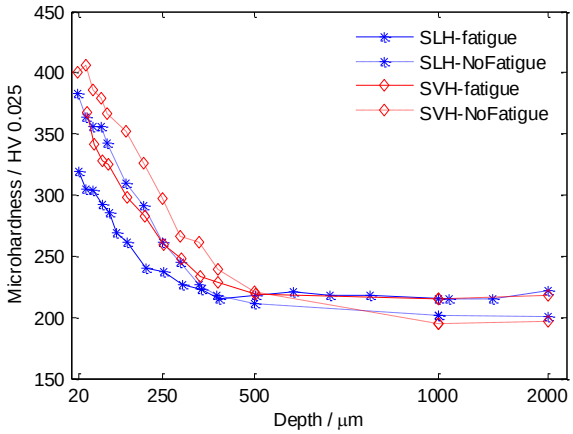

Fig. 2-18. Hardness variation as a function of depth from the treated surface for SLH and SVH specimens after fatigue tests. The curves for specimens after SMAT presented in Fig. 2-6 are also given for the sake of comparison.

2.4 Microstructure evolution during cyclic loading

It is indicated in Section 2.3 that the SMATed specimens present significantly improved cyclic stress amplitudes, and undergo very different cyclic hardening/softening behaviour under the studied strain amplitudes. This should be attributed to the microstructure evolution of the SMAT affected region. This section analyses microstructure evolution for SVH specimen through comparison of the material states before and after LCF with $\Delta\varepsilon=\pm1.25\%$.

2.4.1 Plastic slips

Fig. 2-19 shows the plastic slip traces present in the edge periphery area of the SVH specimen before and after fatigue test as well as the comparison with the centre of the sample. The scan step size is 50 nm and the ultra-fine grain area is not indexed in this case. As already described above, the SMAT induces a large number of plastic slips in the near surface region (Fig. 2-7 and Fig. 2-19b). Then, during fatigue loading, the density of the plastic slip traces increases (Fig. 2-19c). Red crosses shown in Fig. 2-19b and Fig. 2-19c indicate the planes {111} of the activated systems which are confirmed to be {111} <110> in this study. Similar phenomenon is also observed in the intermediate area. As a matter of fact, plastic slips newly activated by fatigue loading can further split the grains and consequently increase the intragranular disorientations inside each grain. Moreover, Comparing Fig. 2-19b and Fig. 2-19c, the plastic slips in each grains for SVH state is irregular, whereas the plastic slips in each grains after fatigue loading are in around 45° with respect to the loading direction. This could be mainly due to the difference of plastic deformation mechanism between SMAT and cyclic fatigue loading. During SMAT treatment, the surface is randomly impacted by high-speed shots with different trajectories, and thus the material is plastically deformed with complex stress state. While under a given loading-unloading direction during uniaxial fatigue, the material is plastically deformed in a constant stress state, for example uniaxial stress state in this study, the plastic slips should be preferably oriented under the effect of uniaxial loading.

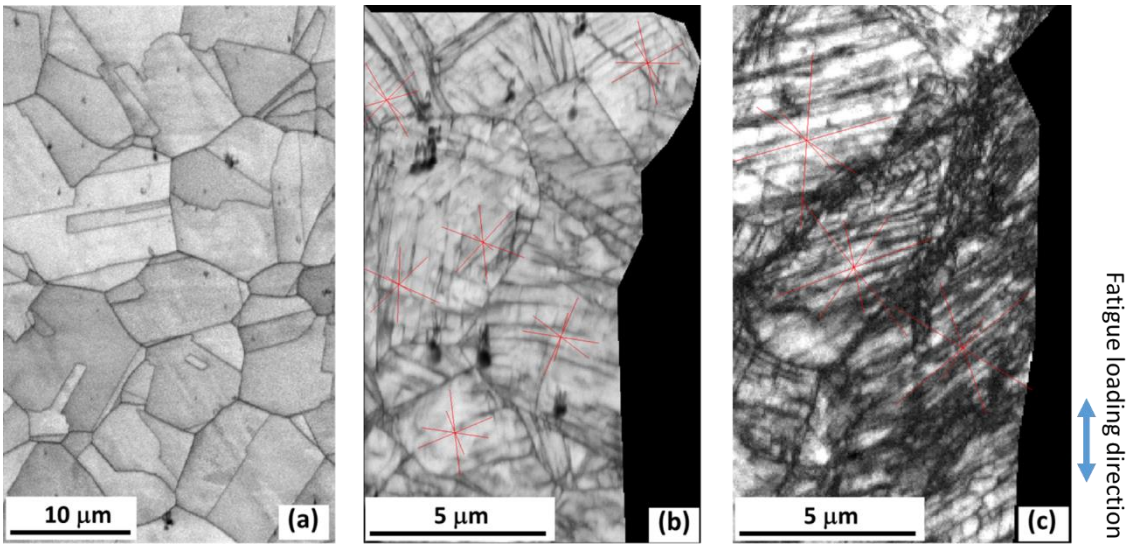

Fig. 2-19. Image quality (IQ) maps illustrating (a) the absence of plastic slip lines in the SMATed sample center which appear in (b) the edge periphery area of the SMATed sample, and in (c) the edge periphery area of the SMATed sample after fatigue loading. {111} plane traces are indicated by red crosses.

2.4.2 Misorientation

Fig. 2-20 shows the average GOS through radius of the SVH specimen in states before and after fatigue (±1.25%). A GOS lower than about 1.5°, as in the centre and in the periphery areas, is the characteristic of a recrystallized material. This is consistent with the fact that these two areas are not affected by SMAT and hence remain in the as-received state. However, SMAT increases the intragranular misorientation from the top surface to the bulk, including the edge periphery and the intermediate area, as indicated in Fig. 2-20. The average GOS value in ultra-fine grain area is not high, indicating that this area is less misoriented, which is consistent with Fig. 2-9b.

After fatigue tests with $\Delta\varepsilon=\pm1.25\%$, in all the regions except the ultra-fine grain area, GOS has been increased under the effect of cyclic fatigue loading, with respect to the unloaded material state. These GOS changes shown in Fig. 2-20 must be due to plastic deformation generated by cyclic loading. As indicated in [243], plastic deformation in polycrystalline materials is able to generate intragranular disorientations, and consequently an increase of the grain orientation spread. The plastic slips newly activated during cyclic loading can further split the grains and consequently increase the intragranular disorientations inside each grain. These results are in good agreement with the plastic slip distribution presented in Fig. 2-19.

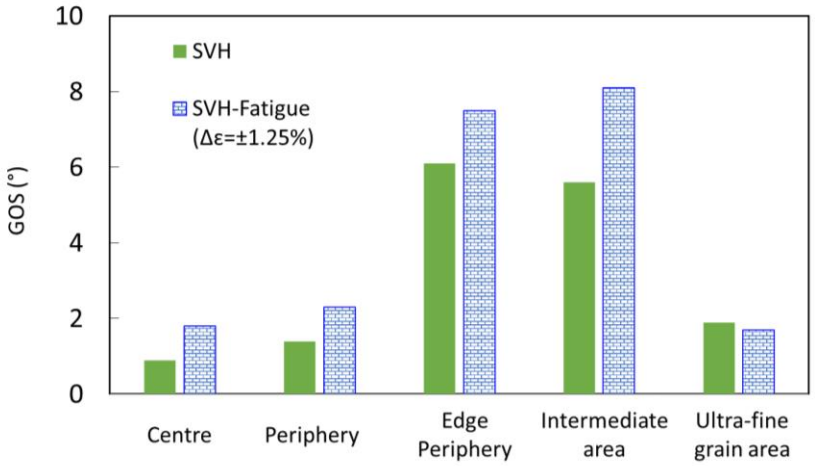

Fig. 2-20. GOS distribution calculated in different areas of SVH specimen before and after fatigue tests (Δε=±1.25%) corresponding to Fig. 2-7.

More detailed GOS information in the ultra-fine grain, the intermediate area and the edge periphery region is shown in Fig. 2-21. In the ultra-fine grain area, nearly no change of grain orientation spread is caused by fatigue loading (Fig. 2-20 and Fig. 2-21a), which means there is almost no plastic slip activated by cyclic loading. This must be due to the fact that the yield stress of the nanostructured layer (with nanoscale grain size) is much higher than that of the work hardened layer or the interior of the material where the grains have an ordinary size, according to the Hall-Petch relation (Eq. (1-1)). It is well known in the literature that the grain interior slip resistance increases with the decrease of grain size. The activation of plastic slip is thus more difficult in ultra-fine grain area, which is consistent with the previous results on the mechanical behaviour of nanocrystalline or ultra-fine grained materials [244–246].

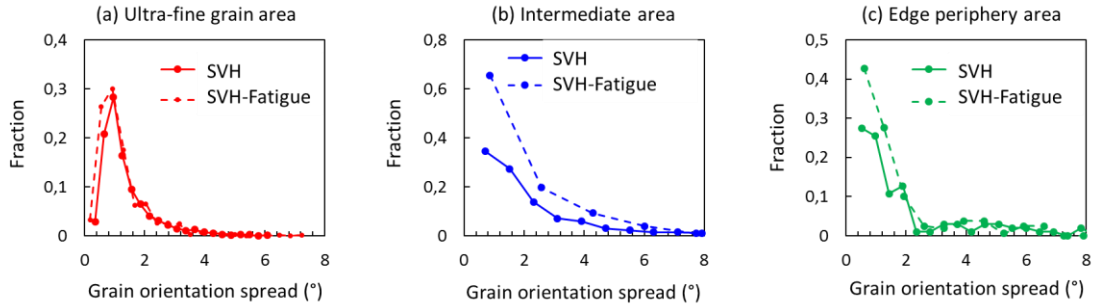

Fig. 2-21. GOS distribution for different areas: (a) ultra-fine grain area, (b) intermediate area, and (c) edge periphery area, for SVH state (S) as well as SVH-fatigued state (SF)..

For the intermediate area (Fig. 2-21b) and the edge periphery area (Fig. 2-21c), it shows that the fraction of grains with small GOS values increases much more than the grains with larger GOS values in the both areas. On the one hand, the grains with a larger GOS value

which corresponds to a larger plastic deformation, have a larger deformation resistance during fatigue loading; On the other hand, as discussed in Section 2.4.1, the difference of loading-unloading mechanism contributes to the different misorientation distributions of grains. Therefore, the plastic slip and misorientation in the grain, which is not activated by SMAT, are much more easily to be reactivated during fatigue loading.

2.4.3 Grain size

Fig. 2-22 illustrates the comparison of grain diameter distribution for the SVH specimen before and after fatigue ($\Delta\varepsilon=\pm1.25\%$). It can be seen that there is small area fraction decrease of the small grains (50-250 nm) in both the ultra-fine grain area and the intermediate area, which indicates that the size of some small grains is increased during the fatigue cyclic loading. This is consistent with some recent studies [33,39,40], in which the nanocrystalline and ultra-fine grains can undergo mechanically-driven recrystallization and grain growth during cyclic loading and monotonic loading conditions. However, the mechanism of the mechanically-driven recrystallization or grain growth has not yet been thoroughly understood.

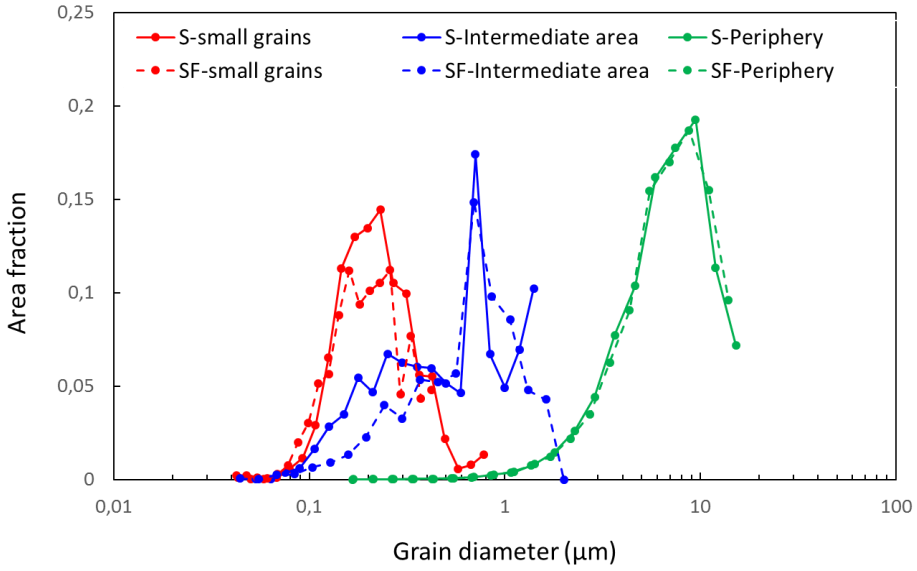

Fig. 2-22. Distribution of grain diameter of different areas for the specimen SMATed (S) and the one SMATed and fatigued (SF).

2.5 Conclusion

In this chapter, the gradient microstructure features of a 316L austenitic stainless treated by SMAT is characterized using EBSD and XRD. The LCF behaviour of SMATed specimens and evolution of the microstructure features are studied in LCF regime.

EBSD observation shows that the SMAT condition with higher treatment intensity (SVH) can generate a grain size gradient at the treated surface. From ultra-fine grain area to the non-affected bulk of the specimen, a transition layer with a gradient distribution of plastic deformation is observed. This gradient plastically affected region is evaluated by plastic slips, KAM and GOS parameters. According to XRD analysis, no martensitic transformation is detected. In addition, a compressive residual stress field was generated by SMAT with the highest value around -530MPa. The in-depth micro-hardness test and FWHM analysis indicate that this plastically affected region can reach a depth of about 600 µm from the treated surface.

Strain-controlled LCF tests with strain amplitudes ranging from ±0.5% to ±1.25% were carried out. Results show that cyclic stress amplitude of SMATed specimens is significantly enhanced due to higher strength of the SMAT affected region. During cyclic loading, SMAT affected region undergoes cyclic softening, whereas the unaffected central region is hardened under high strain amplitude (±0.8%, ±1.25%), and softened under low strain amplitude (±0.5%). Moreover, comparison of hysteresis loops between different cycle numbers indicates that SMAT mainly affects cyclic behaviour in the early stage of fatigue test, and this effect is gradually attenuated as cyclic loading goes on.

EBSD analysis of the SVH specimens before and after fatigue tests indicates that new plastic slips were activated in the mechanically deformed region during cyclic loading, which consequently led to an increase of grain orientation spread. These new activated plastic slips are preferably concentrated and oriented in the periphery region of SMATed specimen due to the uniaxial cyclic loading. However, in the ultra-fine grain area, no obvious change of GOS value can be observed. This could be due to the fact that the slip resistance is higher in nanocrystalline or ultra-fine materials. Moreover, strain-driven grain growth could be observed for small grains at the treated surface during cyclic loading.

The work presented in this chapter about fine analysis including microscopic mechanism and macroscopic mechanical behaviour provides interesting perspectives for modelling and numerical simulation of the cyclic behaviour of the SMATed material.

Chapter 3: Comparison between SMAT and conventional shot peening

Chapter 2 investigates the macroscopic cyclic behaviour and the associated microstructure evolution of a 316L austenitic steel treated by SMAT in LCF regime. It is shown that SMAT generates typical gradient microstructures in the near surface region of the material, including grain refinement, compressive residual stress, and work hardening. These gradient features can significantly affect the LCF behaviour of the material, and they evolve as well during cyclic loading, through for example dislocation rearrangement, grain growth, residual stress relaxation.

As presented in Chapter 1, both conventional shot peening (CSP) and SMAT can improve the fatigue properties of materials thanks to the presence of high compressive residual stresses in the near surface region. However, these two mechanical surface treatment techniques can modify the surface topography and roughness which are non-negligible factors for crack initiation and fatigue life. In addition, compared to CSP, SMAT can generate a nanostructured layer at the treated surface, which should have considerable effects on the mechanical behaviour of materials. In this chapter, comparisons of the surface properties of a 316L steel treated by SMAT and CSP is performed, including surface topography, roughness, residual stress and work hardening. Moreover, their effects on LCF properties are comparatively analysed through fatigue tests under several typical loading amplitudes.

3.1 Material and experimental procedure

The investigated material in this chapter is an another type of 316L ASTM F138 austenitic stainless steel, which has the same nominal chemical composition and heat treatment condition as the steel studied in Chapter 2, as listed in Tab. 2-1. However, this 316L steel was provided by another supplier, and thus can exhibit different mechanical behaviour compared to the previous 316L steel.

Cylindrical dumbbell shaped specimens with the same dimensions were prepared for SMAT and CSP treatment, as shown in Fig. 2-1. SMAT and CSP were performed so as to cover the entire gauge length of the fatigue specimens. SMAT is based on the vibration of spherical shots (3 mm diameter in our case) boosted by a high frequency (20 kHz) ultrasonic generator, as indicated in the above chapter. In CSP, shot is usually propelled by air blast systems. S460H shot was chosen according to MIL-S-13165C standard with an average size of 1.17 mm in order to be able to reach a treatment intensity corresponding to an Almen value of 50A. One of the differences between these two technologies is the loading direction during shot impact. In fact, during SMAT, the shot impacts are randomly multi-directional, which promotes the subdivision of grains by plastic slips and consequently leads to the formation of nanostructured layer [1,24]. In contrast, in the case of CSP, the impacts are usually unidirectional, as shown in the Fig. 1-1, and the formation of a nanostructured layer is possible only when the treatment intensity is extremely high, i.e. in the case of Severe Shot Peening (SSP) [25,247]. To compare these two different techniques, the same Almen intensity and coverage are chosen for SMAT and CSP. Almen intensity and coverage are the two most important parameters that characterize the CSP process. In this work, two Almen intensities (22A, 50A) and two coverages values (125%, 3000%) are considered for SMAT and CSP, as listed in Tab. 3-1. It has to be noted that the highest coverage (3000%) is not actually used in industrial applications, and it was used in this study just to compare with SMAT in order to discern the underlying difference between these two techniques.

Tab. 3-1. Almen intensity and coverage of SMAT and CSP for different specimens and with the corresponding SMAT conditions.

SMAT						
Specimen No.	Shot size (mm)	Generator power	Time (minutes)	Distance (mm)	Almen intensity	Coverage
SULF	3	27%	112 seconds	18	22A	125%
SULM		27%	45 minutes		22A	3000%
SUHF		52%	100 seconds		50A	125%
SUHM		52%	40 minutes		50A	3000%

3.2 Surface characteristics

3.2.1 Surface topography

Fig. 3-1 presents the surface topography and the roughness profile of the as-received specimens, which were obtained respectively using a digital optical microscopy and a

Taylor-Hobson Roughness tester (Taylor Hobson Ltd., Leicester, UK). In Fig. 3-1, turning traces can be clearly observed at the surface of an as-received specimen with an interval of about 150 µm. A clear undulating surface with a sharp tuning angle is illustrated in Fig. 3-1c for the as-received specimen. The difference of height between neighbouring peaks and troughs is around 10 µm.

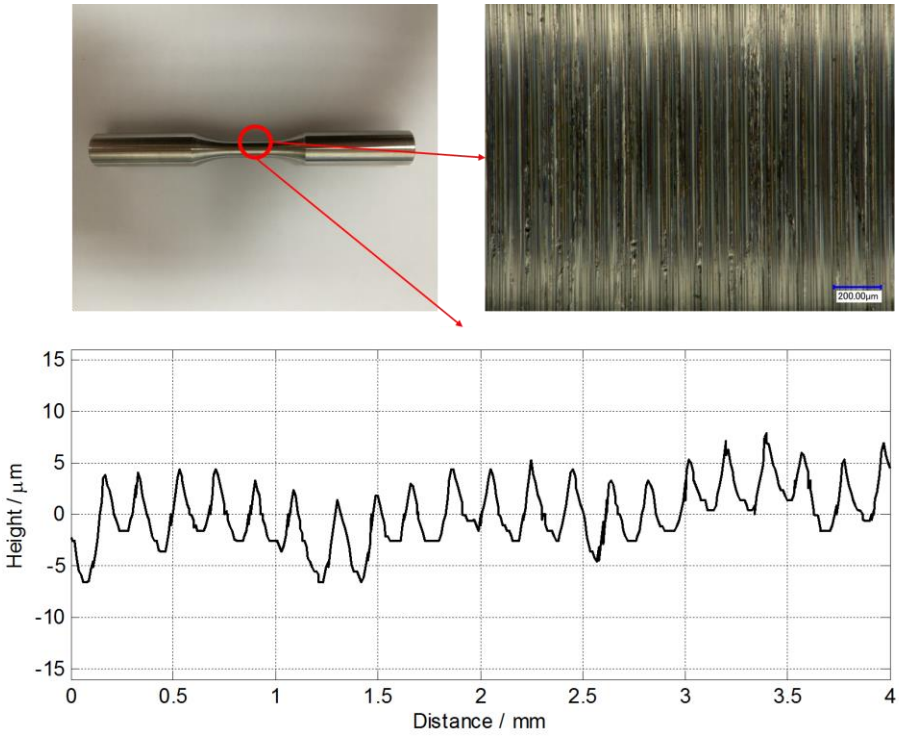

Fig. 3-1. Surface topography and roughness profile of the as-received specimens.

During a peening process, the surface of a material is impacted by high kinetic energy shot, and the induced local plastic deformation at the surface can significantly change the surface topography. Fig. 3-2 illustrates very different surface topographies induced by SMAT and CSP with different Almen values and coverage. Globally, for the SMATed samples, impact imprints can be clearly seen (Fig. 3-2a and Fig. 3-2c), which seems to be progressively reduced when the coverage increases (Fig. 3-2c). In the case of CSP, the topography of the obtained surfaces is totally different from that obtained by SMAT. It seems that the global appearance of the surfaces is flatter than the surfaces of the SMATed samples. However, it is characterized by the presence of many micro-cracks generated by the impacts, especially under higher coverage (Fig. 3-2d). These micro-cracks present at the surface of the samples could somehow deteriorate the fatigue strength of the material by promoting crack initiation.

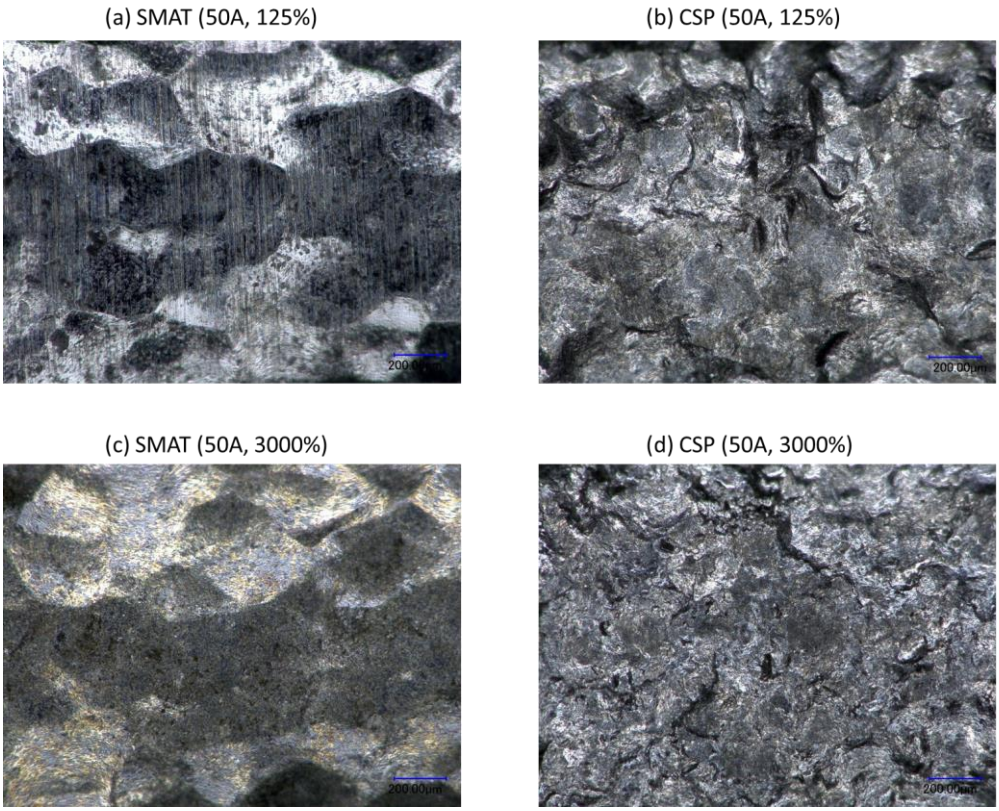

Fig. 3-2. Surface topography of samples treated by SMAT and CSP with an Almen intensity of 50A and different coverage: (a) SMAT with 125%, (b) CSP with 125%, (c) SMAT with 3000%, and (d) CSP with 3000%.

Typical surface profiles of the samples treated by SMAT and CSP are illustrated in Fig. 3-3, which gives an idea about their surface topographies obtained with different treatment conditions. It can be seen that for the samples treated by CSP (Fig. 3-3b), the maximum height of the profile is much more pronounced and the turning angle is sharper than those of the samples treated by SMAT (Fig. 3-3a). In addition, the comparison between the dotted curve and the solid curve in each figure of Fig. 3-3 seems to indicate that the increase in coverage does not much change the surface profile.

Fig. 3-4 presents the surface topographies of specimens treated by SMAT with the Almen intensity of 22A and different coverage. It shows that the turning traces are not completely erased by SMAT with the coverage of 125% due to the short time duration (Tab. 3-1). Comparatively, the surface topography in Fig. 3-4b was completely modified by SMAT with a longer treatment time (coverage of 3000%). In addition, the treated surface shows smaller impact imprints compared to the Fig. 3-2c due to the lower impact energy under the Almen intensity of 22A.

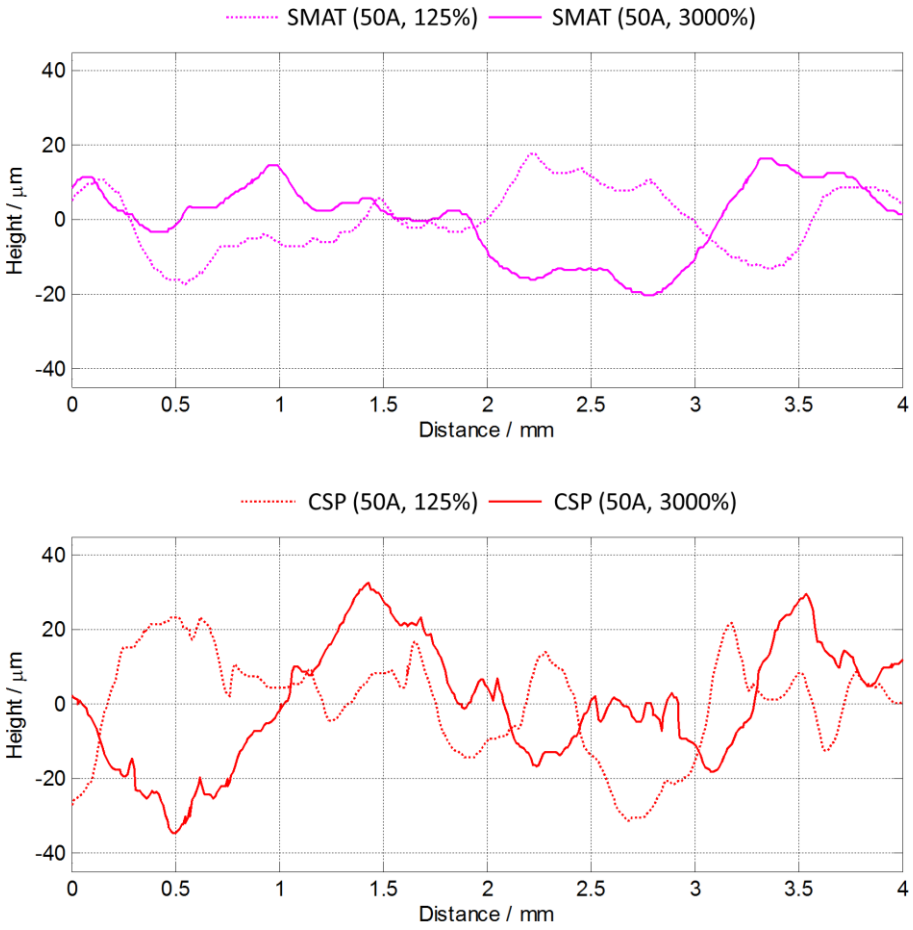

Fig. 3-3. Examples of surface profiles measured along the axial direction of samples treated by: (a) SMAT, and (b) CSP, with an Almen intensity of 50A and a surface coverage of 125% and 3000%.

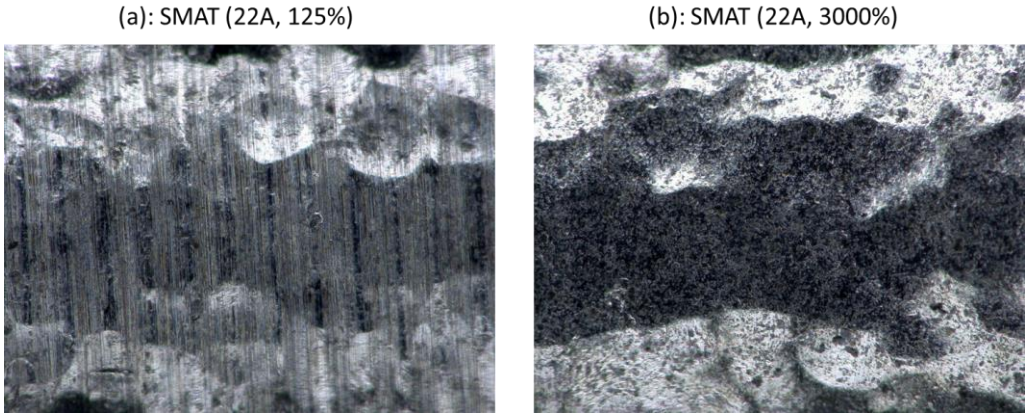

Fig. 3-4. Surface topography of specimens treated by SMAT with the Almen intensity of 22A and different coverage: (a) SMAT with 125%, (b) SMAT with 22A, 3000%.

The surface profiles of the specimens treated by SMAT (22A, 125%) and SMAT (22A, 3000%) are illustrated in Fig. 3-5. It can be found that the coverage of 125% and 3000% generate nearly the same surface profiles at the Almen intensity of 22A, which indicates the same phenomena with the surface profiles obtained by higher Almen intensity (50A)

treatment of SMAT and CSP (Fig. 3-3). Nevertheless, the two surface profiles shown in Fig. 3-5 present smaller height difference between contiguous peaks and troughs compared to the specimens treated by SMAT (50A, 125%) and SMAT (50A, 3000%), as illustrated in Fig. 3-3.

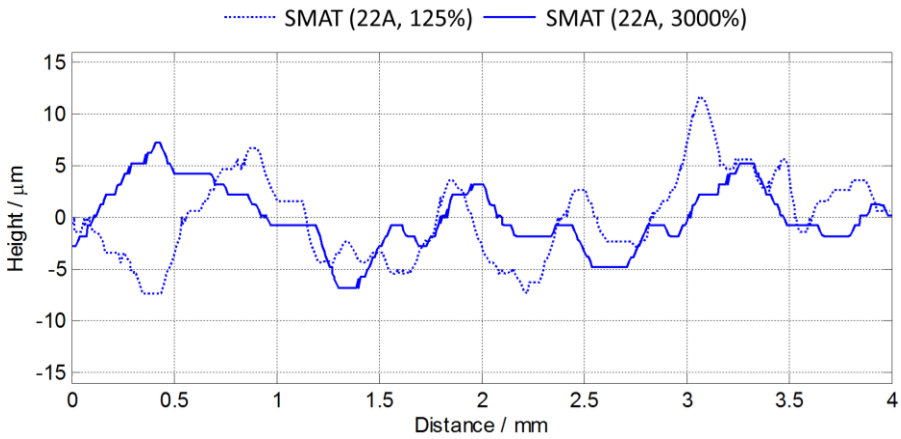

Fig. 3-5. Examples of surface profiles measured along the axial direction of specimens treated by SMAT with an Almen intensity of 22A and a surface coverage of 125% and 3000%.

3.2.2 Surface roughness analysis

To quantitatively analyse the effect of different peening conditions at the surface topography of the material, three roughness profiles (for example shown in Fig. 3-1, Fig. 3-3, Fig. 3-5) were measured at the surface in each specimen using Taylor-Hobson Surtronic 3+ Roughness gage (Taylor Hobson Ltd., Leicester, UK). The roughness parameters were calculated statically according to the reference [248] and the standard (ISO. 4287) for each specimen. Tab. 3-2 lists the average value of the several typical roughness parameters for the specimens with different treatment conditions.

Tab. 3-2. Average surface roughness parameters for the specimens with different treatment conditions.

Specimen	Ra (µm)	Rq (µm)	Rp (µm)	Rv (µm)	Rz (µm)	Rdq (°)	Rpc (pics/cm)
CSP (50A, 125%)	4.25	5.23	11.26	8.74	20.00	14.63	26.07
CSP (50A, 3000%)	3.39	4.21	9.65	7.15	16.80	15.63	35.40
SMAT (50A, 125%)	1.82	2.20	4.48	3.84	8.33	9.50	16.67
SMAT (50A, 3000%)	1.59	1.88	3.99	2.80	6.80	8.44	19.83
SMAT (22A, 125%)	1.30	1.59	3.37	2.87	6.25	8.05	25.00
SMAT (22A, 3000%)	1.16	1.36	2.52	2.17	4.68	6.84	23.45
UNT	1.98	2.33	5.02	3.72	8.74	13.50	51.03

Ra: Arithmetic average of the absolute values of the profile heights over the evaluation length;

Rq: Root mean square average of the profile heights over the evaluation length;

Rz: Average value of the absolute values of the heights of five highest profile peaks and the depths of five deepest valleys within the evaluation length;
Rp: Maximum height of peaks;
Rv: Maximum height of valleys;
Rdq: Root mean square slope of the profile evaluation length.
Rpc: The number of SAE peaks (ANSI/ASME B46.1.1-1995) per unit length measured at a specified peak count level.

The roughness parameters Ra, Rq, Rp, Rv and Rz in Tab. 3-2 describe the fluctuation in height of the surface. Their values for the specimens with different treatment states are schematically illustrated in Fig. 3-6. It can be seen that SMAT significantly decreases the surface roughness parameters of samples with respective to the untreated ones, whereas CSP increases these parameters. This phenomenon is consistent with the observations presented in the figures from Fig. 3-1 to Fig. 3-5. In addition, Fig. 3-6 shows that a higher coverage can lead to smaller roughness values, and thus a smoother surface of specimens for both CSP and SMAT treatment. It could be attributed to the surface strengthening extent due to the prolonged treatment time duration. At the beginning of treatments, the material at the surface is not yet strengthened, thus each shot can generate a larger dimple at the impacted surface. Under the coverage of 125%, the surface is impacted by a certain number of shots, the multi-impacts can generate a scraggly surface with a larger height difference, as shown in Fig. 3-2a and Fig. 3-2b. When the treatment time duration is prolonged in the case of high coverage, the material at the surface is effectively strengthened. On the one hand, the dimple induced during impact by a shot becomes smaller; on the other hand, the large peaks generated by multi-impacts could be gradually reduced. The difference of height between the peaks and the troughs becomes smaller and smaller, which leads to a smoother surface, as shown in Fig. 3-2c and Fig. 3-2d.

Besides, the tuning angle, which plays an important role in crack initiation, can be reflected indirectly by two roughness parameters: Rdp and Rpc. The two parameters respectively describe the slope of the profile and the density of the peaks. Fig. 3-7 illustrates a comparison of the average Rdp and Rpc values of CSPed, SMATed and UNT specimens. It shows that CSPed specimens have largest profile slopes then other specimens. Comparatively, the profile slopes of SMATed specimens are much smaller than both the UNT and the CSPed specimens. It can be also observed that lower is the Almen intensity, smaller are the slopes. An opposite trend can be observed for the CSPed and SMATed specimens treated by coverage of 125% and 3000%. It shows that the CSPed specimens with the coverage of 3000% have larger profile slopes than the specimens treated with the

coverage of 125%, whereas the SMATed specimens have smaller slopes for higher coverage (3000%) than for lower coverage (125%). This phenomenon could be due to the multi-directional impacts during SMAT, while for the CSPed specimens, the longer treatment time duration can make the micro-cracks appear in a deeper layer of material, which leads to larger profile slopes, as shown in Fig. 3-2b, Fig. 3-2d, and Fig. 3-8.

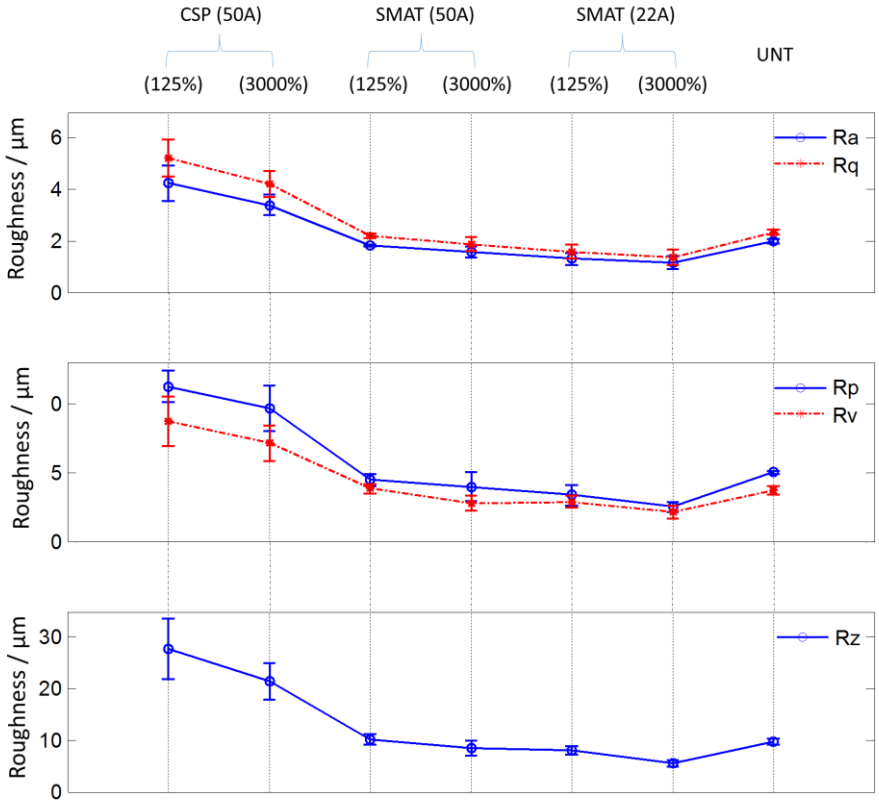

Fig. 3-6. Schematic compariosn of surface roughness parameters (Ra, Rq, Rp, Rv, Rz) of the specimens with different treatment conditions.

For the density of peaks, Fig. 3-7b shows that UNT specimen has very dense peaks and troughs, which are generated by turning. After CSP and SMAT, the peaks density of the specimens is significantly decreased. Moreover, with the increase of coverage, the CSPed specimen has an obvious larger Rpc value. This could be due to the fact that a longer treatment time duration generates a large number of micro-cracks at the surface of material, which will be discussed in Fig. 3-8. For the SMATed specimens, it seems that the higher Rpc value induced by the coverage of 3000% than by 125% is generated by smaller dimple during impacts between shots and strengthened material. In addition, the high Rpc value of specimen treated by SMAT (22A, 125%) could be due to the fact that the tuning traces were not completely erased by a lower treatment intensity and shorter time duration, as shown in Fig. 3-4a.

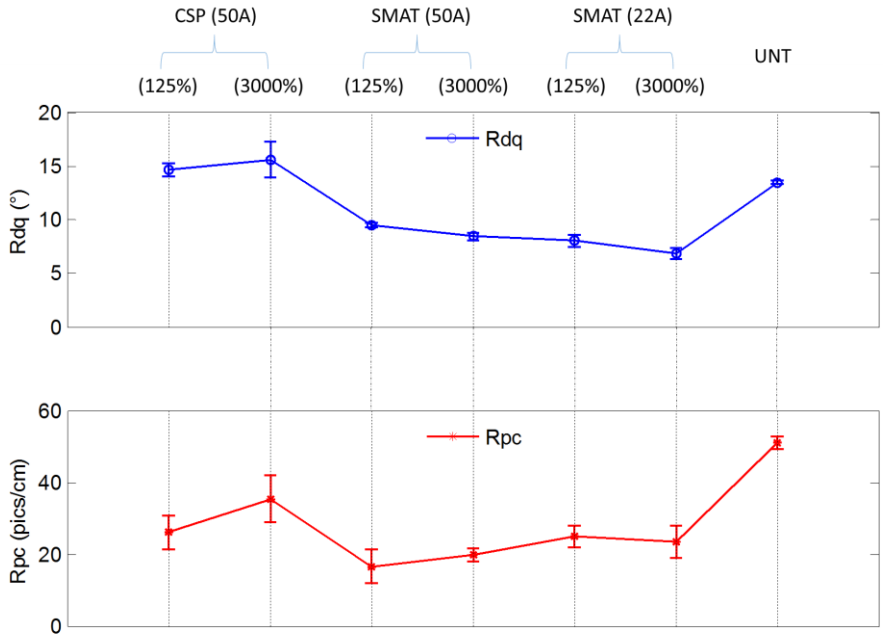

Fig. 3-7. Comparison of surface roughness parameters (Rdq, Rpc) of specimens obtained with different treatment conditions.

In a short, based on the surface topography and the roughness analysis presented in this section, it can be concluded that SMAT and CSP are able to significantly modify the surface of materials, including roughness, micro-cracks. These surface features can cause stress concentration and consequently crack initiation, and thus should have considerable effects on fatigue life of the material.

3.3 Gradient properties

3.3.1 Microstructure observations

All the treated specimens were observed on the cross-section using a digital optical microscopy, in order to investigate the microstructure, especially in the near surface region. Notice that the specimen preparation conditions including the chemical attack are the same for all the samples. The role of the chemical attack is to reveal the grain boundaries, which is based on different kinetics of attack for grains with different orientations.

Fig. 3-8 shows that the global microstructure is different for the samples treated by SMAT and CSP, especially between SMAT and CSP with a same coverage of 3000%. It seems that after CSP, the quantity of grain boundaries which can be revealed by a chemical attack is much more reduced with respect to the samples treated by SMAT, in which the grain boundaries can be easily distinguished. This implies that the plastic deformation state for these two samples treated by SMAT and CSP are different. However, it is important to

remind that for these two samples (Fig. 3-8c and Fig. 3-8d), the same Almen intensity and coverage (Almen intensity of 50A and coverage of 3000%) were applied. Considering the features of these two processes, as mentioned in Section 2, this difference of plastic deformation state is most likely due to the fact that SMAT can induce plastic deformation by multi-directional shot impacts, whereas in the case of CSP, the plastic deformation is generated by unidirectional impacts.

In addition, it can also be seen that the treated surface seems smoother for SMAT than for CSP, which is consistent with the investigation performed using a roughness tester (Fig. 3-3). Moreover, Fig. 3-8d shows several discontinued dark lines at the surface of the sample treated by CSP (50A, 3000%). These lines probably correspond to CSP induced micro-cracks (see Fig. 3-2d) which are also revealed by the chemical attack applied on the cross-section.

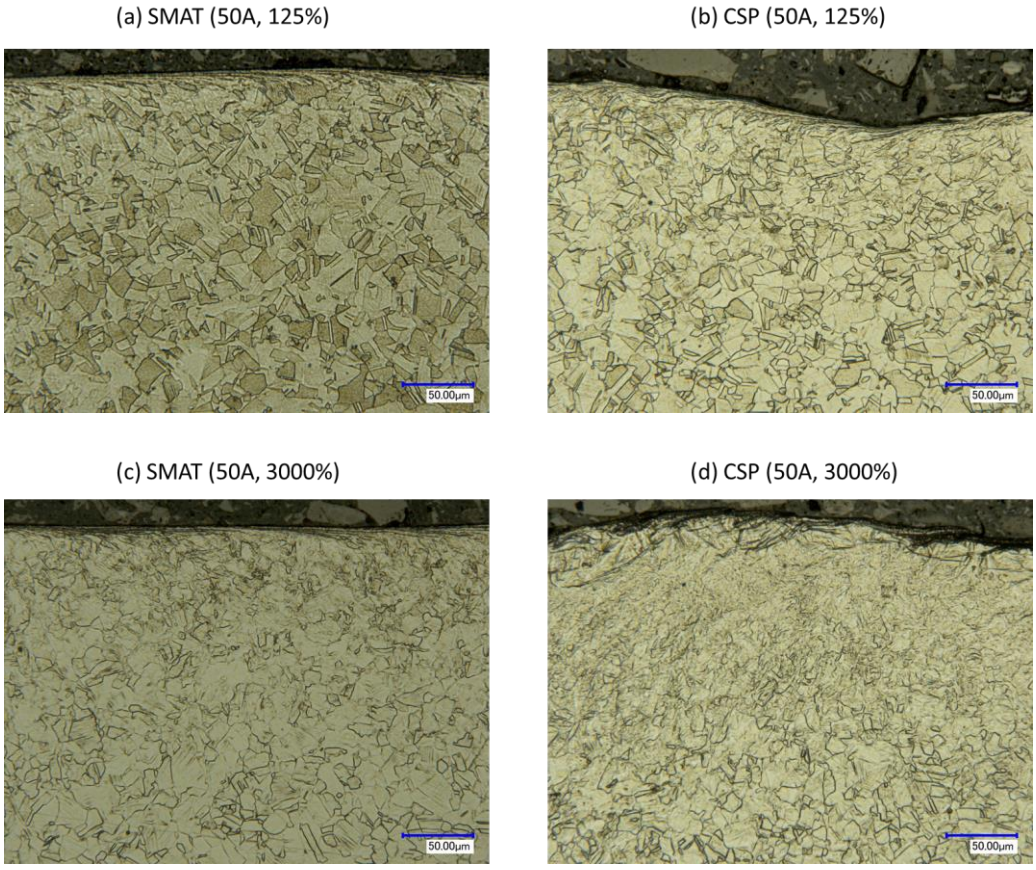

Fig. 3-8. Micrography of samples treated with an Almen intensity of 50A and different coverage values: (a) SMAT with 125% coverage, (b) CSP with 125%, (c) SMAT with 3000%, and (d) CSP with 3000%.

3.3.2 Residual stresses

Residual stresses in both the axial and the circumferential directions were measured using XRD for the samples treated by SMAT and CSP. Fig. 3-9 illustrates the corrected true

residual stresses in the axial directions and circumferential directions of the specimens treated by SMAT and CSP with an Almen intensity of 50A and different coverages.

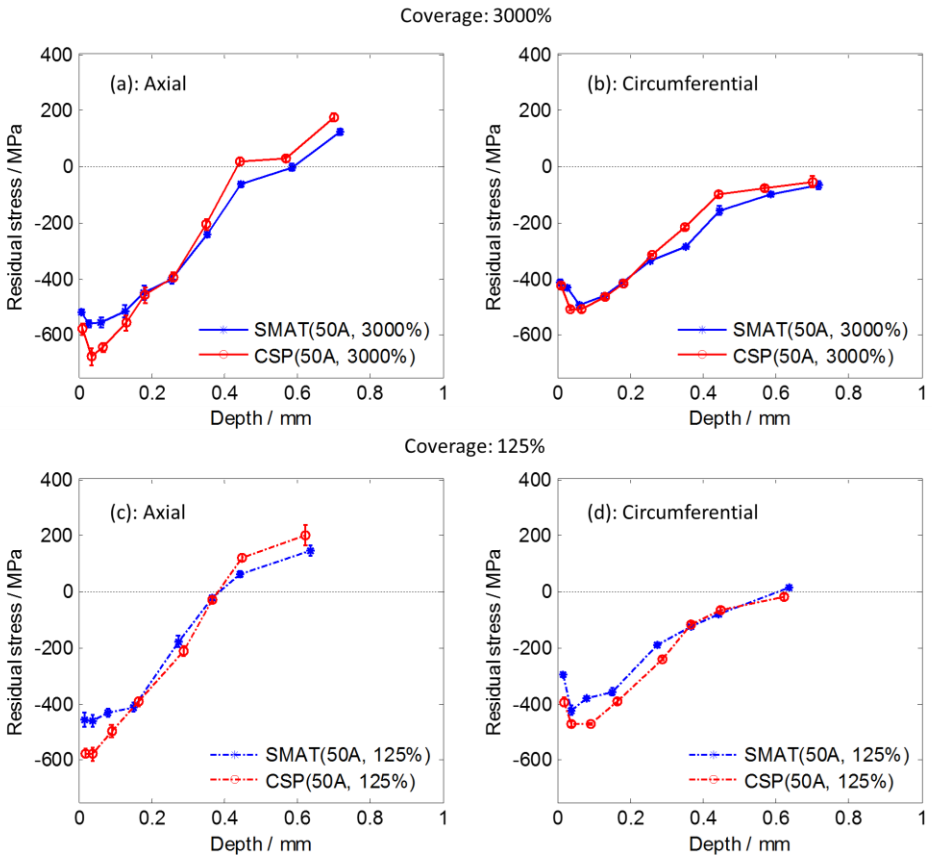

Fig. 3-9. In-depth variation of axial and circumferitial residual stresses for specimens treated by SMAT and CSP with the Almen intensity of 50A and different coverage.

Globally the residual stress profiles generated by SMAT and CSP present very similar trends, as shown in Fig. 3-9. After a drastic decrease of residual stresses in the near surface region, they progressively increase towards the bulk of the samples. It seems that the depth within which the axial residual stress is compressive is slightly larger for SMAT than for CSP. However, the maximum compressive residual stress obtained with CSP is higher than that obtained with SMAT (Fig. 3-9a and Fig. 3-9c), and they are located at around 20~40 μm beneath the treated surfaces for both 125% and 3000% coverage. The difference between the residual stress generated by SMAT and CSP with the same Almen intensity and coverage could be related to the difference of impact mechanism between these two techniques, as indicated in Section 3.3.1. For CSP, as the shot impacts are unidirectional, the material is repeatedly strengthened but always in one direction. The plastic deformation generated by previous impacts cannot be even partially released, which leads to the formation of high compressive residual stress. However, in the case of SMAT, the shot impact loading is multidirectional. Thus the plastic slips activated by actual shot impacts

are on the slip plans oblique to the slip plans on which some plastic slips have already been created by previous shot impacts. This slip interaction activity could partially release the plastic deformation generated by previous shot impacts. Thus the finally obtained maximum compressive residual stress is lower for SMAT than for CSP . Nevertheless, the interpretation given above is rather qualitative, and there are many factors (such as the speed and the diameter of shot) involved in the process. A specific study is needed to quantitatively clarify this point.

For the specimens treated by SMAT with a lower Almen intensity (22A), the compressive residual stresses are obviously lower than the samples treated by the higher Almen intensity (50A), as shown in Fig. 3-10. This is due to the fact that higher treatment intensity can induce severer plastic deformation, and thus generate higher residual stresses in a larger depth beneath the treated surface. Similarly, higher coverage (3000%) can generate higher compressive residual stresses than lower coverage (125%) as well, as indicated in Fig. 3-9 and Fig. 3-10.

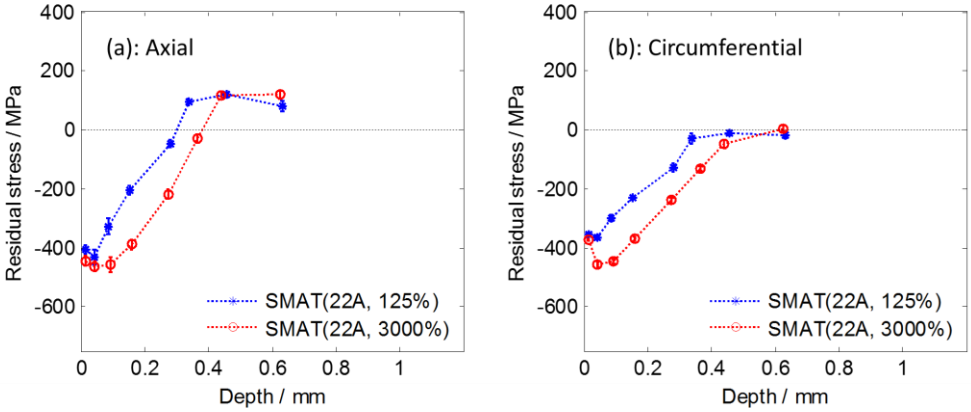

Fig. 3-10. In-depth variation of axial and circumferential residual stresses of specimens treated by SMAT with an Almen intensity of 22A and different coverage: (a) axial residual stress, (b) circumferential residual stress.

3.3.3 FWHM

X-ray diffraction peaks broaden when the crystal lattice becomes imperfect due to, for example, the presence of dislocations. It is well known that the broadened diffraction peak can characterize the micro-strains and micro-stresses which are related to the microstructural state of materials [9,113,249]. According to the theory of kinematical scattering, X-ray diffraction peaks broaden either when crystallites become smaller than about a micrometre or if lattice defects are present in large enough abundance [249]. In addition, the diffraction peak would be broadened considerably when the material

undergoes plastically deformation. Accordingly, FWHM is widely used to represent this evolution of diffraction broadening, and has been considered as an effective approach to estimate the plastic deformation during shot peening [43,136,137,140].

Fig. 3-11 illustrates the measured in-depth variation of average FWHM values in axial and circumferential directions of the treated specimens, and compared to the untreated one. It shows that the measured FWHM in the axial direction has nearly the same values as that in the circumferential direction for all the specimens. According to Fig. 3-11, it can also be found that the FWHM has the highest values at the material surface, and it decreases gradually with the increase of depth. Beyond a certain depth depending on the treatment intensity, it remains almost constant for all the treated specimens with the same constant value of around 0.9. This value is nearly equal to the constant value in the interior of the untreated specimen (black curve in Fig. 3-11). Therefore, the value of 0.9 could be supposed as the FWHM of material which is not plastically deformed, and the region with a constant FWHM value could thus be considered as the non-plastically affected region due to SMAT and CSP.

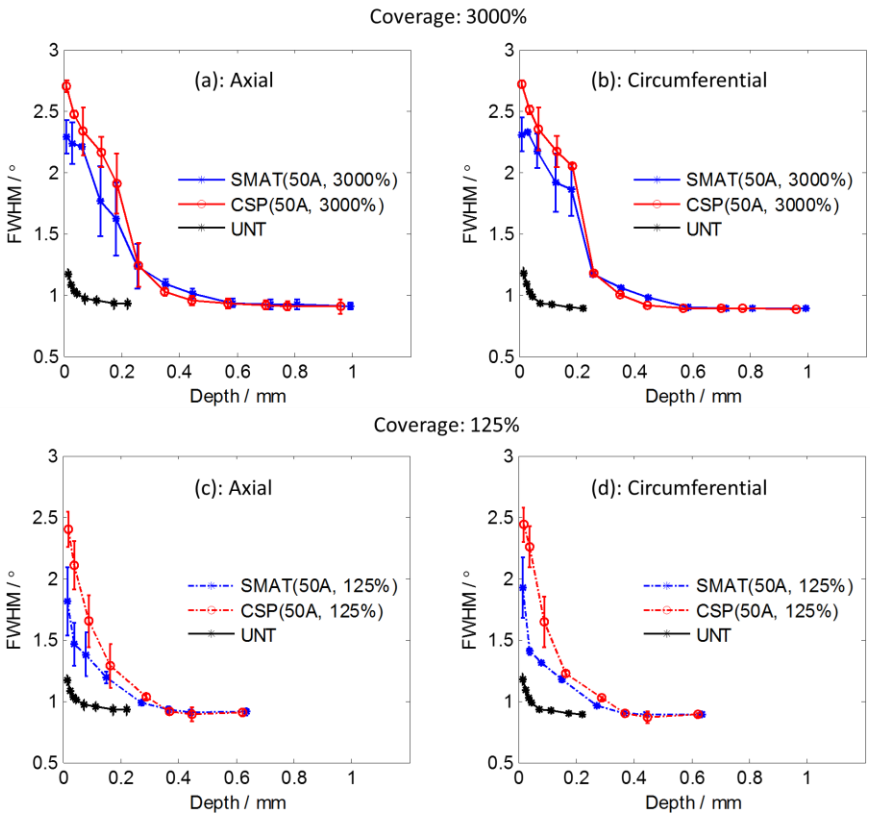

Fig. 3-11. In-depth variation of average axial FWHM value of specimens treated by SMAT and CSP with the Almen intensity of 50A and different coverage.

Under treatment with the Almen intensity of 50A and the coverage of 3000%, the SMATed specimens have a lower FWHM value closed to the treated surface compared to

the specimens treated by CSP, as shown in Fig. 3-11a and Fig. 3-11b. This should be attributed to the fact that CSP can induce a higher severe plastic deformation in the near surface region, as has been discussed in Section 3.3.1. However, under the treatment with coverage of 3000%, the FWHM of specimens treated by SMAT becomes larger than that treated by CSP from the depth of around 0.26 mm and reached the same constant values in the depth of around 0.6 mm. This phenomenon indicates that CSP can induce a higher severe plastic deformation closed to the surface, but this effect decreases more dramatically than SMAT with the same Almen intensity and saturated coverage.

Compared with the Fig. 3-11a and Fig. 3-11c, it shows that the higher coverage can induce higher and deeper plastic deformation due to a longer treatment time duration. The same trend can also be observed for the specimens treated by SMAT (22A, 125%) and SMAT (22A, 3000%), as illustrated in Fig. 3-12. It shows that the higher coverage induced severer plastic deformation in the near surface region and deeper plastically affected region. In addition, the plastic deformation extent in the near surface region and the depth of the plastically affected region are significantly smaller than the specimens treated by SMAT with the higher Almen intensity (50A) in Fig. 3-11.

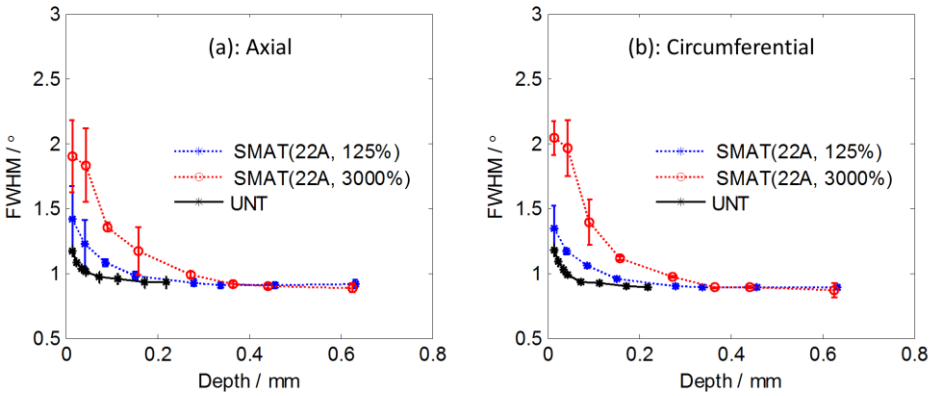

Fig. 3-12. In-depth variation of average axial and circumferential FWHM values of specimens treated by SMAT with the Almen intensity of 22A and different coverage.

In summary, the comparison of residual stress and work hardening performed above implies that the higher Almen intensity and larger coverage can induce higher and deeper compressive residual stress and plastic deformation. Compared with CSP (50A, 3000%), smaller compressive residual stress and plastic deformation were generated by SMAT (50A, 3000%) closed to the surface, but they become larger in the near surface region in the case of SMATed specimens.

3.4 Nanoindentation measurements

Section 3.3 discussed the gradient features of specimens processed by SMAT and CSP with different treatment conditions, including microstructure, residual stress and plastic deformation. These gradient features can induce a gradient mechanical response of material with the depth from the treated surface, which should have a significant effect on the global mechanical behaviour of the structure. However, the local mechanical behaviour induced by SMAT and CSP is not easy to be characterized through the conventional test approaches, such as tensile and compression tests with mechanical specimens.

As a kind of instrumented indentation test method, nanoindentation allows flexible controlling and monitoring the force (P) and displacement (h) response during indenting in a micrometre scale. Different from the conventional hardness and micro-hardness tests, the mechanical parameters are always evaluated based on the P-h curve during the whole loading and unloading regime. It has been confirmed to be an effective approach to estimate the local mechanical behaviour of materials, such as Young's modulus, hardness, yield strength [250,251]. In fact, some studies have been performed to characterize the gradient mechanical behaviour of shot peened materials using nanoindentation by taking into account the influence of nanocrystalline, residual stress, work hardening. [43,58,137].

In this section, variations of Young's modulus and hardness in the near surface region of treated specimens are estimated through nanoindentation measurement. The samples were prepared by cutting the specimens longitudinally, as shown in Fig. 3-13. Then the samples were mechanically polished to a mirror-like finish and then polished with an OPS solution. The nanoindentation tests were performed using the Nano indenter®XP (MTS systems corporation, Eden Praire, USA) with a Berkovich indenter. In order to obtain reliable measurement results, five indentations were performed in each depth with sufficiently spaced to avoid the influence of the adjacent indentations. The final Young's modulus and hardness values in each depth were then calculated by averaging the measured values in the same depth. The other experimental parameters for nanoindentation are listed in Tab. 3-3.

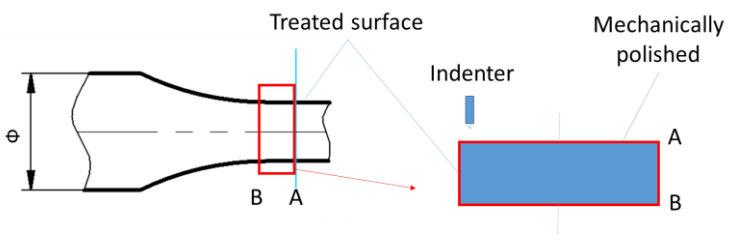

Fig. 3-13. Schematic preparation of samples for nanoindentation tests.

Tab. 3-3. Nanoindentation parameters.

Depth limit	Strain Rate Target	Maximum Calculation Depth	Minimum Calculation Depth
500 nm	0.05 s^{-1}	480 nm	250 nm

The Force-displacement curve (P-h) obtained in each indentation test was then used to determine the Young's modulus and hardness using the software as well as Oliver and Pharr's methods [252]. The measured values of contact hardness and Young's modulus through nanoindentation were respectively calculated with Eq. (3-1) and Eq. (3-2).

$$H = \frac{P_{\max}}{A} \tag{3-1}$$

$$E_r = \frac{\sqrt{\pi}}{2\beta}\frac{S}{\sqrt{A}} \tag{3-2}$$

where $P_{\max}$ is the maximum load, A is the projected contact area, S is the contact stiffness, defined as the initial slope of unloading curve. β is a correction factor for the geometric shape of the indenter, and the value of 1 is taken for axisymmetric indenters (e.g. conical and spherical indenters). For a Berkovich diamond indenter, which will be used in this study, the value is generally recommended to be 1.034. The projected contact area A can be calculated by the contact depth h_c through the following Eq. (3-3):

$$A = 24.56h_c^2 \tag{3-3}$$

where, the contact depth h_c is given by:

$$h_c = h - \beta P_{\max}/S \tag{3-4}$$

3.4.1 Young's modulus

Fig. 3-14 illustrates a comparison of in-depth Young's modulus variation of the untreated, SMATed and CSPed specimens. It shows that the Young's modulus of SMATed and CSPed specimens is nearly constant in the region from the depth of 0.5 mm towards the interior. Comparatively, it seems that there is a small increase of the measured Young's modulus close to the treated surface, and then it decreases to the constant value in the depth of 0.5 mm. In general, the grain refinement which is generated by SMAT is in a small depth at the treated surface, for example 5 µm beneath the treated surface (Fig. 2-7). Therefore, this small fluctuation of measured Young's modulus in the near surface region could be attributed to the compressive residual stress and work hardening, which indirectly affect the

true area of contact during nanoindentation [253]. However, the effect of compressive residual stress and work hardening on Young's modulus should be further addressed.

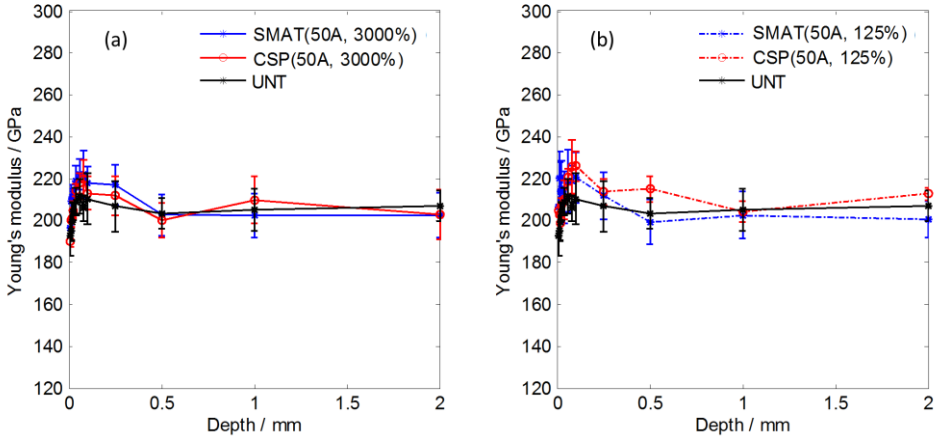

Fig. 3-14. Compariosn of Young's modulus variation as a function of depth from the treated surface for SMATed and CSPed specimens with the Almen intensity of 50A and different coverage, and in comparison with the untreated specimen.

3.4.2 Hardness

Fig. 3-15 shows the in-depth variation of hardness of the untreated, SMATed and CSPed specimens. It shows that the hardness close to the treated surface was significantly increased. For the specimens treated by SMAT (50A, 3000%) and CSP (50A, 3000%), the hardness values can reach as high as around 6 GPa at the treated surface, and then gradually decrease to about 3.2 GPa at the depth of 1 mm (Fig. 3-15a). Beneath, the hardness values of SMATed and CSPed specimens become smaller than the untreated one. In addition, Fig. 3-15a shows that the CSPed specimen has a higher hardness value than the SMATed specimen from the treated surface to a depth of around 0.2 mm, and then the hardness becomes smaller than the SMATed one until the depth of around 1 mm. This phenomenon is consistent with what has been observed for residual stress variations presented in Fig. 3-9a. Moreover, according to the comparison between Fig. 3-15a and Fig. 3-15b, it could be concluded that the coverage of 3000% for SMAT and CSP can induce a higher hardness in the near surface region due to the higher generated residual stress (Fig. 3-9) and plastic deformation (Fig. 3-11). The UNT specimen presents a decrease of hardness close to the surface, and then have a small increase between the depth of 0.5 mm to 1 mm, which could be attributed to the hardening effect during mechanical processing (turning).

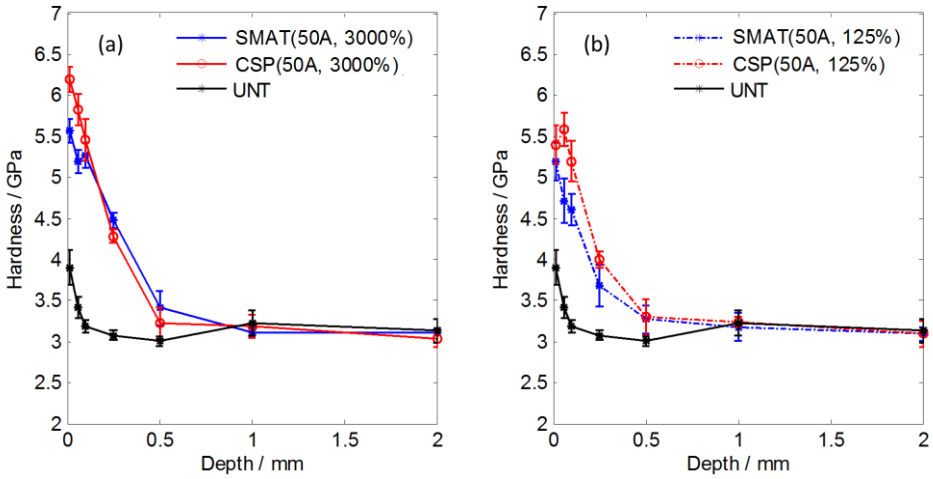

Fig. 3-15. Hardness variation as a function of depth from the treated surface for specimens treated by SMAT and CSP with the Almen intensity of 50A and different coverage.

3.4.3 Discussion

The different hardness variations illustrated in Fig. 3-15 should be caused by the generated gradient features during SMAT and CSP. It is well known that the hardness could be affected by many factors, such as residual stress, plastic deformation, and phase transformation. Studies have shown that a compressive residual stress can induce a larger measured hardness, whereas a tensile residual stress can induce a decrease of the measured hardness. In addition, the hardness can be affected by some other microstructures, such as grain refinement, martensitic transformation. However, no martensitic phase has been detected for the studied material in all the untreated, SMATed and CSPed states, as shown in Fig. 2-10. Section 2.2.2 indicates that a grain-refined layer with a depth of 5 μm was generated for the studied SMAT condition. Therefore, the difference of hardness variations presented in Fig. 3-15 could be due to the residual stress and work hardening. Fig. 3-16 illustrates a comparison of circumferential residual stresses, FWHM, and hardness variations of the untreated, SMATed and CSPed specimens with the treatment condition of (50A, 3000%).

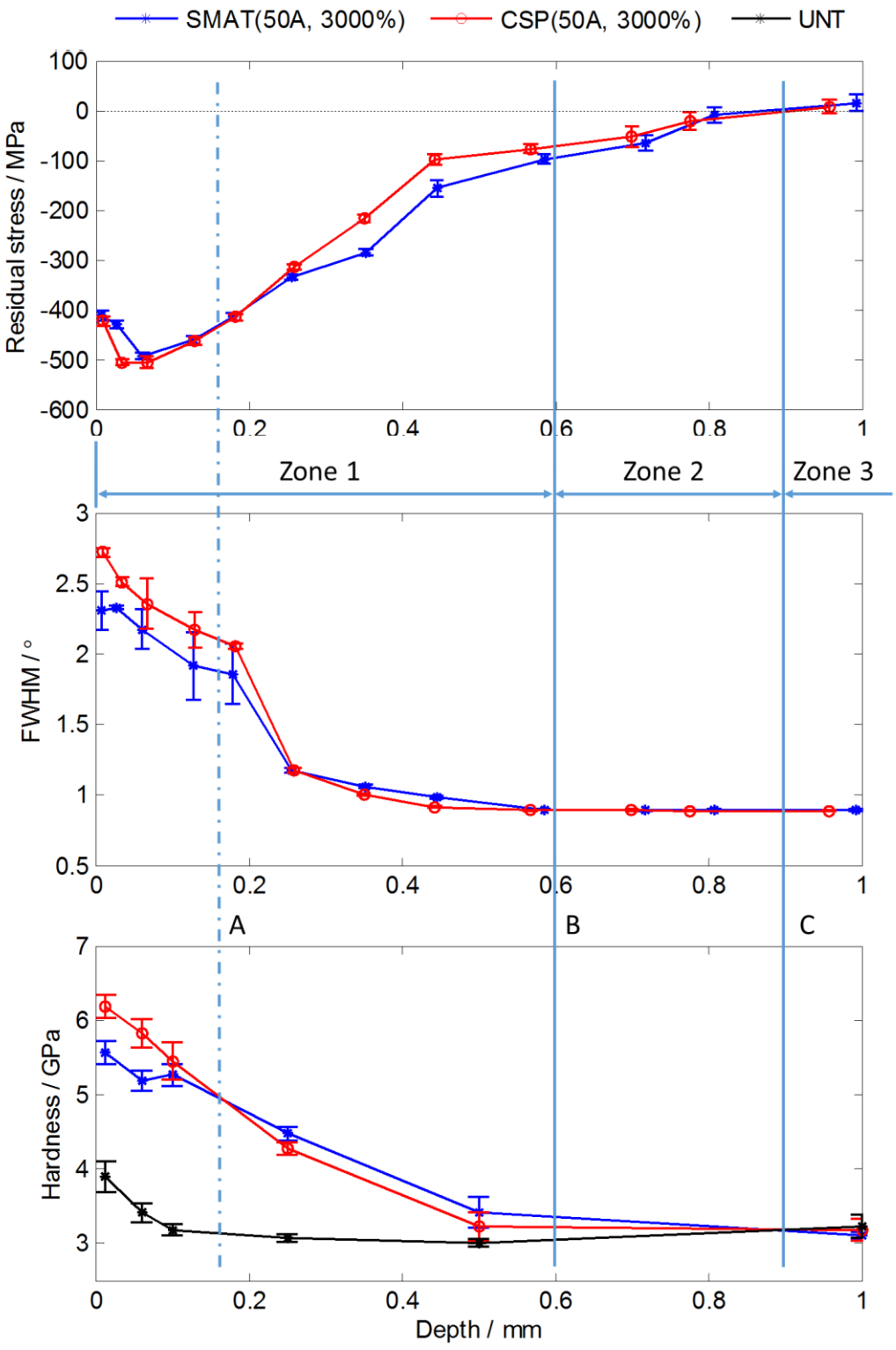

Fig. 3-16. Comparison of residual stress, FWHM and hardness variations for untreated, SMATed and CSPed specimens with the treatment condition of (50A, 3000%).

It should be noted that the nanoindentation measurement is performed on the cross-section of the specimens, as shown in Fig. 3-13. Consequently, the axial residual stress at the measured surface should have been completely relaxed, and thus the residual stresses

with only the circumferential and the radial directions are able to affect the hardness variation. Therefore, the circumferential residual stress and FWHM variations are considered in Fig. 3-16 to analyse their effects on hardness variations of specimens with different treatment states. To compare the circumferential residual stress and FWHM variations of the specimens treated by SMAT (50A, 3000%) and CSP (50A, 3000%), three zones in the cross-section can be defined, as indicated in Fig. 3-16. The first zone represents the plastically affected region due to SMAT and CSP. It can be found in Fig. 3-11a and Fig. 3-11b that the FWHM value (obtained in both axial and circumferential directions) gradually decreases from the treated surface to a depth of around 0.6 mm. Beneath this depth, the FWHM values become constant to the interior of material. This implies that the SMAT and CSP treatment conditions can lead to a plastic deformation reaching a depth of 0.6 mm. Beneath is the as defined second zone, where the material was not plastically deformed. Both Zone 1 and Zone 2 constitute the compressive residual stress area in the near surface region of the treated specimens. According to the stress self-equilibrium condition, there should be the presence of tensile residual stress in the central region (Zone 3) to equilibrate the compressive residual stresses in the near surface region. As indicated in Fig. 3-16, the Zone 3 is thus defined as the tensile residual stress region.

A rough division of different regions of the SMATed and CSPed specimens is presented in Fig. 3-17. Besides, the grain-refinement at the treated surface can be generated by SMAT (as indicated in Fig. 2-7), and these features are not depicted in this section. It should be noted that Zone 2 and Zone 3 shown in Fig. 3-16 are just divided through the circumferential residual stress. In fact, it is not easy to clearly distinguish the boundary between the compressive residual stress and tensile residual stress regions because of the co-existence of the axial, circumferential and radial residual stresses in the treated specimens. These three stresses could have different tensile or compressive natures in the same material point. Moreover, it is hard to clearly divide the zone 3 and the non-affected region due to the difficulty of experimental measurement.

As indicated above, the residual stress and the work hardening can have an important effect on hardness of the material. In the region close to the treated surface (above the boundary A (Fig. 3-16)), both the plastic deformation and the residual stress of the CSPed specimen are higher than the SMATed specimen, which leads to higher measured hardness of CSPed specimen, as shown in Fig. 3-16. At the boundary A, the residual stress of SMATed specimen becomes larger than CSPed specimen. Accordingly the hardness of SMATed specimen tends to be greater than the CSPed specimen as well even though the

plastic deformation is still smaller. This phenomenon indicates that the higher measured hardness is mainly attributed to the higher compressive residual stress. This trend continues until the depth of about 0.9 mm (Boundary C), in which the residual stresses of both SMATed and CSPed specimens are nearly equal to zero. These two specimens have thus the same hardness values as the untreated specimen from this depth, as shown in Fig. 3-16.

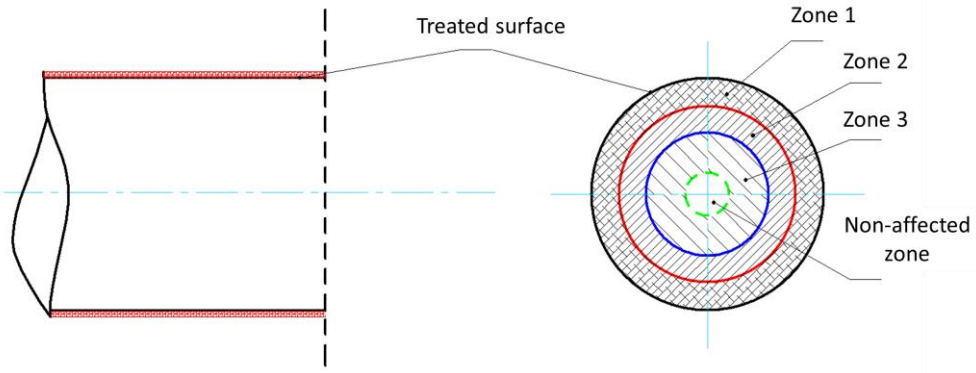

Fig. 3-17. Schematic presentation of different regions in the cross-section of SMATed and CSPed specimens.

In a short, Fig. 3-16 implies that both residual stress and work hardening contribute to the hardness variations of the treated specimens. Furthermore, compared to the work hardening, compressive residual stress can play a more important role in hardness increase of material. This point can be concluded from other SMAT and CSP conditions presented above (Fig. 3-15b).

3.5 LCF properties

LCF tests were carried out on untreated, SMATed and CSPed specimens at room temperature using a servo-hydraulic machine. Uniaxial tension-compression loadings were applied under total strain control with a load ratio $R_\varepsilon = -1$. An extensometer with a gauge length of 10 mm was used to control the strain, and a constant strain rate of $4 \times 10^{-3} s^{-1}$ was imposed for all the fatigue tests. By the end of fatigue test, when the stress amplitude drop reaches 30%, the specimen is considered failed and the fatigue test stops. Tab. 3-4 lists the experimental conditions used for the LCF tests.

Tab. 3-4. Experimental conditions used for LCF tests.

Process	Surface treatment conditions		LCF test conditions ($\Delta\varepsilon/2$)			
	Almen intensity	Coverage	±0.3%	±0.5%	±0.8%	±1.25%
Untreated	-	-	√	√	√	√
SMAT	22A	125%		√		√
		3000%		√		√
	50A	125%		√		√
		3000%	√	√	√	√
CSP	50A	125%		√		√
		3000%		√		√

3.5.1 Cyclic behaviour analysis

Cyclic stress amplitude evolution as number of cycles gives a good description of the cyclic behavior of materials regarding hardening/softening phenomenon. Actually, the hardening/softening behavior of a material can be altered by a treatment. Fig. 3-18 shows stress amplitude evolution curves of samples treated by SMAT (50A, 3000%) and CSP (50A, 3000%) obtained under total strain amplitudes of ±0.5% and ±1.25%. It can be seen that the curves obtained after SMAT (blue dotted curves) and CSP (red dotted curves) are globally very similar. This implies that the treatment conditions applied for these two techniques are equivalent to some extent.

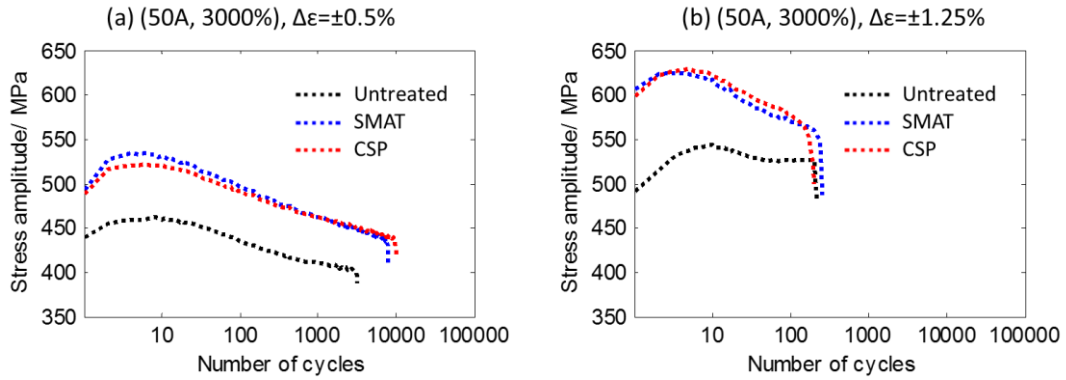

Fig. 3-18. Stress amplitude evolution curves of samples treated with Almen intensity of 50A and coverage of 3000%: (a) under Δε/2 = ±0.5%, (b) under Δε/2 = ±1.25%.

Most stress amplitude evolution curves presented in Fig. 3-18 are characterized by an initial hardening during the first several cycles, followed by a gradual long-term softening until fracture. The initial cyclic hardening can be attributed to an increase in the dislocation density especially in regions close to the grain boundaries [49], whereas the long-term softening may be caused by the dislocation rearrangement resulting from the activation of secondary slips [49]. For the untreated sample tested under Δε/2=±1.25%, the curve exhibits a flat stage by the end of the fatigue test, which means that the material tends to be saturated

before fracture. Another phenomenon which can be observed is that for all the treated samples, the maximum stress amplitude is reached earlier than for the untreated samples. Furthermore, for a same imposed strain amplitude, the stress level of the curves obtained with samples treated by SMAT and CSP is clearly higher than the curve obtained with untreated samples.

The increase of stress amplitude for the treated specimens with respect to the untreated ones is due to the mechanically affected region. In fact, the work hardening generated by shot impacts can increase the mechanical strength due to dislocation entanglement which can impede further permanent deformation of materials. It is worth mentioning that in the case of SMAT, a nanostructured layer should have been generated according to previous investigation performed in Section 2.2.2. However, this nanostructured layer might have a small contribution to the global mechanical behavior because of its very thin thickness (5 µm) compared to the thickness of the mechanically affected region (about 600 µm) and the diameter of the sample (6 mm) (Fig. 2-7).

Fig. 3-19 illustrates the comparison of hysteresis loops between the specimens with the treatment conditions of UNT, SMATed (50A, 3000%) and CSPed (50A, 3000%). It shows that the stresses of SMATed and CSPed specimens are significantly higher than the untreated one. It can be also observed that the differences between these hysteresis loops decreases gradually as cyclic loading continues. As discussed in Section 2.3.1, it should be due to the softening behaviour of the material in the mechanical affected region (Fig. 2-18) resulted from residual stress relaxation and dislocation rearrangement (as indicated in Fig. 2-19). Furthermore, it shows that the SMATed and CSPed specimens have nearly the same hysteresis loops during the different cyclic loading stages.

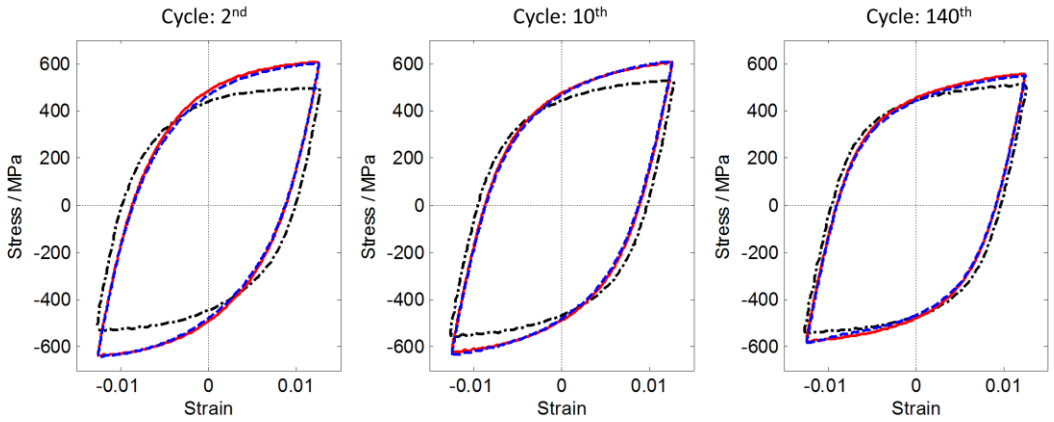

Fig. 3-19. Hysteresis loops of the untreated, SMATed and CSPed specimens with the treatment condition (50A, 3000%) under strain amplitude of ±1.25% for: (a) 2nd cycle, (b) 10th cycle, and (c) 140th cycle.

It is well known that the yield strength of a material could be considered as proportional to its hardness. Therefore, the effect of residual stress and work hardening on the mechanical behavior of the whole specimen could be roughly estimated by the hardness variations of the two treated specimens. We assume that the yield strength σ_y of the material can be approximately expressed by:

$$\sigma_y = \alpha \cdot HV \tag{3-5}$$

where α and HV are respectively the proportionality coefficient and the measured hardness value.

Accordingly, the yield strength of the whole specimen could be considered as the average value over the area of whole cross-section A:

$$\bar{\sigma}_y = \frac{1}{A}\int \sigma_y d_A = \frac{\alpha}{A}\int HV d_A \tag{3-6}$$

In order to calculate the integral of hardness over the whole cross-section of the specimen, a linear interpolation method was used to disperse and sleek the measured in-depth variations of hardness in the near surface region. In addition, we assume that the hardness is constant from the depth of 0.85 mm (Fig. 3-16), and then the average yield strength of the two specimens treated by SMAT (50A, 3000%) and CSP (50A, 125%) are respectively marked in the Fig. 3-20. It shows that the SMATed and the CSPed specimens have nearly the same estimated average yield strength, and thus the two treatment conditions could have the same strengthening effect on the whole specimens, as illustrated in Fig. 3-18 and Fig. 3-19.

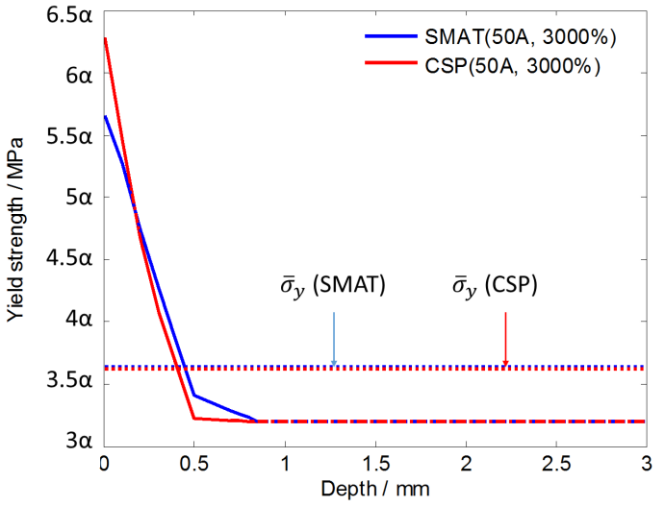

Fig. 3-20. Estimated yield strength in-depth variation of the specimens treated by SMAT (50A, 3000%) and CSP (50A, 3000%).

The effect of SMAT and CSP on the cyclic behaviour of the studied material with a lower coverage (125%) is presented in Fig. 3-21. Contrary to the results presented in Fig. 3-18, significant difference between the curves obtained after SMAT and CSP can be observed under $\Delta\varepsilon/2 = \pm 1.25\%$ (Fig. 3-21b). Nevertheless, the two curves of the samples treated by SMAT and CSP are almost superposed under $\Delta\varepsilon/2 = \pm 0.5\%$ (Fig. 3-21a).

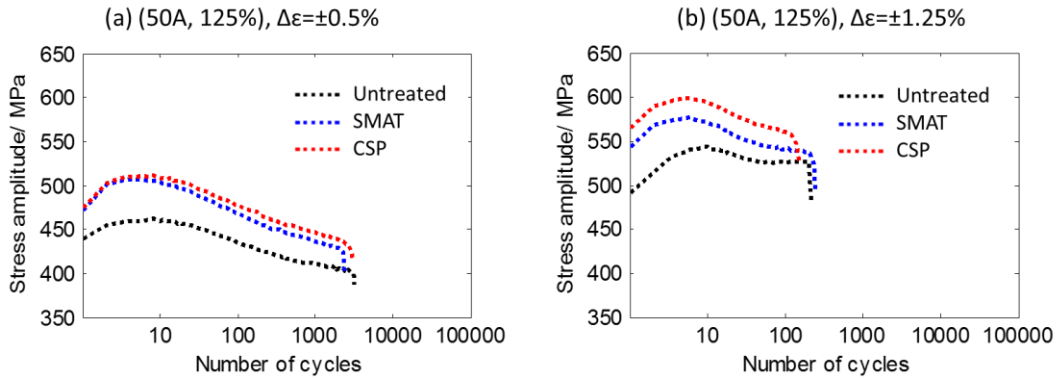

Fig. 3-21. Stress amplitude evolution curves of samples treated with Almen intensity of 50A and coverage of 125%: (a) under $\Delta\varepsilon/2 = \pm 0.5\%$, (b) under $\Delta\varepsilon/2 = \pm 1.25\%$.

This strain amplitude dependence for samples treated by SMAT and CSP is probably due to the difference of plastic slip activity of the plastically affected region. For the coverage of 125%, the material state induced by SMAT and CSP is not saturated due to the short treatment time duration, and thus very different work hardening state can be generated by these two techniques, as assessed by hardness measurement (Fig. 3-15b). Under low strain amplitude (±0.5%), the loading level is not high enough, and only the plastic slips of first order can be activated. Thus there is no notable difference between the two curves (Fig. 3-21a). However, under higher strain amplitude (±1.25%), the loading level is high enough to activate more plastic slips, for example those of the second order. As indicated in Section 3.3, the state of plastic slips generated by SMAT and CSP is different, which could lead to different cyclic behaviour when the loading level is high. This difference of cyclic behaviour can be demonstrated through the first hysteresis loops of the samples treated by these two techniques, as shown in Fig. 3-22. It can be seen that the two specimens nearly share the same curve under $\Delta\varepsilon/2 = \pm 0.5\%$, whereas noticeable difference between the two curves can be observed under $\Delta\varepsilon/2 = \pm 1.25\%$ for both tensile and compressive goings (indicated by red circles).

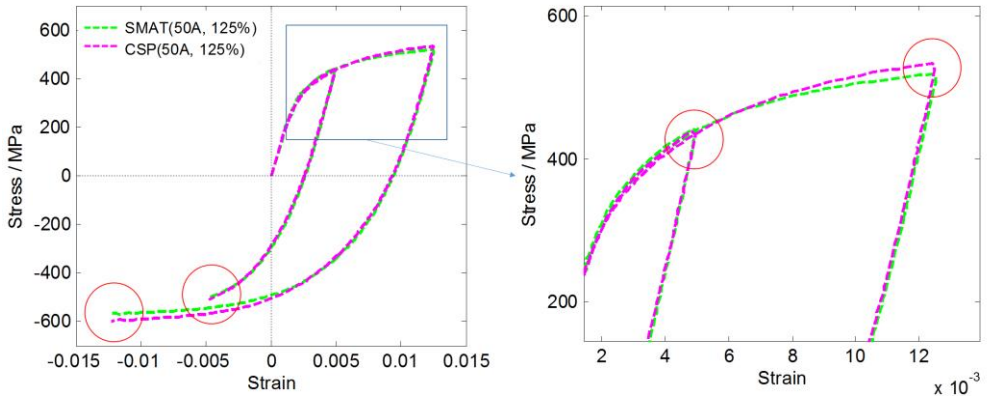

Fig. 3-22. The first hysteresis loops of speicmens treated by SMAT (50A, 125%) and CSP (50A, 125%) under strain amplitude of ±0.5% and ±1.25%.

By contrast, for a coverage of 3000%, much longer time duration was applied to treat the samples. In this case, the material state induced by SMAT and CSP is well saturated, and even under the highest strain amplitude (±1.25%), only the plastic slips of first order can be activated. Hence, there is no significant difference in cyclic behaviour for SMAT and CSP under the two strain amplitudes studied in this work (Fig. 3-18).

3.5.2 Fatigue life

Shot peening is an effective approach to improve fatigue properties of materials due to the generated compressive residual stress, which can inhibit crack initiation and propagation. However, the studies performed above shows that the different peening conditions could significantly modify the surface topography and generate different variations of residual stress and work hardening in the near surface region, as well as surface nanocrystalline for SMAT. It has been confirmed in previous studies that SMAT and CSP are able to improve fatigue life of materials under high cycle fatigue, i.e. under low stress/strain amplitudes. Nevertheless, for LCF, especially under strain-controlled cyclic loading with high strain amplitudes, the benefits of SMAT and CSP are sometimes controversial.

The effect of SMAT and CSP on the fatigue life of 316L steel is analysed in this section. Tab. 3-5 summarizes the number of cycles to failure for the samples treated with different intensities under different strain amplitudes ranging from ±0.3% to ±1.25%. It can be seen that the fatigue life of samples treated by SMAT and CSP with a coverage of 3000% is significantly improved compared to the untreated samples under $\Delta\varepsilon/2 = \pm 0.5\%$. By contrast, a small decrease in the fatigue life of the samples treated by SMAT and CSP with a coverage of 125% can be observed under $\Delta\varepsilon/2 = \pm 0.5\%$, with the numbers of cycles being 2417 and 3099 respectively for SMAT and CSP. Under a higher strain amplitude $\Delta\varepsilon/2 = \pm 1.25\%$, all the samples treated by CSP show a slight decrease in fatigue life with

respect to the untreated samples. Moreover, under a lower strain amplitude (±0.3%), the fatigue life is significantly increased up to more than 200 000 cycles, which indicates that SMAT can significantly improve the fatigue life of the material in the range of low loading amplitude. This investigation is consistent with previous studies reported in the literature concerning cyclic loading of materials under small strain amplitude [65,254].

Tab. 3-5. Number of cycles to failure of specimens treated by SMAT and CSP under different strain amplitudes.

Process	Surface treatment conditions		LCF test conditions ($\Delta\varepsilon/2$)			
	Almen intensity	Coverage	±0.3%	±0.5%	±0.8%	±1.25%
UNT	-	-	43616 37119	3486 3297	818	223 218
SMAT	F22A	125%		2788		267
		3000%		5215		304
	F50A	125%		2417		241
		3000%	>200000	8040 9224	1114	252 236 294
CSP	F50A	125%		3099		158
		3000%		10063		205 160

A more straightforward comparison of fatigue life of all the samples is given in Fig. 3-23. In Fig. 3-23a, it can be observed that with the decrease in strain amplitude, the advantage of SMAT and CSP in terms of fatigue life becomes more pronounced when the coverage is high (3000%). However, in the case of a low coverage (125%), there is no such advantage, and it seems that both SMAT and CSP decrease the fatigue life with respect to the untreated samples (Fig. 3-23b).

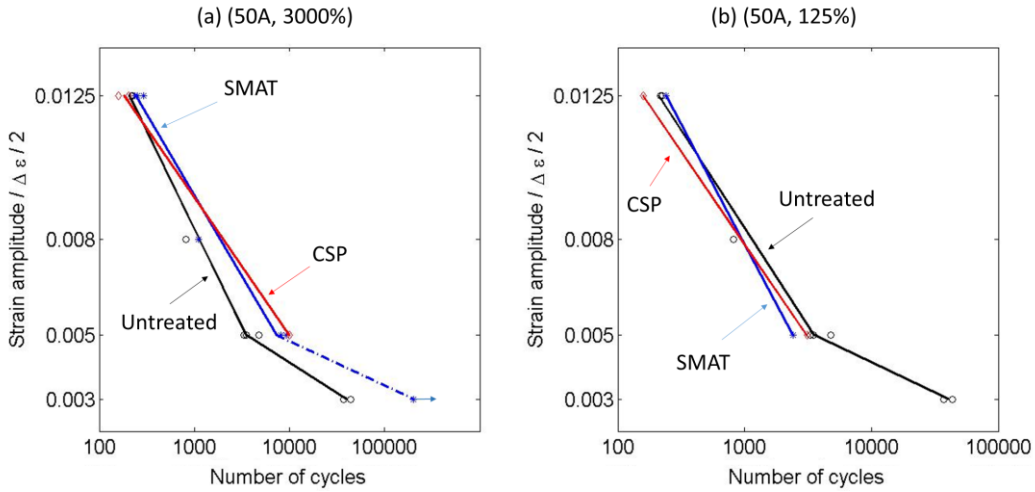

Fig. 3-23. Linear fitting of fatigue life for untreated, SMAT and CSP processed samples with the treatment conditions: (a) 50A, 3000% and (b) 50A, 125%.

All these results can be interpreted by the competition between the surface topography and the residual stress. In fact, residual stress relaxation is strongly dependent on the load amplitude applied during fatigue tests [73]. Fig. 3-24 illustrates the residual stress states of specimens treated by SMAT (50A, 3000%) and CSP (50A, 3000%) after fatigue under strain amplitude of ±0.5% (blue curves) and ±1.25% (red curves), and compared to those before fatigue (black curves). It shows that after fatigue test under $\Delta\varepsilon/2 = \pm 0.5\%$, almost half the initial compressive residual stress is still present for both the SMATed and CSPed specimens. This presence of a great part of the initial compressive residual stress means that the compressive residual stress might have played a significant beneficial role throughout the fatigue tests. Thus an improvement of fatigue life can be observed for SMAT and CSP treated samples with respect to the untreated ones, as shown in Fig. 3-23a.

In addition, information concerning the comparison between SMAT and CSP can also be obtained from Fig. 3-24. It can be seen that the maximum compressive residual stress is much higher for the samples treated by CSP than those treated by SMAT after fatigue tests. This investigation is consistent with the result that the fatigue life of CSP treated samples is higher than the fatigue life of SMATed samples under $\Delta\varepsilon/2 = \pm 0.5\%$. This result signifies that under lower strain amplitude (±0.5%), the effect of residual stress on fatigue life is dominant for both the SMAT and the CSP treated samples, as its relaxation is slow.

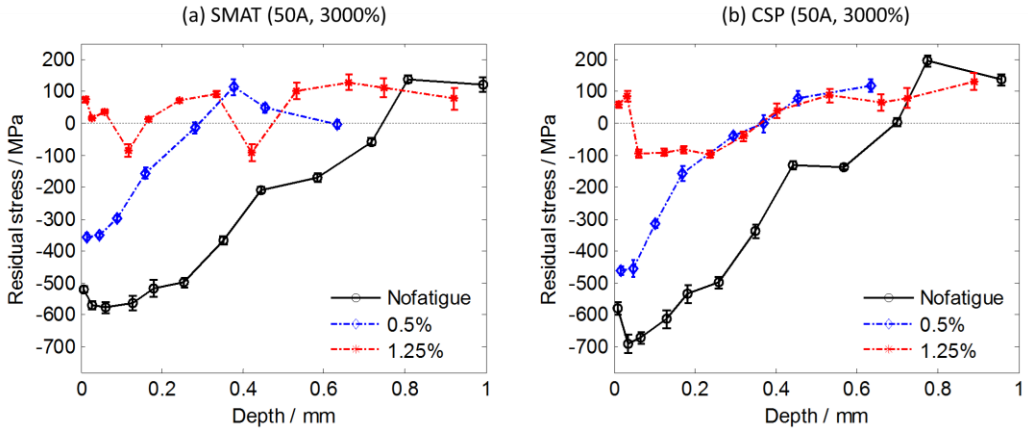

Fig. 3-24. Residual stress profile along the axial direction measured after fatigue tests for: (a) SMAT (50A, 3000%); (b) CSP (50A, 3000%), compared to the residual stress profile before fatigue tests (black curves).

Fig. 3-24 also indicates that under a higher strain amplitude (±1.25%), the residual stresses within the treated samples are almost totally relaxed. According to [42], the relaxation occurs essentially during the very first several cycles, especially under high strain amplitudes. This means that the effect of residual stress on fatigue life should be very small under $\Delta\varepsilon/2 = \pm 1.25\%$, and thus it should be the surface topography that has a major effect

on the fatigue life. As it has been discussed in Section 3.2, CSP generated many micro-cracks at the surface and sharper turning angles for the surface profile (Fig. 3-6 and Fig. 3-7), which should promote crack initiation from the treated surface. As a result, a lower fatigue life is obtained for the CSPed specimens, compared to the untreated ones as well as the specimens treated by SMAT which usually generates smoother surface topography, as discussed in Section 3.2. In addition, for the samples treated by SMAT, it shows that the fatigue life is not decreased with respect to the untreated ones (Fig. 3-23a and Fig. 3-23b), which could be attributed to the smoother surface and the nanostructured layer obtained by SMAT. Note that the nanostructured layer can be only generated when the treatment intensity and coverage are high enough.

Besides, the work hardening should also have a significant effect on fatigue life of materials [182,206]. In addition, the fatigue life is strongly related to the work hardening path, for example uniaxial pre-hardening, shear pre-hardening. [182,206].

Another phenomenon can be observed that the fatigue life is not increased compared to the untreated specimens for the coverage of 125% for both SMATed and CSPed ones, as shown in Fig. 3-23b. In fact, under the coverage of 125%, the material is not saturated and the residual stress is not high enough to compensate the harmful effect of the decrease of rougher surface due to SMAT and CSP. Moreover, the small decrease of fatigue life could aslo be attributed to the inhomogeneity of the treated surface. When the treatment duration is not very long, the impacted number and the impacted intensity of the material are not uniform over the whole surface of the treated specimens. Accordingly, it can induce a high inhomogeneity of the materials at the treated surface with the non-uniformly distributed residual stress and work hardening. It is thus speculated that the small decrease of fatigue life for the SMATed specimens with the coverage of 125% could be due to the inhomogeneity of materials at the treated surface which was resulted from the short-time peening process (as listed in Tab. 3-1). However, this point should be further studied.

3.5.3 Fracture surface analysis

To highlight the difference of damage mechanisms, all the fracture surfaces were examined using a digital optical microscope. According to the fracture surfaces shown in Fig. 3-25, it seems that the basic damage mechanism is similar for SMAT and CSP. For all the test conditions investigated in this work, crack initiation likely occurs on the external surfaces i.e. there is no crack initiation site transition from the surface to the interior of the specimens due to the surface treatments. Furthermore, for both SMAT and CSP treated samples, the crack initiation occurs around the circumferential surface. However, according

to the comparison of all the fracture surfaces for the samples treated by SMAT and CSP, it can be observed that the fracture surfaces of samples treated by CSP are bumpier or rougher than those of samples treated by SMAT. For all the fracture surfaces, after crack initiation and slow propagation stage, cracks propagated inward in transgranular mode with the presence of fatigue striations. No intergranular facet is detected at crack initiation sites which are distributed on the circumferential surface. Thus crack initiation is of transgranular nature and must have occurred from slip bands, whose generation is strongly related to the surface roughness of samples.

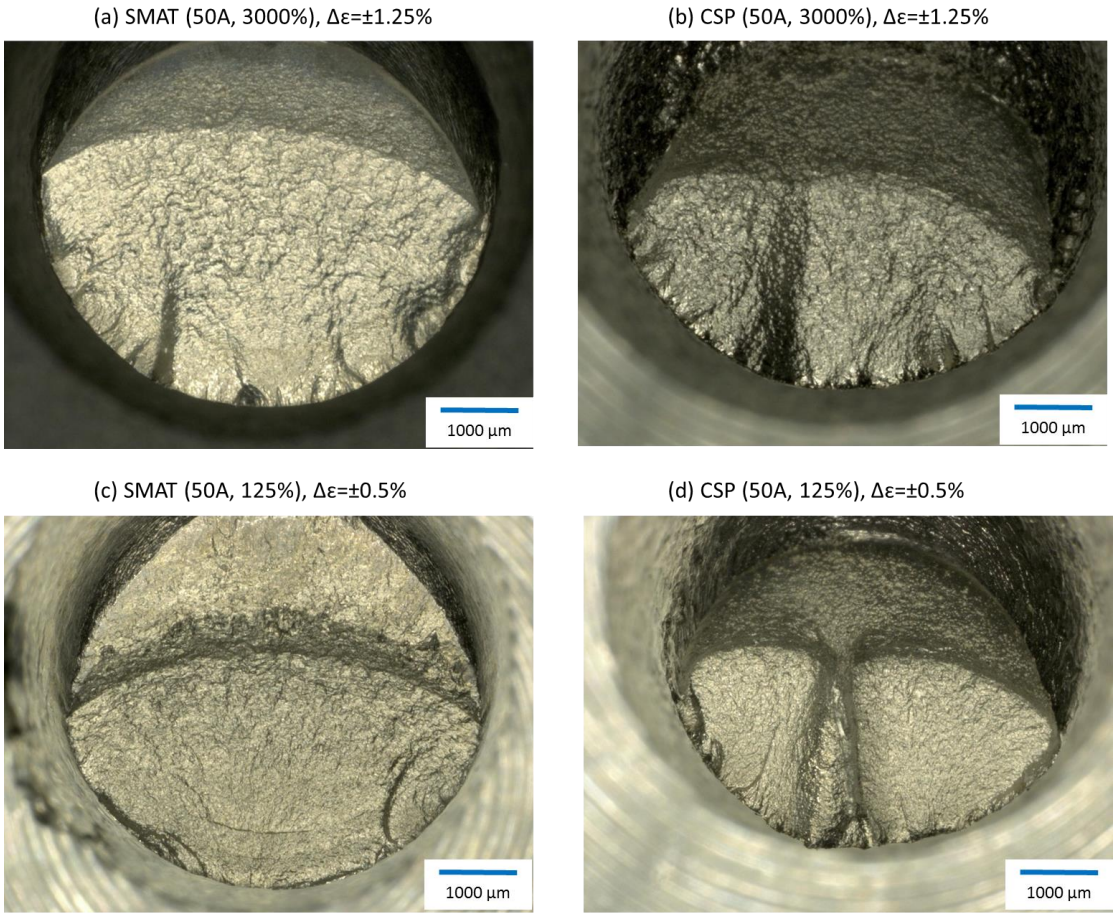

Fig. 3-25. Fracture surface for samples obtained with: (a) SMAT (50A, 3000%) under $\Delta\varepsilon/2 = \pm 1.25\%$, (b) CSP (50A, 3000%) under $\Delta\varepsilon/2 = \pm 1.25\%$, (c) SMAT (50A, 125%) under $\Delta\varepsilon/2 = \pm 0.5\%$, and (d) CSP (50A, 125%) under $\Delta\varepsilon/2 = \pm 0.5\%$.

The outer surfaces of the failed samples were also observed using a digital optical microscope, and examples are illustrated in Fig. 3-26. It can be seen that for both SMAT and CSP treated samples, the presence of micro and even macro cracks perpendicular to the loading direction can be detected. As a matter of fact, during fatigue loading, many micro-cracks were initiated around the outer surface of the samples. Under subsequent fatigue cycling, only one or several micro-cracks then propagated and joined together, which led to

the final rupture of samples. It seems that the samples treated by CSP have fewer surface cracks than the SMATed ones, but with larger size (Fig. 3-26b), which is probably due to the pre-existence of micro-cracks generated by CSP, as shown in Fig. 3-2.

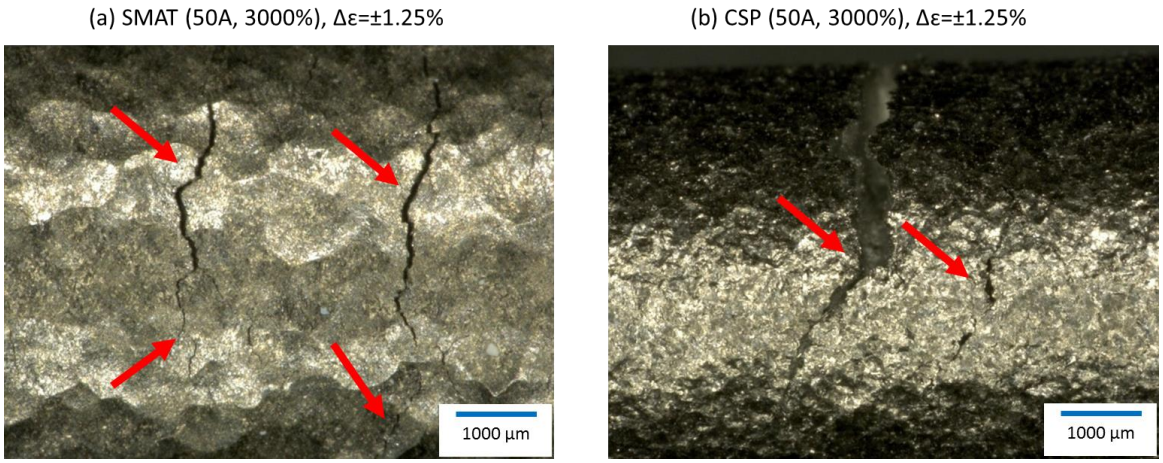

Fig. 3-26. Observation of the outer surface of failed samples for: (a) SMAT (50A, 3000%) under Δε/2= ±1.25%, and (b) CSP (50A, 3000%) under Δε/2= ±1.25%.

3.6 Conclusions

In this chapter, a comparison between SMAT and CSP with the same Almen intensity and coverage was investigated using a 316L austenitic stainless steel by analysing surface topography, residual stress, work hardening, as well as their effects on LCF behaviour.

Analysis of surface topography and the typical surface roughness parameters (Ra, Rq, Rp, Rv and Rz, Rdp, Rpc) indicate that CSP can reduce the surface quality and sometimes deteriorate the treated surface by generating a large number of micro-cracks, while a flatter surface can be obtained by SMAT. These surface features can cause stress concentration and consequently crack initiation, and thus should have considerable effects on fatigue life of the material.

CSP can generate a higher compressive residual stress and severer plastic deformation closed to the treated surface. While the specimens treated by SMAT with the same Almen intensity and coverage present a deeper variation of compressive residual stress and plastic deformation. This indicates that CSP have a more pronounced effect at the treated surface, whereas the influence of SMAT can reach a deeper layer. Moreover, analysis of hardeness implies that compressive residual stress palys a more important role in hardening increase of the material than the work hardening which is characterized by the value of FWHM.

Concerning the LCF analysis, the following main conclusions can be drawn:

(1) Cyclic stress amplitudes of both SMAT and CSP treated samples are enhanced due

to higher strength of the mechanically affected region. However, these samples manifest significant long-term softening which follows the initial hardening occurring during the first several cycles.

(2) The difference of fatigue life between SMAT and CSP treated samples compared to untreated ones can be attributed to the competition between the residual stress and the surface topography obtained after SMAT and CSP.

(3) The fatigue life of samples treated by CSP is higher than those treated by SMAT under a low strain amplitude ($\Delta\varepsilon/2 = \pm 0.5\%$). This is due to the fact that the compressive residual stress close to the surface is higher for samples treated by CSP than those treated by SMAT throughout the fatigue tests, as the residual stress relaxation is slow under $\Delta\varepsilon/2 = \pm 0.5\%$.

(4) In contrast, under a higher strain amplitude ($\Delta\varepsilon/2 = \pm 1.25\%$), the fatigue life obtained with samples treated by CSP is lower than that obtained with SMATed samples. In this case, the beneficial effect of the compressive residual stress is much attenuated due to its quick relaxation under $\Delta\varepsilon/2 = \pm 1.25\%$ for all the specimens. The fatigue life of the samples treated by CSP is mainly controlled by the surface micro-cracks and the rough surface generated by CSP.

(5) Fracture analysis implies that within the strain amplitude range studied in this work, the fatigue cracking mechanisms are similar for all the samples including those treated by SMAT and CSP, and the crack initiation occurred around the circumferential surface of the samples.

The interpretation given in this paper concerning the strengthening mechanisms for SMAT and CSP and effect of fatigue life are rather qualitative. In fact, work hardening should also have a significant effect on fatigue life of materials. More quantitative and refined investigation deserves to be systematically performed.

Chapter 4: Cyclic behaviour analysis and constitutive modelling of 316L steels

Chapter 2 and Chapter 3 presented the cyclic behaviour of SMATed specimens and the evolution of gradient microstructure during cyclic loading. In addition, the effects of SMAT and conventional shot peening were studied by comparing the obtained surface topography, residual stress and work hardening, as well as the fatigue life. In the following chapters, LCF behaviour of the studied steels will be further studied through numerical modelling approaches based on macroscopic continuum plasticity and physically based crystal plasticity.

In this chapter, experimental analysis and cyclic constitutive modelling of 316L austenitic stainless steels in the LCF regime are first conducted. LCF tests of two 316L steels were carried out with strain amplitudes ranging from ±0.3% to ±1.5%. A series of analyses concerning monotonic tensile and cyclic behaviour is then performed, including elastic modulus, yield point, cyclic plastic flow behaviour and Bauschinger effect. Afterwards, the cyclic behaviour of steel 316L-A is described in the classical combined kinematic/isotropic hardening framework, and a nonlinear kinematic hardening rule is proposed to describe the observed cyclic hardening/softening and strain range memory effect.

4.1 Material and experimental procedures

The investigated materials in this work are two types of 316L ASTM F138 austenitic stainless steels, named 316L-A and 316L-B, which respectively corresponds to the steels studied in Chapter 2 and Chapter 3. Fatigue specimens have a cylindrical dumbbell shape with a gauge length of 12 mm and a diameter of 6 mm in the gauge section, as presented in Fig. 2-1. LCF tests were carried out at room temperature using a servo hydraulic machine, with fully reversed tension-compression cyclic loading under strain control ($R_\varepsilon = -1$). An extensometer with a gauge length of 10 mm was used to control the total strain. In this paper,

different total strain amplitudes ranging from ±0.3% to ±1.5% were applied. The rate-dependent character of 316L steels at room temperature highlighted in the literature [255,256] was not studied. All the tests were thus carried out at a constant strain rate of $4 \times 10^{-3}\mathrm{s}^{-1}$.

For the analysis of cyclic behaviour, the characteristics of a hysteresis loop can be described by a series of parameters, as indicated in Fig. 4-1. For example, the elastic modulus and the yield point can be used to describe the elastic tensile/compressive range; the strain and the stress amplitudes reflect the load magnitude; the effective stress and the back stress represent respectively the size and the position of the yield surface during plastic flow.

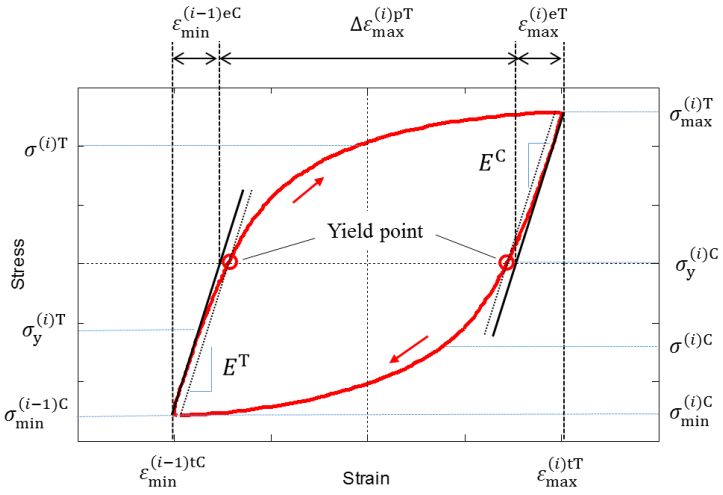

Fig. 4-1. Different parameters used to characterize a hysteresis loop.

In this work, each hysteresis loop is considered starting with the tensile going and finishing with the compressive going. The superscripts appearing in Fig. 4-1 are defined as follows: e, p and t applied to ε denote respectively elastic strain, plastic strain and total strain; T and C denote the tensile-going phase and compressive-going phase, respectively; (i) indicates the i^{th} hysteresis loop. The subscripts 'max' and 'min' respectively correspond to the maximum and the minimum loading positions in each half cycle. In addition, it is defined in this paper that the superscripts 'e' to σ denotes effective stress.

The procedure with which the parameters are determined from a hysteresis loop can be succinctly described as follows. First, the maximum/minimum stresses and strains can be obtained directly from the two extreme points of the hysteresis loop. A linear fitting for elastic unloading regime after each loading-unloading transition is performed to determine the elastic modulus for the tensile going and the compressive going, respectively denoted

as E^{T} and E^{C}. The yield point is generally evaluated by using a plastic strain offset $\Delta\varepsilon^{\mathrm{p}*}$, as done in some previous studies [179,257]. A plastic strain offset of 2.5×10^{-5} is used in this work. This offset depends on the sensitivity of the extensometer, the sampling frequency and signal analysis [258,52]. Plastic strain increments for tensile going and compressive going can be calculated using the maximum/minimum stresses and the corresponding elastic modulus:

$$\begin{cases} \Delta\varepsilon^{(i)\mathrm{pT}} = \left(\varepsilon^{(i)\mathrm{tT}} - \varepsilon_{\min}^{(i-1)\mathrm{tC}}\right) - \left(\sigma^{(i)\mathrm{T}}/E^{\mathrm{T}} - \sigma_{\min}^{(i-1)\mathrm{C}}/E^{\mathrm{T}}\right) \\ \Delta\varepsilon^{(i)\mathrm{pC}} = \left(\varepsilon^{(i)\mathrm{tC}} - \varepsilon_{\max}^{(i)\mathrm{tT}}\right) - \left(\sigma^{(i)\mathrm{C}}/E^{\mathrm{C}} - \sigma_{\max}^{(i)\mathrm{T}}/E^{\mathrm{C}}\right) \end{cases} \tag{4-1}$$

When i =1, then $\varepsilon_{\min}^{(0)\mathrm{tC}} = 0, \sigma_{\min}^{(0)\mathrm{C}} = 0$, which implies that the specimen has no initial strain and stress at the beginning of cyclic loading.

With the plastic strain increment $\Delta\varepsilon^{(i)\mathrm{p}}$ during each half hysteresis loop, the accumulated plastic strain p during the tensile-going phase and the compressive-going phase can be calculated respectively with the following equations:

$$\begin{cases} p^{(n)\mathrm{T}} = \sum_{i=1}^{n-1}\left(\Delta\varepsilon_{\max}^{(i)\mathrm{pT}} + \left|\Delta\varepsilon_{\min}^{(i)\mathrm{pC}}\right|\right) + \Delta\varepsilon^{(n)\mathrm{pT}} \\ p^{(n)\mathrm{C}} = \sum_{i=1}^{n-1}\left(\Delta\varepsilon_{\max}^{(i)\mathrm{pT}} + \left|\Delta\varepsilon_{\min}^{(i)\mathrm{pC}}\right|\right) + \Delta\varepsilon_{\max}^{(n)\mathrm{pT}} + \left|\Delta\varepsilon^{(n)\mathrm{pC}}\right| \end{cases} \tag{4-2}$$

In the classical combined kinematic/isotropic hardening framework, the stress under uniaxial loading can be divided into back stress *X*, isotropic hardening variable *R*, and initial yield stress *k*. We define the sum of the isotropic stress *R* and the initial yield stress *k* as effective stress σ^{e}. According to Cottrell [204]'s method, the back stress and the effective stress can be quantitatively obtained from the hysteresis loops. This method has been widely used in studying the evolution of back stress and effective stress during cyclic loading [259,52,49,179,182]. The back stresses at extreme points ($X_{\max}^{(i)\mathrm{T}}, X_{\min}^{(i)\mathrm{C}}$) corresponding to the current half cycle can be calculated using the stresses at the extreme points ($\sigma_{\max}^{(i)\mathrm{T}}, \sigma_{\min}^{(i)\mathrm{C}}$) and the yield stress obtained in the next half cycle ($\sigma_{\mathrm{y}}^{(i)\mathrm{C}}, \sigma_{\mathrm{y}}^{(i+1)\mathrm{T}}$), as:

$$\begin{cases} X_{\max}^{(i)\mathrm{T}} = \left(\sigma_{\max}^{(i)\mathrm{T}} + \sigma_{\mathrm{y}}^{(i)\mathrm{C}}\right)/2 \\ X_{\min}^{(i)\mathrm{C}} = \left(\sigma_{\min}^{(i)\mathrm{C}} + \sigma_{\mathrm{y}}^{(i+1)\mathrm{T}}\right)/2 \end{cases} \tag{4-3}$$

Similarly, the effective stresses at extreme points ($\sigma_{\max}^{(i)\mathrm{eT}}, \sigma_{\min}^{(i)\mathrm{eC}}$) can be calculated with the following relations:

$$\begin{cases} \sigma_{\max}^{(i)\mathrm{eT}} = \left(\sigma_{\max}^{(i)\mathrm{T}} - \sigma_{\mathrm{y}}^{(i)\mathrm{C}}\right)/2 \\ \sigma_{\min}^{(i)\mathrm{eC}} = \left(\sigma_{\mathrm{y}}^{(i+1)\mathrm{T}} - \sigma_{\min}^{(i)\mathrm{C}}\right)/2 \end{cases} \tag{4-4}$$

4.2 Analyses of monotonic and cyclic behaviour

4.2.1 Monotonic behaviour

The initial tensile stress-strain curves of the two studied 316L steels are illustrated in Fig. 4-2. It can be first found that both steels underwent an initial linear elastic deformation. Then the plastic flow was activated when the stress level was high enough. Beyond the yield point (indicated in Fig. 4-2b), the stress increase rate gradually diminished, which was followed by a plastic regime with a nearly constant hardening slope (as shown in Fig. 4-2a). Even though the two 316L steels have very similar elastic modulus, yield point and saturated hardening rate, they experienced different stress–strain behaviour, especially in the elastic-plastic transition region just beyond the yield point.

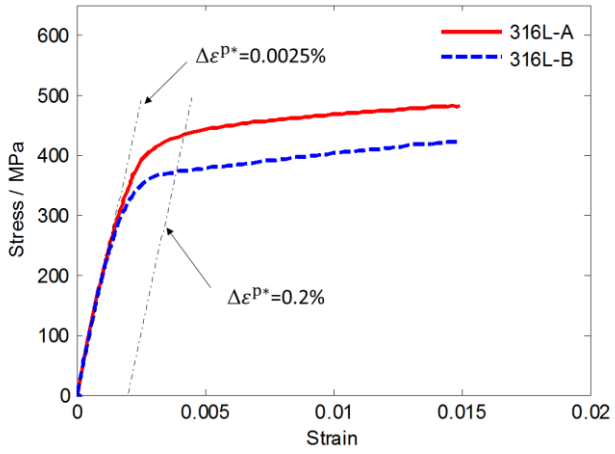

Fig. 4-2. Monotonic stress-strain curves of the two 316L steels.

In the literature, proportionality limit, elastic limit and offset yield stress (e.g. 0.2%) are used to represent the yield stress beyond which a material begins to deform plastically. Tab. 4-1 lists the basic mechanical parameters of the two studied steels obtained from the two monotonic tensile curves presented in Fig. 4-2. It is worth mentioning that the elastic modulus in Tab. 4-1 is given by averaging all the measured elastic modulus over different strain amplitudes from ±0.3% to ±1.5%. This choice will be discussed in Section 4.2.3.2. The elastic limit and the yield stress (0.2%) are respectively determined through a plastic strain offset of 2.5×10-5 and 0.2%, as indicated in Fig. 4-2. It shows that both steels have nearly the same proportionality limit. However, the yield strength defined with 0.2% strain

offset shows an obvious difference between the two 316L steels, which is due to the considerable difference of plastic flow behaviour just beyond the yield point, as shown in Fig. 4-2. This indicates that the plastic flow among the elastic-plastic transition region plays an important role in the subsequent plastic deformation of materials.

Tab. 4-1. Basic mechanical properties of the two 316L steels obtained from the monotonic tensile curves.

Material	Elastic modulus (GPa)	Elastic limit (MPa)	Yield stress (0.2%) (MPa)
316L-A	196.5	222.7	433
316L-B		199.7	370.4

4.2.2 Bauschinger effect

Bauschinger effect represents the loss of yield stress when the material is subjected to further loading which is inverse to the initial loading direction. Fig. 4-3 illustrates the first hysteresis loops of 316L-A including only the initial tensile and reversed compressive going under strain amplitudes from ±0.3% to ±1.5%. The yield points for the curves of compressive-going phase are also indicated. The yield points in the unloading stage for all the strain amplitudes were determined based on the hysteresis curves through the average elastic modulus (196.5 GPa) and the plastic strain offset of 2.5×10^{-5}. It can be observed that the stress at the yield point during compressive going increases with the increase of strain amplitude, whereas the difference between the maximum stress $\sigma_{\max}^{(1)\mathrm{T}}$ and the yield stress $\sigma_{\mathrm{y}}^{(1)\mathrm{C}}$ is nearly unchanged under different strain amplitudes.

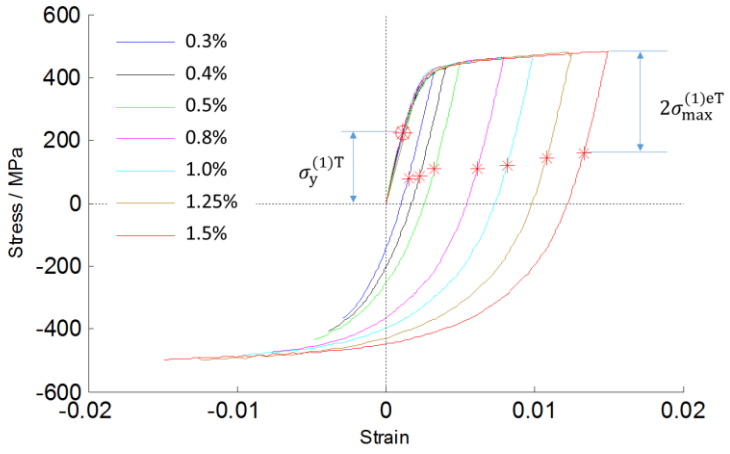

Fig. 4-3. Representation of yield points in the first hysteresis loop of 316L-A for both the tensile and the compressive going under different strain amplitudes.

The effective stresses at the maximum extreme points calculated using Eq. (4-4) for different strain amplitudes are listed in Tab. 4-2. It can be seen that all the effective stresses

$\sigma_{\max}^{(1)eT}$ under different strain amplitudes are around 170 MPa, smaller than the obtained initial proportionality limit (213.5 MPa, as shown in Tab. 4-1). This phenomenon of effective stress decrease is contradictory to some cyclic plasticity studies, in which the monotonic and the cyclic behaviours were described by a single initial hardening due to isotropic hardening variables.

Tab. 4-2. Effective stress in the tensile-going phase of the first cycle for different strain amplitudes.

Strain amplitude	±0.3%	±0.4%	±0.5%	±0.8%	±1.0%	±1.25%	±1.5%
Effective stress (MPa)	168.54	172.02	169.26	177.47	172.97	167.84	162.35

4.2.3 Hysteresis loops

The results of initial tension presented in Section 4.2.1 indicate that the difference of stress-strain curves in the plastic deformation regime between the two 316L steels is mainly attributed to the elastic-plastic transition behaviour just beyond the yield point. Actually, in this elastic-plastic transition region, the hardening rate drastically changes and the deformation mechanisms are complex due to the activation of plastic slips. It is thus difficult to precisely model the mechanical behaviour of the material in this transition region. Therefore, compared to the case of cyclic loading under higher strain amplitudes where the loading-unloading transition occurs in a rather saturated strain hardening stage, it would be more challenging to precisely model the cyclic behaviour of the material under lower strain amplitudes, especially when the applied strain amplitudes are located in the elastic-plastic transition region.

Fatigue tests were carried out for the two 316L steels under total strain amplitudes ranging from ±0.3% to ±1.5%. Fig. 4-4 illustrates the first two hysteresis loops for each strain amplitude. It can be found that the loading-unloading occurred in the elastic-plastic transition region under lower strain amplitudes (±0.3%, ±0.4% and ±0.5%). Moreover, lower strain amplitudes give much narrower hysteresis loops, which imply a small plastic strain increment in each cycle. In addition, none of the two steels reached a stabilized stress state during each cyclic deformation, even for higher strain amplitudes (±1.25% and ±1.5%).

The secondary hardening behaviour can also be observed during cyclic loading under stress-controlled tension-compression [260,261], and under torsion and combined axial-torsion with constant strain rate [262]. Accordingly, the hardening-softening-hardening behaviour exists in both strain-controlled and stress-controlled cyclic loading tests, and it

seems that it is rarely dependent on the stress state. However, this assumption should be further verified through experimental studies.

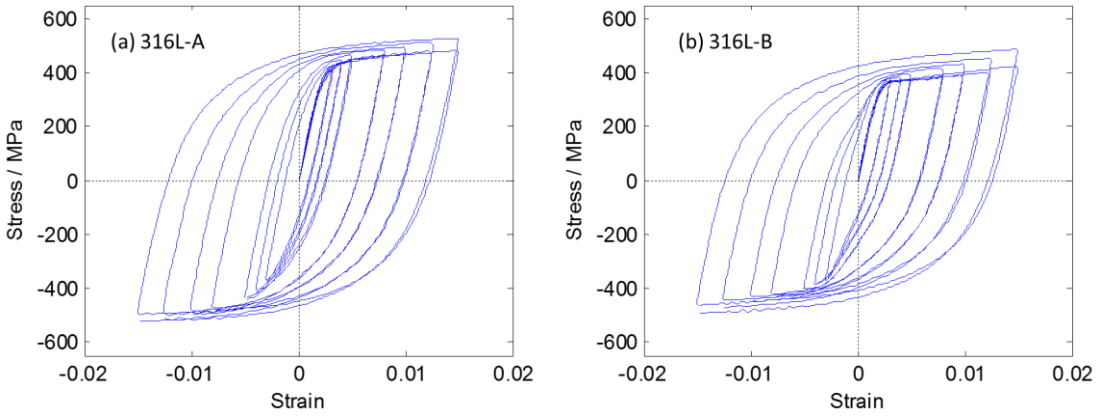

Fig. 4-4. First two hysteresis loops obtained under strain amplitudes from ±0.3% to ±1.5% for: (a) 316L-A, and (b) 316L-B.

4.2.3.1 Cyclic stress amplitude

Cyclic stress amplitude, calculated from the maximum and the minimum stresses of a hysteresis loop using Eq. (4-5), evolves during cyclic loading, and illustrates the path by which a material arrives at the final cyclic flow stress level.

$$\sigma_{\mathrm{m}}^{(i)} = \left(\sigma_{\max}^{(i)\mathrm{T}} - \sigma_{\min}^{(i)\mathrm{C}}\right)/2 \tag{4-5}$$

Fig. 4-5 shows the evolution of cyclic stress amplitude with the number of cycles for the two 316L steels. For both of them, the evolution of cyclic stress amplitude is characterized by an initial hardening during the first several cycles, followed by gradual softening and subsequent stabilization. In addition, under lower strain amplitudes, although the cyclic hardening rate is smaller in the initial hardening stage, the maximum stress amplitude was reached earlier especially for 316L-B, and a long softening range lasted until fracture. However, under very low strain amplitudes (±0.3% and ±0.4%), there is no obvious stabilization of stress amplitudes after the long softening range.

Another phenomenon which can be observed only for 316L-B, is that under higher strain amplitudes from ±0.8% to ±1.25%, there is the occurrence of secondary hardening after the softening range (Fig. 4-5b). In contrast, for the 316L-A steel (Fig. 4-5a), the presence of secondary hardening is not obvious, and it is considered that the material underwent an initial hardening and a longer softening range. As for the fracture, it occurred after a process of saturation or before the occurrence of secondary hardening. Furthermore, for both steels, the softening and secondary hardening behaviour under a strain amplitude of ±1.5% is not obvious, and the fracture occurred earlier due to high plastic strain

increments in each cycle. Globally, the difference between the curves obtained with different strain amplitudes implies the existence of a significant strain range memory effect for the two steels.

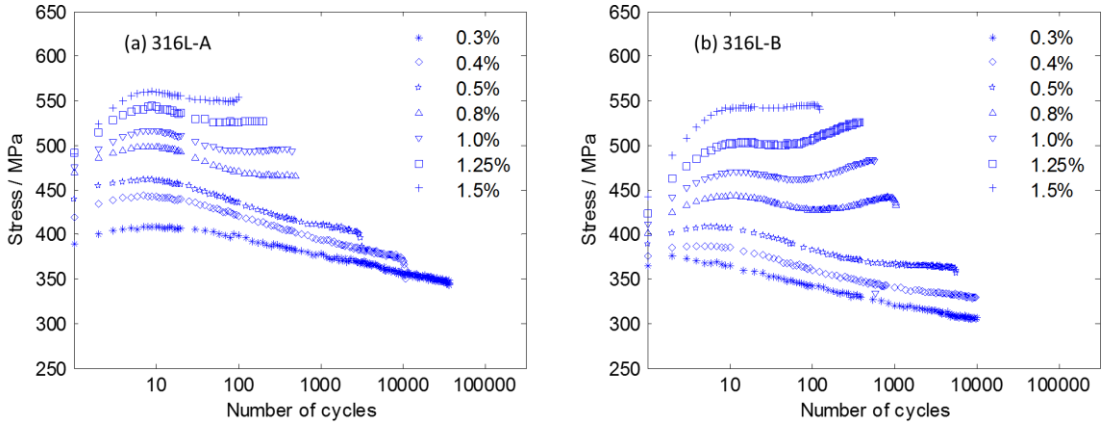

Fig. 4-5. Cyclic stress amplitude evolution with the number of cycles under different strain amplitudes for: (a) 316L-A, and (b) 316L-B.

4.2.3.2 Elastic modulus

As indicated in Fig. 4-1, the elastic modulus in each cycle for tensile-going phase and compressive-going phase can be obtained by fitting stress-strain curve in the elastic range after each loading-unloading transition. The slope of the fitted line is considered as the elastic modulus of the material for the corresponding tensile-going or compressive-going half cycle. Fig. 4-6 shows the elastic modulus variation with the number of cycles for 316L-A under four typical strain amplitudes. It can be found that the tensile-going and the compressive-going half cycles nearly have the same elastic modulus, and both remain constant with an increase of the number of cycles. The average elastic modulus of all the tensile-going phases and that of all the compressive-going phases under different strain amplitudes are shown in Fig. 4-7. It seems that cyclic loading does not change the elastic modulus of the material in the range of strain amplitudes considered in this work. As a matter of fact, the elastic modulus is generally considered as a constant physical parameter of a material during elastic-plastic deformation at room temperature, especially in small strain range. In this paper, the elastic modulus of 316L-A is calculated by averaging the measured elastic modulus over different strain amplitudes from ±0.3% to ±1.5% (Fig. 4-7). The obtained value is 196.5 GPa which is consistent with the theoretical elastic modulus of 316L steels.

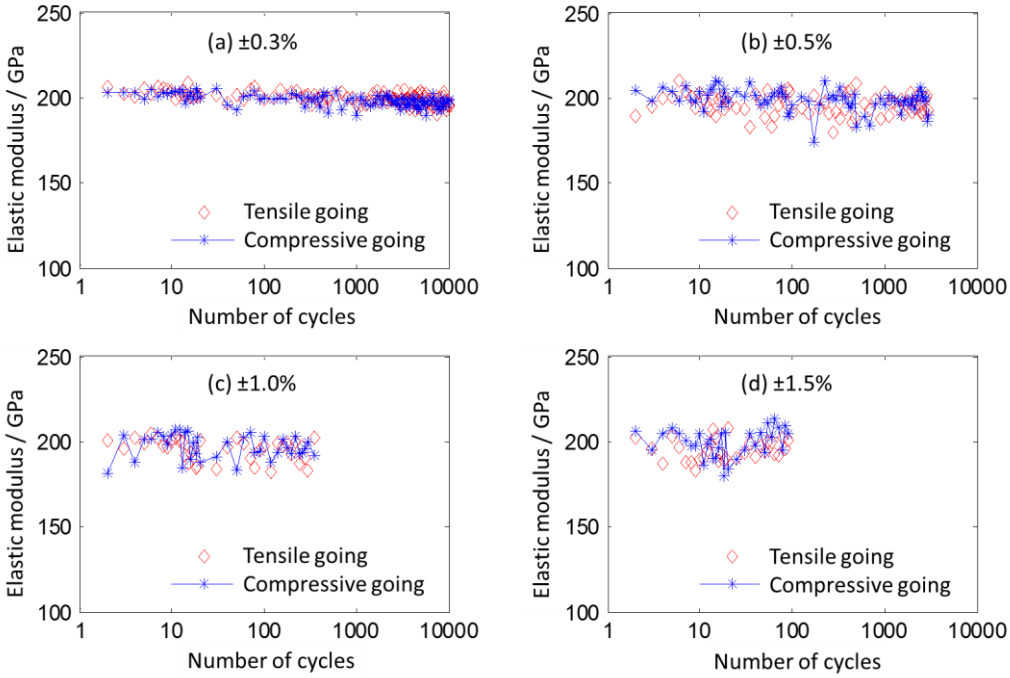

Fig. 4-6. Elastic modulus variation with the number of cycles for 316L-A under strain amplitudes of (a) ±0.3%; (b) ±0.5%; (c) ±1.0%; (d) ±1.5%.

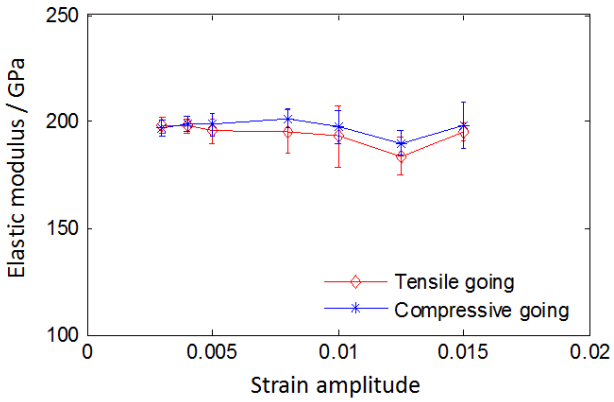

Fig. 4-7. Average elastic modulus of 316L-A under different strain amplitudes.

4.2.3.3 Peak effective stress and peak back stress

The yield stress in each half cycle is evaluated based on the hysteresis curves with the average elastic modulus obtained in Section 4.2.3.2 and a plastic strain offset of 2.5×10^{-5}. As indicated in Fig. 4-1, the yield stress in each half cycle can be obtained based on the hysteresis curves. Using the calculated yield stress for a compressive-going phase and the maximum stress, the effective stress and back stress at the maximum extreme point can be respectively calculated with Eq. (4-4) and Eq. (4-3), defined as peak effective stress and peak back stress, respectively. Their variations with the accumulated plastic strain (calculated by Eqs. (4-1) and (4-2)) are illustrated in Fig. 4-8.

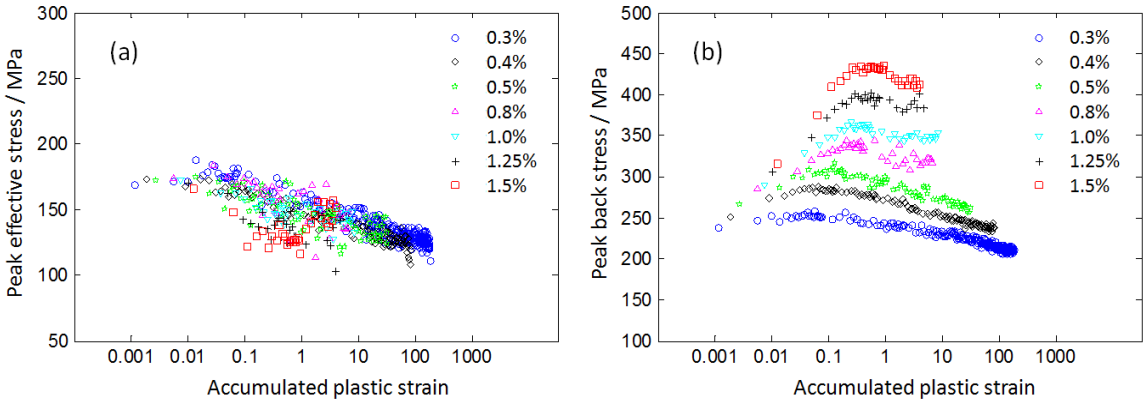

Fig. 4-8. Variations of (a) peak effective stress and (b) peak back stress with the accumulated plastic strain under different strain amplitudes for 316L-A.

Fig. 4-8a shows that the peak effective stresses obtained with different loading levels seem to have the same trend, and there is a slight dispersion for the case of ±1.5%. In contrast, Fig. 4-8b shows very different peak back stress variations. The trend of these peak back stress variations is very similar to that of the stress amplitude variations presented in Fig. 4-5. For all the peak back stress variation curves, globally there is an increase of peak back stress during the first several cycles. Under higher strain amplitudes (±0.8%, ±1.0%, ±1.25% and ±1.5%), the peak back stresses increase more quickly, and then there is a slight decrease, which is followed by a quasi-saturated stage until fracture. However, under lower strain amplitudes (±0.3%, ±0.4% and ±0.5%), instead of quasi-saturation stage, there is a continuous decrease of peak back stress until fracture. In addition, Fig. 4-8 shows that the hardening/softening behaviour highlighted by stress amplitude evolution curves (see Fig. 4-5) is mainly attributed to the back stress, which is consistent with some previous studies [49].

All the phenomena shown in Fig. 4-8 imply that the back stresses have a significant hardening/softening effect during cyclic loading, which is consistent with the considerations by some other authors [263,199]. On the one hand, the peak back stress variation shows significant hardening/softening effect. On the other hand, the strain range memory effect can be clearly observed and it is attributed to the back stress. This is contradictory to some previous studies, in which the strain range memory effect was considered through the asymptotic value of isotropic hardening constants [103,186,264,265,83,183]. Furthermore, the presence of the strain range memory effect can be confirmed through the comparison of the $\left(\sigma^{(i)\mathrm{C}} - \sigma_{\max}^{(i)\mathrm{T}}\right)$ versus $\left(\varepsilon^{(i)\mathrm{pC}} - \varepsilon_{\max}^{(i)\mathrm{pT}}\right)$ curve at different numbers of cycles, as shown in Fig. 4-9, for the two steels.

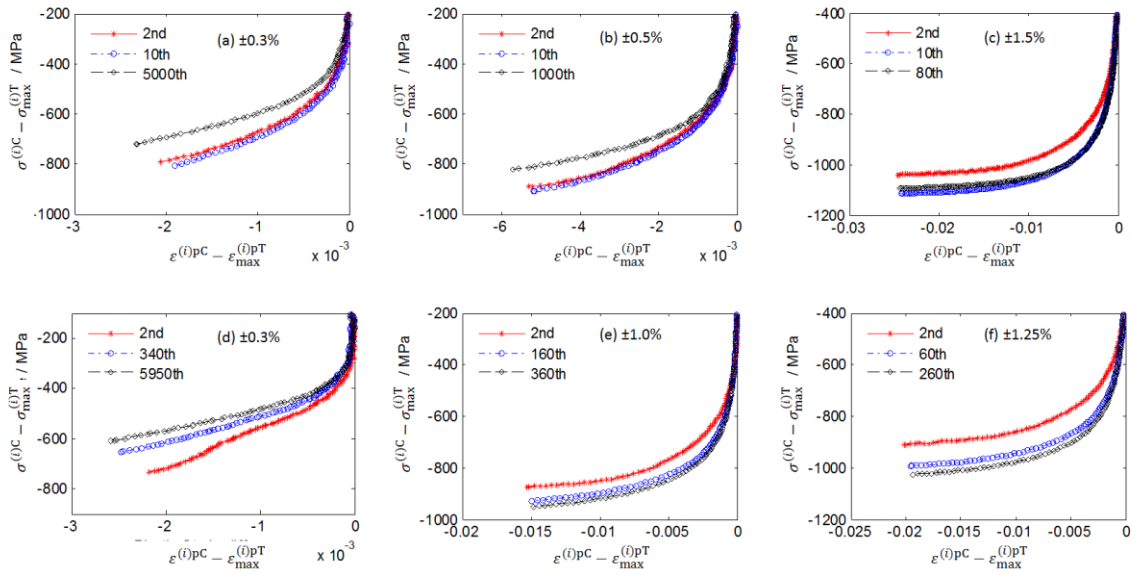

Fig. 4-9. Comparison of $\sigma^{(i)\mathrm{C}} - \sigma_{\max}^{(i)\mathrm{T}}$ vs $\varepsilon^{(i)\mathrm{pC}} - \varepsilon_{\max}^{(i)\mathrm{pT}}$ curves in compressive-going phase of the i^{th} cycle under some typical strain amplitudes for 316L-A: (a), (b), (c); and 316L-B: (d), (e), (f).

In Fig. 4-9, the red-star, blue-circle and black-diamond curves respectively represent different numbers of cycles corresponding to different stages of cyclic loading. It can be seen that the black-diamond curve is located above the red-star curve (corresponding to the beginning stage of cyclic loading) for Fig. 4-9a, Fig. 4-9b, and Fig. 4-9d, which signifies a cyclic softening of the material with respect to the 2$^{\mathrm{nd}}$ cycle. By contrast, Fig. 4-9c, Fig. 4-9e and Fig. 4-9f indicate a cyclic hardening behaviour of the material. The six figures shown in Fig. 4-9 clearly indicate significant hardening/softening effect and strain range memory effect involved in the back stress of the two steels.

Based on the above analyses, it can be concluded that:

(1) According to the analysis of the Bauschinger effect, a phenomenon of yield stress decrease in the compressive going phase can be observed compared to the initial yield stress obtained under initial monotonic tension.

(2) The stress amplitude analysis indicates that the two steels undergo an initial hardening, followed by a long softening range under lower strain amplitudes, and a secondary hardening occurs for the 316L-B steel under higher strain amplitudes (±0.8%, ±1.0% and ±1.25%). In addition, obvious strain range memory effect can be observed for both steels.

(3) The elastic modulus is nearly constant and is very similar for the tensile-going and compressive-going phases during cyclic loading under different strain amplitudes.

(4) The peak effective stress variation as a function of the accumulated plastic strain

follows the same trend for different strain amplitudes. Obvious hardening/softening effect can be observed in the peak back stress variation curves, and the strain range memory effect of the two steels should be taken into account.

4.3 Constitutive modelling and parameter identification

4.3.1 Classical combined kinematic/isotropic hardening constitutive model

As indicated above, the rate-dependent character of austenitic stainless steels highlighted in the literature [255,256,266] is not taken into account in this work. This work is actually focused on describing the complex cyclic hardening/softening behaviour along with the strain range memory effect in the LCF regime. The time-independent plasticity is thus considered with the classical combined kinematic/isotropic hardening constitutive law of Chaboche [264,83]. In the framework of small strain, material is assumed isotropic. Based on Hooke's law, the elastic relation is expressed as follows:

$$\underline{\sigma} = \underline{\underline{\boldsymbol{C}}} : \left(\underline{\varepsilon} - \underline{\varepsilon}^{\mathrm{p}}\right) \tag{4-6}$$

where $\underline{\sigma}$ is the stress tensor, $\underline{\underline{\boldsymbol{C}}}$ is the fourth-order stiffness tensor, $\underline{\varepsilon}$ and $\underline{\varepsilon}^{\mathrm{p}}$ are respectively the total strain tensor and plastic strain tensor.

The elastic and plastic regimes can be defined by the following yield function with the stress tensor $\underline{\sigma}$, back stress tensor $\underline{X}$, isotropic hardening variable R, and initial yield stress k:

$$f\left(\underline{\sigma}, \underline{X}, R\right) = J_2\left(\underline{\sigma} - \underline{X}\right) - R - k \tag{4-7}$$

The second invariant J_2 is defined by the deviatoric stress tensor $\underline{\sigma}^*$ and the deviatoric back stress tensor $\underline{X}^*$ as:

$$J_2\left(\underline{\sigma} - \underline{X}\right) = \sqrt{\frac{3}{2}\left(\underline{\sigma}^* - \underline{X}^*\right) : \left(\underline{\sigma}^* - \underline{X}^*\right)} \tag{4-8}$$

with:

$$\begin{cases} \underline{\sigma}^* = \underline{\sigma} - \dfrac{1}{3}\mathrm{tr}\left(\underline{\sigma}\right) I \\ \underline{X}^* = \underline{X} - \dfrac{1}{3}\mathrm{tr}\left(\underline{X}\right) I \end{cases} \tag{4-9}$$

where, 'tr' indicates the trace, and I is the second-order unit tensor.

Plastic flow rate is given by the normality rule:

$$\underline{\dot{\varepsilon}}^{\mathrm{p}} = \frac{3}{2}\dot{\lambda}\frac{\underline{\sigma}^{*} - \underline{X}^{*}}{J_2(\underline{\sigma} - \underline{X})} \tag{4-10}$$

where $\dot{\lambda}$ is the plastic multiplier, determined by the consistency condition $f = \dot{f} = 0$ in the rate-independent framework.

The back stress tensor $\underline{X}$ can be expressed by using the multi-equations of AF rule [264]:

$$\underline{\dot{X}} = \sum_{i=1} \underline{\dot{X}}_i \tag{4-11}$$

$$\underline{\dot{X}}_i = \frac{2}{3}C_i\underline{\dot{\varepsilon}}^{\mathrm{p}} - \gamma_i\underline{X}_i\dot{p}_i \tag{4-12}$$

The accumulated plastic strain p has the following relation with the plastic strain tensor $\underline{\varepsilon}^{\mathrm{p}}$:

$$\dot{p} = \sqrt{\frac{2}{3}\underline{\dot{\varepsilon}}^{\mathrm{p}} : \underline{\dot{\varepsilon}}^{\mathrm{p}}} \tag{4-13}$$

Similarly, isotropic hardening variable R can be given by the following decomposed forms to better describe the cyclic hardening/softening behaviour:

$$\dot{R} = \sum_{i=1} \dot{R}_i \tag{4-14}$$

$$\dot{R}_i = b_i(Q_i - R_i)\dot{p} \tag{4-15}$$

In addition, for the back stress tensor $\underline{X}$, a parameter φ related to the accumulated plastic strain p can be introduced to consider the isotropic effect [263]:

$$\underline{\dot{X}} = \sum_{i=1} \underline{\dot{X}}_i = \sum_{i=1} \left(\frac{2}{3}C_i\underline{\dot{\varepsilon}}^{\mathrm{p}} - \varphi(p)\gamma_i\underline{X}_i\dot{p}\right) \tag{4-16}$$

where, $\varphi(p)$ is a material dependent function defined by:

$$\varphi(p) = \varphi_\infty + (\varphi_0 - \varphi_\infty)\exp(-\omega p) \tag{4-17}$$

In Eqs. (4-12), (4-15), (4-16) and (4-17), C_i, γ_i, Q_i, b_i, φ_0, φ_∞, and ω are material parameters, and they should be identified from experimental results.

4.3.2 Strain range memory effect

As indicated above, the studied 316L steels show obvious strain range memory effect during cyclic loading. In order to model this strain range dependent phenomenon during cyclic loading, Chaboche et al. [103] proposed the concept of memory surface in the plastic strain space. In this theory, a new internal variable is introduced to memorize the largest previous plastic strain range through a new index function F:

$$F = I\left(\underline{\varepsilon}^{\mathrm{p}} - \underline{\varsigma}\right) - q = \sqrt{\frac{2}{3}\left(\underline{\varepsilon}^{\mathrm{p}} - \underline{\varsigma}\right):\left(\underline{\varepsilon}^{\mathrm{p}} - \underline{\varsigma}\right)} - q \tag{4-18}$$

The plastic flow inside the domain defined by Eq. 18 does not change the 'memory state' defined by $\underline{\varsigma}$ and q, which respectively represent the translation tensor of the memory surface and its radius. The evolutions of these two internal variables $\underline{\varsigma}$ and q are respectively determined using the two following equations:

$$\dot{q} = \eta H(F)\langle n : n^{*}\rangle \dot{p} \tag{4-19}$$

$$\underline{\dot{\varsigma}} = \sqrt{\frac{3}{2}}(1-\eta)H(F)\langle n : n^{*}\rangle n^{*}\dot{p} \tag{4-20}$$

where n and n^{*} are respectively the unit vectors normal to the yield surface $f = 0$ and to the memory surface $F = 0$. More detailed description could be referred to [103,264].

In Eqs. (4-19) and (4-20), $H(F)$ is a Heaviside step function, and its values are defined by Eq. (4-21). The coefficient η is introduced to characterize the progressive memory ($\eta < 0.5$) [186,183]. Particularly, when $\eta = 0.5$, the memorization is instantaneous and the stabilization occurs after one cycle [103,264].

$$H(F) = \begin{cases} 1, F = 0 \text{ and } \dfrac{\partial F}{\partial \underline{\varepsilon}^{\mathrm{p}}} : \underline{\dot{\varepsilon}}^{\mathrm{p}} > 0 \\ 0, F < 0 \text{ or } \dfrac{\partial F}{\partial \underline{\varepsilon}^{\mathrm{p}}} : \underline{\dot{\varepsilon}}^{\mathrm{p}} \leq 0 \end{cases} \tag{4-21}$$

Under uniaxial loading, the strain range memory effect equations Eqs. (4-18), (4-19) and (4-20) can be simplified as follows:

$$F = |\varepsilon^{\mathrm{p}} - \varsigma| - q \tag{4-22}$$

$$\dot{q} = \eta H(F)\dot{p} \tag{4-23}$$

$$\dot{\varsigma} = (1-\eta)H(F)\dot{p}\frac{\partial F}{\partial \varepsilon^{\mathrm{p}}} \tag{4-24}$$

In general, the connexion between the cyclic plastic flow and the plastic strain range is introduced by considering asymptotic isotropic hardening variables through parameters Q_i in Eq. (4-15) and q in Eqs. (4-18) and (4-19) or Eqs. (4-22) and (4-23), as described by the following differential form shown in Eq. (4-25) and integral form shown in Eq. (4-26) [103,186,264,183,191]:

$$\dot{Q} = 2\mu(A-Q)\dot{q} \tag{4-25}$$

$$Q = Q_M + (Q_0 - Q_M)\mathrm{e}^{-\mu q} \tag{4-26}$$

where $\mu, A,\ Q_0, Q_M$ are material parameters.

4.3.3 Non-linear kinematic hardening rule

In most previous studies, the strain range memory effect was modelled by using additional state variables and their link with the asymptotic isotropic hardening values Q_i (as Eqs. (4-25) and (4-26)). However, for the steels studied in this work, the analysis performed in Section 4.2.3 implies that the strain range memory effect is mainly attributed to the back stress (Fig. 4-8b and Fig. 4-9), whereas the peak effective stress variation is very similar for different strain amplitudes (Fig. 4-8a). As a consequence, the strain range memory effect during cyclic loading should be taken into account in back stress through the hardening/softening effect. Nevertheless, the studied steels show complex cyclic behaviour which couples the hardening/softening and the strain range memory effect. It is thus difficult to represent these complex behaviours with Eqs. ((4-16) and (4-17)) and to perform the identification of all the material parameters. Therefore, another solution should be found. In fact, it can be observed in Fig. 4-9 that the stress difference $\sigma^{(i)\mathrm{C}} - \sigma_{\max}^{(i)\mathrm{T}}$ for each half cycle has a similar variation trend. For simplicity, a new non-linear kinematic hardening rule can be proposed by applying a scale coefficient φ, as shown in the following expression:

$$\underline{\dot{X}} = \varphi \cdot \sum_{i=1} \underline{\dot{X}}_i = \varphi \cdot \sum_{i=1} \left(\frac{2}{3} C_i \underline{\dot{\varepsilon}}^{\mathrm{p}} - \gamma_i \underline{X}_i \dot{p}\right) \tag{4-27}$$

where φ is a scale factor, here named kinematic hardening coefficient.

It is considered that the back stresses in different cycles can be correlated using this kinematic hardening coefficient. By contrast, the non-linear kinematic hardening rule of Eq. (4-16) actually considers the hardening/softening effect with all the parameters γ_i in the

classical decomposed AF rules (Eq. (4-12)), and the proposed rule (Eq. (4-27)) considers this hardening/softening effect with a more simplified form by introducing a new coefficient φ of back stress. The multiplicative expression of Eq. 27 was introduced by Ohno et al. [259] to take into account the isotropic effect which was observed depending on the maximum plastic strain during 'strain-controlled' ratchetting experiments of 316FR steel at high temperature (650 °C). Recently, the evolution of plastic strain range under cyclic loading was taken into account in the multiplier φ by Ohno et al. [267] to consider both the strain range reduction and the cyclic hardening behaviour through back stress.

According to the above analysis, the hardening/softening effect and the strain range memory effect, which are respectively associated with the accumulated plastic strain p and the radius of the memory surface q, can be characterized by this kinematic hardening coefficient φ, as shown in Eq. (4-28):

$$\varphi = \varphi(p, q) \tag{4-28}$$

In the following section, a complete functional relation of the expression $\varphi(p, q)$ will be presented based on more detailed analyses.

4.3.4 Identification procedure and strain range memory effect modelling

The cyclic constitutive model presented above takes into account isotropic hardening, kinematic hardening and strain range memory effect, associated with many material parameters to identify. A general identification procedure of material parameters for the classical combined kinematic/isotropic hardening constitutive model was illustrated in several studies [103,177]. In this procedure, the decomposed groups of kinematic hardening parameters C_i and γ_i are first identified based on stabilized cycles. Then the parameters related to the isotropic hardening and the plastic strain range can be obtained based on the initial monotonic stress-strain curves and cyclic stress amplitudes variations. However, for the developed cyclic constitutive model, the identification methodology mentioned above is not sufficient due to the fact that both the hardening/softening effect and the strain range memory effect are included in the proposed kinematic hardening rule (Eq. (4-27)).

In this work, a new identification procedure is proposed for the new kinematic hardening rule (Eqs. (4-27) and (4-28)), coupled with the isotropic hardening equations (Eqs. (4-14) and (4-15)). Moreover, a complete expression of $\varphi(p, q)$ associated with the accumulated plastic strain p and the radius of the memory surface q is established based on the cyclic behaviour of 316L-A.

4.3.4.1 Step 1: Material parameters related to effective stress

The analysis presented in Section 4.2.3 implies that the peak effective stress variation obtained under different strain amplitudes have very similar trend. As indicated above, effective stress consists of two parts respectively corresponding to isotropic hardening variable R and initial yield stress k. For the isotropic hardening, two decomposed variables R_i (Eqs. (4-14) and (4-15)) are used in this work to describe the initial hardening and the subsequent softening behaviour due to effective stress (see Fig. 4-8a), with the asymptotic values $Q_1 > 0, Q_2 < 0$.

In this step, an optimisation algorithm can be implemented to fit the effective stress variation with respect to the accumulated plastic strain under all the strain amplitudes, with the two isotropic hardening variables presented by Eqs. (4-14) and (4-15) and the initial yield stress k.

4.3.4.2 Step 2: Kinematic hardening coefficient φ

Knowing the obtained isotropic hardening parameters Q_i, b_i, and the initial yield stress k, the peak back stresses can be calculated based on the peak stresses (the maximum stress in each hysteresis loop) as well as the peak effective stresses, and the results are shown in Fig. 4-10. It is important to note that the variables at maximum kinematic/isotropic points in each hysteresis loop are used for parameter identification.

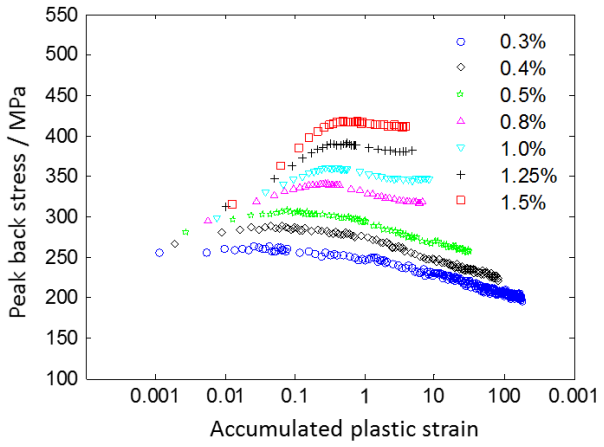

Fig. 4-10. Recalculated peak back stress variation as function of accumulated plastic strain under different strain amplitudes for 316L-A.

Under uniaxial loading, the decomposed AF rules (Eq. (4-12)) could be integrated as the following expression with the initial plastic strain $\varepsilon_0^{\mathrm{p}}$ and initial back stresses $X_{i,0}$:

$$X_i = v\frac{C_i}{\gamma_i} + \left(X_{i,0} - v\frac{C_i}{\gamma_i}\right)\mathrm{e}^{-v\gamma_i\left(\varepsilon^{\mathrm{p}} - \varepsilon_0^{\mathrm{p}}\right)} \tag{4-29}$$

where, v =1 represents the tensile-going phase, while $v = -1$ corresponds to the compressive-going phase.

The kinematic hardening coefficient φ characterizes the hardening/softening effect during cyclic loading, and thus it is firstly assumed as constant in each half hysteresis loop from the 2nd cycle. Then, the back stress under uniaxial loading can be expressed as:

$$X = \varphi \cdot \tilde{X} = \varphi \cdot \sum_{i=1} X_i \tag{4-30}$$

Eq. (4-30) presents an integrated form of Eq. (4-27) involving the coefficient φ and the kinematic hardening variable $\tilde{X}$, which is defined in this work as the sum of the decomposed AF rules. However, both the coefficient φ and the decomposed AF rules X_i are unknown in Eq. (4-30). Actually, during cyclic loading under a given strain amplitude, plastic strain increment in each half hysteresis loop is nearly constant. Hence, according to Eq. (4-29), we assume that the kinematic hardening variable at maximum extreme points $\tilde{X}_{\max}^{(i)\mathrm{T}}$ remains stable from the 2nd cycle in the step 2, and the following relations is thus applied:

$$\tilde{X}_{\max}^{(2)\mathrm{T}} \approx \tilde{X}_{\max}^{(3)\mathrm{T}} \approx \cdots \approx \tilde{X}_{\max}^{(n)\mathrm{T}} \tag{4-31}$$

Therefore, we get the value of the kinematic hardening coefficient at maximum extreme points $\varphi_{\max}^{(i)}$ as follows ($i \geq 2$):

$$\varphi_{\max}^{(i)} = X_{\max}^{(i)\mathrm{T}} / \tilde{X}_{\max}^{(i)\mathrm{T}} = X_{\max}^{(i)\mathrm{T}} / \left(X_{\max}^{(2)\mathrm{T}} / \varphi_{\max}^{(2)} \right) = \varphi_{\max}^{(2)} \cdot \left(X_{\max}^{(i)\mathrm{T}} / X_{\max}^{(2)\mathrm{T}} \right) \tag{4-32}$$

Then, a new scale factor $\Phi^{(i)}$ can be defined as the ratio between $\varphi_{\max}^{(i)}$ and $\varphi_{\max}^{(2)}$ ($i \geq 2$):

$$\Phi^{(i)} = \varphi_{\max}^{(i)} / \varphi_{\max}^{(2)} = X_{\max}^{(i)\mathrm{T}} / X_{\max}^{(2)\mathrm{T}} \tag{4-33}$$

Eq. (4-33) shows that the scale factor $\Phi^{(i)}$ equals to the ratio of the peak back stress between the current cycle (i^{th} cycle) and the 2nd cycle. Fig. 4-11 illustrates the variations of the scale factor $\Phi^{(i)}$ with the accumulated plastic strain obtained from Fig. 4-10. It can be seen that the scale factor $\Phi^{(i)}$ has very similar variation trends to the stress amplitude curves. Under strain amplitudes from ±0.8% to ±1.5%, the scale factor curves are characterized by an initial increase, followed by a gradual decrease, and become almost stable before fracture. However, under lower strain amplitudes (±0.3%, ±0.4% and ±0.5%), a longer decrease range of the scale factor can be observed, and it seems that the specimens were broken before a stable stage was reached.

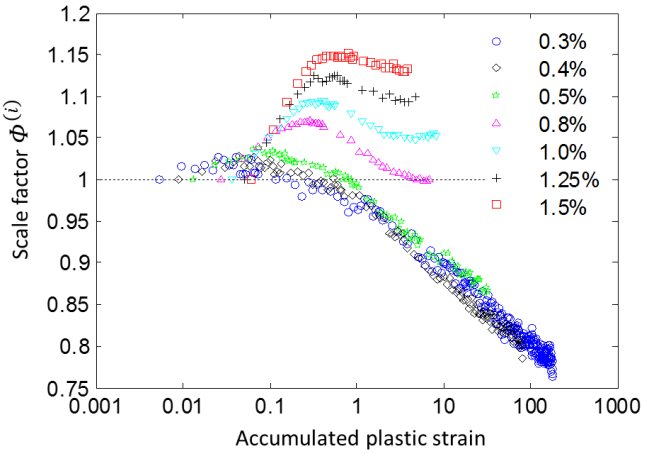

Fig. 4-11. Scale factor $\Phi^{(i)}$ variation with accumulated plastic strain under different strain amplitudes.

Fig. 4-11 also implies significant hardening/softening effect and strain range memory effect in peak back stresses during cyclic loading. For describing this hardening/softening effect through back stress, one of the most popular relations is the exponential function given by Eq. (4-17). In Eq. (4-17), φ_0 denotes the initial value and φ_∞ represents the saturated value of the factor φ. The saturation rate is controlled by the parameter ω. This classical expression was confirmed to be an effective method to characterize the initial hardening behaviour of most metallic materials during cyclic loading [200,263]. However, to model the back stress induced softening behaviour during cyclic loading, very few solutions were proposed, and the softening behaviour of metallic materials is generally described by the isotropic hardening variables (as Eqs. (4-14) and (4-15)).

In this work, a multi-group of exponential functions could be used to describe the relation between the kinematic hardening coefficient φ and the accumulated plastic strain p, as shown in Eq. (4-34). It consists of two parts. The first part φ^{I} has the classical expression (Eq. (4-17)) with the saturated value φ_∞ equal to 1, as shown by Eq. (4-35), which allows to control the initial hardening behaviour of the peak back stress.

$$\varphi = \varphi^{\mathrm{I}} \cdot \varphi^{\mathrm{II}} \tag{4-34}$$

$$\varphi^{\mathrm{I}} = 1 + (\varphi_0^{\mathrm{I}} - 1)\mathrm{e}^{-ap} \tag{4-35}$$

Similarly, another exponential function with the same form as presented in Eq.(4-17) could be used to describe the exponential attenuation of peak back stress. However, Fig. 4-11 shows that there is no obvious saturation of the scale factor $\Phi^{(i)}$ under lower strain amplitudes from ±0.3% to ±0.5%, and a sharp decrease after the initial hardening saturation can be observed, as shown in Fig. 4-12a. Fig. 4-12b gives a normalized variation of the scale

factor $\Phi^{(i)}$ through natural logarithm function $\log\big((\Phi-\Phi_\infty)/(\Phi_0-\Phi_\infty)\big)$, in which the points at the beginning of softening and by the end of decrease are respectively taken as Φ_0 and Φ_∞.

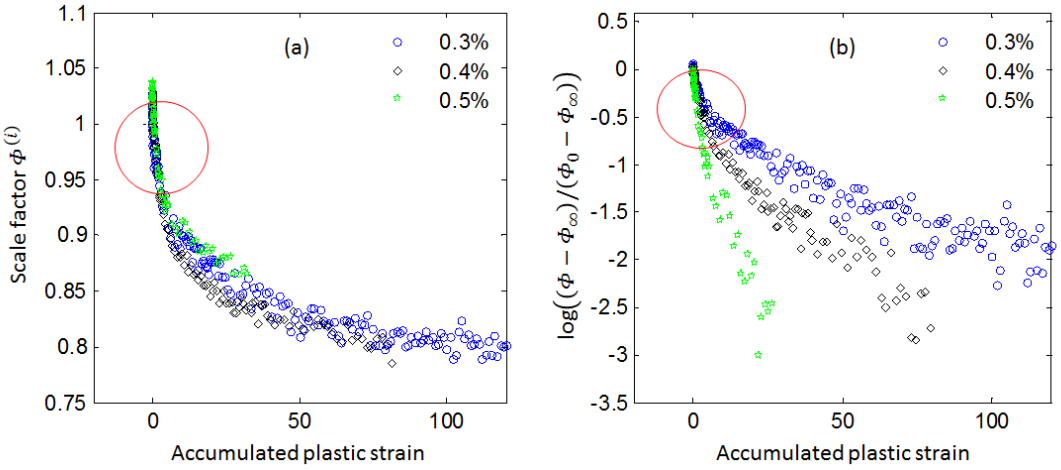

Fig. 4-12. (a) Scale factor $\Phi^{(i)}$ variation and (b) its natural logarithm function variation with accumulated plastic strain under strain amplitudes of ±0.3%, ±0.4% and ±0.5%.

It can be observed that a sharp decrease of the logarithmic value occurs at the beginning (Fig. 4-12b), and then the logarithmic value decreases linearly with a nearly constant slope. This phenomenon indicates that one simple exponential function is not enough to model the whole softening behaviour of the studied steel induced by the attenuation of the peak back stress under lower strain amplitudes (±0.3%, ±0.4% and ±0.5%). As mentioned above, Xu et al. [183] tried to use a logistic function to model the cyclic softening behaviour of BLY160 steel. However, this method is not able to describe the as-observed softening behaviour of the studied steel due to the fact that the evolution of softening cannot be characterized by a 'S' shape curve. Therefore, in this work, another exponential function $(\exp(-cp)+1)/2$ is introduced to describe the initial sharp decrease of the kinematic hardening coefficient φ, and the second part φ^{II} mentioned in Eq. (4-34) can be expressed by the following Eq. (4-36). Tab. 4-3 lists the corresponding bounded cases of the kinematic hardening coefficient φ for $p=0$ and $p\to+\infty$.

$$\varphi^{\mathrm{II}}=\varphi_0^{\mathrm{II}}\cdot\exp(-bp)\cdot(\exp(-cp)+1)/2+\varphi_\infty^{\mathrm{II}} \tag{4-36}$$

Tab. 4-3. Typical extreme values of kinematic hardening coefficient φ.

p	φ^{I}	φ^{II}	φ
0	φ_0^{I}	$\varphi_0^{\mathrm{II}}+\varphi_\infty^{\mathrm{II}}$	$\varphi_0^{\mathrm{I}}\cdot(\varphi_0^{\mathrm{II}}+\varphi_\infty^{\mathrm{II}})$
$+\infty$	1	$\varphi_\infty^{\mathrm{II}}$	$\varphi_\infty^{\mathrm{II}}$

To summarize, the initial hardening and subsequent softening are respectively described by the two parts φ^{I} and φ^{II} in Eq. (4-34), whereas the term $(\exp(-cp)+1)/2$ is used to describe the sharp decrease at the beginning of the softening regime. The constants $\varphi_0^{\mathrm{I}}, \varphi_0^{\mathrm{II}}$, and $\varphi_\infty^{\mathrm{II}}$ determine the initial and asymptotic values of the hardening and the softening regimes, as listed in Tab. 4-3, while a, b, and c govern the hardening and softening rate.

Previous studies presented in the literature were generally focused on the initial hardening behaviour, and only the asymptotic isotropic hardening value Q_i (see Eq. (4-15)) was associated with the radius of the memory surface q to describe the strain range memory effect, as described in Eqs. (4-25) and (4-26). According to the above analysis, the strain range memory effect consists in not only the initial hardening, but also the subsequent softening behaviour. Thus the relations between the kinematic hardening variables φ and the radius of the memory surface q can be built through the following integrated equations:

$$\begin{bmatrix} \varphi_0^{\mathrm{I}} \\ a \\ \varphi_0^{\mathrm{II}} \\ b \\ c \\ \varphi_\infty^{\mathrm{II}} \end{bmatrix} = A + (B - A) \circ \exp(-Mq) \tag{4-37}$$

where the symbol '$\circ$' indicates a Schur product between two matrices with the same dimensions. A, B, and M are six-order vectors of material parameters.

Eqs. (4-34), (4-35) and (4-36) present the functional relations of the kinematic hardening coefficient and the accumulated plastic strain, and Eq. (4-37) makes the kinematic hardening coefficients associated with the strain range memory effect. The following procedure can be implemented to identify these eighteen material parameters involved in the vectors A, B, and M (see Eq. (4-37)):

(1) The values of $\varphi_0^{\mathrm{I}}, a,\ \varphi_0^{\mathrm{II}}, b, c,\ \varphi_\infty^{\mathrm{II}}$ in Eqs. (4-34), (4-35) and (4-36) are calibrated based on the scale factor $\Phi^{(i)}$ variations (see in Fig. 4-11), respectively for different strain amplitudes;

(2) The relations between each parameters ($\varphi_0^{\mathrm{I}}, a,\ \varphi_0^{\mathrm{II}}, b, c,\ \varphi_\infty^{\mathrm{II}}$) with the radius of the memory surface q can be fitted independently with the exponential function presented in Eq. (4-37). Thus the values of the vectors A, B, and M are obtained.

(3) A repetitive optimisation from (1) to (2) is recommended to get a better result.

4.3.4.3 Step 3: Material parameters of kinematic hardening variable $\tilde{X}$

For identification of the kinematic hardening parameters C_i, γ_i, as detailed in most of previous studies (e.g. Chaboche et al., 1979, 2012), the following expression can be given for each stabilized half cycle based on the assumption that the value of kinematic hardening coefficient φ is constant throughout each half cycle:

$$\begin{aligned}\Delta\sigma^{(s)} &= \sigma_{max}^{(s)} - \sigma^{(s)} \\ &= \varphi(p,q)\sum_{i=1}\frac{C_i}{\gamma_i}\left\{\tanh\left(\gamma_i\frac{\Delta\varepsilon^{\mathrm{p}}}{2}\right)(1+\exp(-\gamma_i\varepsilon^{\mathrm{p}})) + \exp(-\gamma_i\varepsilon^{\mathrm{p}}) - 1\right\}\end{aligned} \tag{4-38}$$

which then gives the following expression:

$$\frac{\Delta\sigma^{(s)}}{\varphi(p,q)} = \sum_{i=1}\frac{C_i}{\gamma_i}\left\{\tanh\left(\gamma_i\frac{\Delta\varepsilon^{\mathrm{p}}}{2}\right)(1+\exp(-\gamma_i\varepsilon^{\mathrm{p}})) + \exp(-\gamma_i\varepsilon^{\mathrm{p}}) - 1\right\} \tag{4-39}$$

With the obtained value of $\varphi(p,q)$ in Step 2, the parameters C_i and γ_i can be calibrated by fitting Eq. (4-39) with experimental curves using an optimisation method.

4.3.4.4 Step 4: Re-identifying parameters of φ

With the obtained kinematic hardening parameters C_i and γ_i, the kinematic hardening variables at the extreme points $\tilde{X}_{\max}^{(i)\mathrm{T}}$ in each cycle can be calculated through (4-11) and (4-12) or Eq. (4-29). Then, the kinematic hardening coefficient φ could be re-calculated based on the obtained $\tilde{X}_{\max}^{(i)\mathrm{T}}$ and the peak back stress variation (see Fig. 4-10) with Eq. (4-30). Afterwards, material parameters in the vectors A, B, and M could be re-identified with the obtained kinematic hardening coefficient φ at the extreme points by Eqs. (4-34), (4-35), (4-36) and (4-37).

4.3.4.5 Step 5: Re-identifying parameters of effective stress

In this last step, the peak effective stresses under different loading levels can be re-calculated with the obtained peak back stresses in Step 3 and Step 4, and the identification can be performed once again. Thus, a new group of isotropic hardening constants Q_i and b_i are obtained coupled with a new initial yield stress value of k.

In principle, all the material parameters can be identified through the above five steps. However, in order to obtain a better precision in cyclic behaviour description, it is recommended to perform repetitive iterations from Step 3 to Step 5. A summarized identification procedure for the developed cyclic constitutive model is given by Fig. 4-13.

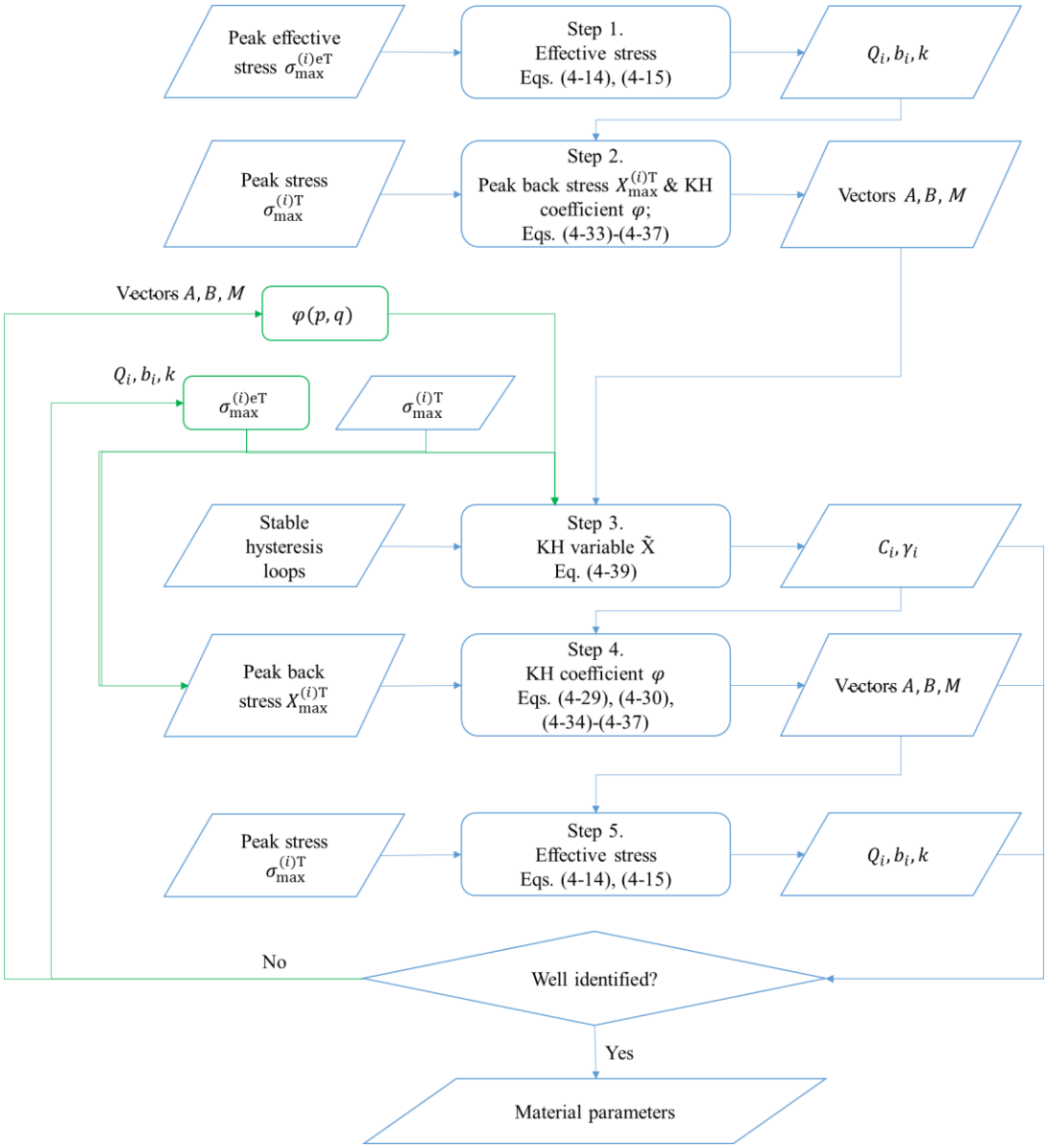

Fig. 4-13. Identification procedure for the developed cyclic constitutive model (KH: kinematic hardening).

4.3.5 Summary of the constitutive modelling and the identification results

The developed cyclic constitutive model and the proposed identification procedures have been presented above. In this section, all the constitutive laws used to describe the cyclic behaviour of the steel 316L-A are listed in Tab. 4-4 for a clearer reference.

Tab. 4-4. Summarized description of the cyclic constitutive model.

Elastic relationship (Hooke's law)
$\underline{\sigma} = \underline{\underline{\boldsymbol{C}}} : (\underline{\varepsilon} - \underline{\varepsilon}^{\mathrm{p}})$
Combined kinematic/isotropic cyclic constitutive model
Yield function:

$f(\underline{\sigma}, \underline{X}, R) = J_2(\underline{\sigma} - \underline{X}) - R - k$
Plastic flow rule:
$\dot{\varepsilon}^{\mathrm{p}} = \frac{3}{2}\dot{\lambda} \cdot (\underline{\sigma}^* - \underline{X}^*)/J_2(\underline{\sigma} - \underline{X})$
Isotropic hardening rule:
$\dot{R} = \sum_{i=1} \dot{R}_i$ $\dot{R}_i = b_i(Q_i - R_i)\dot{p}$
Kinematic hardening rule:
$\underline{\dot{X}} = \varphi \cdot \sum_{i=1} \underline{\dot{X}}_i$ $\dot{X}_i = \frac{2}{3}C_i\dot{\varepsilon}^{\mathrm{p}} - \gamma_i X_i \dot{p}_i$ $\varphi = \varphi^{\mathrm{I}} \cdot \varphi^{\mathrm{II}}$ $\varphi^{\mathrm{I}} = 1 + (\varphi_0^{\mathrm{I}} - 1)\exp(-ap)$ $\varphi^{\mathrm{II}} = \varphi_0^{\mathrm{II}} \cdot \exp(-bp) \cdot (\exp(-cp) + 1)/2 + \varphi_\infty^{\mathrm{II}}$
Strain range memory effect
Memory surface:
$F = I\left(\underline{\varepsilon}^{\mathrm{p}} - \underline{\varsigma}\right) - q = \sqrt{\frac{2}{3}\left(\underline{\varepsilon}^{\mathrm{p}} - \underline{\varsigma}\right) : \left(\underline{\varepsilon}^{\mathrm{p}} - \underline{\varsigma}\right)} - q$
Evolution of memory surface:
$\dot{q} = \eta H(F)\langle n : n^* \rangle \dot{p}$ $\underline{\dot{\varsigma}} = \sqrt{\frac{3}{2}}(1-\eta)H(F)\langle n : n^* \rangle n^* \dot{p}$ $H(F) = \begin{cases} 1, F = 0 \text{ and } \frac{\partial F}{\partial \underline{\varepsilon}^{\mathrm{p}}} : \underline{\dot{\varepsilon}}^{\mathrm{p}} > 0 \\ 0, F < 0 \text{ or } \frac{\partial F}{\partial \underline{\varepsilon}^{\mathrm{p}}} : \underline{\dot{\varepsilon}}^{\mathrm{p}} \leq 0 \end{cases}$
Cyclic refreshing of the kinematic hardening coefficient:
$[\varphi_0^{\mathrm{I}} \quad a \quad \varphi_0^{\mathrm{II}} \quad b \quad c \quad \varphi_\infty^{\mathrm{II}}]^{\mathrm{T}} = A + (B - A) \circ \exp(-Mq)$

As indicated above, all the material parameters of the constitutive model summarized in Tab. 6 can be identified with the procedures presented in section 4.3.4. Tab. 4-5 lists one group of the identified values. The calibration results for the variables in different steps can be seen in the Appendix B.

Tab. 4-5. Material parameters of the developed cyclic constitutive model identified for the steel 316L-A.

Basic elastic constants:
E=196.5 GPa; $v = 0.3$; k =98.8821 MPa;
Isotropic hardening variables:
$Q_1 = 75.1337$ MPa, $b_1 = 139.39$; $Q_2 = -30.7258$ MPa, $b_2 = 3.0912$;
Kinematic hardening variables:
$C_1 = 368784.48$ MPa, $\gamma_1 = 3181.48$; $C_2 = 66483.71$ MPa, $\gamma_2 = 558.47$; $C_3 = 15844.43$ MPa, $\gamma_3 = 114.71$.
Strain range memory effect:
$\eta = 0.5$; $A = [18.5558 \quad 7.0885 \quad 0.0942 \quad 0.0866 \quad 0 \quad 0.5962]^{\mathrm{T}}$; $B = [1.0562 \quad 155.1087 \quad 0.9272 \quad -0.0201 \quad 0.8200 \quad 0.8963]^{\mathrm{T}}$; $M = [-1.6745 \quad 558.6357 \quad 796.0488 \quad -341.4419 \quad 557.8679 \quad -51.6331]^{\mathrm{T}}$.

4.4 Results and discussion

Based on the cyclic behaviour of the steel 316L-A under strain amplitudes from ±0.3% to ±1.5%, a constitutive model was developed coupled with a new non-linear kinematic hardening rule to describe the cyclic hardening/softening behaviour and strain range memory effect, as presented in Tab. 4-4. Considering that nearly all the internal variables are governed by differential equations, Newton-Raphson numerical iteration method was used to resolve the equations for the simulation of strain controlled uniaxial reversed cyclic loading (load ratio $R_\varepsilon = -1$).

As shown in Fig. 6, metallic materials can undergo a large number of cycles before fracture under lower strain amplitudes. In the case of the cyclic loading simulation, it would be very time-consuming to simulate all the cycles of a fatigue test. A cycle jumping scheme was thus used to reduce the computational cost through estimating the mechanical state of the material to the cycle N and the successive cycles.

4.4.1 Initial tensile behaviour

A comparison of initial tensile curve between modelling and experiment is illustrated in Fig. 4-14. It shows that the initial tensile behaviour can be well described by the developed cyclic constitutive model. As indicated in the Section 4.2.1, proportionality limit, elastic limit and offset yield stress are widely used to represent the yield strength of a material, and sometimes considered as the initial yield stress during cyclic deformation. From the viewpoint of deformation mechanism, microscopically dislocations begin to move at a very low stress level, and thus the true threshold stress for plastic deformation should be much lower than the commonly determined macroscopic elastic limit [268]. However, it is nearly impossible to obtain the true yield stress since macroscopically detecting such a

dislocation movement is difficult. In this work, the initial yield stress k used in the model is determined through the fitting of isotropic hardening variables (see Fig. B-4 in Appendix B). It can be found that the value of k (see Tab. 4-5) is much lower than the obtained proportionality limit (see Tab. 4-1).

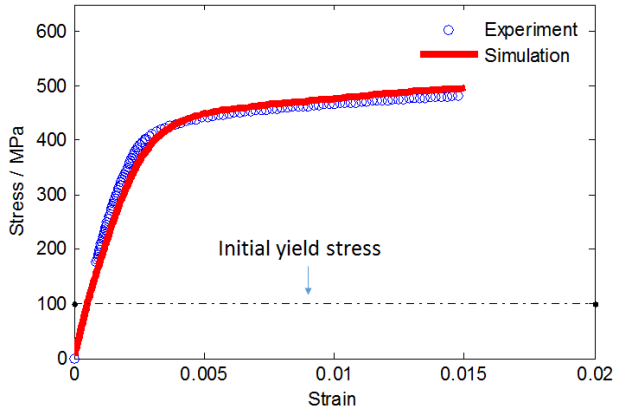

Fig. 4-14. Comparison of initial tensile curve between modelling and experiment.

During the initial tension, the plastic deformation is activated when the stress level reaches the initial yield point. Simultaneously, the back stress and the isotropic hardening also begin to increase beyond the initial yield point, as shown in Fig. 4-15a and Fig. 4-15b. The red curve in Fig. 4-15a shows that the back stress increases drastically at the initial stage of plastic deformation due to the effect of kinematic hardening coefficient φ, while the kinematic hardening variable $\tilde{X}$ (the blue dotted curve in Fig. 16a) and the isotropic hardening (Fig. 4-15b) have a slower increase based on the exponential relations (expressed by Eqs. (4-11) - (4-15)). For the kinematic hardening coefficient φ (Fig. 4-15c), it has a very high initial value, and decreases gradually with respect to the plastic strain due to a gradual increase of the radius of the memory surface in the plastic strain space.

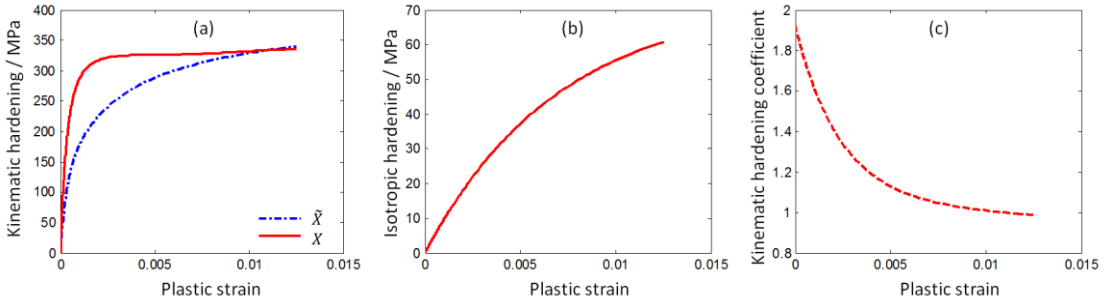

Fig. 4-15. Variation of: (a) back stress X and kinematic hardening variable $\tilde{X}$, (b) isotropic hardening variable R, and (c) kinematic hardening coefficient φ , obtained during the initial tensile simulation.

Fig. 4-15 indicates that the drastic increase of stress just beyond the initial yield stress is mainly due to the back stress through a high initial value of the kinematic hardening

coefficient φ. As the plastic deformation increases, the kinematic hardening coefficient gradually decreases (see Fig. 4-15c), and thus the increase rate of back stress is decreased as well (see Fig. 4-15a), which indirectly induces a reduced hardening rate during the initial plastic flow stage. This is consistent with the microstructure evolution of a 316L steel observed under uniaxial tensile deformation at room temperature [257]. Afterwards, a constant back stress and a slowly increased isotropic hardening together induce a nearly unchanged hardening slop, as shown in Fig. 4-2. The analysis performed above implies that the introduced coefficient φ in back stress (Eq. (4-27)) is capable of well describing the initial tensile behaviour of the studied steel.

4.4.2 Cyclic behaviour

4.4.2.1 Stress amplitude variation

The stress amplitudes of the cyclic curves obtained by modelling can be calculated with Eq. (4-5), and the comparison with experimental results of 316L-A under different strain amplitudes is illustrated in Fig. 4-16. It shows that the hardening/softening and the strain range memory effect can be well described by the developed constitutive model, especially for the lower strain amplitudes (±0.3%, ±0.4% and ±0.5%) under which the steel manifests a longer softening range without stabilization. The biggest error between the modelled and the experimental stress amplitudes is about 10 MPa in the stabilized cycles under a strain amplitude of ±1.5% as well as in the hardening saturated cycles under a strain amplitude of ±0.3%, as shown in Fig. 4-16a.

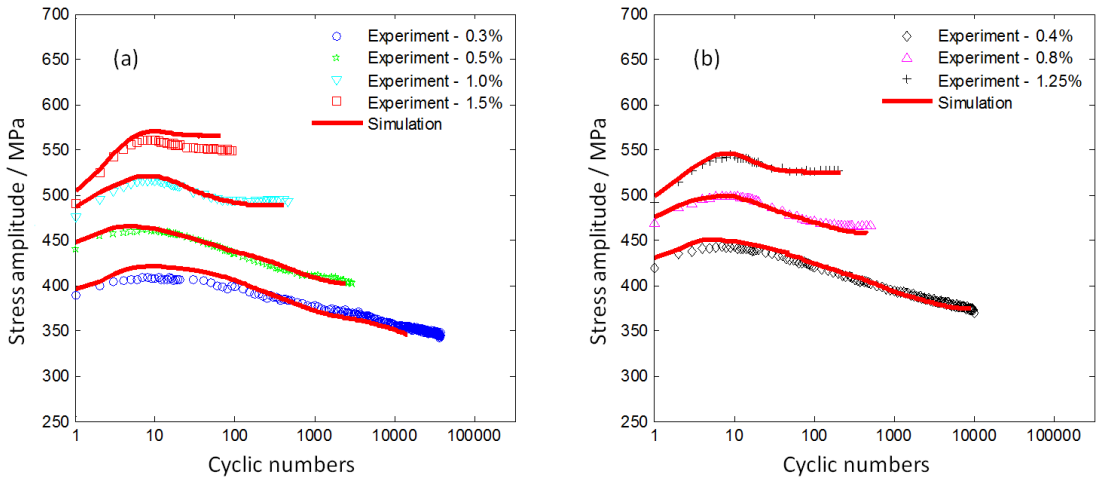

Fig. 4-16. Comparison of modelled and experimental curves of stress amplitudes as a function of the number of cycles under different strain amplitudes (316L-A).

4.4.2.2 Hysteresis loops

Hysteresis loops can reflect the detailed plastic flow behaviour of a material. Stress amplitude evolution curves indicate that the cyclic behaviour throughout the fatigue lifetime of the steel 316L-A can be divided into three stages: initial hardening, softening, and stabilization (for strain amplitudes from ±0.8% to ±1.5%). An initial hardening stage can be observed during the first several cycles. In Fig. 4-17, a comparison of the first two hysteresis loops between modelling and experiment for 316L-A under different strain amplitudes is illustrated. It can be seen that the developed constitutive model can well describe the cyclic behaviour of 316L-A at the beginning of cyclic loading. However, there are some slight differences for tensile-going phase under lower strain amplitudes (±0.3%, ±0.4% and ±0.5%). These differences could be attributed to the large asymmetry on tensile going and compressive going of experimental results during plastic flow at the beginning of cyclic loading under lower strain amplitudes.

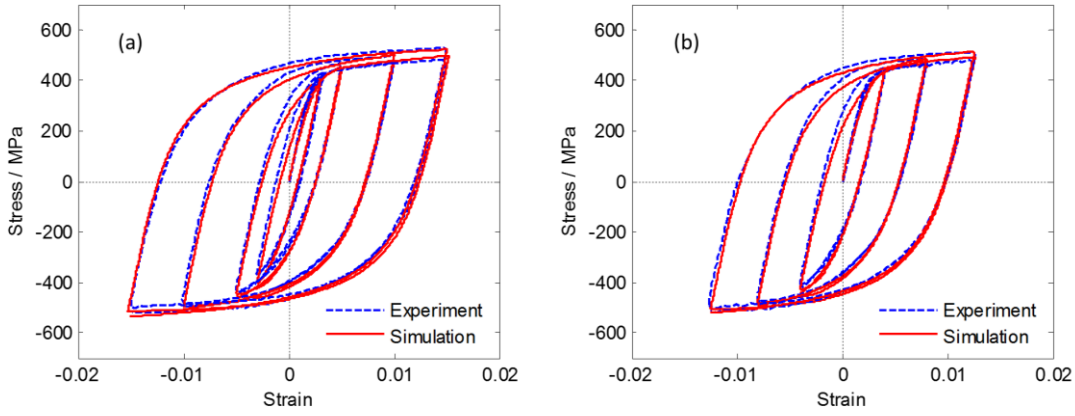

Fig. 4-17. Comparison of the first two hysteresis loops between modelling and experiment for 316L-A under different strain amplitudes (a) ±0.3%, ±0.5%, ±1.0% and ±1.5%; (b) ±0.4%, ±0.8%, and ±1.25%.

As it can be seen on all the experimental curves shown in Fig. 4-5, the cyclic hardening behaviour becomes saturated at about 10^{th} cycle under different strain amplitudes. Thus, the 10^{th} hysteresis loop can be used to characterize the hardening saturation state. Fig. 4-18 shows a very good agreement of the 10^{th} hysteresis loop between modelling and experiment under different strain amplitudes.

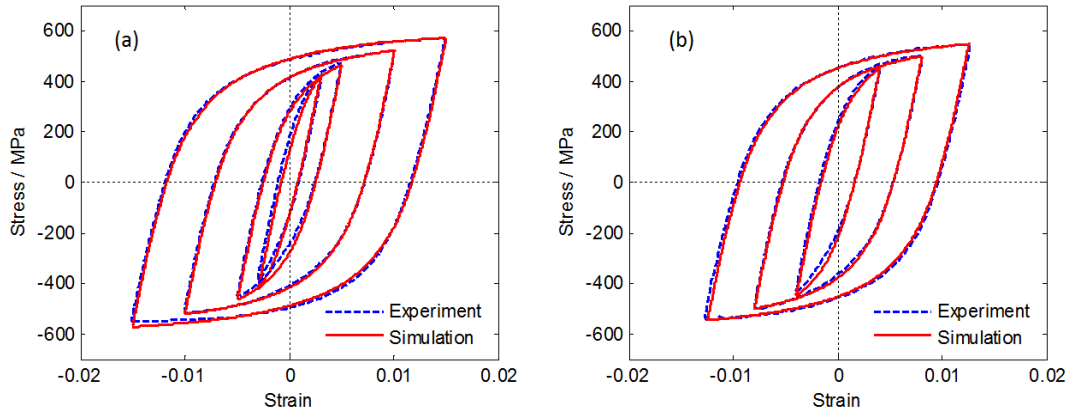

Fig. 4-18. Comparison of 10th hysteresis loop between modelling and experiment of 316L-A under strain amplitudes of (a) ±0.3%, ±0.5%, ±1.0% and ±1.5%; (b) ±0.4%, ±0.8%, and ±1.25%.

After the initial hardening behaviour until about 10th cycle, a longer softening range occurs, as revealed by experiments (Fig. 4-5). An obvious stabilization can be observed after a more or less pronounced softening range under higher strain amplitudes (±0.8%, ±1.0%, ±1.25% and ±1.5%). Fig. 4-19 illustrates a good agreement of hysteresis loops between modelling and experiment at a typical stabilized cycle after the softening range under strain amplitudes from ±0.8% to ±1.5%.

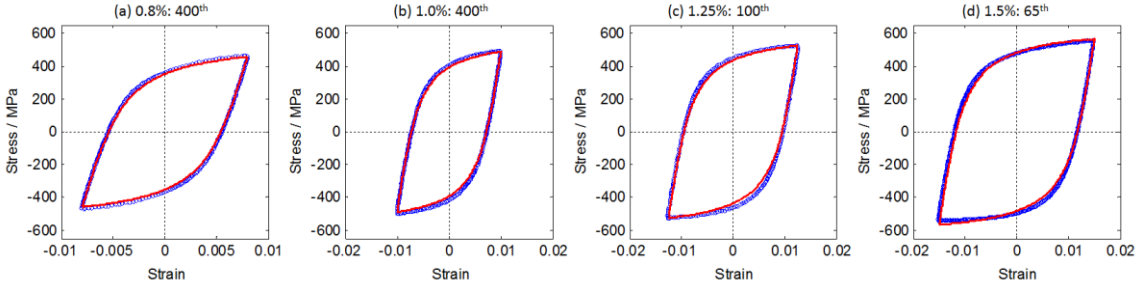

Fig. 4-19. Comparison of stabilized cycles between modelling (red) and experiment (blue) under strain amplitudes of ±0.8%, ±1.0%, ±1.25% and ±1.5%. The corresponding cycle number is also indicated in each figure.

In contrast, under the lower strain amplitudes of ±0.3%, ±0.4%, and ±0.5%, the steel underwent a much longer softening range from the hardening saturation (about 10th cycle) to the final fracture. This long softening range represents a large fraction of fatigue life, and thus plays an important role in fatigue fracture of the material under very low strain amplitudes. Comparisons of several typical hysteresis loops in the whole softening range between modelling and experiment under strain amplitudes of ±0.3%, ±0.4% and ±0.5% are also given in Fig. 4-20. All the twelve figures shown in Fig. 4-20 also present a very good agreement between the modelling results and the experimental results, which signifies that

the developed constitutive model is able to precisely describe the cyclic softening behaviour and the strain range memory effect of the steel 316L-A under very low strain amplitudes.

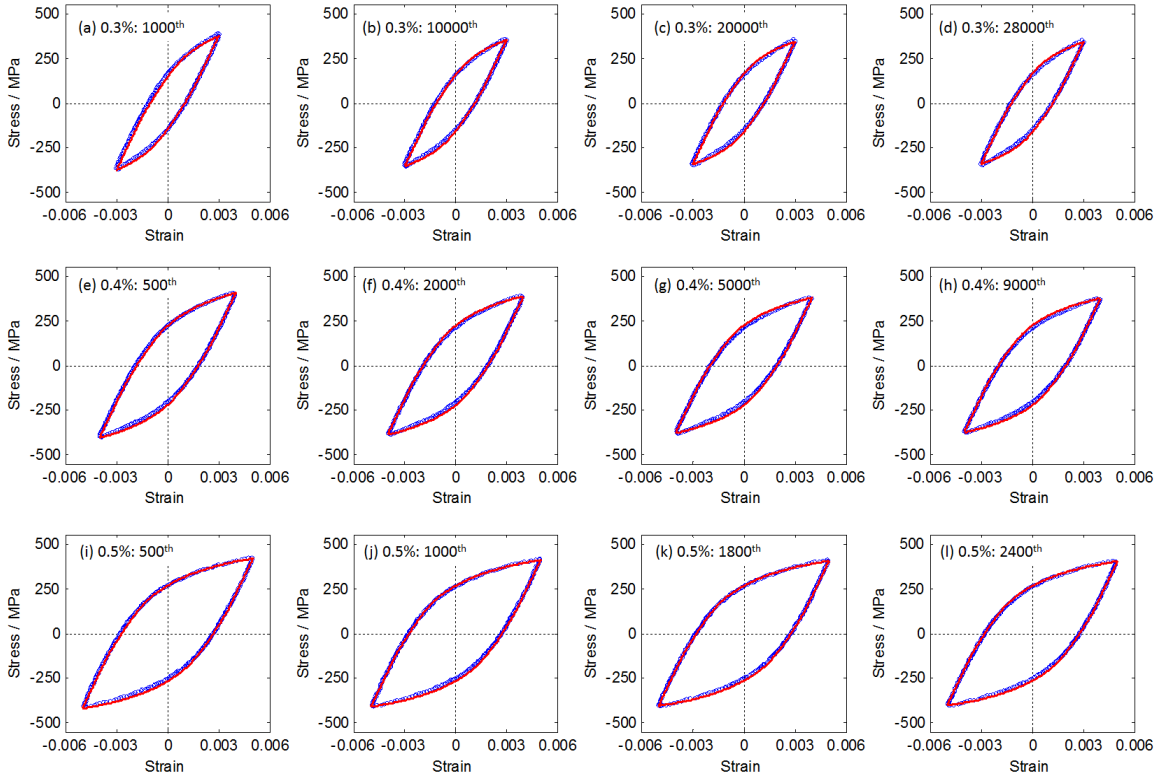

Fig. 4-20. Comparison of several typical hysteresis loops between modelling and experiment for 316L-A under strain amplitudes from ±0.3% to ±0.5% throughout the whole softening range.

4.4.3 Discussion on the non-linear kinematic hardening rule

The comparisons performed above, consisting of initial tension (Fig. 4-14), stress amplitudes (Fig. 4-16), hysteresis loops at different chosen numbers of cycles corresponding to different cyclic deformation stages (Fig. 4-17, Fig. 4-18, Fig. 4-19 and Fig. 4-20), demonstrate that the developed constitutive model is able to precisely describe the cyclic behaviour of the studied steel 316L-A, including the hardening/softening and the strain range memory effect. It is worth mentioning that the introduced kinematic hardening coefficient φ is a flexible scale factor, and its relations with the accumulated plastic strain and the memory surface can be built in order to characterize more complex cyclic behaviour of metallic materials, for example the secondary hardening phenomenon observed for the other austenitic steel 316L-B under strain amplitudes of ±0.8%, ±1.0% and ±1.25% (see Fig. 4-5b).

In Eq. (4-37), the parameters of the kinematic hardening coefficient φ have exponential functions with the radius of the memory surface q. With the material parameters listed in Tab. 4-5, it can be found that when the internal variable q increases, the parameters a, φ_0^{II},

c in Eqs. (4-34), (4-35) and (4-36) tend to be close to the constants 7.0885, 0.0942, and 0 (see in Tab. 4-5), respectively. Hence, the relation between the kinematic hardening coefficient φ and the accumulated plastic strain *p* can be changed into:

$$\varphi = (1 + (\varphi_0^{\mathrm{I}} - 1)\exp(-7.0885p)) \cdot (0.0942\exp(-bp) + \varphi_\infty^{\mathrm{II}}) \qquad (4\text{-}40)$$

Taking the term $(0.0942\exp(-bp) + \varphi_\infty^{\mathrm{II}})$ as a new parameter $\tilde{\varphi}$, Eq. 40 can be written as:

$$\varphi = \tilde{\varphi} + (\varphi_0^{\mathrm{I}} \cdot \tilde{\varphi} - \tilde{\varphi})\exp(-7.0885p) \qquad (4\text{-}41)$$

It can be seen that Eq. (4-41) has the same functional forms as the expressions given in Eq. (4-17). φ_0^{I} and $\tilde{\varphi}$ are two parameters which are related to the accumulated plastic strain *p* and the radius of the memory surface *q* with independent exponential function (Eq. (4-37)). This implies that the kinematic hardening coefficient φ degrades to the classical exponential relation (Eq. (4-17)) under high strain amplitudes, with the initial value $\varphi_0^{\mathrm{I}} \cdot \tilde{\varphi}$ and the asymptotic value $\tilde{\varphi}$ associated with the strain range memory effect.

It should be noted that the model developed in this work aims to accurately describe the complex cyclic hardening/softening behaviour based on the back stress and effective stress identified from experimental results. Only strain-controlled tension-compression fatigue tests were thus considered with single-step loading conditions. Furthermore, the strain range memory effect was characterized through back stress according to the experimental analysis. In practice, materials can undergo very different cyclic behaviours with complex loading path/history, such as strain range evolution, pre-straining, or ratcheting during forming process or in service. Therefore, the complete strain range memory effect (e.g. pre-hardening, strain range evolution) should be included in the cyclic constitutive modelling work. Previous studies confirmed that austenitic stainless steels (e.g. 304L and 316L) present significant strain memory effect inherited from pre-hardening, strain range evolution, ratcheting. Moreover, some studies indicated that the cyclic behaviour and the fatigue life of pre-hardened austenitic stainless steels (304L and 316L) are strongly dependent on the pre-hardening amplitude and paths [260,181,182,206,179]. It is generally accepted that plastic strain with sufficiently high amplitude could erase the memory effect inherited from a smaller pre-hardening amplitude, whereas high pre-hardening effect is usually preserved under subsequent cyclic loading with low plastic strain amplitudes. This phenomenon was experimentally illustrated through pre-hardening effect studies in axial/torsional direction as well as axial cyclic experiments with stepwise increased/decreased strain amplitudes for 304L [181,182] and 316L steels [179].

In this work, the constitutive modelling is based on strain-controlled tension-compression tests with constant strain ranges, and thus the value of 0.5 for the parameter η in Eq. 19 and 20 is acceptable [103,264]. However, this value of η is not valid in the presence of strain range reduction, pre-straining, or ratcheting, which can occur in structural components. The evolution parameter ($0 < \eta < 0.5$) was introduced by Ohno [185] to represent the progressive memory, and it was further extended by Nouailhas et al. [186] through adding a memory erasure term in the evolution equation Eq. (4-19). The evolution parameter η with values ranging between 0 and 0.5, as well as the memory erasure term, has been employed to effectively describe the cyclic behaviour of materials with large pre-straining and/or evolved strain range under cyclic loading [186,269,184,270,187,189,188,183]. Nevertheless, the value of η can be difficult to be appropriately identified. In order to provide a definite value of η, a resetting scheme was newly developed by Ohno et al. [267] to evaluate the plastic strain range irrespective of the amounts of cyclic hardening, pre-straining, and ratcheting. It was demonstrated that, by using the proposed resetting scheme, $\eta = 0.5$ could be employed to correctly evaluate the plastic strain range under proportional cyclic loading in the presence of strain range reduction and/or ratcheting [267]. Therefore, in order to overcome the limitation of $\eta = 0.5$, the resetting scheme could be a choice to extend the model developed in our work for predicting the cyclic behaviour of the studied 316L in the LCF regime by taking into account the evolved strain amplitudes and/or ratcheting effect.

Furthermore, it was highlighted that the memory effect inherited from pre-hardening in axial direction was closely related to back stress [179]. This is consistent with the experimental results observed in the work. However, for the pre-hardening induced by cyclic torsional loading, the effective stress played a much more important role in the strain memory effect than the back stress [182]. To summarize, the memory effect is very complex for 316L steels. It is not only dependent on the pre-hardening amplitude, but also related to the pre-hardening paths (tension, cyclic loading in uniaxial tension-compression or in torsional direction). It could thus be interesting but challenging to precisely describe the complex memory effect of the studied materials.

4.5 Conclusions

This chapter focuses on experimental analysis and constitutive modelling of the cyclic behaviour of two 316L austenitic steels under uniaxial strain controlled LCF tests. The

observed cyclic behaviour and constitutive modelling include both hardening/softening and strain range memory effect, which constitute the original points of this work.

To conclude, the experimental analysis of the two 316L austenitic steels shows that:

(1) The cyclic behaviour of the two steels is characterized by an initial hardening, followed by a longer softening range. Obvious secondary hardening phenomenon occurs for the 316L-B steel under higher strain amplitudes (from ±0.8% to ±1.25%). In addition, significant strain range memory effect is observed for both of the studied steels.

(2) The effective stress variation for different strain amplitudes are very similar, and the cyclic hardening/softening behaviour along with the strain range memory effect are mainly attributed to back stress.

To model the cyclic behaviour of the 316L-A steel, a set of constitutive relations was proposed in the combined kinematic/isotropic hardening framework. This constitutive model was implemented and identified to predict the cyclic behaviour throughout the entire cyclic loading of the studied steel. The following conclusions can be drawn:

(1) A new non-linear kinematic hardening rule is proposed by introducing a kinematic hardening coefficient φ to consider the hardening/softening effect and the strain range memory effect.

(2) A functional relation between the kinematic hardening coefficient φ and the accumulated plastic strain p is given based on the experimental analysis of the cyclic behaviour to describe the hardening/softening effect.

(3) The strain range memory effect is incorporated in the back stress through a functional relation between the memory surface and the kinematic hardening coefficient φ.

(4) A series of identification procedures is implemented to optimise the material parameters involved in the developed constitutive model.

Comparison between the modelling and the experimental results of the austenitic 316L-A steel shows that the developed cyclic constitutive model is able to accurately describe the cyclic behaviour of the studied material in the LCF regime, including the hardening/softening and the strain range memory effect based on back stresses.

Chapter 5: Self-consistent modelling of a 316L steel

In Chapter 4, cyclic constitutive modelling of the studied 316L steel was performed in the framework of combined kinematic/isotropic hardening model. The microstructural characteristics actually determine the macroscopic properties of materials. Macroscopic plasticity models are unable to capture the local deformation mechanisms at the microstructural level. Therefore, crystal plasticity is widely used to describe the mechanical behaviour based on the observation of deformation mechanism of metallic materials. Over the last decades, physically based modelling work has become more and more popular for describing the mechanical behaviour of materials and understanding the deformation mechanism at microscopic scale or cross-scale level. In this chapter, a cyclic modelling of the studied 316L steel is performed based on a single crystal plasticity model coupled with self-consistent method. The cyclic hardening/softening behaviour is represented in each slip system by considering a kinematic hardening term and an isotropic hardening term. The constitutive model and the identification procedure are implemented in order to describe the evolution of the back stress and the effective stress during cyclic loading, as it has been already discussed in Chapter 4.

5.1 Polycrystalline plasticity model

The cyclic behaviour of 316L steels has been well documented in the literature for both the macroscopic mechanical behaviour and the microscopic deformation mechanism. From the viewpoint of microscopic scale, it is characterized by the evolution of tangles, walls, stacking faults, twins and cells [52,53,205,257]. According to Cottrell's stress partitioning method [204], the cyclic stress can be quantitatively separated into effective stress and back stress, which are respectively associated to the short-range and long-range dislocation interactions. The effective stress represents the locally required stress to make dislocations overcome the resistance to dislocation movement, for example forest dislocations, solute

atoms or coherent precipitates. The long-range internal stress is a complex phenomenon resulting from intergranular and intragranular plastic strain incompatibilities. Intragranular long-range internal stress is caused by the mobile dislocations in channels. As for the intergranular long-range internal stress results, firstly from grain boundary region where dislocations are generated in the neighbouring grain, emission from ledges in grain boundaries and passage of dislocations across grain boundary, and secondly from plastic strain incompatibilities between grains in relation to crystallographic orientations [205]. As a kind of microscopic scale model, single crystal plasticity was developed to describe these deformation mechanism in a 'quasi-physical' manner [271].

5.1.1 Single crystal plasticity

At the grain scale, it is assumed that plastic behaviour is due to dislocation slip on crystallographic planes. For FCC polycrystals, 12 octahedral slip systems are considered, based on slip planes {111} and slip directions <100>. The resolved shear stress τ^s for slip system *s* in each grain are determined by the stress in the grain and the Schmid factor tensor m^s:

$$\tau^s = \sigma^g : m^s \tag{5-1}$$

$$m^s = \frac{1}{2}(I^s \otimes n^s + n^s \otimes I^s) \tag{5-2}$$

where, n^s is the vector normal to the slip plane, and I^s is the unit vector in the slip direction.

A viscoplastic framework, as proposed by Méric and Cailletaud [271], is adopted by introducing isotropic hardening variable κ^s and kinematic hardening variable χ^s. The viscoplastic slip rate $\dot{\gamma}^s$ is calculated by the resolved shear stress with the following expression:

$$\dot{\gamma}^s = \langle \frac{|\tau^s - \chi^s| - \kappa^s}{K^s} \rangle^{z^s} \operatorname{sign}(\tau^s - \chi^s) \tag{5-3}$$

where, K^s and n^s are material constants describing the local viscous effect of a material, and they can be obtained from monotonic tensile tests at several loading rates. $\langle\cdot\rangle$ is the Macauley's bracket.

For each slip system, internal variables are introduced to describe the hardening of the material including the isotropic hardening variable κ^s and the kinematic hardening variable χ^s. The non-linear evolution rule for isotropic hardening involves an interaction matrix H_{sr}which represents self-hardening ($s = r$) and latent hardening ($s \neq r$) [227,271]:

$$\kappa^s = \kappa_0 + Q^s \sum_r H_{sr}(1 - \exp(-b^s v^r)) \tag{5-4}$$

where, κ_0 is the initial value of the critical resolved shear stress. $\dot{v}^r = |\dot{\gamma}^r|$. The interaction matrix H_{sr} allows to introduce the cross influence of the slip system r on the hardening of the system s belonging to the same family or not. The quantity $\kappa_0 + Q \sum_r H_{sr}$ is the maximum value that could be reached on a system, for a strain path that would allow all the systems to become active. Under ordinary loadings, this value remains small. In this work, a decomposed form is used to better describe the cyclic hardening/softening behaviour, as expressed in Eq. (5-5).

$$\kappa^s = \kappa_0 + \sum_i \left(Q_i^s \sum_r H_{sr}(1 - \exp(-b_i^s v^r)) \right) \tag{5-5}$$

For the kinematic hardening, non-linear rules are given by employing the macroscopic A-F law with the multi-decomposed forms, as shown in Eq. (5-6) and Eq. (5-7). The decomposition of non-linear hardening variables allows great flexibility to simulate the behaviour of a material [227]:

$$\chi^s = \sum_{i=1} \chi_i^s \tag{5-6}$$

$$\dot{\chi}_i^s = c_i^s \dot{\gamma}^s - d_i^s \chi_i^s \dot{v}^s \tag{5-7}$$

where, c_i^s and d_i^s are material parameters.

In order to describe the isotropic effect through back stress, as has been discussed in Chapter 4, a multiplicative coefficient φ^s is introduced for each slip system, as expressed in Eq. (5-8). The coefficient φ^s corresponding to each slip system is associated to the accumulated shear strain v^s in the given slip system of the crystal.

$$\dot{\chi}^s = \varphi^s(v^s) \cdot \sum_{i=1} \dot{\chi}_i^s \tag{5-8}$$

In fact, a similar form was used by Méric et al. [271], in which the associated coefficient $\varphi^s(v^s)$ is related to the parameter c_i^s in Eq. (5-7). In order to describe the cyclic hardening/softening which is attributed to the back stress (Fig. 4-8), the functional relation Eq. (5-9) is built for each slip system. Similar to Eq. (4-34), the first term in the right hand represents the cyclic hardening, whereas the cyclic softening is characterized by the second

term. Tab. 5-1 lists the corresponding bounded cases of the kinematic hardening coefficient φ^s in each slip system for $\varphi^s = 0$ and $\varphi^s \to +\infty$.

$$\varphi^s = [1 + (\varphi_0^{\mathrm{I}s} - 1) \cdot \exp(-a^s v^s)] \cdot \left[\left(\varphi_0^{\mathrm{II}s} - \varphi_\infty^{\mathrm{II}s}\right) \cdot \exp(-b^s v^s) + \varphi_\infty^{\mathrm{II}s}\right] \tag{5-9}$$

Tab. 5-1. Typical extreme values of kinematic hardening coefficient φ^s.

v^s	$\varphi^{\mathrm{I}s}$	$\varphi^{\mathrm{II}s}$	φ^s
0	$\varphi_0^{\mathrm{I}s}$	$\varphi_0^{\mathrm{II}s}$	$\varphi_0^{\mathrm{I}s} \cdot \varphi_0^{\mathrm{II}s}$
$+\infty$	1	$\varphi_\infty^{\mathrm{II}s}$	$\varphi_\infty^{\mathrm{II}s}$

The granular plastic strain rate can be calculated by all slip systems through a generalized normality rule:

$$\dot{\varepsilon}^{\mathrm{pg}} = \sum_{s=1}^{N_S} \dot{\gamma}^s m^s \tag{5-10}$$

The elastic behaviour of the polycrystal is assumed uniform, isotropic, and compressible. The elastic strain rate at the granular level is defined by the Hook law [91,92,223]:

$$\dot{\varepsilon}^{\mathrm{eg}} = \frac{\dot{\sigma}^{\mathrm{g}}}{2\mu} - \frac{\lambda}{2\mu(2\mu + 3\lambda)} \mathrm{tr}(\dot{\sigma}^{\mathrm{g}}) I \tag{5-11}$$

where I is the second order unit tensor.

According to the hypothesis of small strain, the total granular strain rate can be decomposed as:

$$\dot{\varepsilon}^{\mathrm{g}} = \dot{\varepsilon}^{\mathrm{eg}} + \dot{\varepsilon}^{\mathrm{pg}} \tag{5-12}$$

5.1.2 Transition rule for the polycrystal

An important issue in polycrystalline plasticity is the scale-transition law (or interaction law) from a single grain to the macroscopic polycrystalline aggregate. A powerful approach for realizing the scale transition of polycrystals is the self-consistent method. The self-consistent method describes the overall response of a polycrystal by taking into account the mechanical properties of a single grain and the interaction of each grain with its surroundings.

During the last decades, a series of self-consistent rules have been developed to describe the mechanical behaviour of polycrystals, for example by Krôner [88] and Hill [219], as has been discussed in Section 1.3.4.2. Berveiller and Zaoui [89] proposed an

explicit transition rule in 1978 by taking into account elasto-plastic accommodation through a scalar 'accommodation function'. This explicit rule was further developed by Cailletaud and Pilvin [221,222] through adding a term in the transition rule which can be used to take into account the intergranular kinematic hardening:

$$\sigma^g = \Sigma + C^g \left\{ \sum_{h=1}^{N_g} f^h \beta^h - \beta^g \right\} \tag{5-13}$$

with

$$\dot{\beta}^g = \dot{\varepsilon}^{pg} - a^g \beta^g \sum_{s=1}^{N_s} \dot{\gamma}^s \tag{5-14}$$

where, C^g is the intergranular kinematic hardening modulus; the coefficient a^g describes the nonlinearity of this hardening; f^h is the volume fraction of the grains with a same orientation.

The Cailletaud's model (Eq. (5-13)) has been widely used to describe the cyclic behaviour of polycrystals. This model is able to represent the intergranular kinematic hardening through the term β^g, whereas the intragranular kinematic hardening is considered in each slip system through the single crystal plasticity model (Eq. (5-3)).

In addition, Abdul-Latif et al. [90,223] proposed a new elasto-inelastic interaction rule, with a simplified expression as follows:

$$2A\left(\dot{\sigma}^g - \dot{\Sigma}\right) + Btr\left(\dot{\sigma}^g - \dot{\Sigma}\right)I - \alpha(S^g - S) = \left(\dot{\varepsilon}^g - \dot{E}\right) \tag{5-15}$$

where, $\dot{\sigma}^g$ and $\dot{\Sigma}$ are respectively the granular and macroscopic Cauchy stress rate tensors. S^g and S are the corresponding deviatoric parts of the stress tensors. $\dot{\varepsilon}^g$ and $\dot{E}$ are the granular and macroscopic strain tensors, respectively. α is a new phenomenological parameter which is independent of the deformation history, and it has a great influence on the hardening evolution and consequently on the stress-strain behaviour of polycrystals [91,223]. The constants A and B can be directly determined by the two Lamé parameters μ and λ:

$$A = \frac{-(8\mu + 3\lambda)}{2\mu(14\mu + 9\lambda)} \tag{5-16}$$

$$B = \frac{(6\mu + \lambda)(8\mu + 3\lambda)}{\mu(448\mu^2 + 456\mu\lambda + 108\lambda^2)} \tag{5-17}$$

The second interaction law presented in Eq. (5-15) has also been successfully used to describe the tensile and cyclic behaviour of polycrystalline materials [91,223]. A detailed comparison between the two self-consistent models mentioned above has been performed to predict the elasto-inelastic cyclic behaviour under uni, bi and triaxial cyclic loading conditions [92]. Results show that the two models lead to a similar slip distribution for the same aggregate and loading conditions [92]. In this work, the second interaction law (Eq. (5-15)) will be used because of its few internal variables and material constants.

5.1.3 Homogenization method

After determining the granular plastic strain rate as the sum of contribution from all the activated slip systems, the transition from single crystal to polycrystal is realized by the averaging procedures. The macroscopic elastic strain and plastic strain rates are respectively calculated as follows [92]:

$$\dot{E}^{\mathrm{e}} = \sum_{g=1}^{N_g} f^g \dot{\varepsilon}^{\mathrm{e}g} \tag{5-18}$$

$$\dot{E}^{\mathrm{p}} = \sum_{g=1}^{N_g} f^g \dot{\varepsilon}^{\mathrm{p}g} \tag{5-19}$$

where, f^g represents the volume fraction of the grains with a same orientation.

The overall total strain rate can then be expressed as follows:

$$\dot{E} = \dot{E}^{\mathrm{e}} + \dot{E}^{\mathrm{p}} \tag{5-20}$$

5.2 Numerical implementation and cycle jump method

In this work, the interaction law presented by Eq. (5-15) is used to model the cyclic behaviour of the studied 316L steel. It would be difficult to implement the self-consistent model for cyclic loading simulation. On the one hand, both the interaction rule and the single crystal plasticity model are given with the implicit forms, and solving these equations should be synchronously performed through explicit or implicit iterative approaches. On the other hand, solving the self-consistent model should be a very time-consuming process when the polycrystal has a large number of grains and the material is loaded with a considerable number of cycles.

5.2.1 Numerical implementation

In general, the interaction law for polycrystalline materials is implemented through explicit iteration coupled with the Runge-Kutta method. In order to obtain a higher computational accuracy, implicit iteration approach is employed in this work to solve the interaction law (Eq. (5-15)) and the single crystal plasticity model. Furthermore, stress-controlled loading procedure is used to implement the self-consistent model to simulate the uniaxial cyclic loading with a given strain rate ($\dot{\varepsilon} = 4 \times 10^{-3}$ s $^{-1}$). A detailed implementation procedure is illustrated in Fig. 5-1.

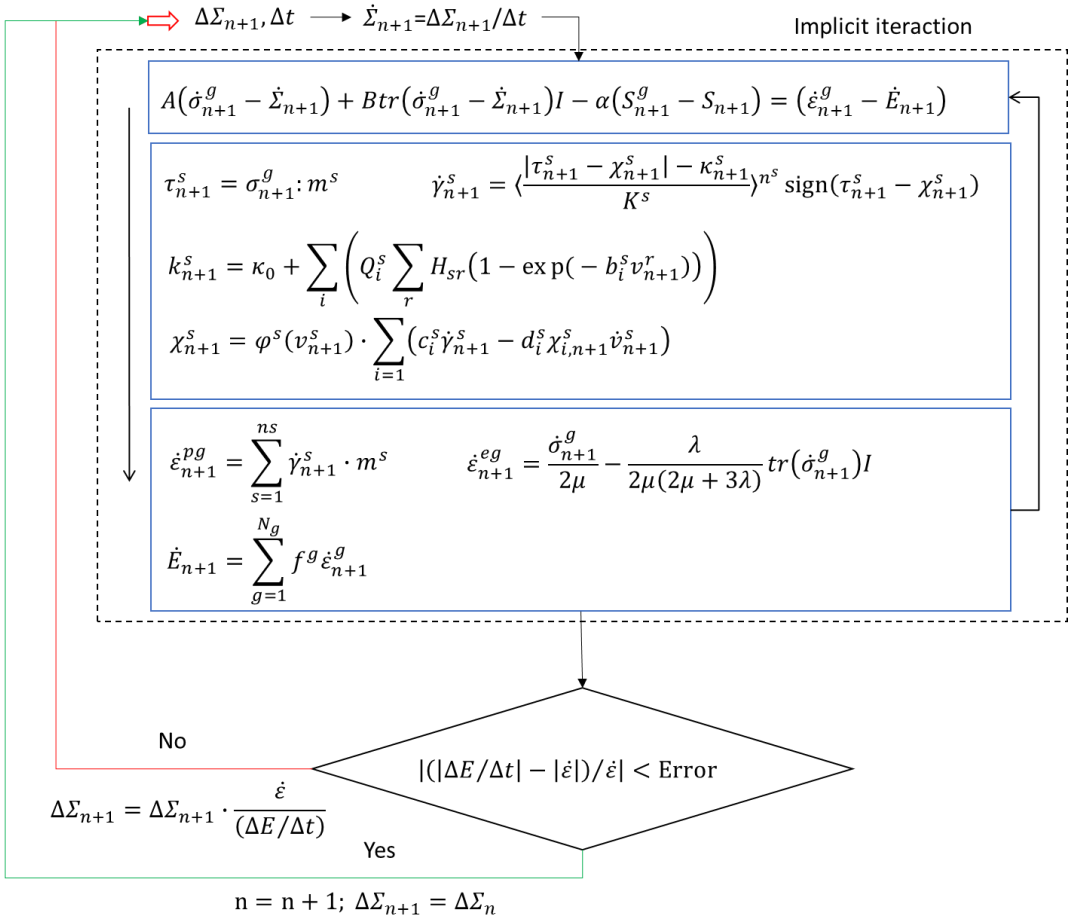

Fig. 5-1. Stress-controlled loading procedure for the self-consistent model.

5.2.2 Cycle jump approach

As indicated above, simulating the cyclic behaviour of a polycrystal with many grains could be a time-consuming process, especially for a fatigue test with a large number of cycles before fracture. Therefore, a cycle jump method can be used to optimize the computational time. In the framework which combines crystal plasticity model and self-consistent law, the cycle jump method can be implemented by tracking the evolution of different internal variables in each loading cycle.

During cyclic loading, each state variables $Y_N \in \{\underline{\sigma}, \chi_i^s, v^s, p, \cdots\}_N$ can be decomposed through Taylor expansion:

$$Y_{N+\Delta N} = Y_N + \dot{Y}_N \cdot \Delta N + \ddot{Y}_N \cdot \frac{\Delta N^2}{2} + \cdots \tag{5-21}$$

where ΔN is the jumping cycles. $\dot{Y}_N$ and $\ddot{Y}_N$ are the first and second "pseudo-derivate" of the variables Y_N in the space of cycles N that can be calculated by a finite difference scheme with the number of successive calculated cycles Δn before the cycle N:

$$\dot{Y}_N = \frac{Y_N - Y_{N-\Delta n}}{\Delta n} \tag{5-22}$$

$$\ddot{Y}_N = \frac{\dot{Y}_N - \dot{Y}_{N-\Delta n}}{\Delta n} \tag{5-23}$$

In this work, the first order approximation of Taylor expansion in Eq. (5-21) is used, and the evolution of state variables during one cycle can be determined from the full numerical simulation of the last cycle:

$$\Delta Y_N = Y_N\big(t = t_{cyc}\big) - Y_N(t = t_0) \tag{5-24}$$

where $t = t_0$ and $t = t_{cyc}$ represent the beginning and the end of the cyclic loading. The long-term scale extrapolation of these variables is linear and the new values of the internal variables after ΔN cycles are given by:

$$\Delta Y_{N+\Delta N+1}(t = 0) = Y_N\big(t = t_{cyc}\big) + \Delta Y_N \cdot \Delta N \tag{5-25}$$

This linear extrapolation approach has been used within the cyclic loading simulation of some previous studies [213]. However, this method could induce instabilities and divergence of the final results when the value of $\Delta Y_{N+1} - \Delta Y_N$ and the jump cycle ΔN are too large. In our case, the state variables extrapolated after each cycle jump by means of Eq. (5-21) do not fulfil a-priori the constitutive equation and thus will lead to an error in the subsequent cycle. The error will be accumulated in each jump. This error can be reduced if the full numerical simulation of the cyclic behaviour is extended for two or more cycles after each jump and the values of ΔY_N for the next cycle jump are extracted from the last cycle simulated at the small time scale. In addition, the cycle jump should be prohibited when the evolution of state variables ΔY_N exceed a given critical value.

5.3 Parameter identification

5.3.1 Basic material parameters

For a polycrystal, plastic flow usually occurs due to slip along certain planes and in certain directions. The studied steel has a typical face-centred cubic (FCC) structure, and the planes of family {111} are the most favourable planes for slipping to take place because they are the most closely packed planes. Therefore, 12 slip systems ({111} <110>) of a FCC structure are considered in the single crystal plasticity model.

For simplicity, we assume that all the grains and the crystallographic slip systems have the same properties. Accordingly, all the grains have the same Lamé parameters μ and λ, and all the slip systems have the same material parameters in the single crystal plasticity model (Section 5.1.1). It should be noted that the interaction matrix H_{sr}, which represents the self-hardening effect of a slip system and latent-hardening effect between different slip systems, is a 12×12 symmetric matrix with 6 independent constants. In this work, the values of the six constants are taken from the previous studies on cyclic behaviour of a 316L steel [228], as listed in Tab. 5-2 and indicated in Fig. 5-2. K^s and z^s in Eq. (5-3) characterize the viscous sensitivity of plastic flow of the material. Viscoplastic flow reaches a rate-independent limit for large values of the parameters z^s and $1/K^s$ [227]. In this work, time-independent plasticity is assumed, and $K^s = 10$ and $z^s = 10$ are used according to the previous study [228].

Tab. 5-2. Values of six independent constants in the interaction matrix H_{sr}.

h_1	h_2	h_3	h_4	h_5	h_6
1	1	0.438	77.2	4.31	2.41

	0	1	2	3	4	5	6	7	8	9	10	11
0	h1	h2	h2	h4	h5	h5	h5	h6	h3	h5	h3	h6
1		h1	h2	h5	h3	h6	h4	h5	h5	h5	h5	h3
2			h1	h5	h6	h3	h5	h3	h6	h4	h5	h5
3				h1	h2	h2	h6	h5	h3	h6	h3	h5
4					h1	h2	h3	h5	h5	h5	h5	h4
5						h1	h5	h4	h5	h3	h6	h5
6							h1	h2	h2	h6	h5	h3
7								h1	h2	h3	h5	h6
8									h1	h5	h4	h5
9										h1	h2	h2
10											h1	h2
11												h1

Fig. 5-2. Interaction matrix H_{sr} for different slip systems of FCC crystals.

For the elastic modulus and Possion ratio of the steel, they are determined according to the experimental analysis which is performed in Chapter 4 ($E = 196.5$GPa and $\nu = 0.3$). Accordingly, the two Lamé parameters in Eq. (5-16) and Eq. (5-17) can be calculated and the values are as follows: $\lambda = 113365.4$ and $\mu = 75.58$ GPa.

The hardening parameter α in the transition rule Eq. (5-15) is independent of deformation history [91]. It could have a great influence on the hardening behaviour and consequently on the stress-strain behaviour of polycrystals. The determination of the parameter α has been studied in the reference [223]. In our work, we take 5×10^{-7} as the value of the parameter α according to the previous study on self-consistent modelling of cyclic behaviour of a 316L steel [91].

Besides, other material parameters in the single crystal plasticity model ($\kappa_0, Q_i^s, b_i^s, c_i^s, d_i^s, \varphi_0^{\mathrm{I}s}, a^s, \varphi_0^{\mathrm{II}s}, b^s, \varphi_\infty^{\mathrm{II}s}$) should be identified based on the cyclic behaviour of the studied material.

5.3.2 Grain number

The microstructure of an aggregate is characterized by the grain orientations, which can be determined by the three Euler angles with respect to the global coordinate system. An aggregate containing a large number of grains with random orientations presents macroscopically isotropic properties. The influence of the grain number ranging from 40 grains to about 2000 grains on the macroscopic response of an aggregate has been investigated in previous studies [90,91,272]. It was shown that an aggregate with 2016 grains with random orientations fulfills almost perfect initial isotropic elastic behaviour [272]. In this work, we focus on the development of the modelling approach, and thus an aggregate with 50 grains is preliminarily considered to reduce the computational cost in the simulations of cyclic loading. The orientations of the grains are randomly generated with three Euler angles φ_1, φ and φ_2 ($0 \le \varphi_1 \le 2\pi$, $0 \le \varphi \le 2\pi, 0 \le \varphi_2 \le 2\pi$). Fig. 5-3 illustrates the pole figures of $\{001\}$, $\{011\}$ and $\{111\}$ of the generated aggregate. It is shown that no texture can be observed. The Euler angles for each grain are listed in Appendix-B.

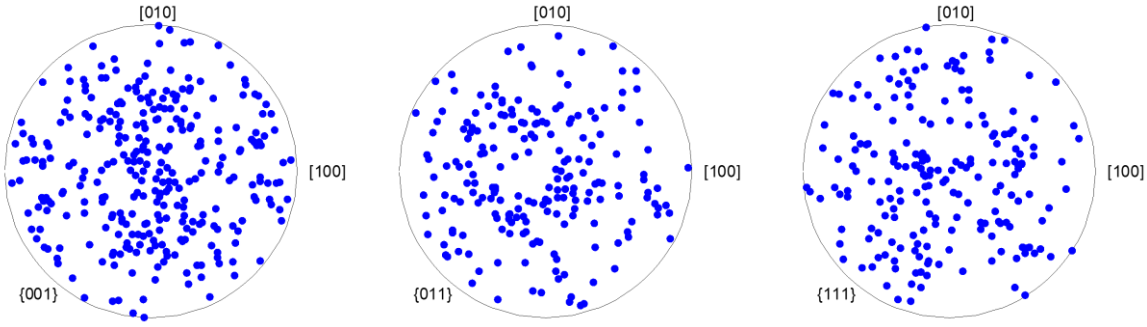

Fig. 5-3. Pole figures of the aggregate with randomly generated grains for the homogenization model.

5.3.3 Cyclic hardening/softening behaviour

The cyclic behaviour of a material can be very complex, due to the presence of different phenomena such as strain range memory effect, ratcheting, creep. For simplicity, the strain range memory effect will not be taken into account for self-consistent modelling work presented in this chapter, and only the cyclic behaviour of the 316-A steel presented in Chapter 4 under strain amplitude of ±1.25% is considered.

5.3.3.1 Cyclic modelling based on the macroscopic continuum plasticity

It has been indicated in Chapter 4 that the cyclic hardening/softening of the studied 316L-A steel is mainly attributed to the back stress. It is thus impossible to directly identify the material parameters which are respectively related to the cyclic hardening/softening and the plastic flow behaviour in each loading cycle, as has been discussed in 4.3.4.2. The identification can be performed with the help of the macroscopic model presented in Chapter 4. Given that the strain range effect is not considered in the constitutive model, Eq. (4-37) will not be considered in this chapter. The simplified form Eq. (5-26) is used to describe the cyclic hardening/softening which is attributed to the back stress under strain amplitude of ±1.25%. The identified parameters are listed in Tab. 5-3, and a comparison between the experimental and the simulated cyclic behaviour are illustrated in Fig. 5-4 and Fig. 5-5.

$$\varphi = (1 + (\varphi_0^{\mathrm{I}} - 1)\exp(-ap)) \cdot (\varphi_0^{\mathrm{II}} \cdot \exp(-bp) + \varphi_\infty^{\mathrm{II}}) \tag{5-26}$$

Tab. 5-3. Material parameters for the macroscopic model under strain amplitude of ±1.25%.

Basic elastic constants:
E=196.5 GPa; $v = 0.3$; k =98.8821 MPa;
Isotropic hardening variables:
$Q_1 = 75.1337$ MPa, $b_1 = 139.39$; $Q_2 = -30.7258$ MPa, $b_2 = 3.0912$;
Kinematic hardening variables:

$C_1 = 368784.48$ MPa, $\gamma_1 = 3181.48$; $C_2 = 66483.71$ MPa, $\gamma_2 = 558.47$; $C_3 = 15844.43$ MPa, $\gamma_3 = 114.71$.
Kinematic hardening coefficient:
$\varphi_0^{\mathrm{I}} = 0.7827$, $a = 8.4824$, $\varphi_0^{\mathrm{II}} = 0.0547$, $b = 1.0713$, $\varphi_\infty^{\mathrm{II}} = 1.0991$

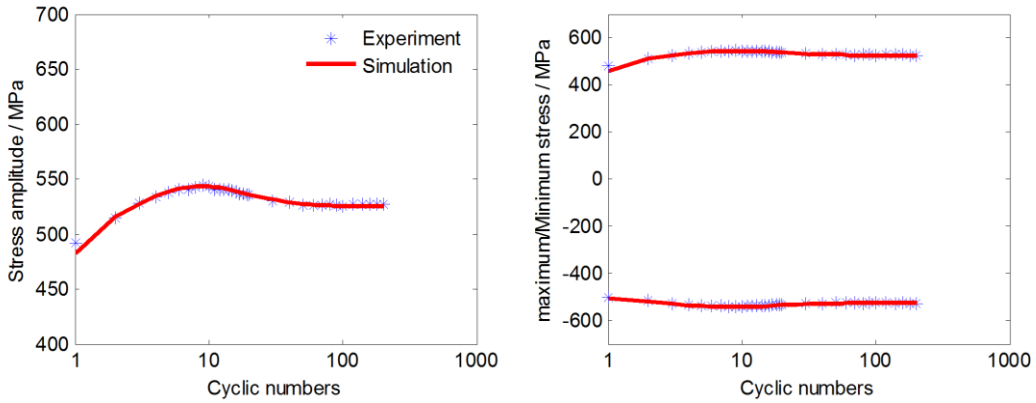

Fig. 5-4. Comparison of stress amplitude evolution curves between experiment and simulation for strain amplitude of 1.25% (316L-A).

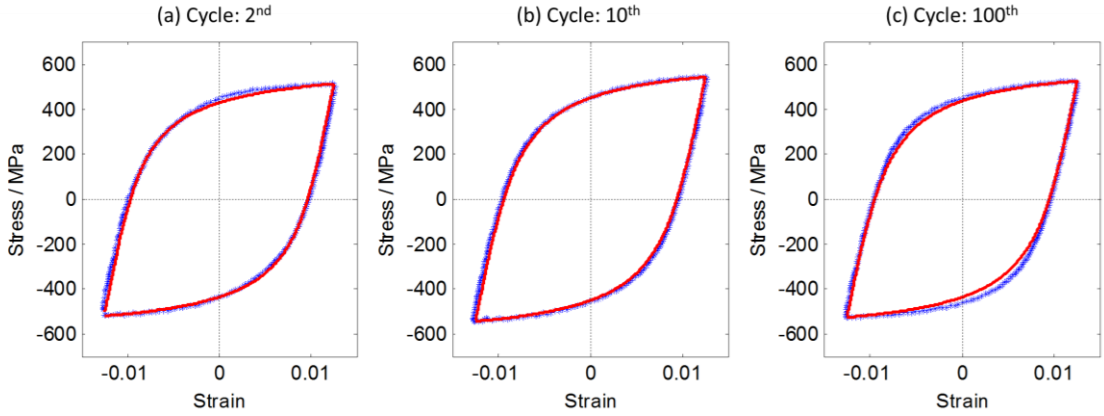

Fig. 5-5. Comparison of cycles between simulation (red) and experiment (blue) under strain amplitude of ±1.25%. The corresponding cycle number is also indicated in each figure.

5.3.3.2 Material parameters corresponding to slip systems

In this work, both the back stress and the effective stress of the macroscopic cyclic behaviour are characterized in the slip systems, respectively through the kinematic hardening term χ^s and the critical shear stress κ^s, with the expressions presented in Section 5.1.1. Due to the complexity of cyclic behaviour, it would be sophisticated to identify all the parameters directly from the experimental results or from the simulated cyclic behaviour using the macroscopic model. In this work, a new identification procedure is proposed for the material parameters at the slip system scale based on the macroscopic plasticity model presented in Section 5.3.3.1, as indicated in Fig. 5-6.

In the first step, the initial critical resolved shear stress κ_0 is identified based on the initial yield stress k (Tab. 5-3) of the macroscopic plasticity model. The value of κ_0 determines the stress at which plastic flow begins during initial tensile loading, and it should thus be independent on the number of grains.

In the second step, the parameters c_i^s, d_i^s in Eq. (5-7) can be identified by fitting the initial tension and the first hysteresis loop which are calculated using the macroscopic plasticity model presented in Section 5.3.3.1, and the condition $\varphi = 1$, $Q_i = 0$, $b_i = 0$ as well as the obtained value of κ_0.

Afterwards, the parameters $\varphi_0^{Is}, a^s, \varphi_0^{IIs}, b^s$ and φ_∞^{IIs} are calibrated by fitting the stress amplitude evolution curves obtained based on the macroscopic plasticity model, and with the condition $Q_i = 0$, $b_i = 0$ as well as the obtained value of κ_0, c_i^s and d_i^s.

In the last step, the parameters Q_i^s and b_i^s are determined by calibrating the stress amplitude evolution curves calculated using the macroscopic plasticity model, and with all the values of the parameters listed in Tab. 5-3 and the obtained value of κ_0, c_i^s, d_i^s, $\varphi_0^{Is}, a^s, \varphi_0^{IIs}, b^s$ and φ_∞^{IIs}.

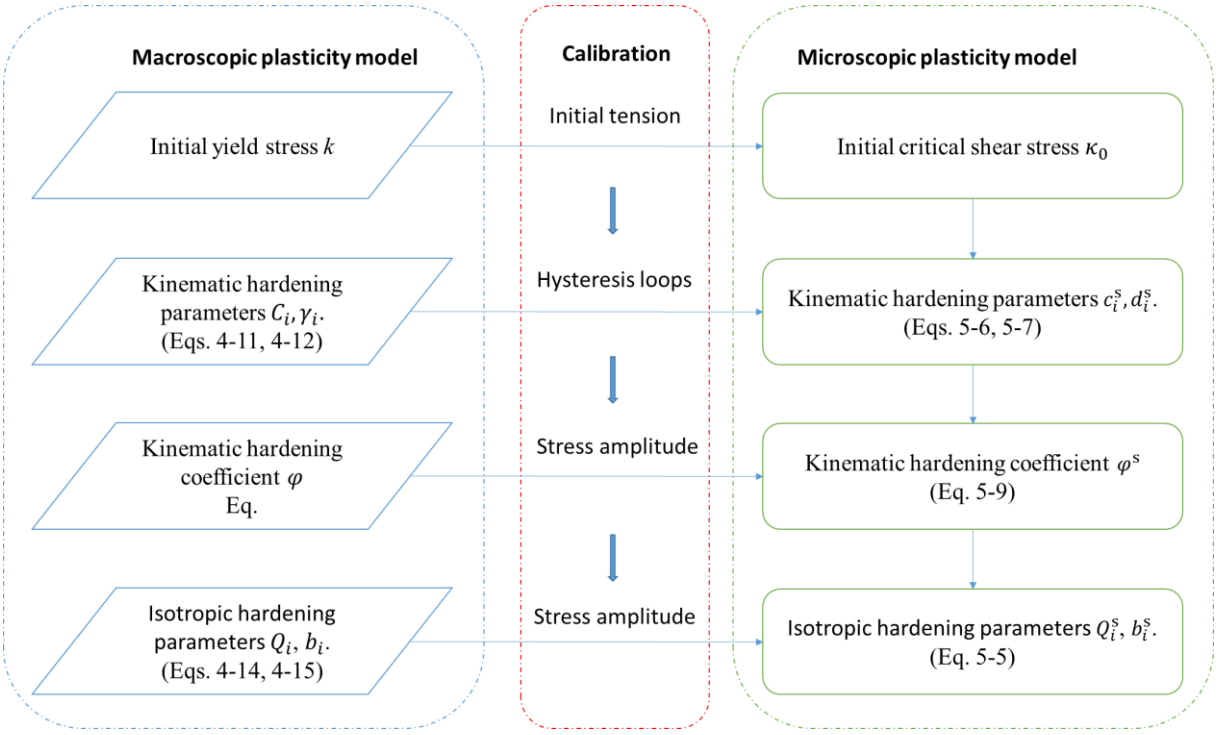

Fig. 5-6. Identification procedure for the parameters involved in the self-consistent model.

5.4 Results and discussion

5.4.1 Results of identification

All the material parameters of the developed single crystal plasticity model can be identified with the procedures presented in Fig. 5-6. Tab. 5-4 lists one group of the identified values.

Tab. 5-4. Material parameters of the developed cyclic constitutive model identified for the steel 316L-A.

Basic elastic constants:
E=196.5 GPa; $\nu = 0.3$; κ_0 =46.02 MPa;
Parameter in the transition rule:
$\alpha = 5 \times 10^{-7}$
Viscous parameters:
$K^s = 10; z^s = 10$
Kinematic hardening variables:
$c_1^s = 146277, d_1^s = 6840.71;\ c_2^s = 2038.02$ MPa, $d_2^s = 180.01;$
Kinematic hardening coefficient:
$\varphi_0^{\mathrm{I}s} = 0.677, a^s = 10.8;\ \varphi_0^{\mathrm{II}s} = 1.25, b^s = 1.45;\ \varphi_\infty^{\mathrm{II}s} = 1.13$
Isotropic hardening variables:
$Q_1^s = 1.116, b_1^s = 815;\ Q_2^s = -0.921, b_2^s = 164;$

Fig. 5-7 gives a comparison of the simulated variations of stress amplitude (Fig. 5-7a) and maximum/minimum stress (Fig. 5-7b) with the number of cycles between the macroscopic plasticity model and the self-consistent model. The biggest difference between the two curves in Fig. 5-7a is less than 5 MPa. This signifies that the developed self-consistent model can well describe the cyclic hardening/softening behaviour of the material.

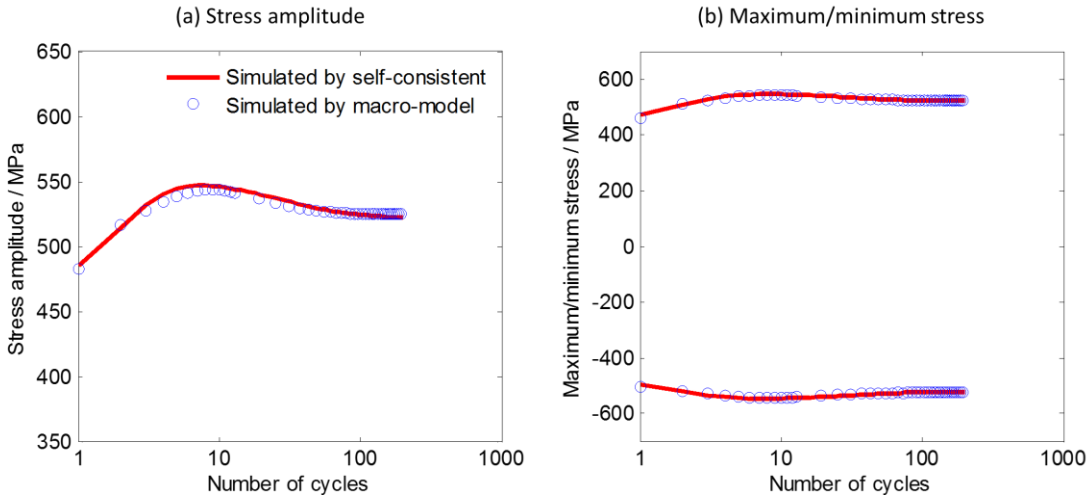

Fig. 5-7. Comparison of (a) stress amplitudes and (b) maximum/minimum stresses between the simulated results through self-consistent model and macroscopic model under strain amplitude of 1.25%.

In Fig. 5-8, a comparison of the first two hysteresis loops (Fig. 5-8a), as well as 10th (Fig. 5-8b) and 180th hysteresis loops (Fig. 5-8c) between the simulated results through the macroscopic plasticity model and through the self-consistent model is illustrated. It can be seen that the developed self-consistent model can well describe the cyclic behaviour of the studied 316L steel throughout the cyclic loading under strain amplitude of ±1.25%.

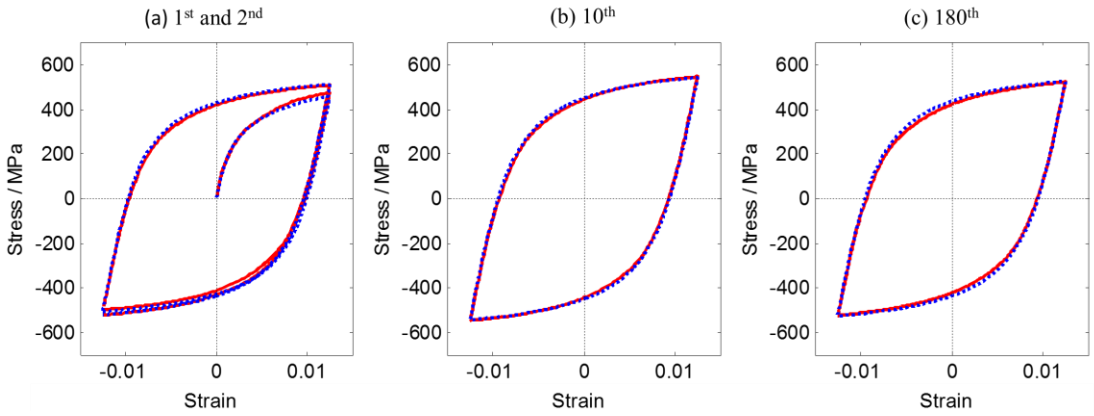

Fig. 5-8. Comparison of the hysteresis loops: (a) 1st and 2nd, (b) 10th, (c) 180th, between the simulated results through the self-consistent model (red curves) and the macroscopic model (blue curves) under strain amplitude of 1.25%.

5.4.2 Grain discretization effect

As mentioned above, 50 grains are considered for the aggregate with randomly generated orientations to identify material parameters at the scale of slip system. However, as the number of grains plays an important role in the isotropic properties of polycrystals, a large number of grains should be taken into account for an aggregate. In order to evaluate the influence of number of grains, a series of tension simulations is performed with different numbers of grains. Ten different aggregates with randomly generated orientations are simulated for the same grain amounts. The stress-strain curves corresponding to the aggregates with 20, 50, 100, and 400 grains are plotted in Fig. 5-9. The stress-strain curves have smaller range of dispersion when the number of grains increases. An aggregate with more than 400 grains should be considered for the polycrystalline material, and the material parameters can be further optimized based on the values shown in Tab. 5-4.

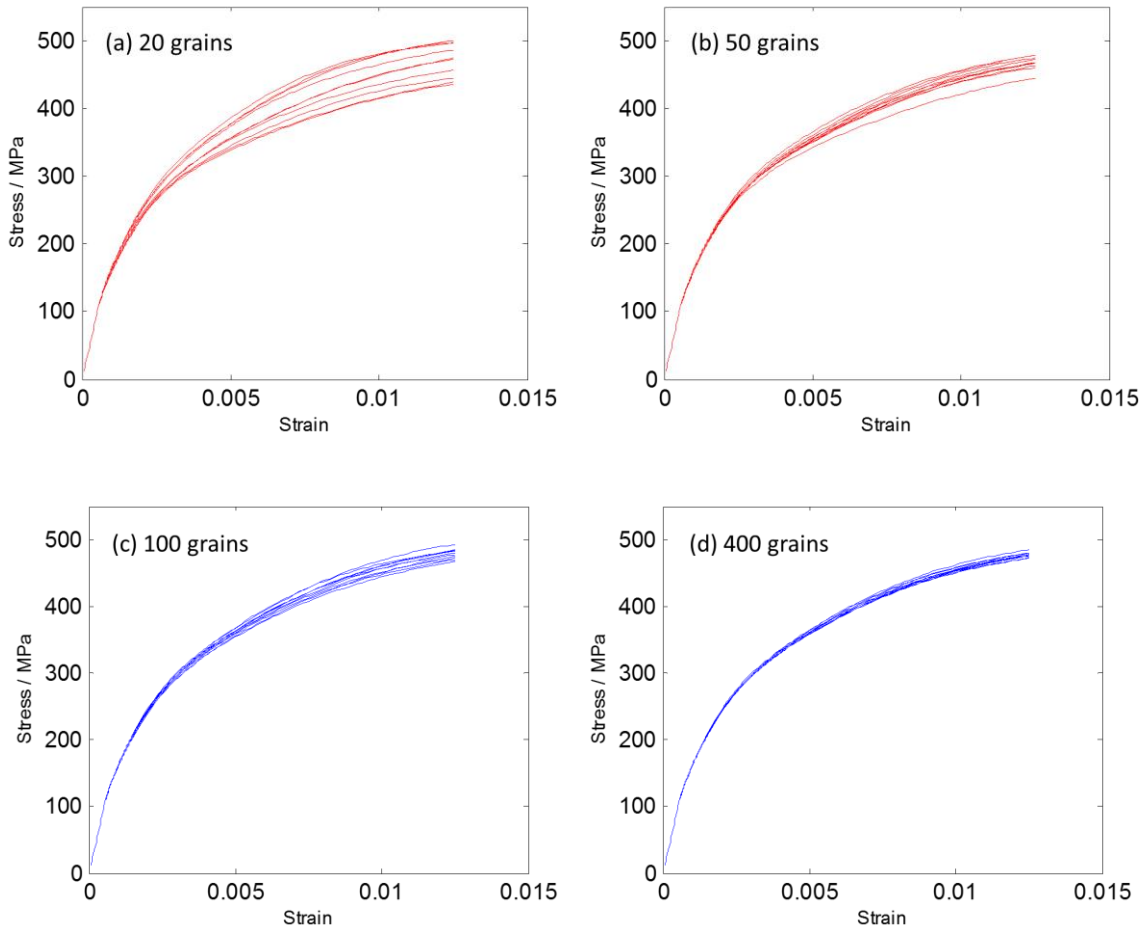

Fig. 5-9. Comparison of monotonic tensile curves between the aggregates with different numbers of grains along with different randomly generated orientations for: (a) 20 grains, (b) 50 grains, (c) 100 grains and (d) 400 grains.

5.4.3 Strain rate effect

As indicated in Chapter 4, 316L steels present rate-dependent characters at room temperature [255,256]. However, this phenomenon is not considered in this work. Even though a viscous constitutive law is used in the single crystal plasticity model (Section 5.1.1) to describe the plastic slip in each slip system, as indicated in Eq. (5-3), the rate-dependent effect is not considered in this work by using a large values for the parameters z^s and $1/K^s$. In order to evaluate the strain rate effect for the self-consistent model, a series of tension simulation is performed under different strain rates using the identified parameters shown in Tab. 5-4 and the aggregate which has been employed for the identification under a strain rate of 4×10^{-3} s^{-1} in Section 5.3.1. Fig. 5-10 illustrates the comparison of the simulated tensile curves under strain rates ranging from 4×10^{-3} s^{-1} to 1 s^{-1}. It can be seen that the strain rate has a small effect on the stress during tension loading.

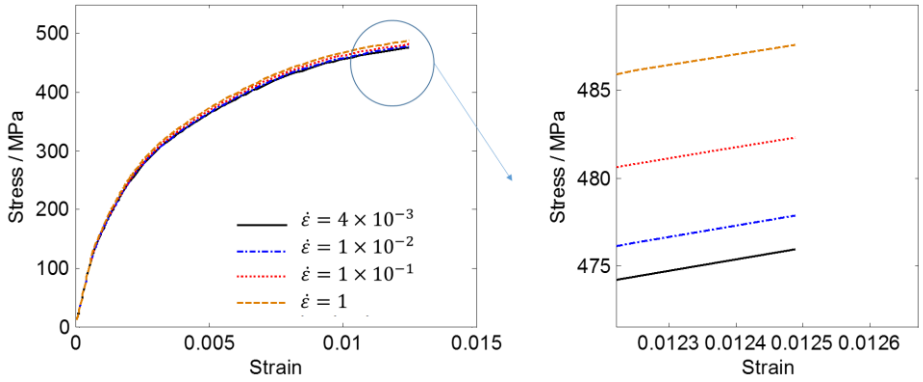

Fig. 5-10. Comparison of the tensile curves simulated using the self-consistent model with different strain rates.

5.5 Conclusion

In this chapter, a single crystal plasticity model is adapted and coupled with the self-consistent method to model the cyclic hardening/softening behaviour of the studied 316L steel. A non-linear kinematic hardening rule is proposed at the slip system scale to describe the cyclic hardening/softening behaviour induced by the back stress. An elastic-inelastic self-consistent model proposed by Abdullatif et al. [91,223] for polycrystals is employed as the transition rule from the scale of single grains to the scale of aggregate. Implicit iteration and cycle jump method are used to numerically implement the self-consistent model and simulate the cyclic loading. In order to describe the cyclic hardening/softening behaviour which is respectively related to the back stress and the isotropic hardening, an identification procedure is proposed to determine all the material parameters at the slip system scale with the help of the macroscopic plasticity model.

In this work, 50 grains are considered for the aggregate with randomly generated orientations. All the material parameters at the slip system scale are identified based on the macroscopic plasticity model under strain amplitude of ±1.25%. Comparison between the modelling results through the self-consistent model and through the macroscopic plasticity model shows that the developed self-consistent model is able to well describe the cyclic hardening/softening behaviour of the studied material. The single crystal plasticity model, the self-consistent method, and the identification procedure developed in this chapter is useful for the following multi-scale modelling of the LCF behaviour of the SMATed material.

Chapter 6: Multi-scale modelling of LCF behaviour of SMATed materials

LCF properties of the two 316L steels processed by SMAT are experimentally studied in Chapter 2 and Chapter 3. In Chapter 4, the observed cyclic behaviour is described with constitutive modelling using the macroscopic continuum plasticity theory. Afterwards, qusi-physically based cyclic constitutive modelling using single crystal plasticity model and self-consistent method is presented in Chapter 5 to describe the cyclic hardening/softening of the studied 316L steel. In this chapter, multi-scale modelling of LCF behaviour of the SMATed material will be performed based on the analysis given in precedent chapters. This chapter aims to propose and implement a methodology to model the residual stress as well as the work hardening, and to study their effects on LCF behaviour of materials. Firstly, the modelling method of residual stress and work hardening will be presented and discussed. Secondly, the reconstruction of residual stress and work hardening for a SMATed structure is performed based on the experimental evaluation and analysis of deformation history. Then, cyclic loading simulation of the SMATed structure is realized to study the effects of residual stress and work hardening on the mechanical behaviour of materials from both the macroscopic and the microscopic scales.

6.1 Basic theories and analysis

6.1.1.1 Plastic flow during shot peening

Shot peening is a complex process with the involvement of repetitive impacts by high speed media. When a hard shot hits a structure with high kinetic energy, it can create a small dimple at the surface of the material. During this process, the surface is indented under a tensile stress and simultaneously an opposite compressive stress can be induced beneath the dimple. If the magnitude of the generated stresses reaches the yield strength of the material, a residual compressive stress will remain due to inhomogeneous springback and plastic

deformation. After a great number of impacts, a stable compressive residual stress field can be produced in the near surface region, and simultaneously a tensile stress field will be generated in the interior region to ensure the stress self-equilibrium of the structure [12]. Under the effect of repeated impacts, it can be considered that the material in the plastically affected region undergoes intricate cyclic plastic deformation during the peening process. Based on the constitutive framework described above, the material should experience reciprocating evolutions of yield surface during the repetitive plastic flow because of the impacting and the unloading processes.

Fig. 6-1 schematically illustrates an impact process and qualitatively describes the associated evolution of the yield surface of a material point. The material point is first deformed under an external force during the impacting by a shot. The unloaded state of the material point corresponds to a residual state in which the external force is released when the shot leaves the surface, as shown in Fig. 6-1a. Fig. 6-1b and Fig. 6-1c describe the evolution of the yield surface of the material point induced by two successive shot impacts. The black circle represents the initial yield surface without any initial stress and hardening, while the red and the blue circles respectively represent the yield surfaces in the impacted and unloaded states, with the associated variables denoted by the superscripts 'im' and 'rs'. In addition, '(i)' signifies the i^{th} impact and the i^{th} unload. Fig. 6-1b shows that after the $(n-1)^{\mathrm{th}}$ impact, the initial yield surface is changed to a new state (red circle), coupled with new kinematic hardening $\underline{X}^{\mathrm{im}(n-1)}$ and isotropic hardening $R^{\mathrm{im}(n-1)}$. When the shot leaves the surface, inhomogeneous spring back of the structure impels the stress state changed to $\underline{\sigma}^{\mathrm{rs}(n-1)}$, involving the evolution of the yield surface to a new state. The new yield surface obtained after the $(n-1)^{\mathrm{th}}$ impact is characterized by a new centre position described by $\underline{X}^{\mathrm{rs}(n-1)}$ and a new size represented by $(R^{\mathrm{rs}(n-1)}+k)$, as illustrated in Fig. 6-1b. Subsequently, as indicated in Fig. 6-1c, the material is loaded by the next impact (n^{th}), and a new yield surface is obtained, coupled with the new centre position $\underline{X}^{\mathrm{im}(n)*}$ and the new size $(R^{\mathrm{im}(n)}+k)$. After the external force is removed, a new yield surface is obtained, and the residual stress ($\underline{\sigma}^{\mathrm{rs}(n)}$) and the residual hardening variables ($\underline{X}^{\mathrm{rs}(n)}$ and $R^{\mathrm{rs}(n)}$) are generated. Through the analysis given above, it can be concluded that both the residual kinematic hardening ($\underline{X}^{\mathrm{rs}(n)}$) and the residual isotropic hardening ($R^{\mathrm{rs}(n)}$) are strongly dependent on the deformation history of material during shot peening.

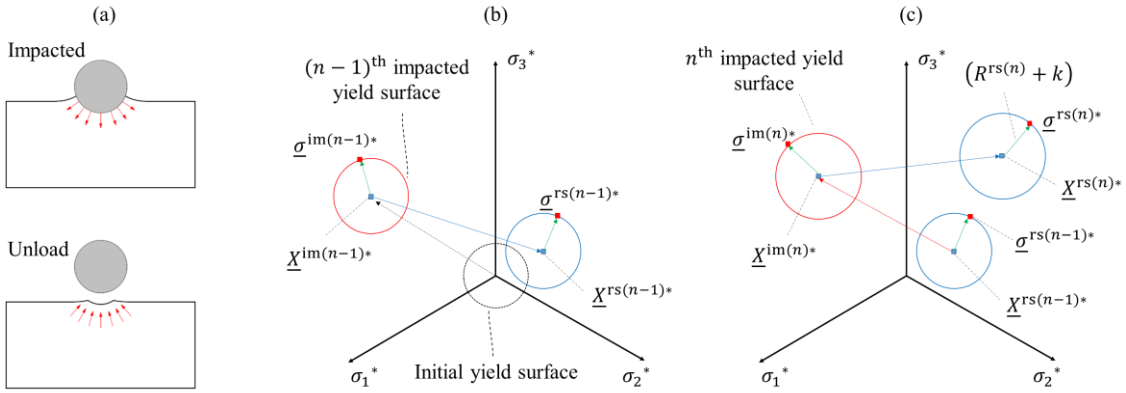

Fig. 6-1. Schematic presentation of (a) impacted and unloaded states, and (b) the yield surface evolution during $(n)^{\text{th}}$ impacting-unloading in the deviatoric stress space.

6.1.1.2 Elastic-plastic equilibrium

Section 6.1.1.1 discussed the typical evolutions of yield surface of a plastically affected material element during repetitive impact process. In fact, the real plastic flow of material is rather sophisticated due to the complex stress field during impacting. Nevertheless, according to the consistency condition, the stress state should always be located on/inside the yield surface. As indicated above, a stable residual stress field can be generated inside the structure after shot peening, which is always associated with a work hardening field. The total residual strain $\underline{\varepsilon}^{\text{rs}}$ for a material element can be decomposed into the reversible and irreversible parts, respectively described by the residual elastic strain $\underline{\varepsilon}^{\text{rsE}}$ and the residual inelastic strain (permanent strain, or plastic strain) $\underline{\varepsilon}^{\text{rsP}}$:

$$\underline{\varepsilon}^{\text{rs}} = \underline{\varepsilon}^{\text{rsE}} + \underline{\varepsilon}^{\text{rsP}} \tag{6-1}$$

Simultaneously, accumulated plastic strain p^{rs} can be generated through the repetitive impact-unload processes, and it is calculated with Eq. (6-2):

$$p^{\text{rs}} = \int \sqrt{2/3\,\dot{\underline{\varepsilon}}^{\text{p}} : \dot{\underline{\varepsilon}}^{\text{p}}}\,\mathrm{d}_t \tag{6-2}$$

According to the Hooke's law, the residual stress tensor $\underline{\sigma}^{\text{rs}}$ is linearly proportional to the residual elastic strain $\underline{\varepsilon}^{\text{rsE}}$:

$$\underline{\sigma}^{\text{rs}} = \underline{\underline{C}} : \underline{\varepsilon}^{\text{rsE}} = \underline{\underline{C}} : \left(\underline{\varepsilon}^{\text{rs}} - \underline{\varepsilon}^{\text{rsP}}\right) \tag{6-3}$$

In addition, the hardening behaviours of the material are associated to the residual plastic strain $\underline{\varepsilon}^{\text{rsP}}$ and the accumulated plastic strain p^{rs} [83], as described by the two functions expressed in Eq. (6-4).

$$\begin{cases} \underline{X}^{\mathrm{rs}} = \mathrm{G}_{\underline{X}}\left(\underline{\varepsilon}^{\mathrm{rsP}}, p^{\mathrm{rs}}\right) \\ R^{\mathrm{rs}} = \mathrm{G}_{R}\left(p^{\mathrm{rs}}\right) \end{cases} \tag{6-4}$$

It is well documented that the residual stress tensor $\underline{\sigma}^{\mathrm{rs}}$ can be measured with various techniques, for example destructive or non-destructive methods [9,113]. However, the hardening variables, $\underline{X}^{\mathrm{rs}}$ and R^{rs}, are strongly dependent on the plastic flow history, and it could be challenging to accurately evaluate them through experimental approaches. It is important to notice that for a material treated by shot peening, with the presence of residual stress and work hardening inside, the following relation should be satisfied:

$$f\left(\underline{\sigma}^{\mathrm{rs}}, \underline{X}^{\mathrm{rs}}, R^{\mathrm{rs}}\right) = J_2\left(\underline{\sigma}^{\mathrm{rs}} - \underline{X}^{\mathrm{rs}}\right) - R^{\mathrm{rs}} - k \leq 0 \tag{6-5}$$

Besides the stress equilibrium condition and the boundary conditions, Eq. (6-3) and Eq. (6-5) together constitute the elastic-plastic equilibrium condition of the shot peened material.

6.1.1.3 Discussing elements about the reconstruction of residual stress and work hardening

Residual strain and stress fields can be reconstructed in a FE model through for example the eigenstrain method, with the stress equilibrium condition as well as the boundary conditions being satisfied. However, when the elastic-plastic equilibrium condition Eq. (6-3) and Eq. (6-5) is not satisfied in a material element, plastic flow will be activated to reach another equilibrated state. It is first assumed that a group of residual stress and hardening variables are introduced in a material element, respectively denoted as $\underline{\sigma}^{\mathrm{in}}$, $\underline{X}^{\mathrm{in}}$ and R^{in}. Based on the relationship between these introduced variables, Fig. 6-2 schematically illustrates several cases of elastic-plastic self-equilibrium of the material element in the 2D stress space $(\sigma_\theta, \sigma_z)$.

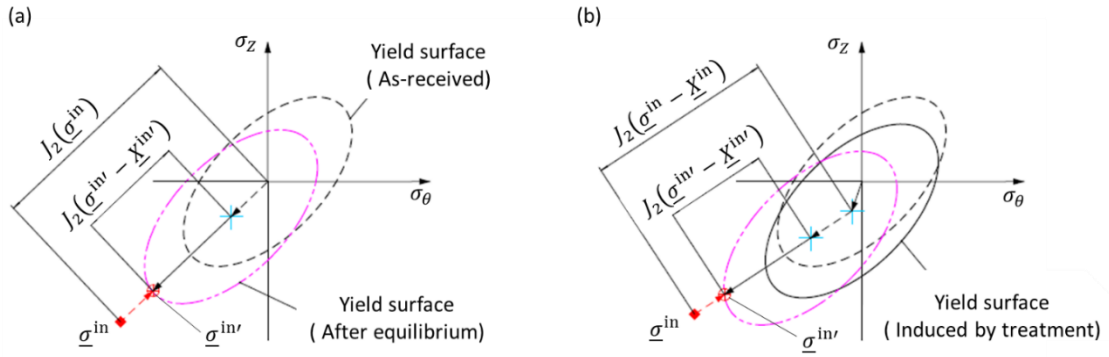

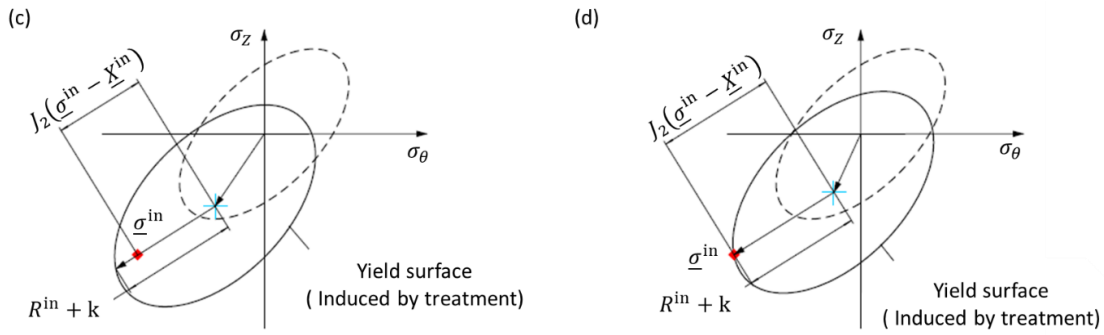

Fig. 6-2. Several cases of elastic-plastic flow while the residual stress and hardening variables are introduced in a material element.

In Fig. 6-2, black dotted ellipses correspond to the original yield surface of the as-received material state, and solid ellipses (Fig. 6-2b, 2c et 2d) represent the induced yield surface after treatment based on different configurations of introduced hardening variables $\underline{X}^{in}$ and R^{in}. The superscripts 'in' and 'in'' denote the introduced and self-equilibrated states, respectively. For the cases presented in Fig. 6-2a and Fig. 6-2b, the initial stress state is located outside the initial yield surface (the black dotted ellipse) or the induced yield stress (the solid ellipse). Plastic flow induces thus an updated stress state $\underline{\sigma}^{in\prime}$ and yield surface, which is determined by the hardening variables $\underline{X}^{in\prime}$ and $R^{in\prime}$, as described by the pink ellipses in the two figures. For Fig. 6-2c and Fig. 6-2d, the stress tensor is located inside (Fig. 6-2c) or on (Fig. 6-2d) the yield surface, and thus the elastic-plastic equilibrium condition is satisfied.

In fact, the stress updating and the plastic flow shown in Fig. 6-2 are always associated with an evolution of elastic strain, plastic strain and accumulated plastic strain, and thus can result in an evolution of the reconstructed strain fields. Comparatively, for the eigenstrain method, a linear elastic or elastic perfectly plastic behaviour is generally assumed for the reconstruction of residual stress. Elastic-plastic self-equilibrium will occur when the hardening behaviour is considered in the subsequent analysis, which could result in an inconsistency of the reconstructed stress field with the measured residual stress values. Accordingly, besides the stress equilibrium and boundary conditions, the elastic-plastic equilibrium relation should also be considered in the reconstruction of residual stress and work hardening of a shot peened structure. Thereby, a new reconstruction approach of residual stress and work hardening is proposed in this paper, and it is schematically illustrated in Fig. 6-3. The approach will be discussed in the following sections.

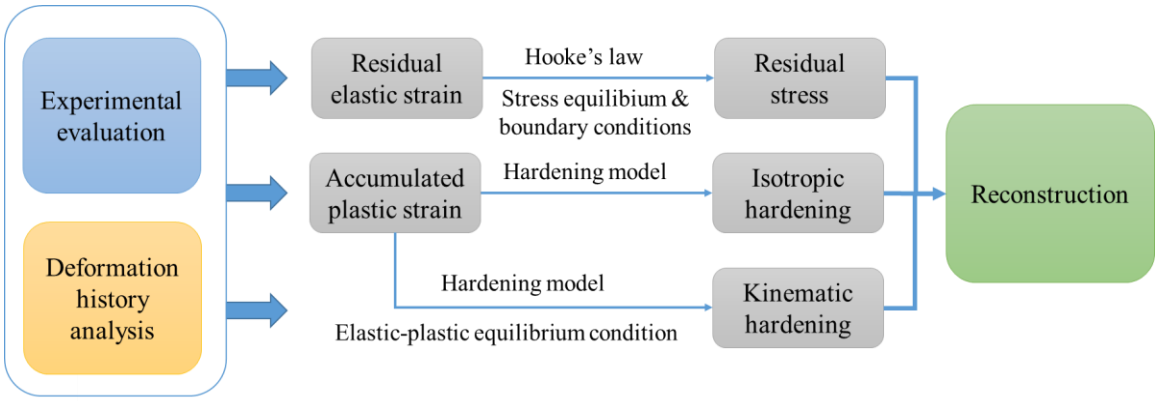

Fig. 6-3. Schematic description of reconstruction procedure for residual stress and work hardening.

6.2 Reconstruction of residual stress

6.2.1.1 Residual stress measurement

In this work, the SMATed specimen with the treatment condition (50A, 3000%) is considered. As indicated in the Chapter 3, residual stress analysis was performed on the treated sample by XRD with a Cr-Kα radiation using classical $\sin^2\psi$ method. To obtain the in-depth variation of residual stress in the near surface region, iterative electrolytic polishing (See Appendix A) was used to progressively remove the material from the surface of the sample, and subsequent XRD measurements were carried out to evaluate the residual stresses. Considering that the studied structure has a cylindrical geometry, the residual stress state can be expressed by the following stress tensor in the cylindrical coordinate system:

$$\underline{\sigma}^{\mathrm{rs}} = \begin{bmatrix} \sigma_r^{\mathrm{rs}} & \sigma_{r\theta}^{\mathrm{rs}} & \sigma_{rz}^{\mathrm{rs}} \\ \cdot & \sigma_\theta^{\mathrm{rs}} & \sigma_{\theta z}^{\mathrm{rs}} \\ \cdot & \cdot & \sigma_z^{\mathrm{rs}} \end{bmatrix} \tag{6-6}$$

In the case of a cylindrical sample, when a periphery volume of material is removed by electrolytic polishing, the sample will have a new equilibrium state, which is characterized by a change of residual stress field more or less pronounced depending on the thickness of the removed layer [113]. Therefore, the measured stresses (σ_z^m and σ_θ^m) are the ones after re-equilibrium, and they do not really correspond to the true residual stresses inside the sample [113].

Fig. 6-4 illustrates the measured in-depth variations of residual stress components of the shot peened sample. From the two normal stress components $\sigma_\theta^{\mathrm{m}}$ and σ_z^{m}, it shows that the treated surface has very high compressive residual stresses which reach the highest values at the depth of about 40-50 µm. Beneath the depth of 50 µm, the two residual stress components decrease gradually with the depth.

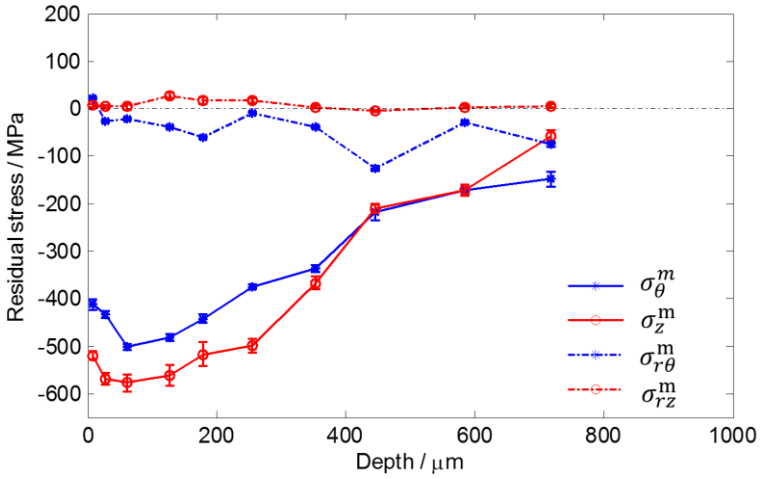

Fig. 6-4. Measured in-depth variation of residual stress components.

In addition, Fig. 6-4 indicates that the shear stress components $\sigma_{r\theta}^{\mathrm{m}}$ and σ_{rz}^{m} are very small compared to the normal stress components $\sigma_\theta^{\mathrm{m}}$ and σ_z^{m}. Thus the shear stress and the shear strain will be not considered for the sake of simplicity, as done in many previous studies [152,160,167]. Accordingly, the stress equilibrium condition for each material element can be simplified as:

$$\begin{cases} \dfrac{\partial \sigma_r^{\mathrm{rs}}}{\partial r} + \dfrac{\sigma_r^{\mathrm{rs}} - \sigma_\theta^{\mathrm{rs}}}{r} + f_r = 0 \\ \sigma_r^{\mathrm{rs}} = 0, r = R \\ \sigma_r^{\mathrm{rs}} = \sigma_\theta^{\mathrm{rs}}, r = 0 \end{cases} \tag{6-7}$$

According to the stress equilibrium condition and the stress coupling relationship in a structure, the true residual stresses in the treated sample ($\sigma_r^{\mathrm{rs}}, \sigma_\theta^{\mathrm{rs}}, \sigma_z^{\mathrm{rs}}$) can be corrected from the measured stresses ($\sigma_\theta^{\mathrm{m}}, \sigma_z^{\mathrm{m}}$) [113]. Fig. 6-5 illustrates the in–depth variations of the true residual stress components ($\sigma_r^{\mathrm{rs}}, \sigma_\theta^{\mathrm{rs}}, \sigma_z^{\mathrm{rs}}$). A clear difference can be observed between the as-measured residual stresses (Fig. 6-4) and the corrected true residual stresses (Fig. 6-5), especially for the axial stress σ_z^{rs} in the region far from the treated surface. In addition, the radial residual stress σ_r^{rs} which is experimentally inaccessible, can be calculated based on the stress equilibrium condition and stress coupling relationship.

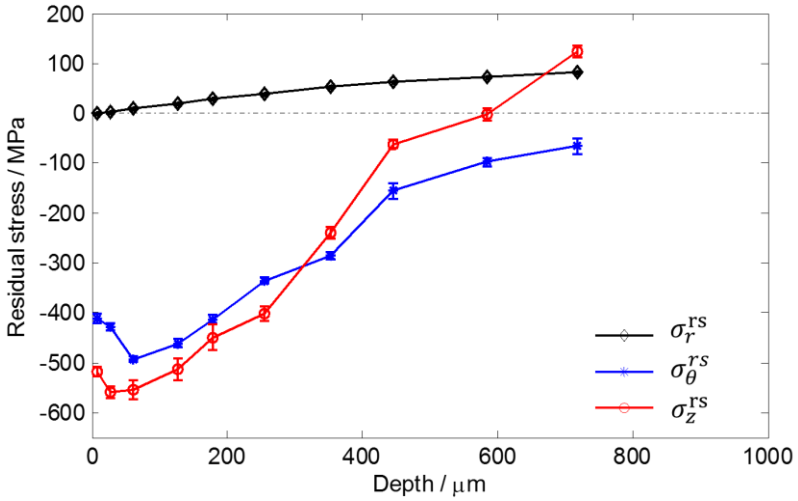

Fig. 6-5. In-depth variation of the corrected true residual stresses components.

6.2.1.2 Reconstruction of residual stress field

It should be noted that Fig. 6-5 illustrates the residual stresses only in the near surface region. As a matter of fact, it is not easy to measure the residual stresses in a deeper layer due to the difficulty of performing electrolytic polishing. The residual stresses in a deeper layer could also be roughly evaluated according to the stress equilibrium condition described by Eq. (6-7). For this purpose, a series of exponential functions are used to model the in-depth residual stress variation as shown in Eqs. (6-8) and (6-9). As the structure is not subjected to any load, the resultant axial and circumferential residual stresses should be equal to zero on each cross-section. Therefore, the axial and circumferential residual stresses as function of the radius r can be expressed by the two following sets of equations:

$$\begin{cases} \sigma_Z^{\mathrm{rs}} = \sum_{i=1}^{2} L_i\left(\mathrm{e}^{-l_i(R-r)}\right) + L_0 \\ \int_0^R \sigma_Z^{\mathrm{rs}} \cdot 2\pi r d_r = 0 \end{cases} \tag{6-8}$$

$$\begin{cases} \sigma_\theta^{\mathrm{rs}} = \sum_{i=1}^{2} T_i\left(\mathrm{e}^{-t_i(R-r)}\right) + T_0 \\ \int_0^R \sigma_\theta^{\mathrm{rs}} d_r = 0 \end{cases} \tag{6-9}$$

where, R is the radius of the gauge section of the sample; L_0, L_i, l_i, T_0, T_i and t_i are constants;

The radial residual stress σ_r^{rs} can thus be calculated by integrating Eq. (6-8) using the initial conditions ($r = R, \sigma_r^{\mathrm{rs}} = 0$; r =0,$\sigma_r^{\mathrm{rs}} = \sigma_\theta^{\mathrm{rs}}$):

$$\begin{cases} \sigma_r^{\mathrm{rs}} = \dfrac{1}{r}\left[\sum_{i=1}^{2}\dfrac{T_i}{t_i}\left(\mathrm{e}^{-t_i(R-r)}-1\right)-T_0\cdot(R-r)\right], \text{when } r>0. \\ \sigma_r^{\mathrm{rs}} = \sigma_\theta^{\mathrm{rs}}, \text{when } r=0. \end{cases} \tag{6-10}$$

In order to identify the parameters in Eqs. (6-8) and (6-9), a nonlinear optimization algorithm was used to fit the residual stress variations presented in Fig. 6-5. Tab. 6-1 lists the calibrated values. Afterwards, the radial residual stress field can be calculated through Eq. (6-10) with the calibrated parameters T_0 and T_i.

Tab. 6-1. Parameters for residual stress calculation.

Axial	L_1 / (MPa)	l_1	L_2 / (MPa)	l_2	L_0 / (MPa)
	33883.23	5.64	-34572.85	5.484	179
Circumferential	T_1 / (MPa)	t_1	T_2 / (MPa)	t_2	T_0 / (MPa)
	607.9	10.025	-1101.47	3.096	98.36

Fig. 6-6 illustrates a comparison between the experimentally obtained true residual stresses and the fitted residual stresses varying from the surface to the centre of the sample. It is assumed in this work that the residual stresses are constant in the centre region of the sample.

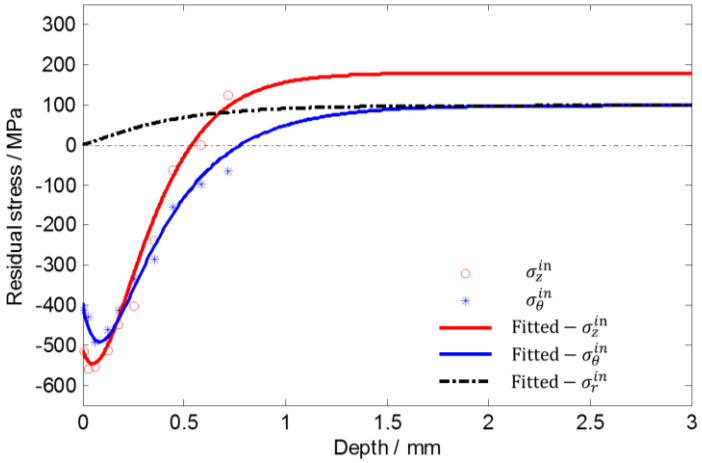

Fig. 6-6. In-depth residual stress variations throughout the treated sample. Experimental data are also given for comparison.

6.3 Reconstruction of work hardening

6.3.1 Discussion element about work hardening

Shot peening is a process involving a large number of ball impacts against the surface of a metallic component. As discussed in Section 1.3.2, various simulations about shot

peening have been performed in previous studies based on finite element method with dynamic or static elastic-plastic constitutive laws [93,101,109,273]. In general, residual stress variation and plastic strain are the most concerned physical variables, as well as the influence of various process conditions, such as treatment intensity and time duration. However, the plastic flow behaviour and the work hardening evolution during multi impacts have rarely been studied, even though they can play important roles in the residual stress generation and consequently determine the mechanical behaviour of materials.

Work hardening can be evaluated by physically based microscopic features, such as dislocation density, plastic slip. At the macroscopic scale, it is generally agreed that work hardening is difficult to be quantitatively characterized by experimental methods. In some studies, various approaches were used to identify the equivalent plastic strain of a shot peened material, for example through diffraction peak broadening obtained by XRD [136–138]. Fig. 6-7 illustrates the in-depth variation of the measured full width at half maximum (FWHM) of the shot peened and untreated samples obtained by XRD. It shows a gradual decrease of FWHM with the depth, and FWHM becomes constant beyond the depth of around 0.675 mm. In this work, the material beneath the depth of 0.675 mm is thus considered as non-plastically affected.

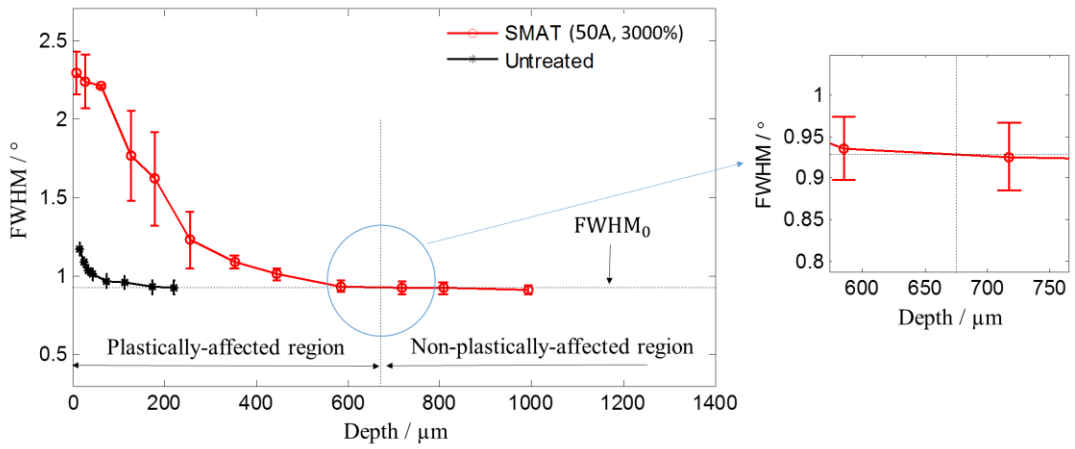

Fig. 6-7. In-depth variation of measured FWHM of the shot peened sample. FWHM of the untreated sample is given for comparison.

We assume that the residual accumulated plastic strain p^{rs} presented in Eq. (6-2) is proportional to ΔFWHM (which is defined by the difference between the measured FWHM and the reference value FWHM_0 for non-plastically-affected material), as expressed by Eq. (6-11):

$$p^{\mathrm{rs}} = \alpha \cdot \Delta\mathrm{FWHM} = \alpha \cdot (\mathrm{FWHM} - \mathrm{FWHM}_0) \tag{6-11}$$

where α is a coefficient of proportionality.

Based on Fig. 6-7, the value of FWHM_0 can be determined as 0.93°, and the critical depth for plastically-affected region is 0.675 mm. A piecewise function given by Eq. (6-12) is thus used to describe the in-depth variation of ΔFWHM, with the calibrated parameter of 4.9896 in Eq. (6-12). The calibration result is presented in Fig. 6-8.

$$\Delta\mathrm{FWHM} = \begin{cases} 4.9896 \cdot \left(0.675 - (R - r)\right)^3 \\ 0, \text{when } r < R - 0.675 \end{cases} \tag{6-12}$$

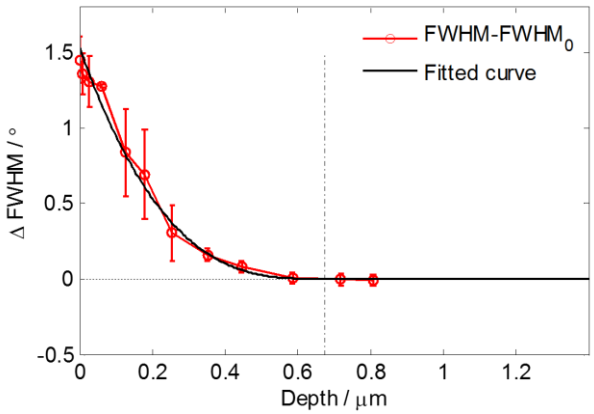

Fig. 6-8. In-depth variation of ΔFWHM and the fitted curve.

Accordingly, the in-depth variation of residual accumulated plastic strain can be expressed by Eq. (6-13):

$$p^{\mathrm{rs}} = \begin{cases} p_0^{\mathrm{rs}}/0.3075 \cdot \left(0.675 - (R - r)\right)^3 \\ 0, \text{when } r < R - 0.675 \end{cases} \tag{6-13}$$

Where p_0^{rs} is equal to $0.3075 \times 4.9896\alpha$, representing the residual accumulated plastic strain at the treated surface. The value of p_0^{rs} is related to the plastic deformation intensity and the treatment duration, as indicated in Eq. (6-2).

For the kinematic hardening and the plastic strain tensors, it should be challenging to experimentally characterize them at microscopic and macroscopic scales. According to Eq. (6-4), the kinematic hardening tensor should be located on/inside the stress sphere, which is defined in the deviatoric stress space by taking the deviatoric residual stress tensor $\underline{\sigma}^{\mathrm{rs}*}$ as the centre, and the value of $\sqrt{2/3}(R^{\mathrm{rs}} + k)$ as the radius, as illustrated in Fig. 6-9.

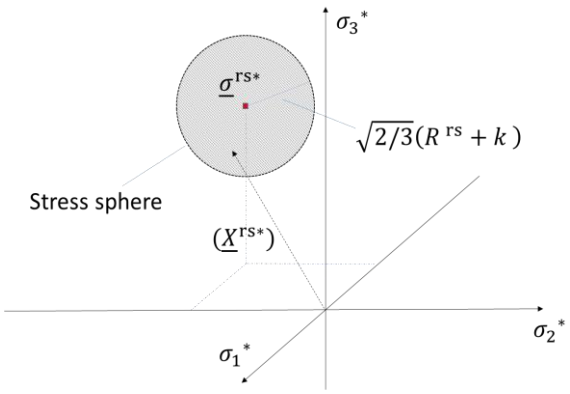

Fig. 6-9. Schematic description of the three typical initial kinematic hardening states.

6.3.2 Reconstruction of work hardening at microscopic scale

6.3.2.1 Discussion on the work hardening reconstruction

In the literature, linear elastic or elastic perfectly plastic behaviour was generally used to describe the mechanical behaviour of materials while predicting inelastic strain and reconstructing the residual stress field through the eigenstrain method [150,151,157–160,162,169]. Thereby, the hardening behaviour of materials is not considered in the eigenstrain method, as has been discussed in Section 1.3.3.2.

As indicated above, shot peening is a complex physical process based on dynamic and random impacts between the shot and the material, and simulation of shot peening could be very sophisticated. In general, rate dependent constitutive model for example Johnson-Cook model is used to describe the mechanical behaviour of a material, and dynamic simulation is performed to predict the residual stress field and plastic strain distribution. In addition, some efforts have been made to simulate the shot peening process at a microscopic scale for example using crystal plasticity model [108]. However, it should be a rather time-consuming work to simulate the whole shot peening process, especially using the crystal plasticity model. In some work, crystal plasticity model and macroscopic continuum plasticity model were integrated in one FE model to simulate plastic deformation [274]. It is a good choice to simulate the shot peening process by combing the microscopic physically based model and the macroscopic continuum constitutive model.

In this section, we focus on developing a methodology of work hardening reconstruction based on a microscopic scale model by taking into account the plastic deformation history. A representative volume element (RVE) is used to represent a material point at the treated surface. According to the analysis performed in Section 6.1, the work hardening should consist of both a tensor feature (kinematic hardening or plastic strain) and a scalar feature (isotropic hardening or accumulated plastic strain). The accumulated plastic

strain characterizes the accumulated effect of plastic deformation, whereas the kinematic hardening should be strongly dependent on the plastic flow history which is related to the evolution of stress state, as indicated in Fig. 6-1. Therefore, we propose to simulate the stress evolution history during multi impacting and unloading processes in order to obtain the kinematic hardening tensor, as has been discussed in Section 6.1.1.1.

Fig. 6-10 schematically illustrates typical impacted and unloaded states of a material point at the treated surface. In fact, the stress state of the material point is dependent not only on the position with respect to the contact centre, but also on the impact condition and the mechanical behaviour of the material. As a preliminary attempt of work hardening reconstruction, several assumptions are used for the sake of simplicity. First, only the impact with an incident angle of 90° is taken into account. Second, the dynamic effect is not considered, and the mechanical behaviour of the material point (RVE) is assumed rate-independent. In addition, we assume that the stress state under impacted state and unloaded state is only determined by the position with respect to the contact centre. It means that the previous impact effect is not considered for the stress state of the material point under the given impacted and unloaded states.

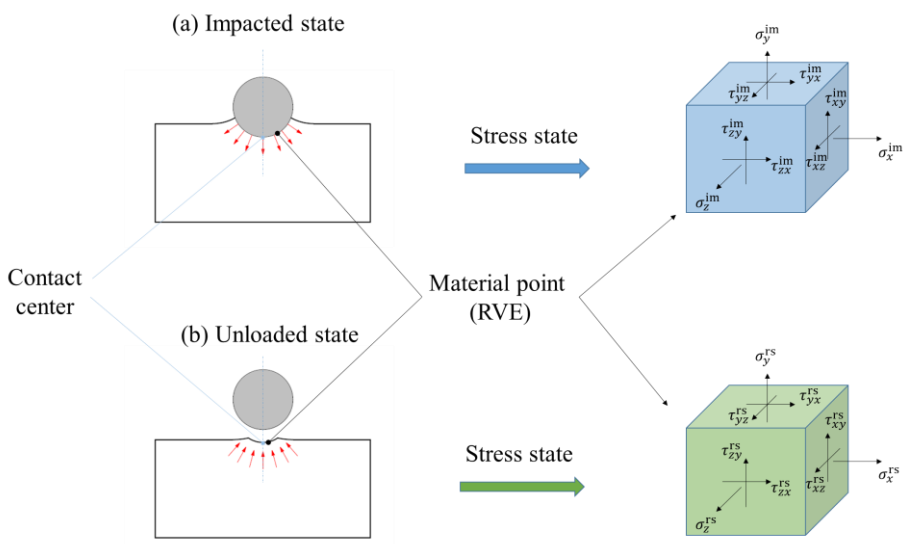

Fig. 6-10. Schematic presentation of (a) impacted and (b) unloaded states as well as the associated stress tensors of a material point at the surface of contact.

Based on the assumption that each impact occurs with an incident angle of 90°, the shot can be randomly projected to the surface at any position, and the material point can thus be plastically loaded under a typical stress state. This typical stress state is related to the position of the material point with respect to the contact centre, as indicated in Fig. 6-10. From the mathematical viewpoint, all the material points at the treated surface which will

be affected by the given impact can be described by a set M, as expressed in Eq. (6-14). Each element m_i in the set M corresponds to a material point which is affected by a given impact. This material point represents a typical stress state induced by the given impact. Accordingly, each element m_i should include an impacted stress state ($\underline{\sigma}^{\mathrm{im}}$) and an unloaded stress state ($\underline{\sigma}^{\mathrm{rs}}$). The effect of multi impacts can be simulated by repetitively and randomly applying the impacted stress state ($\underline{\sigma}^{\mathrm{im}}$) and the unloaded stress state ($\underline{\sigma}^{\mathrm{rs}}$) on the RVE, as in Fig. 6-11.

$$M = \{m_1, m_2, m_3, \cdots, m_n\} \tag{6-14}$$

Furthermore, the hardening behaviour is strongly related to the plastic flow path. In this work, the evolution of stress state is implemented by proportional loading or unloading with respect to the stress tensor. After the multi loading-unloading simulation, a work hardening can be generated in the RVE, which includes not only the kinematic hardening, but also the isotropic hardening. In the last step, the true residual stress at the treated surface is applied on the RVE.

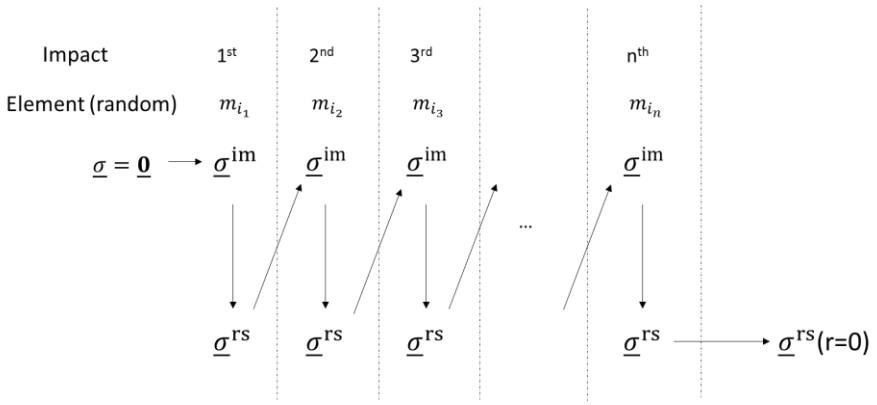

Fig. 6-11. Simulation procedure of multi impacts.

6.3.2.2 Analysis of typical stress states at the treated surface.

Hertz' theory can be used to evaluate the pressure on the contact surface and stress field inside an elastic body. However, it is very difficult to calculate the interior stress field and plastic strain for a material with elastic-plastic behaviour. In this work, the typical stress states generated by single impact at the treated surface are evaluated through the FE method.

An impact between a rigid sphere and the surface of material can be considered as a cold hardening process. The elastic-plastic constitutive law as well as the parameters are given in Section 5.3.3.1 and Tab. 5-3. The simulation is carried out with a three-dimensional FE model using the commercial software ABAQUS. Based on the symmetrical condition, one-half of the cylindrical specimen is built and meshed with 8-node linear brick elements

with reduced integration (C3D8R). The cylindrical FE model has a gauge length of 12 mm with a diameter of 6 mm, while the rigid sphere has a radius of 1.5 mm. Much finer elements with the smallest size of 45 µm are used around the impact region to have a better precision. The two sides of the structure are constrained against all the displacements (ENCASTRE), and the symmetrical boundary condition (XSYMM) is applied on the axial plane. 'Surface to Surface' contact feature is defined between the rigid ball and the specimen, and no friction is taken into account. Fig. 6-12 illustrates the whole FE model and the corresponding coordinate system.

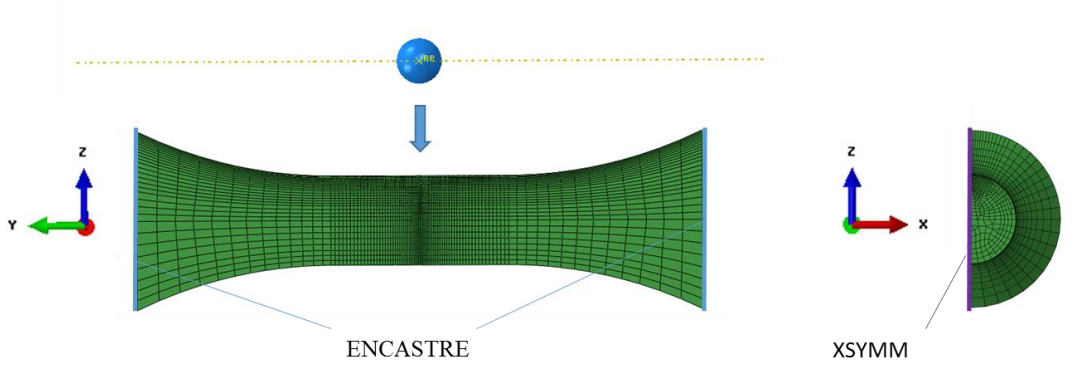

Fig. 6-12. FE model of a cylindrical specimen with a shot and the associated boundary conditions.

A displacement Uz is imposed on the rigid sphere. The analysis procedure is composed of two steps. The first step is the impacting process to obtain the interior strain/stress field (Fig. 6-1a). In this step, the sphere progressively moves towards the cylindrical sample, and an elastic-plastic deformation field can thus be generated in the structure when the sphere locally deforms the material. As has been indicated in Section 6.3.1, SMAT treatment (50A, 3000%) can induce a plastic deformation field with a depth of 0.675 mm in the near surface region (Fig. 6-7). Accordingly, a displacement is imposed so that the plastic deformation reaches the depth of 0.675 mm from the surface. Afterwards, this step is followed by an unloading step. Springback can occur inside the structure in this step, as discussed in Section 6.1.1.1.

Fig. 6-13 illustrates the fields of equivalent Mises stress and accumulated plastic strain (PEEQ) under the impacted state on the cross-section of the cylindrical structure. The centre of the contact area has the maximum Mises stress and accumulated plastic strain. The values of Mises stress and accumulated plastic strain decrease gradually with the distance from the centre region. In addition, it can be observed that the plastic deformation is focused on a roughly hemispherical zone with the contact centre point as the sphere centre. Moreover,

Fig. 6-13b shows that the PEEQ value is zero at the depth around 0.675 mm, which corresponds to the experimentally measured value.

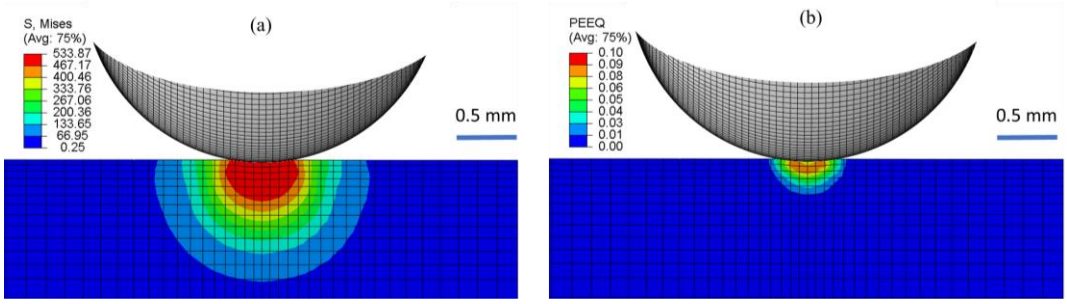

Fig. 6-13. (a) Equivalent Mises stress field and (b) accumulated plastic strain field in the impacted state.

A symmetric plastically affected region can be observed at the treated surface. In this work, the typical stress states are extracted from the 10 elements in the observed plastically affected region, as shown in Fig. 6-14. The set M can thus be expressed by Eq. (6-15). Each element in the set M corresponds to an FE element in the plastically affected region, and thus represents typical stress states respectively in the impacted and in the unloaded states, as given in Tab. 6-2 and Tab. 6-3.

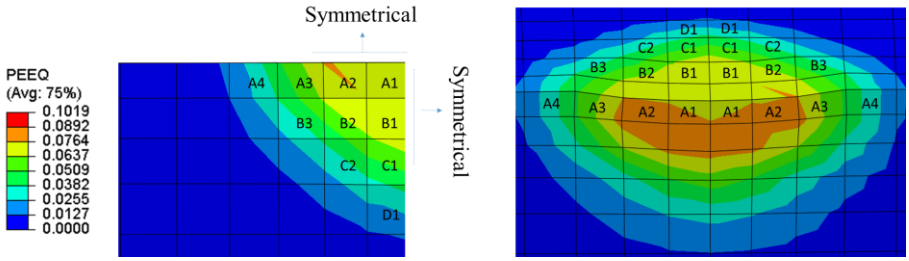

Fig. 6-14. Typical elements with plastic deformation during impacting on the contact surface of the sample.

$$M = \{A_1, A_2, A_3, A_4, B_1, B_2, B_3, C_1, C_2, D_1\} \quad (6\text{-}15)$$

Tab. 6-2. Stress state of typical elements in impacted state within the sample (MPa).

Elements	A1	A2	A3	A4	B1	B2	B3	C1	C2	D1
σ_r^{im}	-1314.82	-1498.42	-1208.19	-66.37	-1538.81	-1697.70	-781.03	-939.99	-833.16	233.92
σ_θ^{im}	-789.33	-1021.12	-855.52	-30.37	-951.04	-1163.83	-597.94	-708.27	-680.29	-348.45
σ_z^{im}	-789.80	-942.43	-913.26	-482.52	-1120.19	-1187.90	-652.29	-719.26	-588.73	40.64
$\sigma_{r\theta}^{rs}$	4.93	-40.91	72.16	105.74	-49.01	28.86	85.68	278.06	223.85	-62.11
σ_{rz}^{rs}	15.40	-35.98	223.16	-14.29	-23.52	14.44	251.30	-13.37	96.13	-7.13
$\sigma_{\theta z}^{rs}$	-6.59	41.28	26.16	-59.20	22.14	21.80	-101.07	9.30	-110.81	-41.54

Tab. 6-3. Stress state of typical elements in unloaded state within the sample (MPa).

Elements	A1	A2	A3	A4	B1	B2	B3	C1	C2	D1
σ_r^{im}	-63.14	20.68	-14.96	-48.75	35.25	68.56	-82.09	-28.27	-94.22	-19.38
σ_θ^{im}	-9.00	-107.60	-134.21	101.82	-75.54	-152.22	-116.42	-177.36	-201.16	-297.65
σ_z^{im}	-45.38	-113.35	-216.47	-328.72	-163.56	-174.09	-167.95	-136.92	-129.62	83.24
$\sigma_{r\theta}^{rs}$	-45.94	0.13	7.37	-26.96	-5.41	-42.72	-44.07	-68.08	-43.68	-24.83
σ_{rz}^{rs}	-38.46	-1.85	-83.91	-44.69	-26.32	-30.01	-60.25	22.78	-46.97	-33.08
$\sigma_{\theta z}^{rs}$	4.36	8.33	-4.52	-47.36	-1.29	-16.78	-96.44	-12.76	-107.54	-45.68

6.3.2.3 Simulation of multi impacts based on a self-consistent method

The reconstruction method and the typical stress states at the treated surface are respectively discussed and obtained in Section 6.3.2.1 and 6.3.2.2. For the simulation of multi impacts, the mechanical behaviour of the material point is described by the self-consistent model presented in Section 5.1 and the material parameters in Tab. 5-4. 50 grains with randomly generated grain orientations (APPENDIX 3) is considered for the RVE. In this work, 100 times of impact is preliminarily considered. However, the number of impacts should be evaluated according to the treatment coverage, which is indirectly related to the treatment conditions, as has been discussed in Chapter 3.

After the simulations based on the self-consistent method, the plastic slip and the shear stress in each slip system of all the grains can be obtained. Fig. 6-15 presents the distribution of plastic slip and shear stress in a slip system with respect to the angle between the slip direction and the positive axial direction of the whole structure. It can be found in Fig. 6-15a that the plastic slip is extensively activated in the direction perpendicular to the axial direction of the whole structure and thus parallel to the peening direction (Fig. 6-16). This phenomenon can be confirmed by the EBSD observation presented in Fig. 2-19b. On the contrary, the shear stress in slip system does not present any obvious dependence on grain orientation.

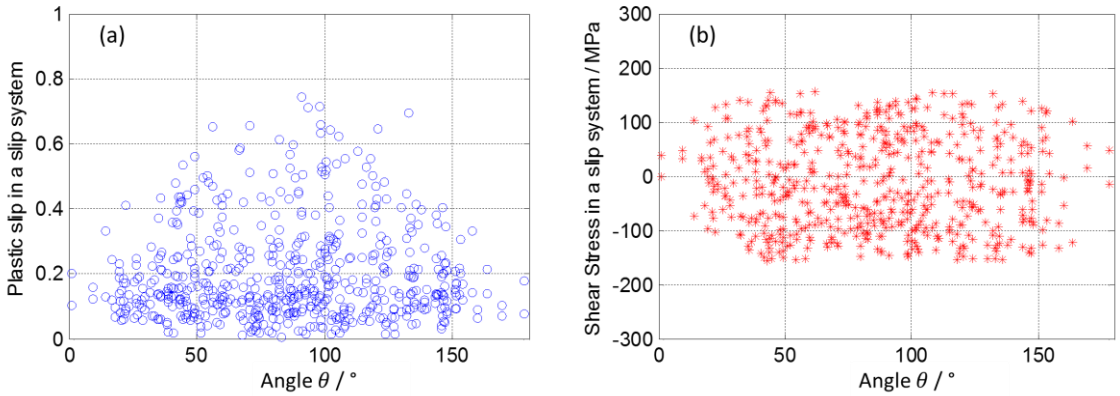

Fig. 6-15. Distribution of plastic slip (a) and shear stress (b) in a slip system with respect to the angle between the slip direction and the positive axial direction of the whole structure.

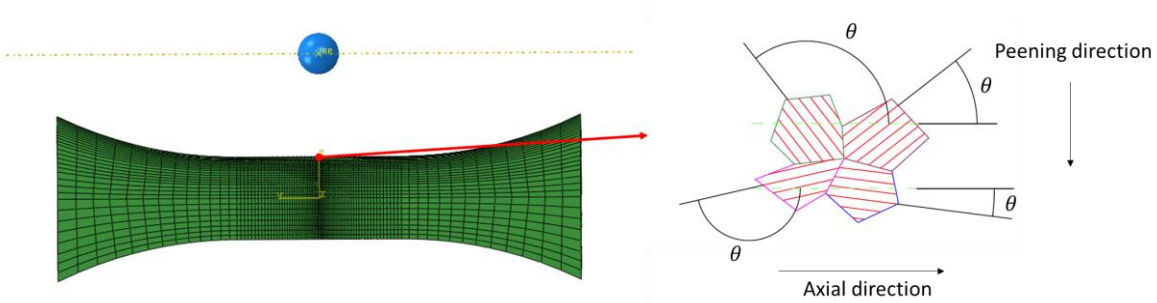

Fig. 6-16. Schematic description of the orientation of the slip direction with respect to the axial direction of the whole structure.

6.3.3 Reconstruction of work hardening with macroscopic model

During the simulation presented in Section 6.3.2.3, the plastic strain rate is calculated with Eq. (5-19), and thereby the residual accumulated plastic strain ρ^{rs} and the kinematic hardening tensor $\underline{X}^{\mathrm{rs}}$ at the contact surface ($r = 0$) can be obtained through the following equations:

$$p^{\mathrm{rs}}(r=0) = \int \sqrt{2/3\ \underline{\dot{\varepsilon}}^{\mathrm{p}} : \underline{\dot{\varepsilon}}^{\mathrm{p}}}\ \mathrm{d}_t \tag{6-16}$$

$$\underline{X}^{\mathrm{rs}}(r=0) = \varphi(\rho^{\mathrm{rs}}) \cdot \sum_i \underline{X}_i^{\mathrm{rs}}(r=0) \tag{6-17}$$

$$\underline{X}_i^{\mathrm{rs}}(r=0) = \left(\int \left(C_i \underline{\dot{\varepsilon}}^{\mathrm{P}} - \gamma_i \underline{X}_i \dot{p} \right) d_t \right) \tag{6-18}$$

Afterwards, the in-depth variation of residual accumulated plastic strain can be obtained according to Eq. (6-13), and the variation of isotropic hardening is calculated by Eq. (6-19):

$$R^{\mathrm{rs}} = \sum_{i=1} Q_i(1 - \exp(-b_i p^{\mathrm{rs}})) \tag{6-19}$$

We assume that the kinematic hardening tensor has the same in-depth variation trend with the variation of the residual accumulated plastic strain p^{rs} (Eq. (6-13)). Accordingly, the kinematic hardening tensor in different depth can be obtained through the following Eq. (6-20):

$$\underline{X}_i^{\mathrm{rs}} = \begin{cases} \underline{X}_i^{\mathrm{rs}}(r=0)/0.3075 \cdot \left(0.675 - (R-r)\right)^3 \\ \underline{0}, \text{when } r < R - 0.675 \end{cases} \tag{6-20}$$

According to the above analysis and Eqs. (6-16) to (6-20), the in-depth variation of residual accumulated plastic strain and kinematic hardening tensor can be calculated and they are presented in Fig. 6-17 and Fig. 6-18. It should be noted that the shear components of the kinematic hardening tensor are not taken into account, just as the simplification for the residual stress field in Section 6.2.1.1. In the following section, the reconstructed residual accumulated plastic strain and kinematic hardening tensor will be introduced in the FE model of a cylindrical structure to study their effects on LCF behaviour of the material.

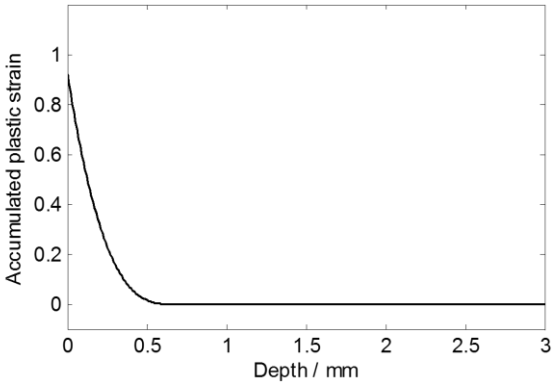

Fig. 6-17. In-depth variations of the residual accumulated plastic strain.

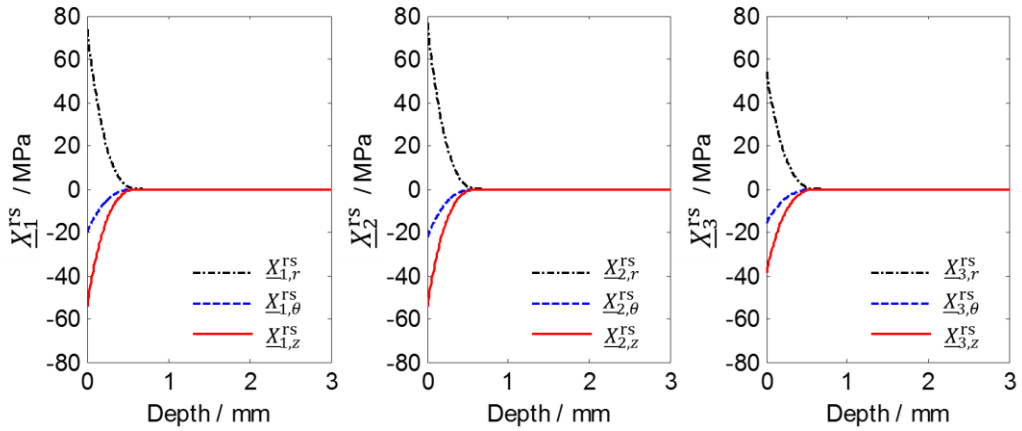

Fig. 6-18. In-depth variations of the kinematic hardening components.

6.3.4 Discussion on the reconstruction method

In Section 6.3, the reconstruction of work hardening of a SMATed structure is discussed and a new reconstruction method is proposed based on macroscopic continuum plasticity and microscopic self-consistent model. The in-depth variation of plastic deformation was firstly evaluated by comparing the FWHM value obtained through XRD between the SMATed and the untreated specimens. A new method of reconstruction of work hardening based on the microscopic scale model is proposed and implemented to simulate the evolution of typical stress states of a material point at the treated surface during multi impacts. The kinematic hardening tensor and the accumulated plastic strain for the macroscopic continuum plasticity model are evaluated through the simulation simultaneously. The in-depth variations of kinematic hardening and accumulated plastic strain are obtained based on the measured FWHM values.

It should be noted that this section focuses on proposing and implementing a new methodology of reconstructing the work hardening of a SMATed structure. Many factors are thus ignored during evaluating and reconstructing the work hardening processes, especially in the microscopic self-consistent model presented in Section 6.3.2.

Firstly, rate-independent constitutive model is used to describe the mechanical behaviour of the studied material, and dynamic loading is not taken into account in this work. In fact, the rate-dependent plastic deformation plays an important role in the generation of residual stress and work hardening during shot peening. The high-speed shot can induce very high strain rate of materials at the contact surface (up to 10^4-10^5) [275]. The strain rate varies sharply from the impact affected region to other regions non-affected by impact loading. Moreover, different strain rate could induce very different mechanical behaviour of materials.

Secondly, in Section 6.3.2.2, the typical stress states in the plastically affected region at the contact surface are obtained by simulating single impact, and hardening/softening of the material point during multi impacts is not taken into account. In reality, a material could undergo very different peak stress state during each impact due to the accumulation of plastic deformation during the previous multi impacts. In addition, the inhomogeneity of the surrounding materials could also significantly affect the stress field and the peak stress states of the material point.

Thirdly, the plastic deformation path is not considered in Section 6.3.2.3. In practice, the material point could undergo very complex non-proportional loading path before reaching the peak stress state. The loading path is mainly determined by the shape of the

structure and the position with respect to the contact centre. On the one hand, the kinematic hardening behaviour is strongly related to the plastic flow history. On the other hand, the material can present very different mechanical behaviour under non-proportional loading.

In addition, there also exist other factors, for example pre-hardening/memory effect, creep, finite deformation. It could be challenging and interesting to precisely characterize the physical mechanisms of shot peening. As indicated above, this section only provides a preliminary reconstruction method of work hardening for a shot-peened structure. Other factors, for example rate-dependent, dynamic effect, memory effect, can be progressively considered in the framework of this reconstruction method.

6.4 Modelling of LCF behaviour of SMATed material

The reconstruction of residual stress and work hardening is discussed in Section 6.1. In Section 6.2 and 6.3, the residual stress field and work hardening of a SMATed sample with the treatment condition of (50A, 3000%) are reconstructed based on experimental evaluation and deformation history simulation. In this section, LCF behaviour of the SMATed sample will be analysed using the reconstructed residual stress field and work hardening to understand their effects on mechanical behaviour of the material.

6.4.1 FE modelling of the SMATed specimen

For simplicity, only the gauge section of the cylindrical sample (Fig. 2-1) is taken into account. According to the symmetries, a 2D-axisymmetric FE model with one-half of the structure is built in ABAQUS, with the symmetric constraint applied on the bottom border, as shown in Fig. 6-19. The FE model is meshed with a 4-node bilinear axisymmetric quadrilateral reduced integration element (CAX4). In order to better capture the radial variation of the variables, finer elements are used at the surface in the radial direction with a mesh size of 0.04 mm, and underneath is a gradient distribution of mesh size from 0.04 mm to 0.188 mm. In the axial direction, a unique mesh size of 0.1 mm is applied. Fig. 6-19c shows the meshed FE structure with the imposed boundary conditions. The two ends of the FE model are both assumed to be plane at any time. A coupling constraint is thus applied so as to keep the upper border plane and always perpendicular to the symmetrical axis. In addition, for the self-equilibrium and cyclic behaviour analysis, only the rotational degree of freedom is constrained for the upper border.

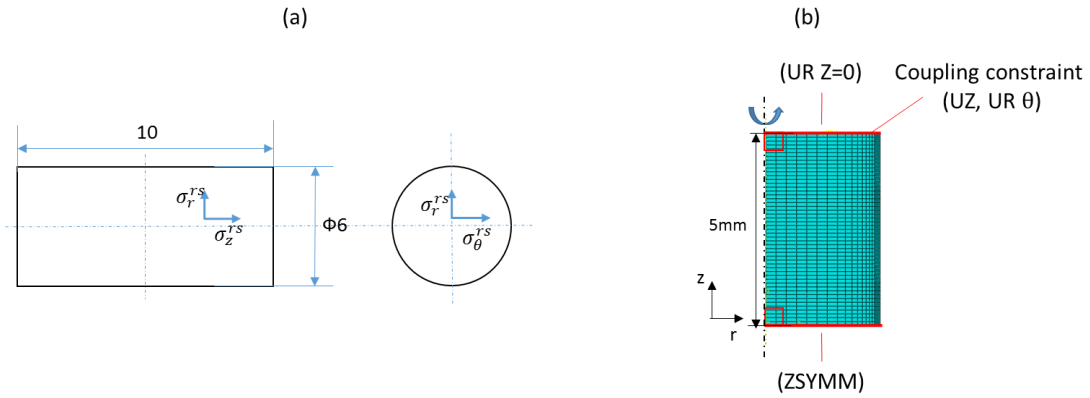

Fig. 6-19. Description of the gauge section of the treated sample: (a) cylindrical coordinate system, and (b) FEM model with the applied boundary conditions.

The constitutive framework and the hardening models are implemented through the subroutine UMAT. In this work, only the cyclic behaviour under strain amplitude of ±1.25% is considered. The cyclic constitutive model and the material parameters presented in Section 5.3.3.1 are implemented. All the initial variables ($\underline{\sigma}^{\text{in}}, \underline{X}^{\text{in}}, p^{\text{in}}$) are introduced into the FE model at the beginning of the analysis through ABAQUS subroutines 'SIGINI' and 'SDVINI' with $\underline{\sigma}^{\text{in}} = \underline{\sigma}^{\text{rs}}$, $\underline{X}^{\text{in}} = \underline{X}^{\text{rs}}$ and $p^{\text{in}} = p^{\text{rs}}$. It should be noted that the shear components for $\underline{\sigma}^{\text{in}}$ and $\underline{X}^{\text{in}}$ are not taken into account. In this work, three initial configurations are considered, as listed in Tab. 6-4. The first one corresponds to the as-received state without initial stress field and hardening variables. In the second configuration, only the initial equilibrated stress field is introduced, while both of the initial stress field and work hardening are introduced in the third configuration. The isotropic hardening is calculated based on the accumulated plastic strain p^{in} through Eq. (6-19).

Tab. 6-4. Three initial configurations for the FE simulation.

Initial configurations	Residual stress field ($\underline{\sigma}^{\text{in}}$)	Accumulated plastic strain (p^{in})	Kinematic hardening ($\underline{X}^{\text{in}}$)
As-received (Case I)	-	-	-
Case II	Fig. 6-6	-	-
Case III	Fig. 6-6	Fig. 6-17	Fig. 6-18

The analysis procedure is composed of two steps. The first step is a self-equilibrium process of the introduced residual stress field and work hardening for the whole structure. During this self-equilibrium step, the displacement in Z direction of the upper border is not constrained. The FE structure could thus deform freely in this direction under the non-equilibrium force. In the second step, a periodic displacement is applied on the upper border of the FE model to simulate strain-controlled uniaxial tension-compression cyclic loading.

In this work, strain amplitude of ±1.25% is considered. Fig. 6-20 presents the loading path for the simulation of uniaxial cyclic loading.

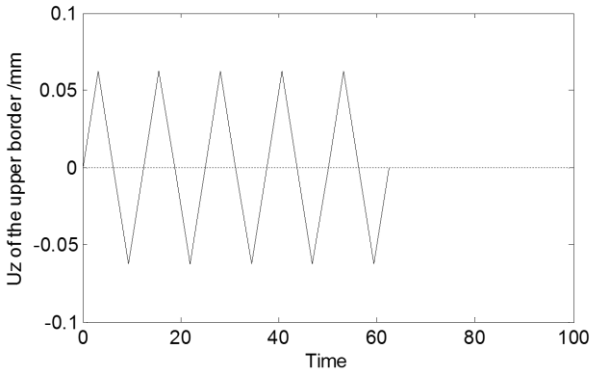

Fig. 6-20. Loading path for uniaxial cyclic simulation of the FE model ($\Delta\varepsilon = \pm 1.25\%$).

6.4.2 Results and discussion

6.4.2.1 Equilibrium verification of initial stress field and work hardening

The axial stress σ_Z distributions before and after self-equilibrium step are illustrated in Fig. 6-21. Fig. 6-21a shows that the residual stress variation presented in Fig. 6-6 is well introduced in the FE model. It can be found in Fig. 6-21c that the stress distribution for Case III after self-equilibrium step remains nearly unchanged with respect to the imposed stress field (Fig. 6-21a). This is due to the fact that the initial stress and work hardening fields satisfy the stress equilibrium condition, the boundary condition and the elastic-plastic equilibrium condition for the cylindrical structure. However, in the case where the accumulated plastic strain and kinematic hardening are not included (Case II), the stress field is obviously redistributed to reach a new equilibrated state (Fig. 6-21b).

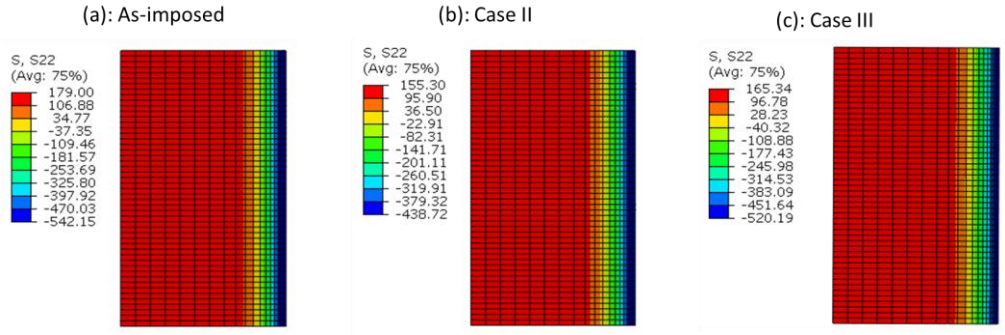

Fig. 6-21. Contours of axial stress σ_Z^{in} (in MPa) of: (a) as-imposed state, and after self-equilibrium for (b) Case II, (c) Case III.

More detailed presentation of the stress redistribution after the self-equilibrium step is presented in Fig. 6-22. Fig. 6-22a shows that there is an obvious redistribution of stress field for Case II, while the three stress components after self-equilibrium are nearly well

consistent with the as-imposed stress curves for Case III, as indicated in Fig. 6-22b. Fig. 6-22a illustrates a significant difference between the as-imposed and the equilibrated states in both the near surface region and the centre region. In fact, an initial stress field corresponding to the experimentally determined residual stress field were introduced in the FE model at the beginning of the analysis for the three cases. However, for Case II, no hardening variables were taken into account, and the elastic-plastic equilibrium condition was not satisfied in the near surface region, as illustrated in Fig. 6-2a. Therefore, an associated plastic flow was activated, and the material reached a new elastic-plastic equilibrated state in this region. A new stress equilibrated state for the whole structure was thus obtained, including the stresses in the centre region (Fig. 6-22a). In summary, the results shown in Fig. 6-21 and Fig. 6-22 imply that the reconstructed variables ($\underline{\sigma}^{\mathrm{in}}, \underline{X}^{\mathrm{in}}, p^{\mathrm{in}}$) for Case III are nearly equilibrated, and the proposed reconstruction method is thus validated. Moreover, the small redistribution of the as-imposed residual stress in Fig. 6-22b could be attributed to the fact that the shear components of the kinematic hardening tensors are not taken into account. In addition, the in-depth variation of the kinematic hardening variables are approximately evaluated through the FWHM profile, which could induce an error for the elastic-plastic equilibrium conditions of the structure.

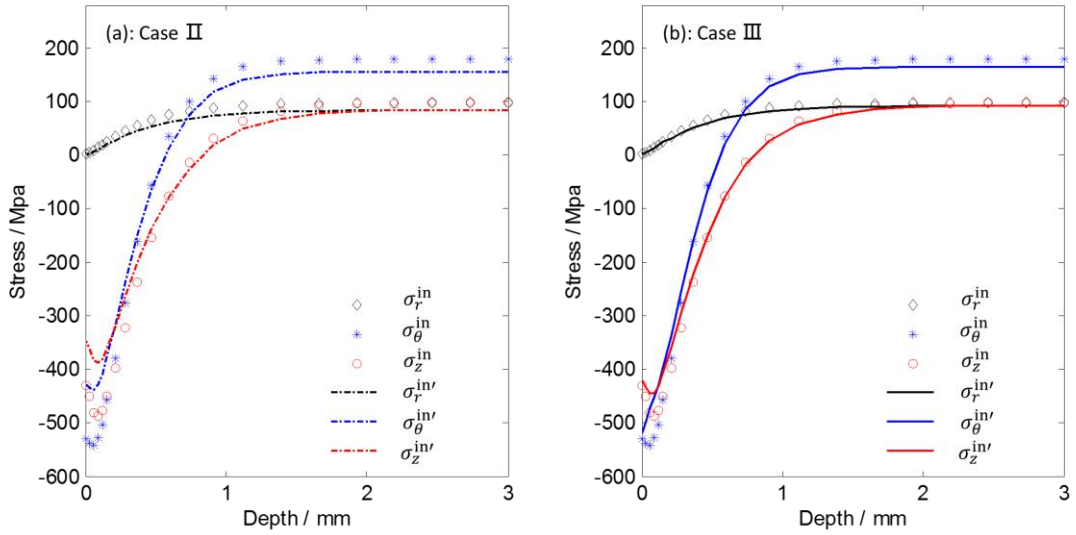

Fig. 6-22. (a) comparison of as-imposed and equilibrated stresses for Case II and Case III.

6.4.2.2 Residual stress relaxation

It is widely accepted that the residual stress relaxation during fatigue is strongly related to the loading amplitudes. In this section, we focus on the initial state of the case III. Fig. 6-23 presents the evolution of three stress components during the first two cycles for the material point at the treated surface and in the centre region. It can be seen that the

circumferential residual stress (σ_θ) at the treated surface is almost relaxed in the first cycle. In addition, the axial residual stress significantly decreases during the first tensile deformation. However, the axial stress value at the treated surface (red solid curve) becomes higher than the stress in the centre region (red dotted curve) from the second cycle. This phenomenon could be due to the combined effect of residual stress and work hardening. On the one hand, the axial residual stress is nearly relaxed during the first cycle. On the other hand, the initial work hardening can induce a higher strength of the material.

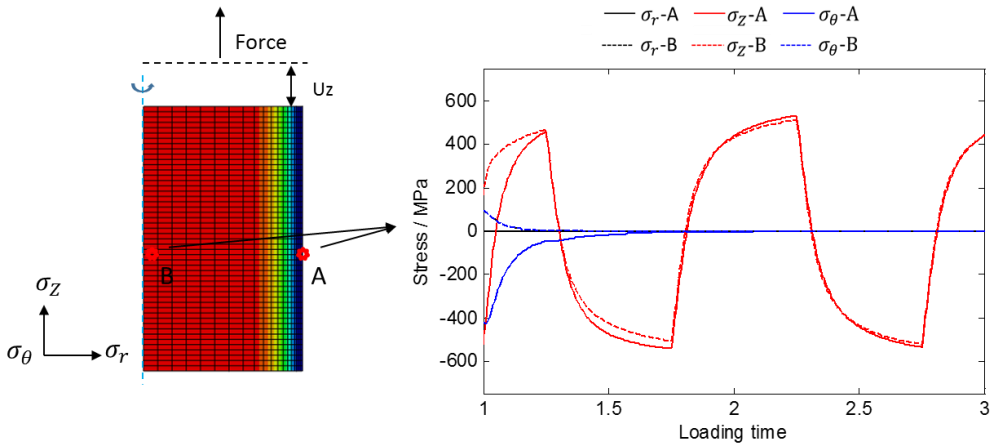

Fig. 6-23. Evolution of three stress components of the material points at the treated surface (point A) and in the centre region (B) during the first two cycles (the black dotted curve and the blue dotted curve are nearly superposed).

A detailed relaxation process of the axial residual stress (σ_z^{rs}) is given in Fig. 6-24. Fig. 6-24 illustrates the force-displacement curve of the upper border during the first two cycles. Four typical points (O, A, B, C) are marked on the cycle to indicate the loading positions where the external force is equal to zero. In fact, these four typical states can be employed to represent a global force-free state in which no external force is applied on the structure. The in-depth variation of axial stress can thus be used to represent the macroscopic residual stress (Type I) in the axial direction inside the structure. Fig. 6-24b illustrates the in-depth variation of axial residual stress in different loading stages. It can be seen that the axial residual stress is almost completely relaxed in the first tensile deformation (Stage A). This phenomenon can be confirmed by some previous studies in which the relaxation of residual stress becomes much faster under higher strain amplitudes, and the residual stress can be completely removed by applying a very high tensile deformation, as has been observed in Fig. 6-24. Accordingly, it can be concluded that the residual stress has not played an important role in fatigue life of the material under high strain amplitudes, for example ±1.25% in the experimental results shown in Section 3.5.2. On the contrary, work hardening can

induce a higher tensile stress at the treated surface, which could promote crack initiation and propagation.

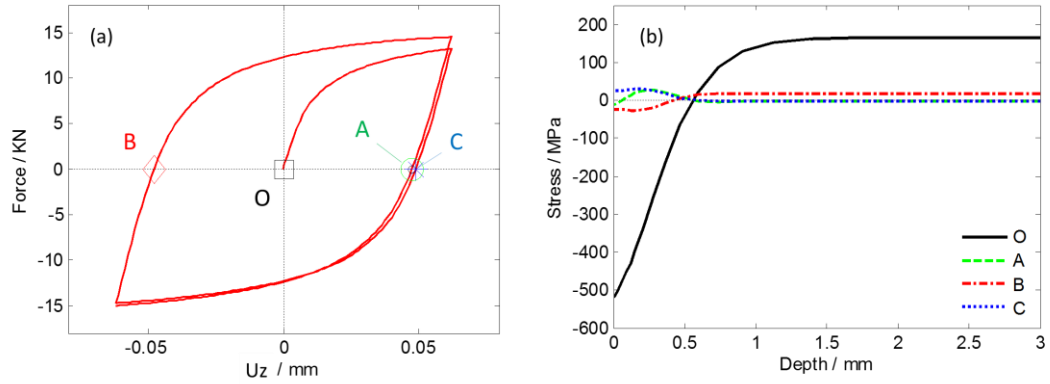

Fig. 6-24. (a) Illustration of the first two loading cycles of the cylindrical structure and (b) in-depth variation of the axial residual stress in different loading places.

Cyclic loading simulation (for $\Delta\varepsilon = \pm 1.25\%$) is also performed based on the self-consistent model for the RVE following the multi impacts simulation in Section 6.3.2.3. Fig. 6-25 illustrates the distribution of plastic slip and shear stress in a slip system with respect to the angle between the slip direction and the positive axial direction of the whole structure after 150 cycles. Contrary to Fig. 6-15a where the distribution is random, Fig. 6-25a shows that the plastic slips are mainly focused in the direction which has an angle of 45° or 135° with the loading direction. This is consistent with the phenomenon observed in Fig. 2-19c, where the plastic slips are preferably oriented under the effect of uniaxial loading. In the case of shear stress presented in Fig. 6-25b, it is also reoriented compared to Fig. 6-15b. The values of the shear stress are obviously higher in the directions with 45° or 135°.

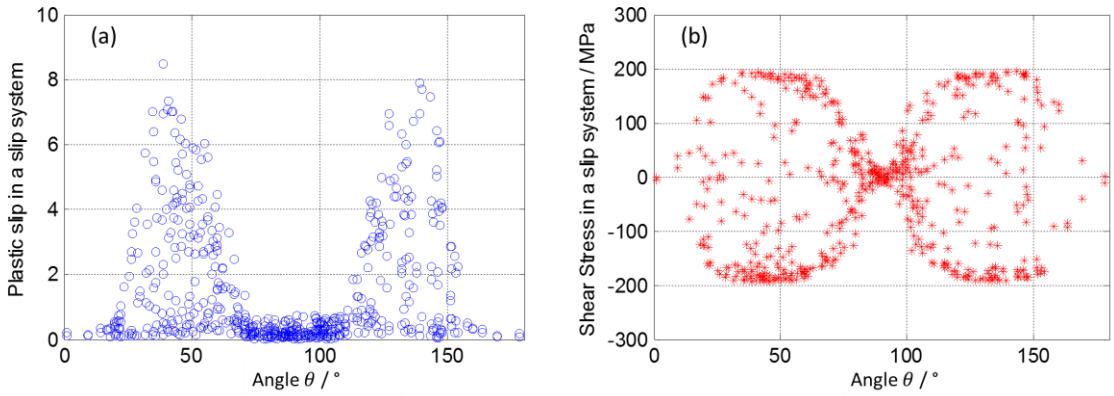

Fig. 6-25. Distribution of plastic slip (a) and shear stress (b) in a slip system with respect to the angle between the slip direction and the positive axial direction of the whole structure after cyclic loading simulation (150^{th}).

6.4.2.3 Global cyclic behaviour of the structure

Using the axial displacement of the upper border U_z and the force F_Z (Fig. 6-23), the true strain/stress for the simulated structure can be calculated with the two following equations:

$$\varepsilon_z = \ln(1 + U_z/S_0) \tag{6-21}$$

$$\sigma_z = F_Z/(\pi \cdot R^2) \cdot (1 + U_z/S_0) \tag{6-22}$$

where S_0 is the initial axial length of the FE model shown in Fig. 6-19b.

Fig. 6-26 illustrates the cyclic stress amplitudes obtained from the simulations of the three cases with different initial conditions (Tab. 6-4). It can be seen that the three curves are nearly superposed during cyclic loading. Especially, the blue curve (Case II) is nearly coincident with the curve of the as-received state (Case I). This phenomenon implies that an initial equilibrated stress field has very small effect on the macroscopic cyclic behaviour of the whole structure. In fact, the difference of mechanical behaviour of the whole structure is essentially due to the involved initial work hardening variables. As it can be observed that the stress amplitude of Case III presents a higher value than the other two curves in the first several cycles in Fig. 6-26. This phenomenon should be attributed to the as-imposed work hardening, like the difference indicated in Fig. 6-23. On the one hand, the initial kinematic hardening can change the position of the yield surface, and thus affect the critical yield stress of the material during plastic deformation (Fig. 6-1b and Fig. 6-9). On the other hand, the residual accumulated plastic strain may induce the cyclic hardening/softening behaviour through the isotropic effect in both kinematic hardening and isotropic hardening (Eq. (6-4)).

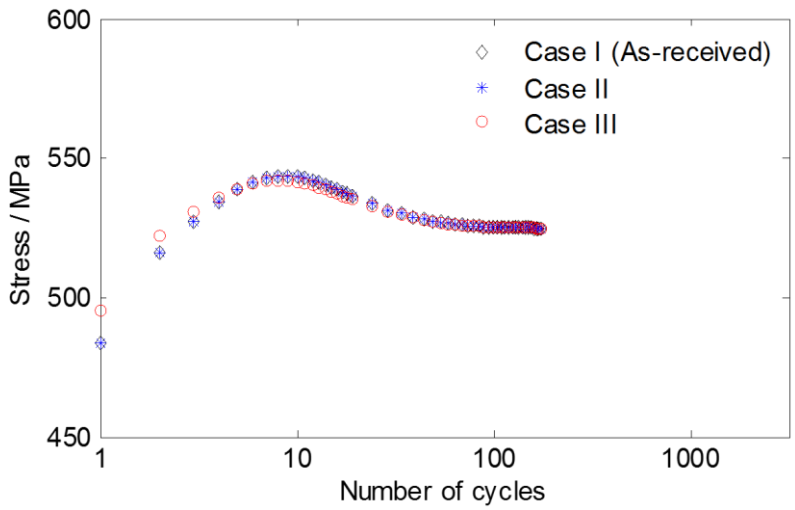

Fig. 6-26. Comparison of cyclic stress amplitude obatined from simulations of the three cases with different initial conditions.

However, experimental analysis given in Chapter 3 shows that the SMATed and shot peened samples present much higher stress amplitudes than the untreated ones (Fig. 3-18). By contrast, Fig. 6-26 presents a very small difference of the simulated cyclic stress amplitudes between Case III and Case I (as-received state), even though the work hardening is reconstructed and taken into account in the simulation of cyclic loading. The significant strengthening phenomenon of SMATed and Shot peened structures presented in 3.5.1 should be attributed to the pre-hardening or memory effect due to severe plastic deformation during the treatments.

In fact, it has been discussed in Chapter 4 that the studied material present significant strain range memory effect. Some studies have also been performed to experimentally evaluate the memory effect of austenitic steels (304L and 316L), including for example pre-tension, uniaxial tension-compression with low-high, high-low and low-high-low strain amplitudes, as well as cyclic torsional loading [179,181,182]. These studies indicate that the austenitic stainless steels (316L and 304L) present significant strain memory effect. The cyclic behaviour and fatigue life of the pre-hardened materials are strongly dependent on the pre-hardening amplitude and paths [179,181,182,206,260]. A high pre-hardening, through for example pre-tension and cyclic loading with uniaxial or torsion paths, can induce a much higher stress amplitude during the subsequent cyclic loadings [179,182]. In addition, it was highlighted that the shear pre-hardening (torsion) presented a more significant cyclic strengthening effect than the pre-hardening in axial direction[182]. Moreover, it is documented that a sufficiently high plastic strain amplitude could erase the memory effect inherited from a small pre-hardening amplitude, whereas high pre-hardening effect can be preserved in low plastic strain amplitudes.

During SMAT and shot peening treatments, the impact with high kinetic energy shot can induce severe plastic deformation of materials in the near surface region, and thus introduce significant pre-hardening effect with complex loading paths. In this chapter, the strain range memory model given in Section 4.3.2 is not included in the constitutive model for reconstruction of residual stress and work hardening as well as the subsequent LCF simulation. Therefore, this model cannot cover all the mechanical effects due to SMAT. In practice, besides grain refinement, SMAT can generate very complex stress/strain fields inside the structure, sometimes coupled with twining and phase transformation.

6.5 Conclusion

In this chapter, a new method of reconstruction of residual stress and work hardening of a SMATed cylindrical structure is developed and discussed. The self-equilibrium relation of the reconstructed residual stress field and work hardening is verified through a FE model. The evolution of residual stress and work hardening during cyclic loading as well as their effects on cyclic behaviour are investigated through simulations of cyclic deformation using the FE model. In summary, the following conclusions can be drawn from the work presented in this chapter:

(1) Plastic flow during shot peening is analysed in the framework of classical combined kinematic/isotropic hardening. It is indicated that residual stress field and work hardening inside a structure should satisfy the stress equilibrium, boundary, and elastic-plastic equilibrium conditions.

(2) A SMATed specimen is taken into account with a treatment intensity of 50A and the coverage of 3000%. The variation of residual stress in the near surface region is evaluated through XRD. The residual stress field in the whole structure is reconstructed based on the stress equilibrium relation and boundary conditions by using a series of exponential functions.

(3) A new reconstruction method is proposed based on macroscopic continuum plasticity and microscopic crystal plasticity. The reconstruction of work hardening in a microscopic scale model is implemented to simulate the evolution of the typical stress state of a material point at the treated surface by taking into account the effect of multi impacts. The kinematic hardening tensor and the accumulated plastic strain are evaluated for the macroscopic continuum model. In the end, the in-depth variation of kinematic hardening and accumulated plastic strain are obtained according to the FWHM measured values.

(4) Self-equilibrium analyses based on FE modelling indicate that the approach developed in this work is efficient to reconstruct equilibrated residual stress and work hardening fields in a cylindrical structure. Cyclic loading simulations of the SMATed structure are performed using the FE model. According to the results, the macroscopic residual stress is nearly completely relaxed in the first cycle. In addition, the reconstructed residual stress and the work hardening variables have small contribution to the global cyclic stress amplitudes. The significant strengthening effect of shot peened samples is essentially due to the pre-hardening/memory effect.

In a word, an approach has been proposed to reconstruct the residual stress field and work hardening gradient of a shot peened structure at different scales, and their effects on LCF behaviour of the material is analysed based on FE simulation. However, some factors are not taken into account during the reconstruction process, for example rate-dependent and pre-hardening/memory effect, creep, loading-unloading path. These factors may have significant effects on the mechanical behaviour of materials. In order to better understand and predict the effect of SMAT, further investigations should be performed by extending the reconstruction method to take into account these factors.

Chapter 7: Conclusions and prospects

7.1 Conclusions

It has been demonstrated that SMAT is able to generate gradient features in the near surface region of metallic materials, including nanostructured layer, residual stress and work hardening. These typical features could have significant effects on fatigue properties of materials. The aim of this thesis is to study the LCF behaviour of austenitic steels treated by SMAT through experimental analysis and multi-scale modelling.

A bibliographic study of the research background is summarized in Chapter 1 from the viewpoints of experimental investigation and modelling. Mechanical surface treatment techniques, gradient microstructures, as well as fatigue properties of SMATed materials are discussed based on previous studies. Afterwards, the work of modelling and numerical simulation concerning mechanical surface treatment is systematically reviewed. They include simulation of shot peening, reconstruction of residual stress and work hardening, constitutive modelling of cyclic plasticity at different scales. Based on the bibliographic study, the investigation of this thesis is focused on experimental analyses and multiscale modelling.

In Chapter 2, the gradient features of a 316L steel treated by SMAT are characterized using different techniques including EBSD and XRD. A nanostructured layer is generated at the treated surface with a depth of about 5 μm. Underneath, the work hardening layer presents a gradient of plastic deformation down to a depth of about 600 μm. The maximum compressive residual stress can reach around -530 MPa, and is located at about 20-40 μm beneath the treated surface. Due to the SMAT affected region, cyclic stress amplitudes of SMATed specimens are significantly enhanced for the strain amplitudes ranging from ±0.5% to ±1.25%. EBSD analysis indicates that new plastic slips were activated in the SMAT affected region during cyclic loading ($\Delta\varepsilon = \pm 1.25\%$), and consequently led to an increase of GOS, while no obvious change of GOS can be observed in the ultra-fine grain area.

Moreover, strain-driven grain growth could be observed for small grains in the nanostructured layer during cyclic loading.

A comparison between SMAT and CSP is performed in Chapter 3 by applying the same Almen intensity and coverage for the two techniques. The surface topography and typical roughness parameters are analysed. Results indicate that CSP can generate rougher surface and sometimes deteriorate the treated surface by generating a large number of micro-cracks, while a smoother surface can be obtained by SMAT. Concerning the residual stress and work hardening, CSP can generate a higher compressive residual stress and more severe plastic deformation closed to the treated surface while the SMATed specimen presents a deeper compressive residual stress and plastic deformation.

The difference of fatigue life between the SMATed and the CSPed specimens can be attributed to a competition between the compressive residual stress and the surface topography. CSP induces a higher fatigue life than SMAT under a low strain amplitude ($\Delta\varepsilon/2 = \pm 0.5\%$) due to the benefits of higher superficial compressive residual stress throughout the fatigue test. In contrast, under a higher strain amplitude ($\Delta\varepsilon/2=\pm 1.25\%$), the compressive residual stress is quickly relaxed, and thus the surface micro-cracks and the rough surface topography of CSPed specimens induce a lower fatigue life than the SMATed ones.

In Chapter 4, the cyclic behaviour of the two studied 316L steels (316-A in Chapter 3 and 316L-B in Chapter 2) are first analysed. The two steels present an initial cyclic hardening, followed by a long cyclic softening range. In addition, obvious secondary hardening phenomenon occurs for the 316L-B steel under high strain amplitudes (from ±0.8% to ±1.25%). Significant strain range memory effect can be observed for both steels. According to the analysis, the effective stress variation for different strain amplitudes are very similar, and the cyclic hardening/softening behaviour along with the strain range memory effect can mainly be attributed to back stress.

To model the cyclic behaviour of the 316L-A steel, a set of constitutive relations was proposed in the combined kinematic/isotropic hardening framework. The hardening/softening effect and the strain range memory effect are considered in the back stress by introducing a coefficient φ in the classical non-linear kinematic hardening rule. A series of functional relations are built between the coefficient φ, the accumulated plastic strain, and the memory surface. A new identification procedure is implemented to determine the material parameters involved in the developed constitutive model. Comparison between the modelling and the experimental results of the austenitic 316L-A steel shows that the

developed cyclic constitutive model is able to accurately describe the cyclic behaviour of the material in the LCF regime.

In Chapter 5, constitutive modelling of the cyclic behaviour of 316-A steel is performed by using a single crystal plasticity model coupled with the self-consistent method. A non-linear kinematic hardening rule is proposed at the slip system scale to describe the cyclic hardening/softening behaviour induced by the back stress. A self-consistent model is used as the transition rule from the scale of single grains to the scale of aggregate. The material parameters, which correspond to the cyclic behaviour of the 316-A steel under a strain amplitude of ±1.25%, are determined by using a newly developed identification procedure and the macroscopic plasticity model. The results show that the developed self-consistent model is able to well describe the cyclic hardening/softening behaviour of the steel.

In Chapter 6, the LCF behaviour of the SMATed steel is studied through a multi-scale modelling. A new method of reconstruction of residual stress and work hardening is presented and applied to a SMATed structure based on the analysis of plastic flow during shot peening, stress equilibrium, boundary, and elastic-plastic equilibrium conditions. Residual stress field is reconstructed for a SMATed cylindrical structure based on XRD evaluation, stress equilibrium relation, and boundary conditions. The reconstruction of work hardening in the microscopic scale model is implemented through a multi impacts simulation. The kinematic hardening tensor and the residual accumulated plastic strain of the material point are calculated for the macroscopic continuum model. In-depth variations of the kinematic hardening and the accumulated plastic strain for the cylindrical structure are then obtained according to the FWHM measured values.

The developed reconstruction method is verified through a self-equilibrium analysis based on FE modelling. Afterwards, cyclic loading simulations of the SMATed structure are performed using a FE model. According to the results, the macroscopic residual stress is nearly completely relaxed in the first cycle. In addition, the reconstructed residual stress and work hardening have small contribution to the global cyclic stress amplitudes. The significant strengthening effect of the SMATed structure could be essentially due to the pre-hardening/memory effect.

7.2 Prospects

In this work, the effects of SMAT on the LCF behaviour of austenitic stainless steels (316L SS) are investigated through experimental analyses, modelling, and numerical

simulations. However, some observed phenomena have not been clearly understood and some modelling methods deserve further improvement.

The grain refinement, the residual stress, and the work hardening of SMATed materials as well as their evolution during cyclic loading were characterized based on EBSD and XRD analyses. In fact, the characteristics of SMATed materials are very complex. On the one hand, the nanostructured layer is generated due to severe plastic deformation, and it could thus be associated with dislocation structures in this region. On the other hand, the microscopic residual stresses (Type II and Type III) and the complex dislocations structures co-exist in the SMAT affected region. More precise characterization approaches, for example TEM, are recommended to precisely study these microstructural characteristics.

The SMATed and shot peened specimens present significant strengthening effect according to the LCF tests. In addition, the SMAT affected region undergoes very different cyclic hardening/softening behaviour compared to the untreated material. The interpretation of the observed phenomena is rather qualitative. More physically based observation and quantitative investigation using for example EBSD and TEM are recommended in order to confirm the mechanisms.

Concerning the fatigue life in LCF regime, the comparison of SMAT and CSP was performed mainly based on the analysis of surface topography and compressive residual stress. In fact, the nanostructured layer could play important role in crack initiation and propagation. Moreover, work hardening could have a significant effect on fatigue life of materials, which depends on the hardening path, for example uniaxial pre-hardening or shear pre-hardening. Therefore, further studies are necessary to clearly and thoroughly understand the effect of the nanostructured layer and the work hardening on crack initiation and propagation.

In terms of multiscale modelling, a methodology of modelling of residual stress and work hardening is proposed in this work. The constitutive modelling of cyclic behaviour performed in Chapter 4 is assumed rate-independent in the framework of small deformation, based on the uniaxial strain controlled cyclic loading tests. In fact, the studied 316L steels could present very complex mechanical behaviour, for example pre-hardening/memory effect, ratcheting, rate-dependent effect…. The constitutive model should be further developed in order to be able to precisely describe more complex mechanical behaviour of the studied steels.

A new method of reconstruction of residual stress and work hardening is proposed in this work. On the one hand, the experimental techniques should be further developed to

measure the residual stress field inside a structure, especially in a higher depth from the treated surface. On the other hand, more advanced experimental and numerical approaches should be developed to quantitatively and precisely characterize the work hardening. Moreover, the simulation of deformation history should take into account a series of factors (for example, strain rate effect, dynamic, loading path.) in order to describe the true deformation mechanism during SMAT. In addition, more physically based constitutive model can be used to thoroughly study the deformation mechanism during impact loading, and multi-scale as well as cross-scale approaches are preferably recommended in the future work.

Résumé en français

1. Introduction

Le grenaillage de précontrainte est un procédé très utilisé en industrie pour améliorer la durabilité de pièces mécaniques. L'un des avantages du grenaillage réside dans le fait qu'il peut augmenter la résistance de matériaux sous chargement cyclique, notamment dans le domaine de la fatigue à grande nombre de cycles. Le renforcement de la résistance en fatigue de matériaux grenaillés est essentiellement lié à la présence de contraintes résiduelles de compression générées par le traitement de grenaillage.

Grâce à ses avantages et sa simplicité d'application industrielle, le grenaillage a été largement étudié dans la littérature. Cette technologie a été étendue pour développer différentes variantes. Une famille de ces variantes est basée sur l'utilisation de générateur par ultrasons (grenaillage par ultrasons). Au sein de la famille de grenaillage par ultrasons, le traitement SMAT (Surface Mechanical attrition Treatment) est l'une des techniques la plus étudiée. La particularité du SMAT réside dans le fait qu'il peut nanocristalliser la surface de matériaux dû aux impacts multidirectionnels de billes avec une énergie cinétique élevée. La présence de contraintes résiduelles de compression générées par SMAT associée à cette couche nanocristalline permet d'améliorer significativement la résistance mécanique de structures/matériaux sous sollicitations de fatigue, de contact.

La plupart des travaux abordés dans la littérature sur la fatigue des matériaux SMATés concernent la fatigue à grand nombre de cycles. A titre d'exemple, Roland et al. [8] ont montré que le SMAT peut augmenter significativement la résistance en fatigue d'un acier 316L, alors qu'un sur-traitement par SMAT peut générer un endommagement au niveau de la surface, ce qui joue un rôle néfaste pour la durée de vie de matériaux. Récemment, le grenaillage a été utilisé pour étudier son effet en fatigue oligocyclique. Par exemple, A. Morançais [thèse d'Amélie] a traité un monocristal en vue d'améliorer sa durée de vie sous sollicitations mécaniques cycliques sévères. Cependant, il est connu que la relaxation des contraintes résiduelles est fortement dépendante du niveau de chargement. Une amplitude de chargement élevée peut engendrer une relaxation de contraintes très rapide [42]. En outre,

sous forts chargements cycliques, l'effet du grenaillage est parfois contradictoire en termes d'amélioration de la durée de vie.

Dans cette thèse, la fatigue oligocyclique de deux aciers inoxydables 316L a été expérimentalement étudiée. Une attention a été portée au comportement cyclique et à la durée de vie de matériaux traités par SMAT et grenaillage conventionnel. Pour ce faire, différentes conditions de traitement (intensité et taux de recouvrement) ont été choisies, ce qui permet une comparaison entre le SMAT et le grenaillage conventionnel. Les contraintes résiduelles ont été mesurées sur des éprouvettes avant et après fatigue sous différents niveaux de chargement en vue d'étudier leur relaxation. Une analyse de la durée de vie pour les éprouvettes SMATées et grenaillées a été effectuée en tenant compte de différents facteurs tels que la topographie de surface, les contraintes résiduelles. Cette analyse permet d'avoir une meilleure compréhension de ces différents facteurs sur la durée de vie des éprouvettes traitées.

Une autre partie de la thèse concerne la modélisation du comportement cyclique du matériau de l'étude (acier inoxydable 316L) et l'analyse par éléments finis des effets de contrainte résiduelle et d'écrouissage sur le comportement mécanique de ce matériau sous chargements cyclique et monotone. Pour ce faire, un modèle macroscopique qui permet de décrire le comportement cyclique (durcissement et adoucissement) a été proposé en se basant sur les modèles existants dans la littérature. Les paramètres du modèle ont été identifiés à partir des résultats expérimentaux. Une approche de modélisation multi-échelle a été également abordée en vue de décrire le comportement cyclique du matériau en se basant sur les mécanismes physiques. Cette approche couple un modèle de plasticité cristalline étendue dans ce travail, et un modèle de transition d'échelle auto-cohérente. Par ailleurs, une nouvelle méthode d'introduction de contraintes résiduelles et d'écrouissage dans une structure cylindrique a été proposée.

2. Fatigue oligocyclique d'un acier 316L traité par SMAT

Dans cette partie, un acier inoxydable 316L est étudié. Pour le distinguer de l'autre acier 316L étudié dans les chapitres suivants, il est dénommé 316L-A. La microstructure générée par SMAT est d'abord observée par EBSD (Diffraction des électrons rétrodiffusés). Ensuite, le comportement cyclique de l'acier est présenté sous forme de l'évolution de l'amplitude de contraintes. Les résultats de fatigue sont enfin analysés en se basant sur les essais de fatigue et l'observation de la microstructure par EBSD.

2.1 Microstructure générée par SMAT

La Fig. 1 montre la microstructure observée pour une éprouvette traitée par SMAT. Dans la région périphérique (periphery region, Fig. 1a), le matériau n'est pas affecté par le SMAT car les grains ne sont pas déformés et il n'y a pas de traces de glissements plastiques. Beaucoup de joints de macle peuvent être facilement identifiés. La taille moyenne de grains dans cette zone est d'environ 15 μm, ce qui correspond à la taille de grains de l'acier dans son état de réception. Il n'y a pas de texture marquée dans cette région selon la figure de pôle fournie. La Fig. 1b montre une région mécaniquement affectée par SMAT avec la présence d'un gradient de microstructure. Une microstructure similaire a été reportée dans la littérature pour le même type d'acier [236]. Différentes caractéristiques peuvent être observées dans cette région affectée mécaniquement. Dans la zone présentée par Fig. 1c (edge periphery area), il semble que la taille de grains n'est pas changée par SMAT. Pourtant, la couleur dans chaque grain n'est plus uniforme par rapport à l'état initial. En effet, dans cette zone les grains sont subdivisés par les glissements plastiques activés par les impacts multi-directionnels de billes lors de traitement par SMAT. Dans la zone intermédiaire (intermediate area) illustrée dans Fig. 1d, un mélange de grains très fins et de grains relativement grands est présent. Dans cette zone, l'intensité d'impact est plus importante que celle dans la zone présentée par Fig. 1c (edge periphery area), et une partie de grains ont été transformés en petits grains sous l'effet de forts glissements plastiques. En ce qui concerne les grains nanocristallins montrés dans Fig. 1e, leur taille varie entre 50 nm to 300 nm. L'épaisseur de cette zone est d'environ 5 μm. Selon la figure de pôle associée à cette zone, il y a une forte texture formée sous l'effet des impacts pendant le SMAT.

On peut conclure que le SMAT a généré un gradient de microstructure depuis une couche nanostructurée au niveau de la surface jusqu'à l'intérieur du matériau avec une taille de grain de quelques dizaines de micromètres, en passant par une région de transition avec la présence, notamment d'une forte quantité de glissements plastiques. Cette modification de microstructure par SMAT conduit sans doute à un changement de comportement mécanique du matériau.

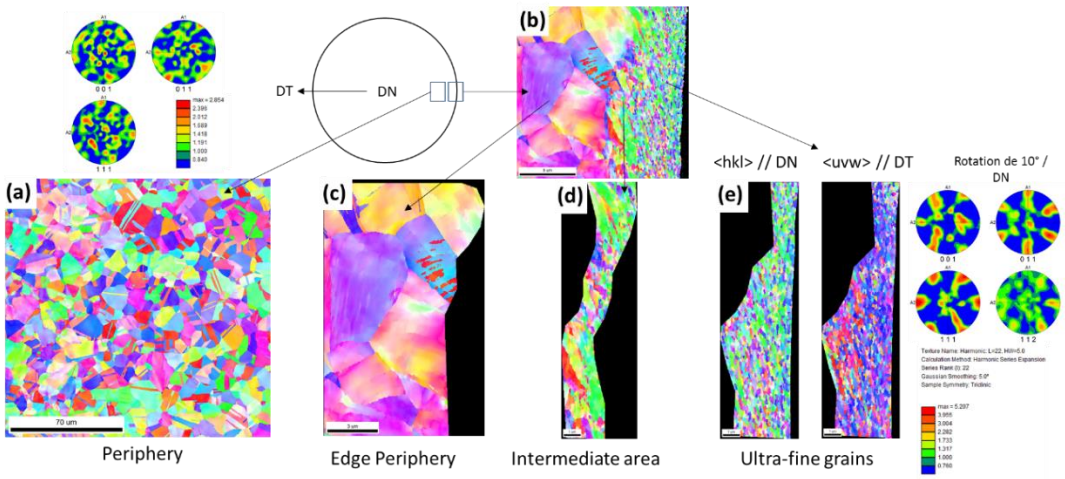

Fig. 1. Observation de la microstructure obtenue par SMAT : (a) microstructure non-affectée par le SMAT dans la région périphérique (periphery region), et (b) gradient de microstructure illustré dans la région affectée mécaniquement avec la présence de (c) la zone « edge periphery », (d) la zone intermédiaire, et (e) la zone nanostructurée.

2.2. Comportement cyclique du matériau traité par SMAT

L'évolution de l'amplitude de contrainte sous chargement cyclique fournit une description du comportement de matériaux en termes de durcissement/adoucissement cyclique. Le comportement cyclique de matériaux peut être changé par les techniques de traitement de surface telles que SMAT.

Fig. 2 montre l'évolution de l'amplitude de contrainte obtenue sous différents niveaux de chargement (±0.5% et ±1.25%) pour les éprouvettes traitées selon différentes conditions. Globalement, on peut constater que le SMAT peut renforcer significativement la résistance mécanique et affecter le comportement cyclique des éprouvettes. L'amplitude de contrainte est d'autant plus élevée que le niveau de déformation imposé est important. Pour une amplitude de déformation donnée, le niveau de l'amplitude de contrainte est plus élevé pour les éprouvettes SMATées que pour les éprouvettes non-traitées. De plus, une intensité de traitement élevée conduit à une amplitude de contrainte plus élevée.

L'augmentation de l'amplitude de contrainte pour les éprouvettes SMATées est liée à la région affectée par le traitement SMAT qui permet d'augmenter la résistance mécanique globale des structures traitées. D'une part, la déformation plastique peut améliorer la résistance mécanique du matériau grâce à des interactions plus importates entre les dislocations générées, et d'autre part la couche nanostructurée produite après SMAT possède une limite d'élasticité plus élevée comme le prévoit la loi de Hall-Petch.

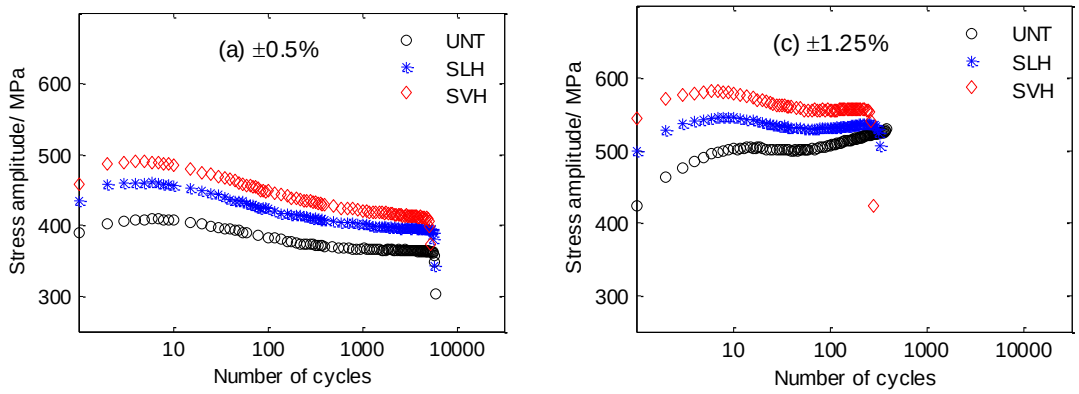

Fig. 2. Evolution de l'amplitude de contrainte pour différents états de matériau sous differents niveaux de chargement avec : (a) ±0.5% et (b) ±1.25%.

Sous chargement cyclique avec une amplitude de contrainte élevée, comme indiqué dans [149], de nouveaux systèmes de glissements plastiques peuvent être activés, ce qui peut conduire à une réorganisation des dislocations initialement générées par SMAT dans la zone écrouie. Fig. 3 montre la distribution du GOS (Grain Orientation Spread) en fonction de la distance par rapport à la surface traitée par SMAT avant et après fatigue (±1,25%). Une valeur de GOS inférieure à 1,5° correspond à un matériau recristallisé, ce qui est le cas du centre de l'éprouvette avant fatigue. Ce constat est cohérent avec le fait que le cœur de l'éprouvette n'est pas affecté par le SMAT. Par contre, comme le montre Fig. 3, le SMAT augmente significativement la désorientation intragranulaire pour la zone proche de la surface traitée, y compris la zone « edge periphery » et la zone intermédiaire.

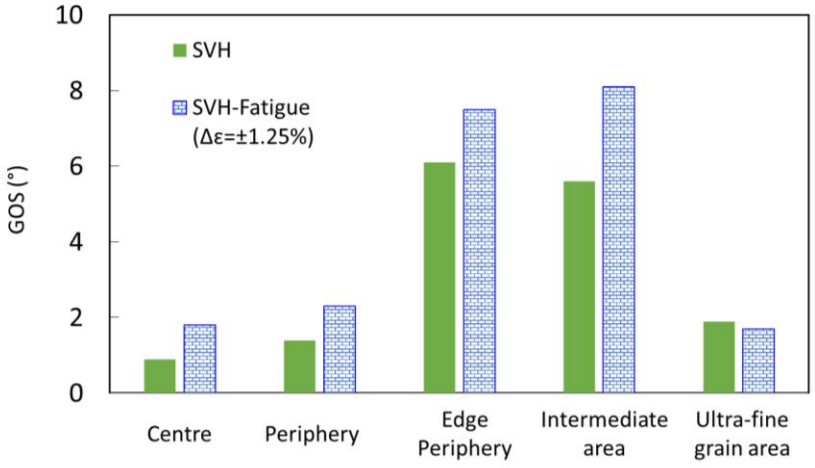

Fig. 3. Distribution du GOS (Grain Orientation Spread) calculé en différentes zones d'une éprouvette traitée par SMAT avant et après fatigue (Δε=±1,25%).

Après les essais de fatigue sous Δε=±1,25%, le GOS a été augmenté dans toutes les régions sauf la couche nanostructurée, par rapport à l'état avant fatigue. La modification du GOS mise en évidence dans la Fig. 3 devrait être due à la déformation plastique générée

par le chargement cyclique. Les glissements plastiques nouvellement activés sous fatigue peuvent subdiviser davantage les grains, ce qui conduit par conséquent à une augmentation de la désorientation intragranulaire.

Au cours de la déformation plastique générée pendant la sollicitation en fatigue, la plupart des contraintes résiduelles engendrées par SMAT sont relaxées, essentiellement pendant les premiers cycles sous une amplitude de contraintes élevée [73]. Dans ce travail, la relaxation des contraintes après les essais de fatigue a été mesurée par diffraction des rayons X (DRX). Les résultats seront présentés dans le chapitre qui suit.

3. Comparaison entre SMAT et grenaillage conventionnel

Dans ce chapitre, l'effet du SMAT et celui du grenaillage conventionnel sur les propriétés en fatigue sont étudiés de manière comparative pour un autre acier 316L (dénommé 316L-B). La présentation des résultats se concentre sur l'influence de ces deux traitements sur la durée de vie en fatigue de cet alliage. Les résultats sont interprétés en se basant sur l'observation de la topographie de surface et sur la mesure de contraintes résiduelles générées par les traitements et leur relaxation due au chargement cyclique.

3.1 Topographie de surface

Pendant un processus de traitement, la surface du matériau est impacté par les billes avec une énergie cinétique élevée, et la déformation plastique locale induite par l'impact peut modifier significativement la topographie de surface. Fig. 4 montre un exemple de topographie de surface obtenues après SMAT et grenaillage avec une même intensité Almen et un même taux de recouvrement. Globalement, pour les éprouvettes traitées par SMAT, des empreintes liées aux impacts peuvent être clairement distinguées (Fig. 4a), ce qui est plus prononcé avec l'augmentation de l'intensité Almen. Pour le cas du grenaillage conventionnel, la topographie de surface obtenue est complètement différente de celle obtenue par SMAT. Il semble que globalement la surface est plus lisse par rapport à la surface de l'éprouvette traitée par SMAT. Par contre, la surface obtenue par grenaillage est caractérisée par la présence d'une grande quantité de microfissures engendrées par les impacts (Fig. 4b). Ce phénomène est d'autant plus prononcé que l'intensité deutraitement augmente. Il est connu qu'une microfissure peut jouer le rôle de concentration de contrainte, et par conséquent conduire à la rupture prématurée des matériaux. Ainsi, la présence de ces microfissures sur les éprouvettes grenaillées pourrait en quelque sorte détériorer la résistance en fatigue du matériau en facilitant l'amorçage de fissures.

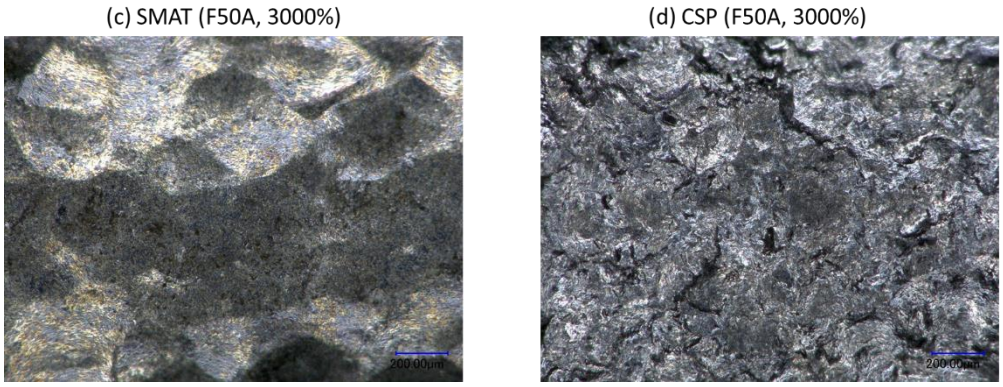

Fig. 4. Exemples de topographie de surface obtenue avec une même intensité Almen (F50A) et un même taux de recouvrement (3000%) pour le : (a) SMAT, et (b) genaillage conventionnel.

3.2 Contraintes résiduelles

Comme mentionné précédemment, les contraintes résiduelles de compression générées par une technique de traitement de surface mécanique peuvent augmenter la résistance en fatigue d'un matériau en retardant le processus de fissuration. Cependant, l'effet de contraintes résiduelles est fortement lié à leur relaxation au cours du chargement cyclique subi par le matériau.

Fig. 5 montre la comparaison des contraintes résiduelles mesurées sur les éprouvettes traitées par SMAT et celles traitées par grenaillage. La relaxation des contraintes résiduelles après fatigue sous différents chargements est également étudiée. Tout d'abord, il est possible de constater que les contraintes résiduelles générées par les deux procédés ont une tendance similaire. Après une diminution rapide des contraintes résiduelles dans la région proche de la surface, elles augmentent progressivement vers l'intérieur (coubes noires dans Fig. 5). L'épaisseur de la couche dans laquelle les contraintes résiduelles sont présentes est un peu plus élevée pour le SMAT que pour le grenaillage. Par contre, la contrainte résiduelle de compression maximale obtenue avec le grenaillage est plus élevée que celle obtenue par SMAT. La différence entre les contraintes résiduelles générées par SMAT et par grenaillage avec la même intensité de traitement peut être liée à la différence de mécanismes d'impact entre les deux techniques. Pour le grenaillage, les impacts de grenaille sont unidirectionnels, et le matériau est impacté de manière répétée toujours dans une même direction (normale à la surface). Ainsi la déformation plastique générée par les impacts précédents, ne peut pas être, même partiellement, relaxée, ce qui conduit à la formation de contraintes résiduelles de compression élevées. En revanche, dans le cas du SMAT, les impacts de billes sont multidirectionnels. Différents systèmes de glissement peuvent ainsi être activés. L'interaction entre les glissements plastiques activés sur différents systèmes de glissement peut partiellement relaxer la déformation plastique générée par les impacts précédents. Ainsi,

la contrainte résiduelle de compression maximale est moins élevée pour le SMAT que pour le grenaillage. Cependant, l'interprétation donnée ci-dessus est plutôt qualitative, et une étude spécifique est nécessaire pour éclairer quantitativement ce point, par exemple par EBSD.

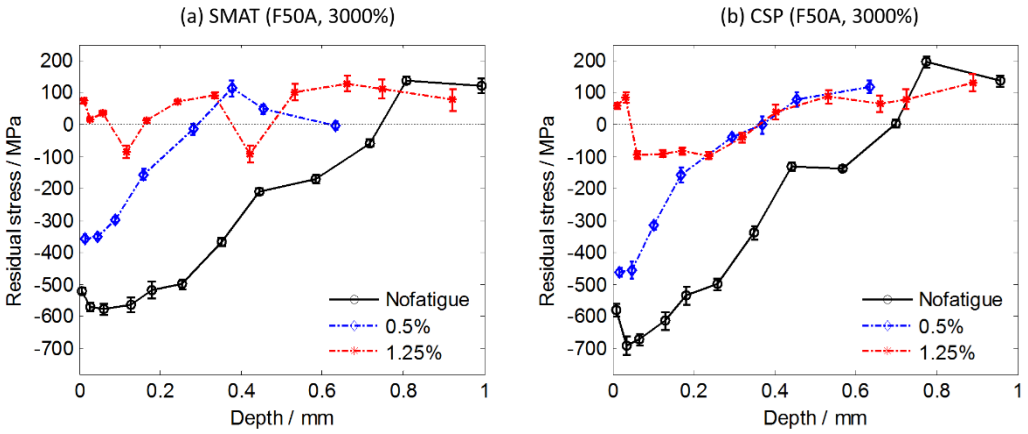

Fig. 5. Contraintes résiduelles dans la direction axiale mesurées après les essais de fatigue : (a) SMAT, et (b) grenaillage conventionnel, en comparaison avec les contraintes résiduelles avant fatigue (courbes noires).

3.3 Durée de vie en fatigue

En ce qui concerne la durée de vie, Fig. 6 présente une comparaison du nombre de cycles à rupture entre les éprouvettes SMATées, grenaillées et non-traitées. On peut constater qu'avec la diminution de l'amplitude de déformation, les avantages du SMAT et du grenaillage en termes de durée de vie en fatigue deviennent de plus en plus prononcés. Ces résultats peuvent être interprétés par la compétition entre la topographie de surface et les contraintes résiduelles de compression. En effet, la relaxation des contraintes résiduelles est fortement dépendante de l'amplitude de chargement imposé [73]. La relaxation des contraintes résiduelles sous l'effet de la fatigue est illustrée dans Fig. 5. Il est montré qu'après les essais de fatigue sous $\Delta\varepsilon/2 = \pm 0.5\%$, il reste presque la moitié des contraintes résiduelles de compression initialement générées pour les éprouvettes traitées par SMAT et grenaillage. Cela signifie que les contraintes résiduelles de compression devraient avoir joué un rôle positif important tout au long des essais de fatigue. Ainsi, une amélioration de la durée de vie peut être constatée pour les éprouvettes traitées par SMAT et grenaillage par rapport aux éprouvettes non-traitées (Fig. 6).

Les informations concernant la comparaison entre le SMAT et le grenaillage peuvent également être obtenues à partir de Fig. 5. On peut constater que la contrainte résiduelle de compression maximale est beaucoup plus élevée pour les éprouvettes traitées par grenaillage que celles traitée par SMAT après les essais de fatigue. Cette observation est

cohérente avec le fait que la durée de vie des éprouvettes grenaillées est plus élevée que celle des éprouvettes SMATées sous $\Delta\varepsilon/2 = \pm 0.5\%$. Ce résultat signifie que sous faible amplitude de déformation (±0.5%), l'effet des contraintes résiduelles sur la durée de vie est prédominant pour les éprouvettes SMATées et grenaillées, comme la relaxation des contraintes résiduelles est faible.

Fig. 5 montre aussi que sous $\Delta\varepsilon/2 = \pm 1{,}25\%$, les contraintes résiduelles dans les éprouvettes traitées sont presque totalement relaxées. Selon la littérature [13 of SMAT-CSP paper], la relaxation se produit essentiellement pendant les premiers cycles, notamment sous fortes amplitudes de déformation. Cela signifie que l'effet de contraintes résiduelles sur la durée de vie ne devrait pas être significatif sous amplitude de déformation élevée (±1.25%). Dans ce cas, c'est probablement la topographie de surface qui a un effet important sur la durée de vie. Comme présenté ci-dessus, le grenaillage conventionnel peut générer une grande quantité de micro-fissures au niveau de la surface. Ces micro-fissures devraient avoir favorisé l'initiation de fissures sur la surface traitée. Par conséquent, une durée de vie plus courte est observée pour les éprouvettes grenaillées, en comparaison avec les éprouvettes non-traitées et celles SMATées.

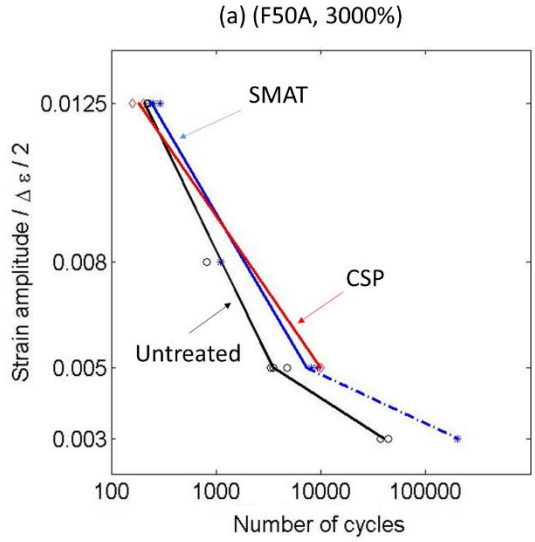

Fig. 6. Durée de vie en fatigue pour les éprouvettes SMATées et grenaillées, en comparaison avec les éprouvcettes non-traitées.

4. Modélisation macroscopique du comportement cyclique

Comme présenté dans les deux chapitres précédents, le comportement cyclique de deux aciers (316L-A et 316L-B) a été étudié avec des amplitudes de déformation entre ±0,3% et ±1,5%. Pour les deux aciers, la présence d'un effet mémoire de déformation plastique sous chargement cyclique est constaté. Selon l'analyse, le durcissement/adoucissement cyclique

ainsi que l'effet mémoire est essentiellement lié à l'écrouissage cinématique, alors que l'écrouissage isotrope a une tendance similaire pour les courbes obtenues sous différentes amplitudes de déformation. Ce chapitre consiste à modéliser le comportement cyclique du matériau en se basant sur les modèles existants dans la littérature.

4.1 Modélisation du comportement cyclique

Pour analyser le comportement cyclique du matériau, les caractéristiques d'une boucle d'hystérésis peuvent être décrites par une série de paramètres, illustrés dans Fig. 7. Par exemple, la contrainte effective (liée à l'écrouissage isotrope) et celle cinématique (liée à l'écrouissage cinématique) représentent respectivement la taille et la position de la surface d'écoulement du matériau.

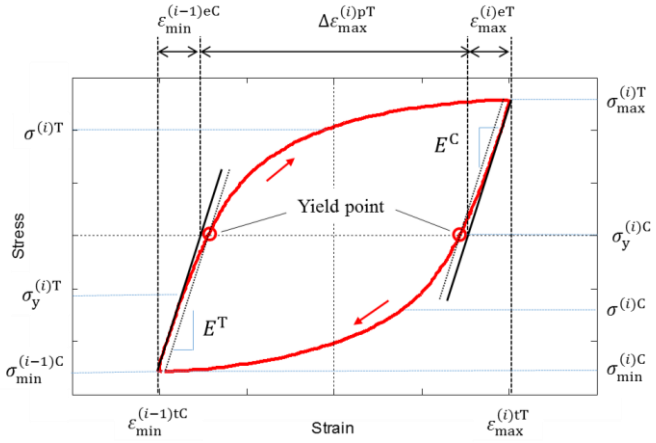

Fig. 7. Présentation de différents paramètres utlisés pour caractériser une boucle d'hystérésis.

En se basant sur ces paramètres déterminés pour tous les cycles de fatigue, les contraintes effectives et cinématiques sur les points extrêmes peuvent être obtenues. Ces contraintes désignées respectivement comme « peak effective stress » et « peak back stress » ont été tracées en fonction de la déformation plastique cumulée calculée aussi à partir des boucles d'hystérésis. Selon Fig. 8a, il semble que les contraintes effectives de pic obtenues avec différents niveaux de chargement suivent la même tendance. En revanche, les évolutions de contraintes cinématiques de pic obtenues sous différentes amplitudes sont très différentes (Fig. b). Sous fortes amplitudes de chargement (de ±0,8% à ±1,5%), la contrainte cinématique de pic augmente rapidement, et elle diminue doucement, ce qui est ensuite suivi par un stade de quasi-saturation de contrainte jusqu'à la rupture. Par contre, sous faibles amplitudes de chargement (de ±0,3% à ±0,5%), au lieu d'avoir un stade quasi-saturé, il y a une diminution continue de la contrainte cinématique de pic jusqu'à la rupture. Par ailleurs, Fig. 8 montre que le durcissement/adoucissement cyclique mis en évidence par

les courbes d'évolution de l'amplitude de contrainte est essentiellement lié à la contrainte cinématique, ce qui est cohérent avec les observations présentées dans la littérature [276,277].

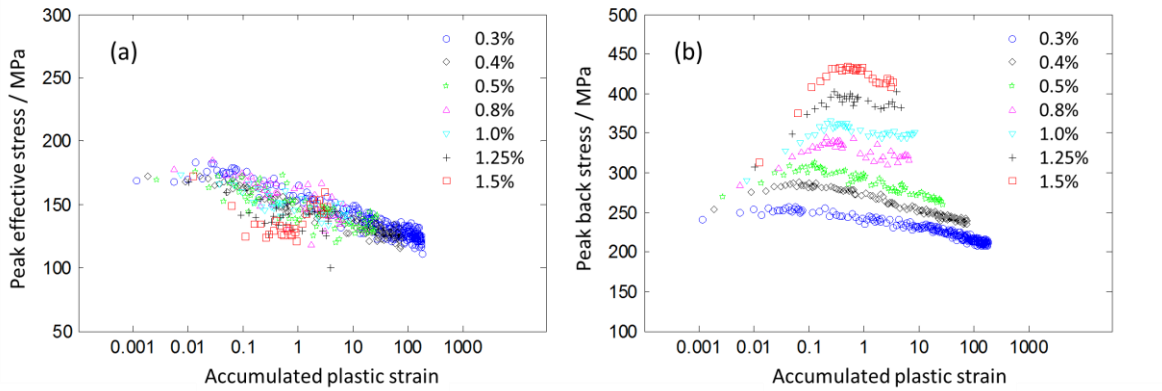

Fig. 8. Variations de (a) contrainte effective de pic, and (b) contrainte cinématique de pic avec la déformation plastique cumulée sous différentes amplitudes de chargement pour l'acier 316L-B.

4.2 Développement du modèle

Le modèle développé dans ce travail est basé sur un modèle classique d'écrouissage isotrope et cinématique [83,177]. Comme mis en évidence ci-dessus, les aciers étudiés manifestent un effet mémoire de déformation significatif sous chargement cyclique. Pour modéliser ce phénomène, Chaboche et al. [103] ont proposé le concept de surface de mémoire dans l'espace de déformation plastique. Dans ce concept, une nouvelle variable interne a été introduite pour mémoriser le plus grand domaine de la déformation plastique précédente en utilisant une nouvelle fonction F:

$$F = I\left(\underline{\varepsilon}^{\mathrm{p}} - \underline{\varsigma}\right) - q = \sqrt{\frac{2}{3}\left(\underline{\varepsilon}^{\mathrm{p}} - \underline{\varsigma}\right) : \left(\underline{\varepsilon}^{\mathrm{p}} - \underline{\varsigma}\right)} - q \tag{1}$$

où $\underline{\varsigma}$ et q représentent le tenseur de transition et le rayon de la surface de mémoire. L'évolution de ces deux variables internes $\underline{\varsigma}$ et q est déterminée respectivement avec les deux équations suivantes :

$$\dot{q} = \eta H(F)\langle n : n^{*}\rangle \dot{p} \tag{2}$$

$$\dot{\underline{\varsigma}} = \sqrt{\frac{3}{2}}(1-\eta)H(F)\langle n : n^{*}\rangle n^{*}\dot{p} \tag{3}$$

où n et n^{*} sont respectivement le vecteur unitaire perpendiculaire à la surface d'écoulement $f = 0$ et celui perpendiculaire à la surface de mémoire $F = 0$. $H(F)$ est une fonction Heaviside. Le coefficient $\eta = 0{,}5$ a été utilisé par Chaboche et al. [103] dans le

développement du modèle de mémoire de déformation pour décrire la mémorisation instantanée.

Dans ce travail, une loi d'écrouissage cinématique non-linéaire est proposée en se basant sur la description décomposée de la loi classique d'Armstrong et Frederick. Pour ce faire, un coefficient φ est introduit en vue d'incorporer l'effet de durcissement/adoucissement lié à la l'écrouissage cinématique :

$$\dot{\underline{X}} = \varphi \cdot \sum_{i=1} \dot{\underline{X}}_i = \varphi \cdot \sum_{i=1} \left(\frac{2}{3} C_i \dot{\underline{\varepsilon}}^{\mathrm{p}} - \gamma_i \underline{X}_i \dot{p} \right) \tag{4}$$

L'effet de durcissement/adoucissement et celui de mémoire de déformation respectivement liés à la déformation plastique cumulée p et au rayon de la surface de mémoire q peuvent être décrits à l'aide du coefficient d'écrouissage cinématique φ. Basé sur le comportement cyclique complexe du matériau étudié, notamment sous faibles amplitudes de déformation (de ±0,3% à ±0,5%), un ensemble de relations entre le coefficient φ et la déformation plastique cumulée est établie, comme présentées dans les équations suivantes:

$$\varphi = \varphi^{\mathrm{I}} \cdot \varphi^{\mathrm{II}} \tag{5}$$

$$\varphi^{\mathrm{I}} = 1 + (\varphi_0^{\mathrm{I}} - 1)\mathrm{e}^{-ap} \tag{6}$$

$$\varphi^{\mathrm{II}} = \varphi_0^{\mathrm{II}} \cdot \exp(-bp) \cdot (\exp(-cp) + 1)/2 + \varphi_\infty^{\mathrm{II}} \tag{7}$$

d'où, φ_0^{I}, a, φ_0^{II}, b, c, et $\varphi_\infty^{\mathrm{II}}$ sont les paramètres de matériau.

Les études antérieures présentées dans la littérature sont généralement focalisées sur le durcissement initial de matériaux. Dans ce cas, seulement les valeurs de l'écrouissage isotrope asymptotique Q_i sont associées au rayon de la surface de mémoire q pour décrire l'effet mémoire de déformation. Selon l'analyse donnée ci-dessus, l'effet mémoire de déformation est présent non seulement dans le durcissement initial, mais aussi dans l'adoucissement qui suit. Ainsi, la relation entre les variables de durcissement cinématique φ et le rayon de la surface de mémoire q peut être construite avec les équations suivantes:

$$\begin{bmatrix} \varphi_0^{\mathrm{I}} \\ a \\ \varphi_0^{\mathrm{II}} \\ b \\ c \\ \varphi_\infty^{\mathrm{II}} \end{bmatrix} = A + (B - A) \circ \exp(-Mq) \tag{8}$$

où le symbole '∘' représente le produit de Schur entre les deux matrices avec une même dimension. A, B, et M sont des vecteurs de l'ordre six liés aux paramètres de matériau.

Une procédure d'identification est développée dans ce travail pour déterminer tous les paramètres du matériau pour le modèle de comportement cyclique développé.

4.3 Résultats de modélisation

La méthode d'itération numérique de Newton-Raphson a été utilisée pour résoudre les équations différentielles afin de simuler le chargement cyclique uniaxial en déformation contrôlée (rapport de charge $R_\varepsilon = -1$). Dans le cas de simulation de chargement cyclique avec un nombre de cycles important, le calcul est lourd si on simule cycle par cycle. La méthode de saut de cycles développée par Labergere et al. [278] a été implémentée afin de réduire le temps de calcul.

L'évolution de l'amplitude de contrainte a été calculée et comparée avec les résultats expérimentaux de l'acier 316L-A sous différentes amplitudes de déformation (Fig. 9). Il montre que le durcissement/adoucissement cyclique et l'effet mémoire de déformation peuvent être bien décrits par le modèle développé dans ce travail, notamment pour de faibles amplitudes de déformation (de ±0,3% à ±0,5%) sous lesquelles l'acier manifeste un stade d'adoucissement long sans saturation de contrainte. L'erreur la plus grande entre les résultats de modélisation et expérimentaux est d'environ 10 MPa en cycle stabilisé sous l'amplitude de déformation de ±1,5% ainsi qu'en cycle saturé sous l'amplitude de déformation de ±0,3%, comme illustré dans Fig. 9.

Les boucles d'hystérésis peuvent aussi représenter le comportement plastique de matériaux sous chargement cyclique. Fig. 10 montre une comparaison des deux premières boucles d'hystérésis entre la modélisation et l'expérimentation pour le 316L-A sous différentes amplitudes de déformation. On peut constater que le modèle de comportement développé dans ce travail peut bien décrire le comportement cyclique du matériau au début de chargement cyclique. Il y a juste une petite différence entre les courbes pendant la phase de traction sous faibles amplitudes de déformation (de ±0,3% à ±0,5%). Ces différences peuvent être attribuées à la forte asymétrie de l'écoulement plastique entre la phase de traction et celle de compression au début du chargement cyclique selon les résultats expérimentaux.

Par ailleurs, une bonne cohérence entre les boucles simulées et celles expérimentales peut être obtenue tout au long du chargement cyclique sous différentes amplitudes de déformation (de ±0,3% à ±1,5%). Les résultats illustrés ci-dessus montrent que le modèle

développé dans ce chapitre peut décrire de manière précise le comportement cyclique de l'acier 316L-A, y compris le durcissement/adoucissement et l'effet mémoire de déformation.

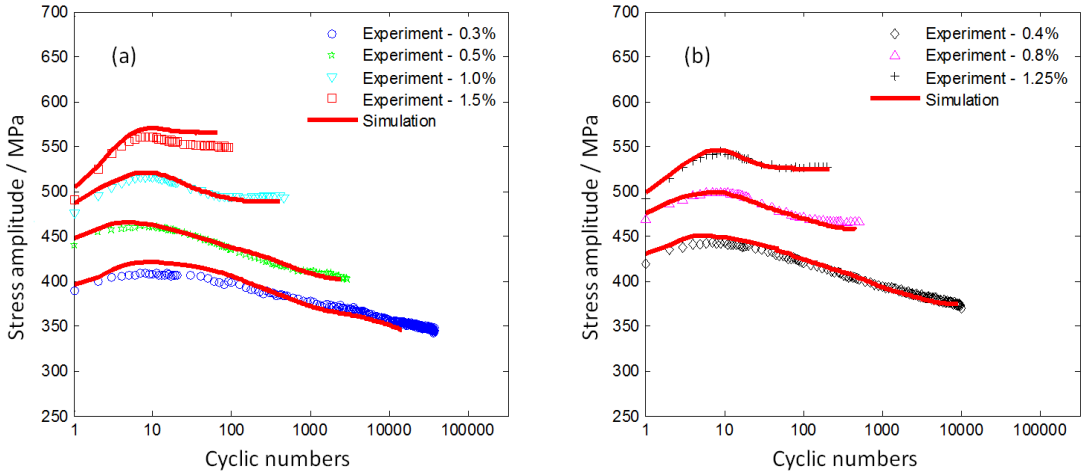

Fig. 9. Comparaison de courbes de l'évolution de l'amplitude de contrainte entre les résultats de modélisation et expérimentaux pour l'acier 316L-A sous différentes amplitudes de déformation.

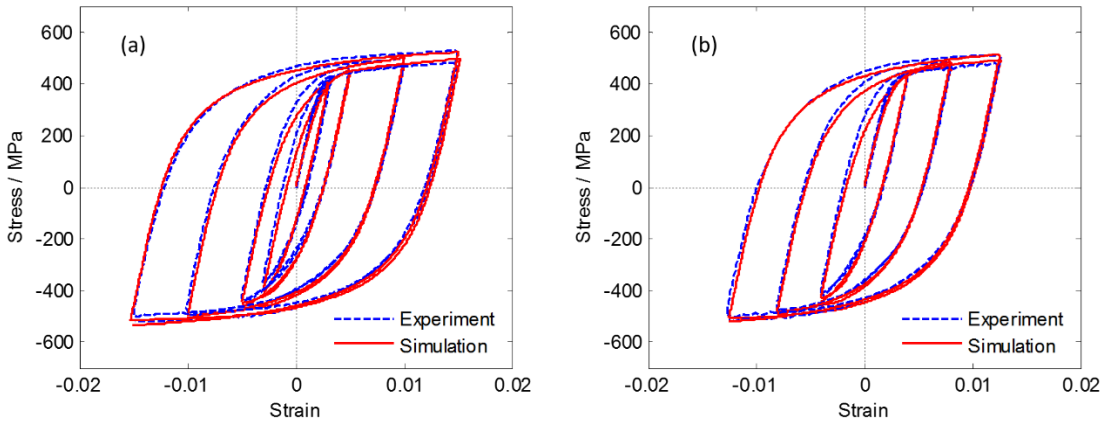

Fig. 10. Comparaison des premières boucles d'hystérésis entre les résultats de modélisation et expérimentaux sous différentes amplitudes de déformation : (a) ±0,3%, ±0,5%, ±1,0% et ±1,5%; (b) ±0,4%, ±0,8%, et ±1,25%.

5. Modélisation du comportement cyclique avec un modèle auto-cohérent

Depuis les dernières décennies, la modélisation basée sur les mécanismes physiques est de plus en plus populaire pour décrire le comportement mécanique des matériaux. Dans ce chapitre, le comportement cyclique de l'acier 316L-A est modélisé à l'aide d'une approche auto-cohérente couplée avec un modèle de plasticité cristalline étendue.

5.1 Modèle de plasticité cristalline étendu

Vue à l'échelle du cristal, la plasticité macroscopique des matériaux métalliques peut s'expliquer par le glissement de dislocations dans les plans cristallographiques. Ces plans cristallographiques correspondent aux familles de plans denses. Dans le cas d'un cristal

cubique à faces centrées (CFC), en général 12 systèmes de glissements sont considérés, basés sur les plans {111} et les directions de glissement <100>. Selon la loi de Schmid, la contrainte de cisaillement résolue (cission résolue) τ^s dans le système de glissement s peut être calculée avec la contrainte dans le grain et le tenseur de Schmid m^s, comme présenté par l'Eq. (9). Dans ce travail, une formulation cinétique dépendante du temps, développée par Méric et Cailletaud [271], est adaptée pour décrire le comportement cyclique de l'acier. Dans ce modèle, le taux de glissement plastique $\dot{\gamma}^s$ dans le système s s'exprime par une fonction de puissance de la cission résolue τ^s (Eq. (10)).

Ce modèle est étendu dans ce travail pour modéliser le durcissement/adoucissement cyclique de l'acier. Pour ce faire, une loi non-linéaire d'écrouissage cinématique est proposée en se basant sur la forme multi-décomposée d'Armstrong et Frederick (Eq. (11)). La décomposition des variables d'écrouissage non-linéaire permet une grande flexibilité pour modéliser le comportement des matériaux [227]. Pour décrire l'effet isotrope via l'écrouissage cinématique, un coefficient multiplicatif φ^s est introduit pour chaque système de glissement (Eq. (12)). Par ailleurs, les formes décomposées sont utilisées pour mieux décrire le durcissement/adoucissement cyclique du matériau (Eq. (13)).

Dans ce travail, le modèle auto-cohérent (Eq. (14)) proposé par Abdul-Latif et al. [90,223] est utilisé pour décrire la transition de l'échelle du grain à l'échelle de l'agrégat. $\dot{\sigma}^g$ et $\dot{\Sigma}$ sont les tenseurs de contrainte de Cauchy à l'échelle du grain et à l'échelle de l'agrégat, respectivement. S^g et S correspondent aux parties déviatoriques de ces tenseurs. α est un paramètre phénoménologique indépendant de l'histoire de déformation. Ce paramètre a une influence importante sur l'évolution de l'écrouissage et par conséquent sur le comportement mécanique de polycristaux [91,223]. Les constantes A et B peuvent être directement déterminées par les paramètres de Lamé, soit μ et λ.

Le taux de déformation plastique au niveau du grain peut être calculé avec les taux de glissement plastique sur tous les systèmes de glissement (Eq. (17)). La déformation élastique et la déformation totale au niveau du grain peuvent être calculées avec les Eqs. (18) et (19). La transition du cristal au polycristal est réalisée en moyennant sur l'ensemble de l'agrégat (Eq. (20), (21) et (22)).

Tab. 1. Equations principales pour décrire le modèle de plasticité cristalline étendu.

Au niveau de système de glissement

$$\tau^s = \sigma^g : m^s \tag{9}$$

$$\dot{\gamma}^s = \left\langle \frac{|\tau^s - \chi^s| - \kappa^s}{K^s} \right\rangle^{z^s} \operatorname{sign}(\tau^s - \chi^s) \tag{10}$$

$$\dot{\chi}^s = \varphi^s(v^s) \cdot \sum_{i=1} \left(c_i^s \dot{\gamma}^s - d_i^s \chi_i^s \dot{v}^s \right) \tag{11}$$

$$\varphi^s = \left[1 + (\varphi_0^{\mathrm{I}s} - 1) \cdot \exp(-a^s v^s) \right] \cdot \left[\left(\varphi_0^{\mathrm{II}s} - \varphi_\infty^{\mathrm{II}s} \right) \cdot \exp(-b^s v^s) + \varphi_\infty^{\mathrm{II}s} \right] \tag{12}$$

$$\kappa^s = \kappa_0 + \sum_i \left(Q_i^s \sum_r H_{sr} \left(1 - \exp(-b_i^s v^r) \right) \right) \tag{13}$$

Au niveau du grain

$$2A\left(\dot{\sigma}^g - \dot{\Sigma}\right) + Btr\left(\dot{\sigma}^g - \dot{\Sigma}\right) I - \alpha(S^g - S) = \left(\dot{\varepsilon}^g - \dot{E}\right) \tag{14}$$

$$A = \frac{-(8\mu + 3\lambda)}{2\mu(14\mu + 9\lambda)} \tag{15}$$

$$B = \frac{(6\mu + \lambda)(8\mu + 3\lambda)}{\mu(448\mu^2 + 456\mu\lambda + 108\lambda^2)} \tag{16}$$

$$\dot{\varepsilon}^{\mathrm{pg}} = \sum_{s=1}^{N_s} \dot{\gamma}^s m^s \tag{17}$$

$$\dot{\varepsilon}^{\mathrm{eg}} = \frac{\dot{\sigma}^{\mathrm{g}}}{2\mu} - \frac{\lambda}{2\mu(2\mu + 3\lambda)} \operatorname{tr}\left(\dot{\sigma}^{\mathrm{g}}\right) I \tag{18}$$

$$\dot{\varepsilon}^{\mathrm{g}} = \dot{\varepsilon}^{\mathrm{eg}} + \dot{\varepsilon}^{\mathrm{pg}} \tag{19}$$

Au niveau macroscopique

$$\dot{E}^{\mathrm{e}} = \sum_{g=1}^{N_g} f^g \dot{\varepsilon}^{\mathrm{e}g} \tag{20}$$

$$\dot{E}^{\mathrm{p}} = \sum_{g=1}^{N_g} f^g \dot{\varepsilon}^{\mathrm{p}g} \tag{21}$$

$$\dot{E} = \sum_{g=1}^{N_g} f^g \dot{\varepsilon}^g \tag{22}$$

$$\dot{\Sigma} = 2\mu + \operatorname{tr}\left(\dot{E}^{\mathrm{e}}\right) I \tag{23}$$

5.2 Identification des paramètres du matériau

L'itération implicite et la méthode de saut de cycles sont utilisées pour implémenter le modèle auto-cohérent et simuler le chargement cyclique. Les paramètres K^s, z^s, H_{sr}, et α impliqués dans la loi de transition (Eq. (14)) sont obtenus à partir de la littérature. Pour décrire le durcissement/adoucissement cyclique lié aux écrouissages cinématique et isotrope, une procédure d'identification est proposée pour déterminer tous les paramètres du matériau. Les paramètres au niveau de système de glissement tels que c_i^s, d_i^s (Eq. (11)), $\varphi_0^{Is}, a^s, \varphi_0^{IIs}, b^s$ et φ_∞^{IIs} (Eq. (12)) peuvent être identifiés en se basant sur le modèle macroscopique de plasticité. Ensuite, les paramètres Q_i^s et b_i^s dans Eq. (13) sont déterminés en calant les courbes de l'évolution de l'amplitude de contrainte.

5.3 Résultats et discussions

Dans ce travail, un agrégat de 50 grains avec orientations aléatoirement générées est considéré. Tous les paramètres du matériau au niveau de système de glissement sont identifiés basé sur le modèle macroscopique de plasticité sous $\Delta\varepsilon/2 = \pm 1{,}25\%$. Fig. 11 présente la comparaison de courbes de l'évolution de l'amplitude de contrainte (Fig. 11a) et de contrainte maximale/minimale (Fig. 11b) entre le modèle macroscopique et le modèle auto-cohérent. Une bonne cohérence entre les courbes signifie que l'approche auto-cohérente couplée avec le modèle de plasticité cristalline étendu peut bien décrire le durcissement/adoucissement cyclique de l'acier étudié.

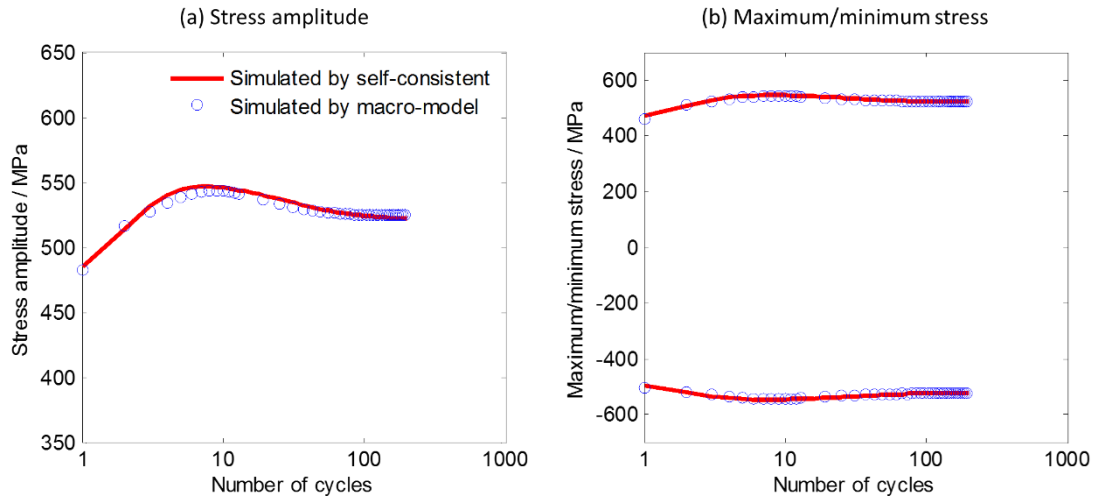

Fig. 11. Comparaison de (a) l'évolution de l'amplitude de contrainte , et (b) la contrainte maxiame/minimale entre les résultats obtenus avec le modèle macroscopique et le modèle auto-cohérent sous amplitude de déformation $\Delta\varepsilon/2 = 1{,}25\%$.

Fig. 12 montre une comparaison des deux premières boucles d'hystérésis (Fig. 12a), ainsi que la 10ème (Fig. 12b) et 180ème boucles (Fig. 12c) entre les résultats obtenus avec les

deux approches. On peut constater que le modèle auto-cohérent développé peut bien décrire le comportement cyclique de l'acier étudié tout au long du chargement cyclique sous l'amplitude de déformation $\Delta\varepsilon/2 = \pm 1{,}25\%$.

Par ailleurs, les effets de nombre de grains et de taux de déformation sont également étudiés avec le modèle de plasticité cristalline développé et les paramètres identifiés. Le modèle de plasticité cristalline, la méthode auto-cohérente, et la procédure d'identification développés dans ce travail sont utiles pour constituer la modélisation multi-échelle du comportement cyclique. Cette approche de modélisation multi-échelle sera présentée dans le Chapitre 6.

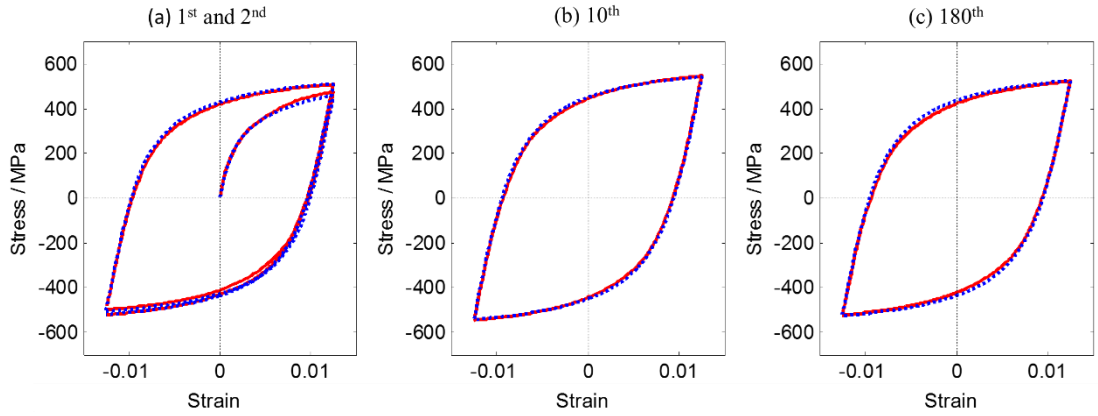

Fig. 12. Comparaison de boucles d'hystérésis pour : (a) 1er et 2ème, (b) 10ème, (c) 180ème, entre les résultats obtenus avec le modèle auto-cohérent (courbes rouges) et le modèle macroscopique (courbes bleues) sous amplitude de déformation $\Delta\varepsilon/2 = 1{,}25\%$.

6. Modélisation multi-échelle du comportement cyclique du gradient de microstructure généré par SMAT

Ce chapitre consiste à présenter une méthodologie de modélisation de contrainte résiduelle et d'écrouissage, et leurs effets sur le comportement cyclique du matériau. Cette méthodologie est développée en se basant sur les travaux présentés dans les précédents chapitres.

6.1 Reconstruction des contraintes résiduelles et de l'écrouissage

Comme décrit ci-dessus, chaque impact de bille pendant le SMAT induit notamment l'évolution de la déformation plastique et celle de la déformation plastique cumulée, ce qui conduit à l'évolution du champ de contraintes résiduelles. Cependant, pour la méthode des Eigenstrain, en général, seulement une loi élastique linéaire ou élastique-plastique parfaite est utilisée lors de la reconstruction des contraintes résiduelles. Comme l'écrouissage du matériau n'a pas été proprement pris en compte, le champ d'écrouissage généré lors de la

reconstruction des contraintes résiduelles ne représente pas le champ d'écrouissage réel au sein du matériau. Par conséquent, en début de l'analyse qui suit, par exemple une traction simple ou un essai de fatigue, une rééquilibrage élastique-plastique se produit lorsque la vraie loi de comportement est appliquée. Cela signifie que le champ de contraintes résiduelles initialement introduit par la méthode des Eigenstrain est modifié et ne représente plus le champ de contraintes résiduelles expérimentalement mesuré qu'on a voulu introduire dans la structure. Ainsi, une loi de comportement qui est capable de décrire le comportement du matériau étudié doit être utilisée lors de la reconstruction des contraintes résiduelles représentatives pour une structure grenaillée. Une nouvelle approche de reconstruction de contraintes résiduelles et d'écrouissage est proposée dans ce travail de thèse, et est schématiquement décrite par Fig. 13.

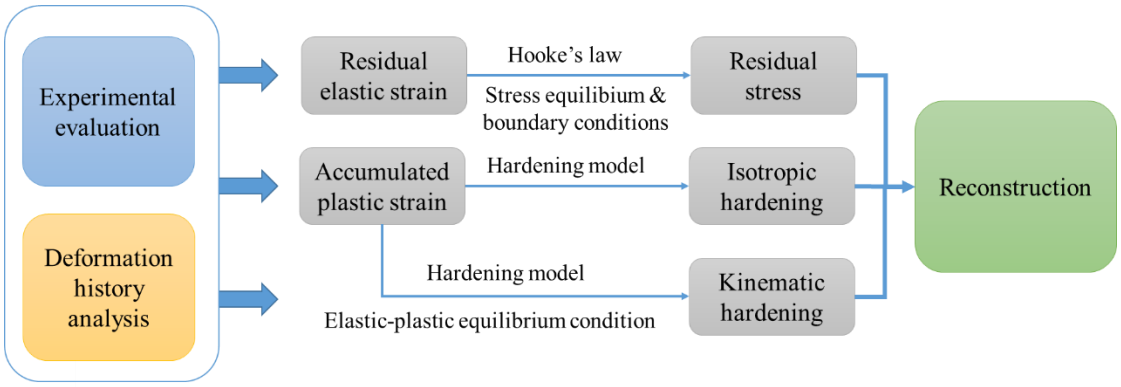

Fig. 13. Description schématique de l'approche de reconstructuion des contraintes résiduelles et de l'écrouissage proposée dans ce travail de thèse.

Cette approche est basée sur la caractérisation du comportement mécanique du matériau sous chargement cyclique, et sur l'évaluation expérimentale de l'histoire de déformation représentée par les contraintes résiduelles et la déformation plastique cumulée. Une loi de comportement qui inclut non seulement l'écrouissage isotrope mais aussi l'écrouissage cinématique est utilisée, et surtout les paramètres de ce modèle doivent être proprement identifiés à partir des résultats expérimentaux. Lors de la reconstruction, on vérifie non seulement l'équilibre des contraintes au sein de toute la structure mais aussi l'équilibre élastique-plastique pour chaque point matériel. De manière itérative, on peut enfin obtenir un champ de contraintes résiduelles qui correspond à celui expérimentalement mesuré, et l'écrouissage isotrope et celui cinématique qui représentent l'histoire de déformation du matériau.

6.2 Reconstruction des contraintes résiduelles

Dans cette partie de reconstruction des contraintes résiduelles, une éprouvette SMATée avec les conditions de traitement (50A, 3000%) est considérée. Comme indiqué dans le Chapitre 3, les contraintes résiduelles sont mesurées par DRX. Pour mesurer les contraintes résiduelles en fonction de la profondeur, le polissage électrolytique est utilisé pour enlever progressivement la matière de la surface de l'éprouvette. Les contraintes de cisaillement de la structure SMATée sont relativement petites et elles ne sont pas prises en compte dans cette étude.

Selon les conditions de l'équilibre de contraintes et du couplage entre les composants du tenseur de contrainte au sein d'une structure, les contraintes résiduelles réelles ($\sigma_r^{\mathrm{rs}}, \sigma_\theta^{\mathrm{rs}}, \sigma_z^{\mathrm{rs}}$) peuvent être corrigées à partir des contraintes mesurées ($\sigma_\theta^{\mathrm{m}}, \sigma_z^{\mathrm{m}}$). Un ensemble de fonctions exponentielles sont établies pour modéliser la variation de contraintes réelles en fonction de la profondeur en se basant sur les conditions aux limites et l'équilibre de contraintes. Fig. 14 montre les variations de contraintes résiduelles au sein de la structure. Les trois courbes représentent les trois composants du tenseur de contrainte reconstruit avec l'approche proposée dans ce travail. La comparaison avec les courbes mesurées (représentées par les points) montre une bonne cohérence, ce qui signifie que l'approche proposée est efficace pour reconstruire le champ de contraintes résiduelles. Noter qu'avec cette approche, le champ de contraintes résiduelles dans la région centrale de la structure, inaccessible expérimentalement due à la difficulté d'effectuer le polissage, peut également être modélisé.

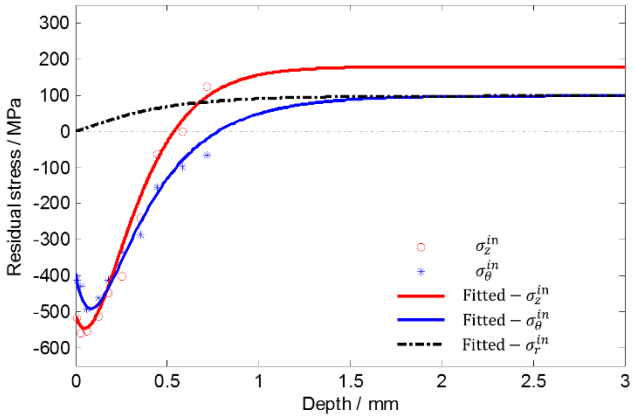

Fig. 14. Variations de contraintes résiduelles en fonction de la profondeur par rapport à la surface de la structure. Les résulats éxpérimentaux sont également présentés pour faciliter la compraison.

6.3 Reconstruction de l'écrouissage

L'écrouissage généré par SMAT est aussi expérimentalement évalué par DRX et pris en compte dans le processus de reconstruction. Fig. 15 montre la variation de la déformation

plastique cumulée représentée par FWHM. Sa distribution est présentée en fonction de la profondeur (voir la courbe rouge avec des marques). Une diminution progressive de FWHM peut être observée, puis devient constante au-delà d'une certaine profondeur. Cette observation signifie que la profondeur du matériau affectée plastiquement par le SMAT est environ 0,675 mm.

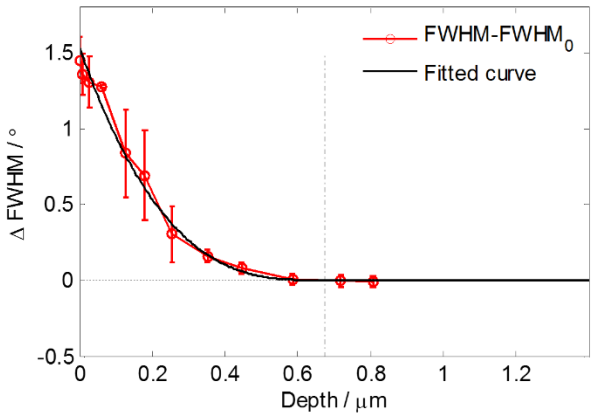

Fig. 15. Variation de ΔFWHM mesurée avec la profondeur (courbe rouge), et celle calée par une fonction établie (courbe noire).

De manière approximative, on considère que la déformation plastique cumulée p^{rs} est proportionnelle à ΔFWHM (qui est défini par la différence entre FWHM mesuré et la valeur de référence FWHM_0 pour le matériau non-affecté plastiquement). Ainsi, la variation de p^{rs} en fonction de la profondeur peut être exprimée comme suit en calant la variation de ΔFWHM:

$$p^{\mathrm{rs}} = \begin{cases} p_0^{\mathrm{rs}}/0{,}3075 \cdot \left(0{,}675 - (R - r)\right)^3 \\ 0, \text{when } r < R - 0{,}675 \end{cases} \tag{24}$$

où p_0^{rs} représente la déformation plastique cumulée sur la surface traitée. La valeur de p_0^{rs} est liée à l'intensité de la déformation plastique et la durée de traitement.

Dans cette section, on se focalise sur le développement d'une méthodologie de reconstruction d'écrouissage basée sur un modèle microscopique tenant compte de l'histoire de déformation. Un volume élémentaire représentatif (VER) est utilisé pour représenter un point matériel au niveau de la surface traitée. Le modèle de plasticité cristalline développé dans le Chapitre 5 est appliqué pour le VER. L'effet dynamique d'impact n'est pas considéré, et le comportement mécanique du point matériel est supposé comme non-dépendant du temps. Le processus de reconstruction est réalisé en appliquant des impacts répétitifs et aléatoires au VER. Cependant, dans ce travail préliminaire, l'angle d'incident

de 90° est appliqué. L'histoire de déformation est évaluée de manière approximative à l'aide de simulation par éléments finis.

Après la simulation de charge-décharge lors d'un impact, les contraintes résiduelles obtenues au niveau de la surface sont appliquées au VER pour le solliciter. L'écrouissage peut être généré au sein du VER, ce qui inclut non seulement la déformation plastique cumulée, mais aussi l'écrouissage cinématique. La variation de la déformation plastique cumulée résiduelle en fonction de la profondeur peut être obtenue selon l'Eq. (24). Dans ce travail préliminaire, nous supposons que le tenseur de l'écrouissage cinématique a la même tendance de variation que la déformation plastique cumulée p^{rs} (Eq. (24)). Ainsi, le tenseur de l'écrouissage cinématique en fonction de la profondeur peut être modélisé avec l'équation suivante :

$$\underline{X}_i^{\mathrm{rs}} = \begin{cases} \underline{X}_i^{\mathrm{rs}}(r=0)/0{,}3075 \times \left(0{,}675 - (R-r)\right)^3 \\ \underline{0}, \text{when } r < R - 0{,}675 \end{cases} \tag{25}$$

6.4 Modélisation du comportement cyclique du matériau SMATé

Dans cette section, le comportement cyclique de la structure SMATée est analysé à l'aide de la simulation en tenant compte des contraintes résiduelles et de l'écrouissage reconstruits. Le modèle éléments finis est montré dans Fig. 16 avec les conditions de symétrie prises en compte. La loi de comportement du matériau avec écrouissages isotrope et cinématique est implémentée dans une subroutine UMAT. Dans ce travail de simulation, seul le comportement obtenu avec $\Delta\varepsilon/2 = \pm 1{,}25\%$ est considéré. Toutes les variables initiales ($\underline{\sigma}^{\mathrm{in}}, \underline{X}^{\mathrm{in}}, p^{\mathrm{in}}$) sont d'abord introduites dans le modèle éléments finis via les subroutines SIGINI et SDVINI. Noter que les composants de cisaillement des tenseurs $\underline{\sigma}^{\mathrm{in}}$ et $\underline{X}^{\mathrm{in}}$ ne sont pas pris en compte. Trois configurations initiales sont considérées. La première correspond à l'état de réception sans la présence des contraintes et d'écrouissage initiaux (Cas I). Dans la seconde configuration, seul le champ de contrainte initial équilibré est introduit (Cas II). Quant à la troisième configuration, les contraintes et l'écrouissage initiaux sont pris en compte tous à la fois (Cas III).

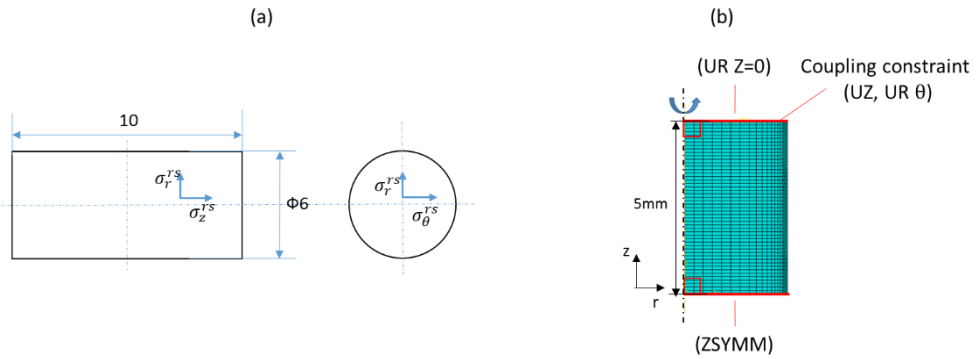

Fig. 16. (a) sytème cylindrique pour la structure, et (b) le modèle éléments finis avec les conditions aux limites appliquées.

La procédure d'analyse est composée de deux étapes. La première étape correspond au processus d'auto-équilibrage des contraintes résiduelles et de l'écrouissage introduits au sein de la structure entière. Pendant cette étape d'auto-équilibrage, le déplacement dans la direction Z (Uz) est libre. Alors que pour la seconde étape, un déplacement périodique est imposé pour simuler le chargement cyclique. Le déplacement est contrôlé pour que l'amplitude de déformation imposé correspond à $\Delta\varepsilon = \pm 1{,}25\%$.

6.4.1 Équilibre des contraintes et de l'écrouissage initiaux

Fig. 17a montre qu'il y a une redistribution apparente du champ de contrainte pour le Cas II dans l'étape d'analyse. Cela est dû au fait qu'il n'y a pas d'écrouissage introduit dans la structure, et les conditions d'équilibre élasto-plastique ne sont pas satisfaites en début de l'analyse. Selon la Fig. 17b, les trois composants du tenseur de contrainte après l'auto-équilibrage sont bien cohérents avec les valeurs imposées pour le Cas III. Cela signifie que les variables reconstruites $(\underline{\sigma}^{\mathrm{in}}, \underline{X}^{\mathrm{in}}, p^{\mathrm{in}})$ pour le Cas III sont presque équilibrées, et la méthode de reconstruction proposée est donc valide. La légère redistribution de contraintes résiduelles montrée en Fig. 17b peut être attribuée aux composants de cisaillement des tenseurs d'écrouissage cinématique qui n'ont pas été pris en compte. De plus, les variables d'écrouissage cinématique sont évaluées de manière approximative à l'aide de la déformation plastique cumulée résiduelle, ce qui peut induire une erreur pour les conditions d'équilibre élasto-plastique de la structure.

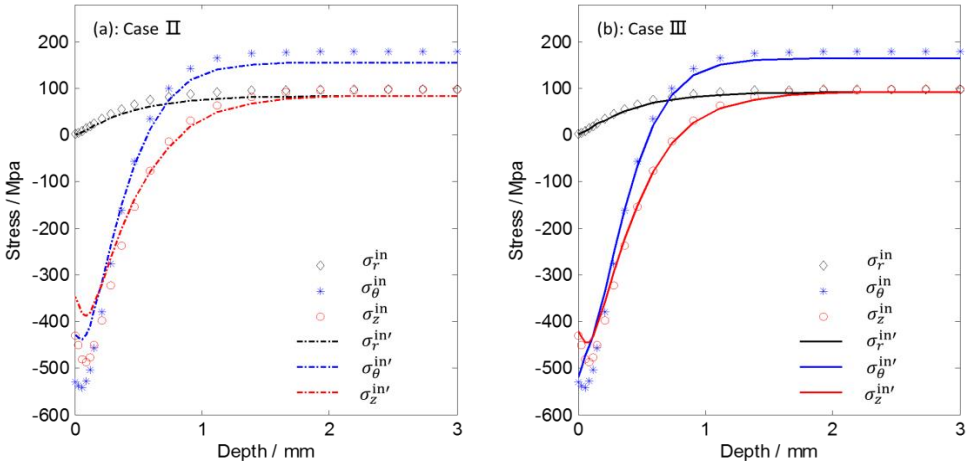

Fig. 17. (a) comparaison entre les contraintes imposées et celles en état équlibré pour les Cas II et Cas III.

6.4.2 Relaxation des contraintes résiduelles

Fig. 18 présente l'évolution des trois composantes de contrainte pendant les deux premiers cycles pour un point matériel au niveau de la surface traitée. On peut constater que les contraintes résiduelles radiale et circonférentielle au niveau de la surface sont presque toutes relaxées pendant le premier cycle. De plus, la contrainte axiale sur la surface traitée est diminuée significativement par rapport à la contrainte axiale au centre de l'éprouvette. Après le premier cycle, la contrainte axiale au niveau de la surface traitée (courbe solide rouge) devient plus élevée que la contrainte au centre de l'éprouvette (courbe pointillée rouge). Ce phénomène doit être dû à l'effet combiné des contraintes résiduelles et de l'écrouissage. La contrainte résiduelle axiale est presque toute relaxée pendant le premier cycle d'une part. L'écrouissage initial peut induire un niveau de contrainte plus élevée pour le matériau d'autre part.

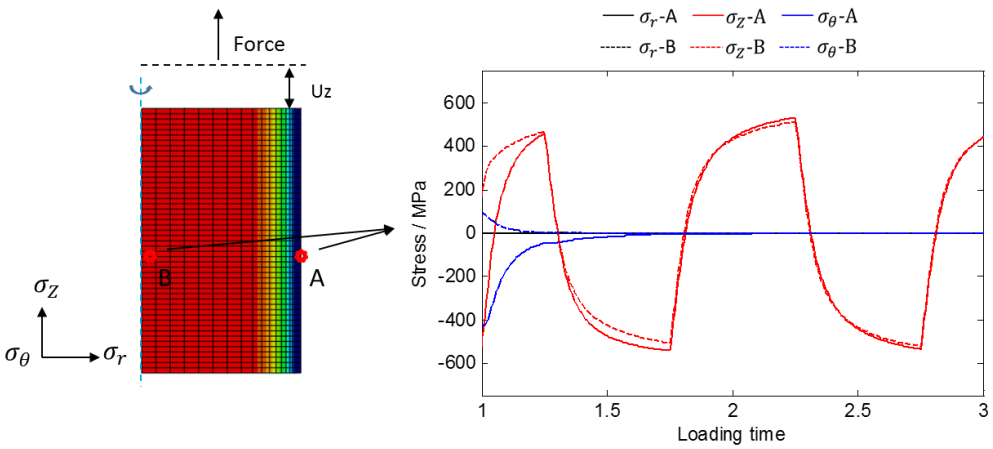

Fig. 18. Evolution des trois composantes du tenseur de contrainte pour les points matériels à la surface (point A) et dans la région centrale (B) pendant les deux premiers cycles.

6.4.3 Comportement cyclique

Fig. 19 illustre les courbes de l'amplitude de contrainte cyclique de ces trois cas avec différentes configurations. On peut constater que la courbe bleue (Cas II) est presque superposée avec la courbe de l'état de réception (Cas I). Ce phénomène signifie qu'un champ de contrainte équilibré a un faible effet sur le comportement cyclique global de la structure. En effet, la différence de comportement mécanique de la structure entière est essentiellement due aux variables de l'écrouissage cinématique impliquées. Il peut être observé que le Cas III présente une amplitude de contrainte plus élevée que les deux autres courbes pendant les premiers cycles. D'une part, l'écrouissage cinématique initial peut changer la position de la surface de charge, et par conséquent il influe sur la limite d'élasticité du matériau pendant la déformation plastique. D'autre part, la déformation plastique cumulée résiduelle peut induire le durcissement/adoucissement cyclique dû à l'effet isotrope impliqué à la fois dans l'écrouissage cinématique et isotrope. Par contre, les analyses expérimentales effectuées dans les Chapitre 2 and Chapitre 3 montrent que les éprouvettes SMATées et grenaillées manifestent des amplitudes de contrainte plus élevées que les éprouvettes non-traitées. Ce phénomène de renforcement significatif des structures SMATées et grenaillées peut être attribué à la pré-déformation ou l'effet mémoire due à la déformation plastique sévère générée par le traitement.

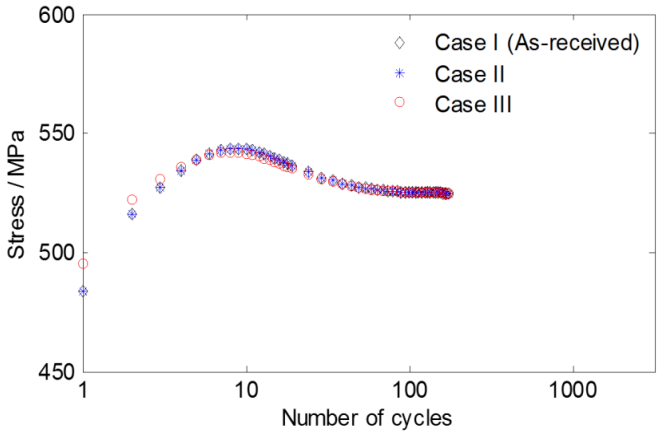

Fig. 19. Comparaison de l'amplitude de contrainte entre les trois cas avec différentes de configurations initiales.

7. Conclusions et perspectives

L'objectif de ce travail de thèse a été d'étudier le comportement cyclique des aciers 316L traités par SMAT à travers des analyses expérimentales et des méthodes de modélisation multi-échelle.

Dans le Chapitre 2, le raffinement des grains, les contraintes résiduelles et l'écrouissage générés par SMAT sont caractérisés avec EBSD, DRX. Les résultats des essais de fatigue

montrent que l'amplitude de contrainte cyclique des éprouvettes SMATées est renforcée significativement avec des amplitudes de déformation de ±0,5% à ±1,25%. L'évolution de la microstructure pendant le chargement cyclique avec $\Delta\varepsilon = \pm 1{,}25\%$ est analysée à l'aide d'observations par EBSD. La comparaison entre SMAT et grenaillage conventionnel est effectuée dans le Chapitre 3 en analysant la topographie de surface, les contraintes résiduelles de compression, et l'écrouissage ainsi que leurs effets sur la durée de vie en fatigue. Noter que la différence de la durée de vie entre les éprouvettes SMATées et grenaillées peut être attribuée à la compétition entre les contraintes résiduelles de compression et la topographie de surface.

Dans le Chapitre 4, le comportement cyclique de deux aciers 316L est analysé expérimentalement sous essais de fatigue oligocyclique. L'effet mémoire de déformation significatif peut être observé pour tous les deux aciers. Selon les résultats, le comportement de durcissement/adoucissement cyclique ainsi que l'effet mémoire de déformation est essentiellement attribué à l'écrouissage cinématique. Un ensemble de relations sont proposées dans le cadre de l'écrouissage cinématique/isotrope combiné en vue de décrire le comportement cyclique de l'acier 316L-A. Dans le Chapitre 5, la modélisation du comportement cyclique avec l'approche auto-cohérente est effectuée. Pour ce faire, une loi d'écrouissage cinématique non-linéaire est proposée à l'échelle du système de glissement pour décrire le durcissement/adoucissement cyclique induit par l'écrouissage cinématique. Les paramètres du matériau, qui correspondent au comportement cyclique de l'acier 316L-A sous l'amplitude de déformation de ±1,25% sont déterminés en utilisant une procédure d'identification développée dans ce travail.

Dans le Chapitre 6, le comportement cyclique du matériau SMATé est étudié avec une modélisation multi-échelle. Une nouvelle méthode de reconstruction de contraintes résiduelles et d'écrouissage est développée et appliquée à une structure SMATée. Le champ de contraintes résiduelles et d'écrouissage sont reconstruits basés sur la mesure de contraintes par DRX, la relation d'équilibre de contrainte, les conditions aux limites ainsi que l'analyse de l'histoire de déformation. La méthode de reconstruction développée est validée à l'aide d'une analyse d'auto-équilibrage avec un modèle éléments finis. La relaxation de contraintes résiduelles et l'effet de renforcement du matériau SMATé sont étudiés avec la simulation de chargement cyclique.

En ce qui concerne les perspectives, des méthodes avancées de caractérisation devraient être utilisées pour comprendre les mécanismes de déformation et les propriétés en fatigue des matériaux SMATés. De plus, des modèles constitutifs devraient être développés

davantage afin de décrire de manière précise le comportement cyclique complexe des matériaux étudiés, par exemple l'effet de la pré-déformation, l'effet mémoire de déformation. Pour la reconstruction des contraintes résiduelles et d'écrouissage, d'une part des approches de caractérisation expérimentale devraient être développées pour caractériser quantitativement l'écrouissage. D'autre part, la simulation de l'histoire de déformation devrait correspondre mieux au mécanisme de déformation réel en tenant compte, par exemple de l'effet de taux de déformation, du trajet de chargement. Par ailleurs, une approche multi-échelle performante est recommandée pour la suite de ce travail.

Appendix

Appendix A: Electrolytic polishing a cylindrical structure

In order to perform XRD analysis in different depth of the cylindrical structure, a polishing procedure is developed, as shown in Fig. A-1. The surface of the cylindrical sample is firstly cleaned using the industrial alcohol. Then, a covering layer is made from polyurethane to protect the surface material against polishing. In addition, two wires are installed at the two sides of the sample for electric conduction, as given in Fig. A-2. For the electrolytic polishing process, the sample is put into the electrolyte which is connected to a cathode, while the sample is connected to an anode. The voltage and the current for the polishing are controlled through a DC power supply (Struers, LectroPol-5).

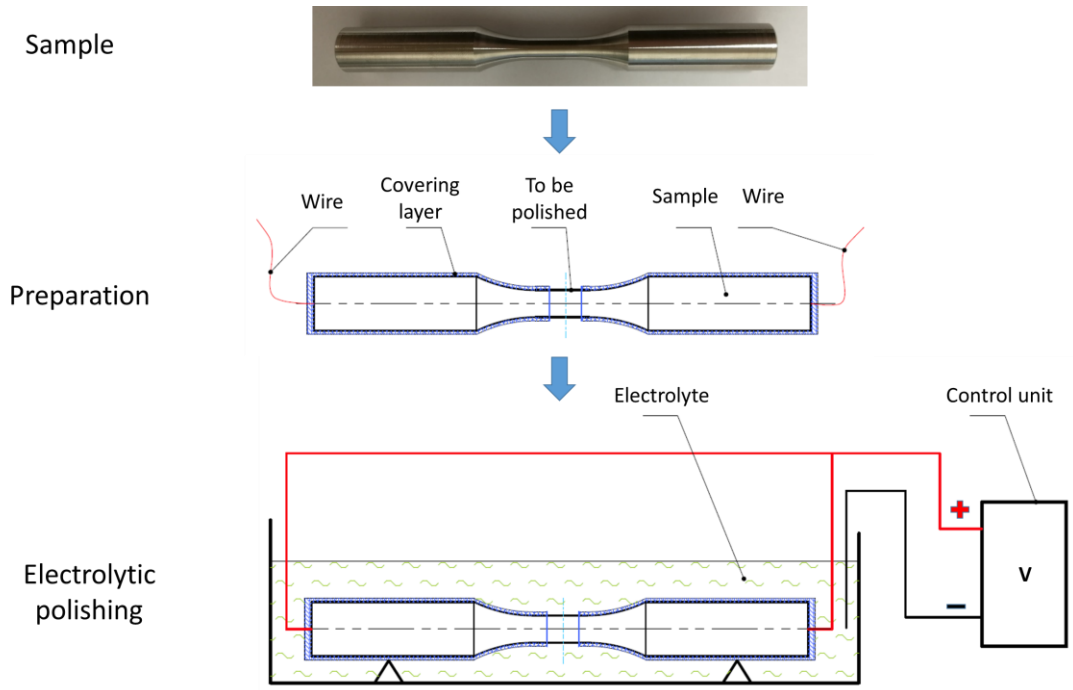

Fig. A-1. Schematic diagram for electrolytic polishing a cylindrical structure.

A screw micrometre is used to measure the diameter in the polished position of the sample, and then the polished depth can be quantitatively calculated. To ensure that the

surface material is uniformly removed, a re-placing process of the sample with a rotation of 90° is preferably recommended during the polishing process.

Using the above procedure, iterative electrolytic polishing is performed on the cylindrical structure, and the subsequent XRD analysis can thus be carried out in the given depth of the sample. Fig. A-2 presents a group of the prepared samples.

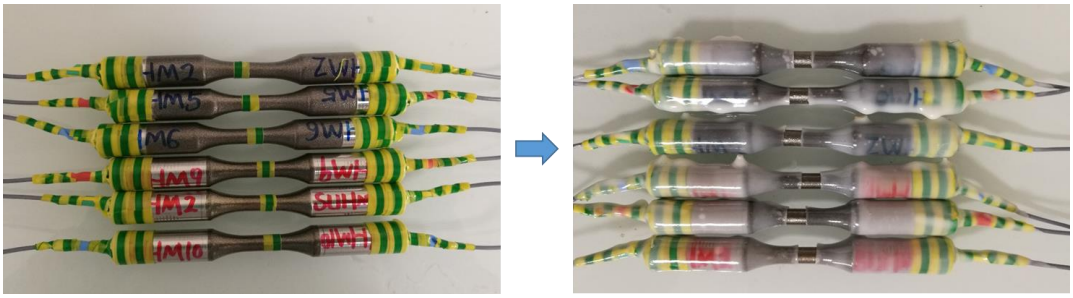

Fig. A-2. A group of the prepared samples.

Appendix B: Calibration results for the macroscopic cycle constitutive modelling

Calibration results for the variables in different identification steps in Chapter are shown in the following four figures. Fig. B-1, 2, 3, 4 respectively illustrate the calibration results of kinematic hardening variable $\tilde{X}$ (Eq. (4-39)), kinematic hardening coefficient φ (Eqs. (4-34), (4-35) and (4-36)), strain range memory effect parameters (Eq. (4-37)) and isotropic hardening parameters (Eqs. (4-14) and (4-15)) coupled with the initial yield stress.

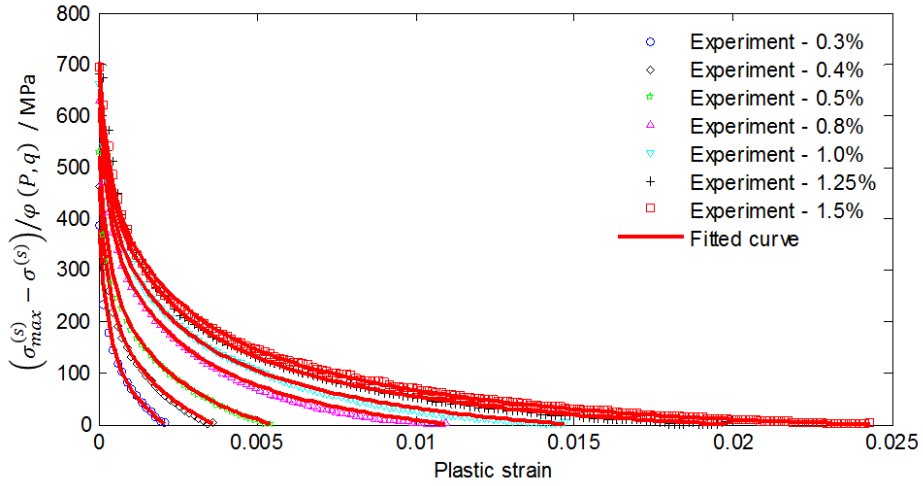

Figure B-1. Calibration of kinematic hardening variable $\tilde{X}$ with Eq. (4-39).

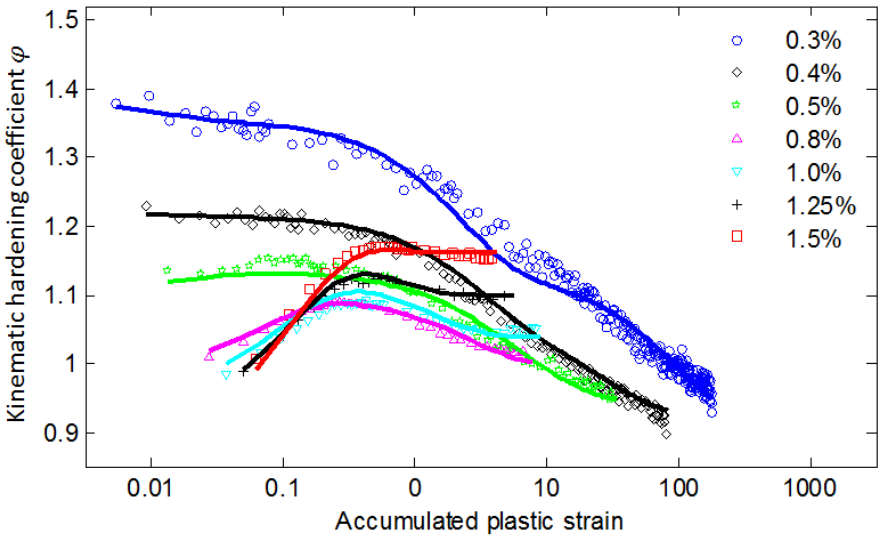

Figure B-2. Calibration of kinematic hardening coefficient φ with Eqs. (4-34), (4-35) and (4-36).

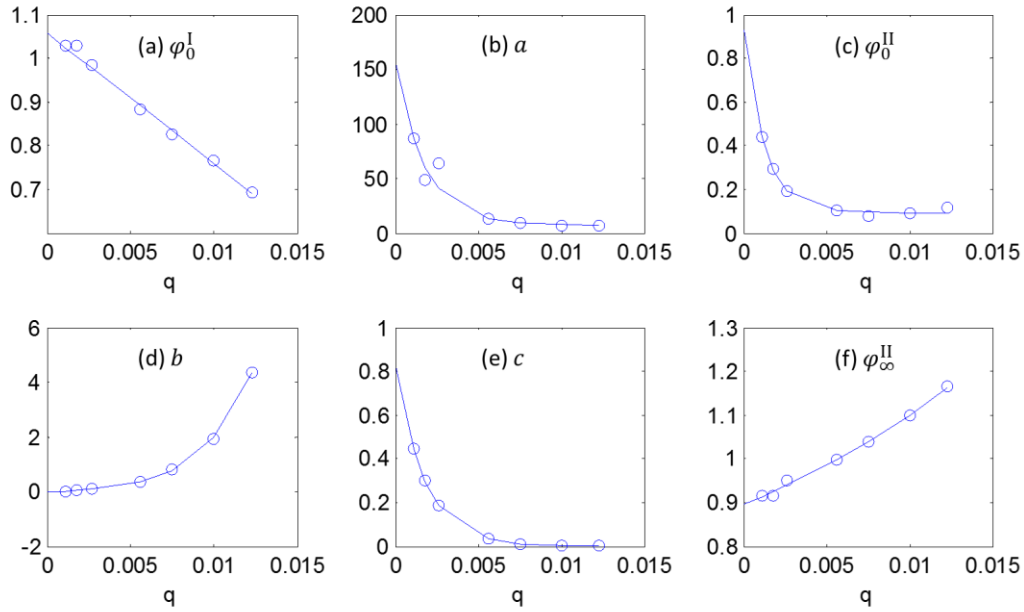

Figure B-3. Calibration of strain range memory effect parameters A, B, M with Eq. (4-37).

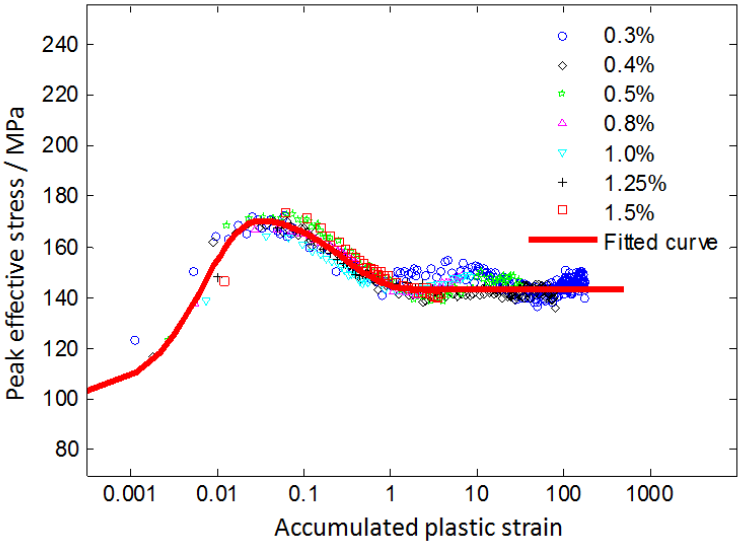

Figure B-4. Calibration of peak effective stress with $R + k$.

Appendix C: Euler angles of the 50 grains for self-consistent modelling work in Chapter 5

Grain number	φ_1	φ	φ_2	Grain number	φ_1	φ	φ_2
1	112.89	143.94	319.94	26	289.90	18.24	231.37
2	199.19	113.44	302.46	27	96.85	12.94	97.79
3	285.14	176.90	87.85	28	156.23	162.81	38.43
4	287.39	28.48	156.82	29	144.65	56.12	21.78
5	310.77	111.00	298.28	30	218.93	106.52	223.88
6	287.27	55.57	54.97	31	277.23	67.97	251.67
7	2.30	15.31	272.86	32	338.80	171.28	98.98
8	331.16	157.83	315.54	33	47.33	133.63	151.91
9	6.47	106.33	180.76	34	92.06	159.68	131.70
10	10.59	54.56	205.30	35	136.19	107.80	29.58
11	256.12	30.25	306.53	36	357.74	124.13	25.12
12	193.83	61.18	354.47	37	122.74	70.40	43.52
13	188.85	12.14	284.48	38	323.84	40.19	244.03
14	180.81	117.63	126.25	39	85.49	23.63	78.82
15	23.64	43.97	180.69	40	79.20	31.05	85.42
16	82.81	136.43	91.88	41	356.79	168.95	3.11
17	42.13	53.82	183.55	42	342.40	6.21	261.76
18	356.32	75.39	28.30	43	229.76	158.32	201.97
19	25.39	10.05	20.12	44	181.49	94.02	198.71
20	21.61	5.55	228.60	45	128.92	145.48	267.21
21	238.17	33.58	222.09	46	276.64	80.56	296.87
22	123.86	48.76	29.33	47	282.37	62.38	141.62
23	46.26	11.92	219.43	48	10.41	136.29	48.94
24	229.37	60.03	196.08	49	18.88	64.84	70.47
25	268.74	8.98	308.13	50	116.43	100.19	259.31

References

[1] Lu K, Lu J. Nanostructured surface layer on metallic materials induced by surface mechanical attrition treatment. Mater Sci Eng A 2004;375:38–45. doi:10.1016/j.msea.2003.10.261.

[2] Bagheri S, Guagliano M. Review of shot peening processes to obtain nanocrystalline surfaces in metal alloys. Surf Eng 2009;25:3–14. doi:10.1179/026708408X334087.

[3] Montross CS, Wei T, Ye L, Clark G, Mai Y-W. Laser shock processing and its effects on microstructure and properties of metal alloys: a review. Int J Fatigue 2002;24:1021–36. doi:10.1016/S0142-1123(02)00022-1.

[4] Gujba KA, Medraj M. Laser Peening Process and Its Impact on Materials Properties in Comparison with Shot Peening and Ultrasonic Impact Peening. Materials 2014;7:7925–74. doi:10.3390/ma7127925.

[5] Altenberger I, Scholtes B, Martin U, Oettel H. Cyclic deformation and near surface microstructures of shot peened or deep rolled austenitic stainless steel AISI 304. Mater Sci Eng A 1999;264:1–16. doi:10.1016/S0921-5093(98)01121-6.

[6] Huang HW, Wang ZB, Lu J, Lu K. Fatigue behaviors of AISI 316L stainless steel with a gradient nanostructured surface layer. Acta Mater 2015;87:150–60. doi:10.1016/j.actamat.2014.12.057.

[7] Chen XH, Lu J, Lu L, Lu K. Tensile properties of a nanocrystalline 316L austenitic stainless steel. Scr Mater 2005;52:1039–44. doi:10.1016/j.scriptamat.2005.01.023.

[8] Roland T, Retraint D, Lu K, Lu J. Fatigue life improvement through surface nanostructuring of stainless steel by means of surface mechanical attrition treatment. Scr Mater 2006;54:1949–54. doi:10.1016/j.scriptamat.2006.01.049.

[9] Withers PJ, Bhadeshia HKDH. Residual stress. Part 1 – Measurement techniques. Mater Sci Technol 2001;17:355–65. doi:10.1179/026708301101509980.

[10] Withers PJ, Bhadeshia HKDH. Residual stress. Part 2 – Nature and origins. Mater Sci Technol 2001;17:366–75. doi:10.1179/026708301101510087.

[11] Roland T, Retraint D, Lu K, Lu J. Enhanced mechanical behavior of a nanocrystallised stainless steel and its thermal stability. Mater Sci Eng A 2007;445–446:281–8. doi:10.1016/j.msea.2006.09.041.

[12] Marsh KJ. Shot peening : techniques and applications. Warley: EMAS; 1993.

[13] Ding K, Ye L. Laser shock peening : performance and process simulation. CRC Press; 2006.

[14] Yin F, Rakita M, Hu S, Han Q. Overview of ultrasonic shot peening. Surf Eng 2017;33:651–66. doi:10.1080/02670844.2017.1278838.

[15] Azadmanjiri J, Berndt CC, Kapoor A, Wen C. Development of Surface Nano-Crystallization in Alloys by Surface Mechanical Attrition Treatment (SMAT). Crit Rev Solid State Mater Sci 2015;40:164–81. doi:10.1080/10408436.2014.978446.

[16] Zhang H., Hei Z., Liu G, Lu J, Lu K. Formation of nanostructured surface layer on AISI 304 stainless steel by means of surface mechanical attrition treatment. Acta Mater 2003;51:1871–81. doi:10.1016/S1359-6454(02)00594-3.

[17] Arifvianto B, Suyitno, Mahardika M, Dewo P, Iswanto PT, Salim UA. Effect of surface mechanical attrition treatment (SMAT) on microhardness, surface roughness

and wettability of AISI 316L. Mater Chem Phys 2011;125:418–26. doi:10.1016/j.matchemphys.2010.10.038.

[18] Wang Z., Tao N., Li S, Wang W, Liu G, Lu J, et al. Effect of surface nanocrystallization on friction and wear properties in low carbon steel. Mater Sci Eng A 2003;352:144–9. doi:10.1016/S0921-5093(02)00870-5.

[19] Singh V, Pandey V, Kumar S, Srinivas NCS, Chattopadhyay K. Effect of Ultrasonic Shot Peening on Surface Microstructure and Fatigue Behavior of Structural Alloys. Trans Indian Inst Met 2016;69:295–301. doi:10.1007/s12666-015-0771-x.

[20] Arifvianto B, Suyitno, Mahardika M. Effects of surface mechanical attrition treatment (SMAT) on a rough surface of AISI 316L stainless steel. Appl Surf Sci 2012;258:4538–43. doi:10.1016/j.apsusc.2012.01.021.

[21] Bagherifard S, Guagliano M. Fatigue behavior of a low-alloy steel with nanostructured surface obtained by severe shot peening. Fract Damage Anal Des 2012;81:56–68. doi:10.1016/j.engfracmech.2011.06.011.

[22] Anand Kumar S, Ganesh Sundara Raman S, Sankara Narayanan TSN, Gnanamoorthy R. Influence of counterbody material on fretting wear behaviour of surface mechanical attrition treated Ti–6Al–4V. Tribol Int 2013;57:107–14. doi:10.1016/j.triboint.2012.07.021.

[23] Chemkhi M, Retraint D, Roos A, Garnier C, Waltz L, Demangel C, et al. The effect of surface mechanical attrition treatment on low temperature plasma nitriding of an austenitic stainless steel. Surf Coat Technol 2013;221:191–5. doi:10.1016/j.surfcoat.2013.01.047.

[24] Tao NR, Wang ZB, Tong WP, Sui ML, Lu J, Lu K. An investigation of surface nanocrystallization mechanism in Fe induced by surface mechanical attrition treatment. Acta Mater 2002;50:4603–16. doi:10.1016/S1359-6454(02)00310-5.

[25] Unal O, Varol R. Surface severe plastic deformation of AISI 304 via conventional shot peening, severe shot peening and repeening. Appl Surf Sci 2015;351:289–95. doi:10.1016/j.apsusc.2015.05.093.

[26] Li WL, Tao NR, Lu K. Fabrication of a gradient nano-micro-structured surface layer on bulk copper by means of a surface mechanical grinding treatment. Scr Mater 2008;59:546–9. doi:10.1016/j.scriptamat.2008.05.003.

[27] Valiev R., Islamgaliev R., Alexandrov I. Bulk nanostructured materials from severe plastic deformation. Prog Mater Sci 2000;45:103–89. doi:10.1016/S0079-6425(99)00007-9.

[28] Azushima A, Kopp R, Korhonen A, Yang DY, Micari F, Lahoti GD, et al. Severe plastic deformation (SPD) processes for metals. CIRP Ann 2008;57:716–35. doi:10.1016/j.cirp.2008.09.005.

[29] Valiev RZ. Structure and mechanical properties of ultrafine-grained metals. Mater Sci Eng A 1997;234–236:59–66. doi:10.1016/S0921-5093(97)00183-4.

[30] Wang ZB, Lu J, Lu K. Wear and corrosion properties of a low carbon steel processed by means of SMAT followed by lower temperature chromizing treatment. Surf Coat Technol 2006;201:2796–801. doi:10.1016/j.surfcoat.2006.05.019.

[31] Rofagha R, Langer R, El-Sherik AM, Erb U, Palumbo G, Aust KT. The corrosion behaviour of nanocrystalline nickel. Scr Metall Mater 1991;25:2867–72. doi:10.1016/0956-716X(91)90171-V.

[32] Mishra R, Balasubramaniam R. Effect of nanocrystalline grain size on the electrochemical and corrosion behavior of nickel. Corros Sci 2004;46:3019–29. doi:10.1016/j.corsci.2004.04.007.

[33] Padilla HA, Boyce BL. A Review of Fatigue Behavior in Nanocrystalline Metals. Exp Mech 2010;50:5–23. doi:10.1007/s11340-009-9301-2.

[34] E O Hall. The Deformation and Ageing of Mild Steel: III Discussion of Results. Proc Phys Soc Sect B 1951;64:747.

[35] N. J. P. The Cleavage Strength of Polycrystals. J Iron Steel Inst 1953;174:25–8.
[36] Balusamy T, Kumar S, Sankara Narayanan TSN. Effect of surface nanocrystallization on the corrosion behaviour of AISI 409 stainless steel. Corros Sci 2010;52:3826–34. doi:10.1016/j.corsci.2010.07.004.
[37] Hao Y, Deng B, Zhong C, Jiang Y, Li J. Effect of Surface Mechanical Attrition Treatment on Corrosion Behavior of 316 Stainless Steel. J Iron Steel Res Int 2009;16:68–72. doi:10.1016/S1006-706X(09)60030-3.
[38] Hanlon T, Tabachnikova ED, Suresh S. Fatigue behavior of nanocrystalline metals and alloys. Fatigue Damage Struct Mater V 2005;27:1147–58. doi:10.1016/j.ijfatigue.2005.06.035.
[39] Höppel HW, Zhou ZM, Mughrabi H, Valiev RZ. Microstructural study of the parameters governing coarsening and cyclic softening in fatigued ultrafine-grained copper. Philos Mag A 2002;82:1781–94. doi:10.1080/01418610208235689.
[40] Witney AB, Sanders PG, Weertman JR, Eastman JA. Fatigue of nanocrystalline copper. Scr Metall Mater 1995;33:2025–30. doi:10.1016/0956-716X(95)00441-W.
[41] Lu J. Prestress Engineering of Structural Material: A Global Design Approach to the Residual Stress. Handb. Residual Stress Deform. Steel, Materials Park, OH: ASM International; 2002, p. 11–26.
[42] Dalaei K, Karlsson B, Svensson L-E. Stability of shot peening induced residual stresses and their influence on fatigue lifetime. Mater Sci Eng A 2011;528:1008–15. doi:10.1016/j.msea.2010.09.050.
[43] Li Y. Shot-peening and low-cycle fatigue of titanium alloys : instrumented indentation and X-ray diffraction. PhD Thesis. Université de technologie de Troyes, 2015.
[44] Salvati E, Korsunsky AM. An analysis of macro- and micro-scale residual stresses of Type I, II and III using FIB-DIC micro-ring-core milling and crystal plasticity FE modelling. Int J Plast 2017;98:123–38. doi:10.1016/j.ijplas.2017.07.004.
[45] Hu J, Chen B, Smith DJ, Flewitt PEJ, Cocks ACF. On the evaluation of the Bauschinger effect in an austenitic stainless steel—The role of multi-scale residual stresses. Int J Plast 2016;84:203–23. doi:10.1016/j.ijplas.2016.05.009.
[46] Black JT, Kohser RA. DeGarmo's materials and processes in manufacturing /. 10th ed. Hoboken, NJ : Wiley,; 2008.
[47] Rollett AD, Kocks UF. A Review of the Stages of Work Hardening. Solid State Phenom 1993;35–36:1–18. doi:10.4028/www.scientific.net/SSP.35-36.1.
[48] Mughrabi H. Dislocation wall and cell structures and long-range internal stresses in deformed metal crystals. Acta Metall 1983;31:1367–79. doi:10.1016/0001-6160(83)90007-X.
[49] Pham MS, Holdsworth SR, Janssens KGF, Mazza E. Cyclic deformation response of AISI 316L at room temperature: Mechanical behaviour, microstructural evolution, physically-based evolutionary constitutive modelling. Int J Plast 2013;47:143–64. doi:10.1016/j.ijplas.2013.01.017.
[50] Sauzay M. Analytical modelling of intragranular backstresses due to deformation induced dislocation microstructures. Int J Plast 2008;24:727–45. doi:10.1016/j.ijplas.2007.07.004.
[51] Feaugas X, Gaudin C. Different levels of plastic strain incompatibility during cyclic loading: in terms of dislocation density and distribution. Dislocations 2000 Int Conf Fundam Plast Deform 2001;309–310:382–5. doi:10.1016/S0921-5093(00)01730-5.
[52] Feaugas X, Gaudin C. Ratchetting process in the stainless steel AISI 316L at 300 K: an experimental investigation. Int J Plast 2004;20:643–62. doi:10.1016/S0749-6419(03)00076-7.

[53] Gaudin C, Feaugas X. Cyclic creep process in AISI 316L stainless steel in terms of dislocation patterns and internal stresses. Acta Mater 2004;52:3097–110. doi:10.1016/j.actamat.2004.03.011.

[54] Kimiecik M, Jones JW, Daly S. The effect of microstructure on stress-induced martensitic transformation under cyclic loading in the SMA Nickel-Titanium. J Mech Phys Solids 2016;89:16–30. doi:10.1016/j.jmps.2016.01.007.

[55] Nishiyama Z, Fine ME, Meshii M, Wayman CM (Clarence M. Martensitic transformation / Zenji Nishiyama ; edited by Morris E. Fine, M. Meshii, C. M. Wayman. New York: Academic Press; 1978.

[56] Wu X, Tao N, Hong Y, Xu B, Lu J, Lu K. Microstructure and evolution of mechanically-induced ultrafine grain in surface layer of AL-alloy subjected to USSP. Acta Mater 2002;50:2075–84. doi:10.1016/S1359-6454(02)00051-4.

[57] Zhu KY, Vassel A, Brisset F, Lu K, Lu J. Nanostructure formation mechanism of α-titanium using SMAT. Acta Mater 2004;52:4101–10. doi:10.1016/j.actamat.2004.05.023.

[58] Huang L, Lu J, Troyon M. Nanomechanical properties of nanostructured titanium prepared by SMAT. Surf Coat Technol 2006;201:208–13. doi:10.1016/j.surfcoat.2005.11.090.

[59] Tumbajoy-Spinel D, Descartes S, Bergheau J-M, Lacaille V, Guillonneau G, Michler J, et al. Assessment of mechanical property gradients after impact-based surface treatment: application to pure α-iron. Mater Sci Eng A 2016;667:189–98. doi:10.1016/j.msea.2016.04.059.

[60] Sun Z, Retraint D, Guelorget B, Waltz L. Micro-pillar compression tests to characterize the mechanical behavior of a nanocrystalline layer induced by SMAT in a 316L stainless steel. Matér Tech 2015;103. doi:10.1051/mattech/2015028.

[61] Petit J, Waltz L, Montay G, Retraint D, Roos A, François M. Multilayer modelling of stainless steel with a nanocrystallised superficial layer. Mater Sci Eng A 2012;536:124–8. doi:10.1016/j.msea.2011.12.085.

[62] Z Sun and M Chemkhi and P Kanoute and D Retraint. Fatigue properties of a biomedical 316L steel processed by surface mechanical attrition. IOP Conf Ser Mater Sci Eng 2014;63:012021.

[63] Kumar S, Chattopadhyay K, Singh V. Effect of ultrasonic shot peening on LCF behavior of the Ti–6Al–4V alloy. J Alloys Compd 2017;724:187–97. doi:10.1016/j.jallcom.2017.07.014.

[64] Pandey V, Rao GS, Chattopadhyay K, Santhi Srinivas NC, Singh V. Effect of surface Nanostructuring on LCF behavior of aluminum alloy 2014. Mater Sci Eng A 2015;647:201–11. doi:10.1016/j.msea.2015.09.021.

[65] Pandey V, Chattopadhyay K, Santhi Srinivas NC, Singh V. Role of ultrasonic shot peening on low cycle fatigue behavior of 7075 aluminium alloy. Int J Fatigue 2017;103:426–35. doi:10.1016/j.ijfatigue.2017.06.033.

[66] Li D, Chen HN, Xu H. The effect of nanostructured surface layer on the fatigue behaviors of a carbon steel. Appl Surf Sci 2009;255:3811–6. doi:10.1016/j.apsusc.2008.10.037.

[67] Zhang K, Wang ZB, Lu K. Enhanced fatigue property by suppressing surface cracking in a gradient nanostructured bearing steel. Mater Res Lett 2017;5:258–66. doi:10.1080/21663831.2016.1253625.

[68] Villegas JC, Shaw LL, Dai K, Yuan W, Tian J, Liaw PK, et al. Enhanced fatigue resistance of a nickel-based hastelloy induced by a surface nanocrystallization and hardening process. Philos Mag Lett 2005;85:427–38. doi:10.1080/09500830500311705.

[69] Holzapfel H, Schulze V, Vöhringer O, Macherauch E. Residual stress relaxation in an AISI 4140 steel due to quasistatic and cyclic loading at higher temperatures. Mater Sci Eng A 1998;248:9–18. doi:10.1016/S0921-5093(98)00522-X.

[70] Altenberger I, Scholtes B, Martin U, Oettel H. Cyclic deformation and near surface microstructures of shot peened or deep rolled austenitic stainless steel AISI 304. Mater Sci Eng A 1999;264:1–16. doi:10.1016/S0921-5093(98)01121-6.

[71] Wick A, Schulze V, Vöhringer O. Effects of warm peening on fatigue life and relaxation behaviour of residual stresses in AISI 4140 steel. Mater Sci Eng A 2000;293:191–7. doi:10.1016/S0921-5093(00)01035-2.

[72] Zhuang WZ, Halford GR. Investigation of residual stress relaxation under cyclic load. Int J Fatigue 2001;23:31–7. doi:10.1016/S0142-1123(01)00132-3.

[73] Dalaei K, Karlsson B. Influence of shot peening on fatigue durability of normalized steel subjected to variable amplitude loading. Int J Fatigue 2012;38:75–83. doi:10.1016/j.ijfatigue.2011.11.011.

[74] Laamouri A, Sidhom H, Braham C. Evaluation of residual stress relaxation and its effect on fatigue strength of AISI 316L stainless steel ground surfaces: Experimental and numerical approaches. Int J Fatigue 2013;48:109–21. doi:10.1016/j.ijfatigue.2012.10.008.

[75] Foss BJ, Gray S, Hardy MC, Stekovic S, McPhail DS, Shollock BA. Analysis of shot-peening and residual stress relaxation in the nickel-based superalloy RR1000. Acta Mater 2013;61:2548–59. doi:10.1016/j.actamat.2013.01.031.

[76] Kim J-C, Cheong S-K, Noguchi H. Residual stress relaxation and low- and high-cycle fatigue behavior of shot-peened medium-carbon steel. Int J Fatigue 2013;56:114–22. doi:10.1016/j.ijfatigue.2013.07.001.

[77] Smith DJ, Farrahi GH, Zhu WX, McMahon CA. Experimental measurement and finite element simulation of the interaction between residual stresses and mechanical loading. Int J Fatigue 2001;23:293–302. doi:10.1016/S0142-1123(00)00104-3.

[78] Nikitin I, Besel M. Correlation between residual stress and plastic strain amplitude during low cycle fatigue of mechanically surface treated austenitic stainless steel AISI 304 and ferritic–pearlitic steel SAE 1045. Mater Sci Eng A 2008;491:297–303. doi:10.1016/j.msea.2008.03.034.

[79] Benedetti M, Fontanari V, Monelli BD. Numerical Simulation of Residual Stress Relaxation in Shot Peened High-Strength Aluminum Alloys Under Reverse Bending Fatigue. J Eng Mater Technol 2009;132:011012-011012–9. doi:10.1115/1.3184083.

[80] Prasannavenkatesan R, McDowell DL. Polycrystal Plasticity Modeling of Cyclic Residual Stress Relaxation in Shot Peened Martensitic Gear Steel. J Eng Mater Technol 2010;132:031011-031011–8. doi:10.1115/1.4001594.

[81] Zaroog OS, Ali A, Sahari BB, Zahari R. Modeling of residual stress relaxation of fatigue in 2024-T351 aluminium alloy. Int J Fatigue 2011;33:279–85. doi:10.1016/j.ijfatigue.2010.08.012.

[82] McDowell DL. A perspective on trends in multiscale plasticity. Spec Issue Honor David McDowell 2010;26:1280–309. doi:10.1016/j.ijplas.2010.02.008.

[83] Chaboche JL. A review of some plasticity and viscoplasticity constitutive theories. Int J Plast 2008;24:1642–93. doi:10.1016/j.ijplas.2008.03.009.

[84] Johnson GR, Cook WH. Fracture characteristics of three metals subjected to various strains, strain rates, temperatures and pressures. Eng Fract Mech 1985;21:31–48. doi:10.1016/0013-7944(85)90052-9.

[85] Ottosen NS, Ristinmaa M. The Mechanics of Constitutive Modeling. Elsevier; 2005.

[86] Roters F, Eisenlohr P, Hantcherli L, Tjahjanto DD, Bieler TR, Raabe D. Overview of constitutive laws, kinematics, homogenization and multiscale methods in crystal plasticity finite-element modeling: Theory, experiments, applications. Acta Mater 2010;58:1152–211. doi:10.1016/j.actamat.2009.10.058.

[87] Eshelby JD. The determination of the elastic field of an ellipsoidal inclusion, and related problems. Proc R Soc Lond Ser Math Phys Sci 1957;241:376. doi:10.1098/rspa.1957.0133.
[88] Kröner E. Berechnung der elastischen Konstanten des Vielkristalls aus den Konstanten des Einkristalls. Z Für Phys 1958;151:504–18. doi:10.1007/BF01337948.
[89] Berveiller M, Zaoui A. An extension of the self-consistent scheme to plastically-flowing polycrystals. J Mech Phys Solids 1978;26:325–44. doi:10.1016/0022-5096(78)90003-0.
[90] Abdul-Latif A, Dingli JP, Saanouni K. Modeling of complex cyclic inelasticity in heterogeneous polycrystalline microstructure. Mech Mater 1998;30:287–305. doi:10.1016/S0167-6636(98)00054-4.
[91] Dingli JP, Abdul-Latif A, Saanouni K. Predictions of the complex cyclic behavior of polycrystals using a self-consistent modeling. Int J Plast 2000;16:411–37. doi:10.1016/S0749-6419(99)00060-1.
[92] Abdul-Latif A. A Comparison of Two Self-Consistent Models to Predict the Cyclic Behavior of Polycrystals. J Eng Mater Technol 2004;126:62–9. doi:10.1115/1.1633572.
[93] Zhang X. Modeling of microstructure evolution induced by Surface Mechanical Attrition Treatment (SMAT) in AISI 316L stainless steel. PhD Thesis. The Hong Kong Polytechnic University, 2012.
[94] Hassani-Gangaraj SM, Cho KS, Voigt H-JL, Guagliano M, Schuh CA. Experimental assessment and simulation of surface nanocrystallization by severe shot peening. Acta Mater 2015;97:105–15. doi:10.1016/j.actamat.2015.06.054.
[95] Bagherifard S, Ghelichi R, Guagliano M. A numerical model of severe shot peening (SSP) to predict the generation of a nanostructured surface layer of material. Surf Coat Technol 2010;204:4081–90. doi:10.1016/j.surfcoat.2010.05.035.
[96] Bagherifard S, Ghelichi R, Guagliano M. On the shot peening surface coverage and its assessment by means of finite element simulation: A critical review and some original developments. Appl Surf Sci 2012;259:186–94. doi:10.1016/j.apsusc.2012.07.017.
[97] Xie L, Wang C, Wang L, Wang Z, Jiang C, Lu W, et al. Numerical analysis and experimental validation on residual stress distribution of titanium matrix composite after shot peening treatment. Mech Mater 2016;99:2–8. doi:10.1016/j.mechmat.2016.05.005.
[98] Frija M, Hassine T, Fathallah R, Bouraoui C, Dogui A. Finite element modelling of shot peening process: Prediction of the compressive residual stresses, the plastic deformations and the surface integrity. Mater Sci Eng A 2006;426:173–80. doi:10.1016/j.msea.2006.03.097.
[99] Dai K, Villegas J, Stone Z, Shaw L. Finite element modeling of the surface roughness of 5052 Al alloy subjected to a surface severe plastic deformation process. Acta Mater 2004;52:5771–82. doi:10.1016/j.actamat.2004.08.031.
[100] Mahmoudi AH, Ghasemi A, Farrahi GH, Sherafatnia K. A comprehensive experimental and numerical study on redistribution of residual stresses by shot peening. Mater Des 2016;90:478–87. doi:10.1016/j.matdes.2015.10.162.
[101] Jebahi M, Gakwaya A, Lévesque J, Mechri O, Ba K. Robust methodology to simulate real shot peening process using discrete-continuum coupling method. Int J Mech Sci 2016;107:21–33. doi:10.1016/j.ijmecsci.2016.01.005.
[102] Klemenz M, Schulze V, Rohr I, Löhe D. Application of the FEM for the prediction of the surface layer characteristics after shot peening. J Mater Process Technol 2009;209:4093–102. doi:10.1016/j.jmatprotec.2008.10.001.
[103] Chaboche JL, Dang Van K, Cordier G. Modelization of the Strain Memory Effect on the Cyclic Hardening of 316 Stainless Steel. SMIRT 5, Berlin, Germany.: 1979.

[104] Heydari Astaraee A, Miresmaeili R, Bagherifard S, Guagliano M, Aliofkhazraei M. Incorporating the principles of shot peening for a better understanding of surface mechanical attrition treatment (SMAT) by simulations and experiments. Mater Des 2017;116:365–73. doi:10.1016/j.matdes.2016.12.045.
[105] Mylonas GI, Labeas G. Numerical modelling of shot peening process and corresponding products: Residual stress, surface roughness and cold work prediction. Surf Coat Technol 2011;205:4480–94. doi:10.1016/j.surfcoat.2011.03.080.
[106] Chen Z, Sun Z, Retraint D, Panicaud B. Numerical simulations of impacts during Surface Mechanical Attrition Treatment using crystal plasticity model in finite element method, AFM, Association Française de Mécanique; 2017.
[107] Moreno AC, Lévesque FT M, Bocher P. Shot Peening FEM Simulation: A Novel Approach Based on Crystal Plasticity, 13th International Conference on Shot Peening; 2017.
[108] Rousseau T, Nouguier-Lehon C, Gilles P, Hoc T. Finite element multi-impact simulations using a crystal plasticity law based on dislocation dynamics. Int J Plast 2017. doi:10.1016/j.ijplas.2017.10.008.
[109] Marini M, Fontanari V, Bandini M, Benedetti M. Surface layer modifications of micro-shot-peened Al-7075-T651: Experiments and stochastic numerical simulations. Surf Coat Technol 2017;321:265–78. doi:10.1016/j.surfcoat.2017.04.054.
[110] Kim T, Lee H, Kim M, Jung S. A 3D FE model for evaluation of peening residual stress under angled multi-shot impacts. Surf Coat Technol 2012;206:3981–8. doi:10.1016/j.surfcoat.2012.03.078.
[111] Meguid SA, Shagal G, Stranart JC. 3D FE analysis of peening of strain-rate sensitive materials using multiple impingement model. Int J Impact Eng 2002;27:119–34. doi:10.1016/S0734-743X(01)00043-4.
[112] Kanou S, Nishikawa M, Soyama H. Analysis of the formation of plastic deformation layer on the surface of polycrystalline metals subjected to a micro-size high-rate shot impact. Int J Mech Sci 2013;75:316–23. doi:10.1016/j.ijmecsci.2013.07.014.
[113] Lu J. Handbook of measurement of residual stresses. Lilburn, GA : Fairmont Press ; Upper Saddle River, NJ : Distributed by Prentice Hall PTR; 1996.
[114] Zhang K, Yuan M, Chen J. General Calibration Formulas for Incremental Hole Drilling Optical Measurement. Exp Tech 2017;41:1–8. doi:10.1007/s40799-016-0008-x.
[115] Treuting RG, Read WT. A Mechanical Determination of Biaxial Residual Stress in Sheet Materials. J Appl Phys 1951;22:130–4. doi:10.1063/1.1699913.
[116] Urriolagoitia-Sosa G, Romero-Ángeles B, Hernández-Gómez LH, Torres-Torres C, Urriolagoitia-Calderón G. Crack-compliance method for assessing residual stress due to loading/unloading history: Numerical and experimental analysis. Theor Appl Fract Mech 2011;56:188–99. doi:10.1016/j.tafmec.2011.11.007.
[117] Fiori F, Girardin E, Giuliani A, Manescu A, Rustichelli F. Neutron and Synchrotron Non-Destructive Methods for Residual Stress Determination in Materials for Industrial Applications. Met. Mater. High Struct. Effic., Springer, Dordrecht; 2004, p. 425–32. doi:10.1007/1-4020-2112-7_43.
[118] Pintschovius L, Jung V, Macherauch E, Vöhringer O. Residual stress measurements by means of neutron diffraction. Mater Sci Eng 1983;61:43–50. doi:10.1016/0025-5416(83)90124-6.
[119] Martinez-Perez ML, Mompean FJ, Ruiz-Hervias J, Borlado CR, Atienza JM, Garcia-Hernandez M, et al. Residual stress profiling in the ferrite and cementite phases of cold-drawn steel rods by synchrotron X-ray and neutron diffraction. Acta Mater 2004;52:5303–13. doi:10.1016/j.actamat.2004.07.036.

[120] Pratihar S, Turski M, Edwards L, Bouchard PJ. Neutron diffraction residual stress measurements in a 316L stainless steel bead-on-plate weld specimen. Int J Press Vessels Pip 2009;86:13–9. doi:10.1016/j.ijpvp.2008.11.010.
[121] Korsunsky AM, James KE, Daymond MR. Intergranular stresses in polycrystalline fatigue: diffraction measurement and self-consistent modelling. Eng Fract Mech 2004;71:805–12. doi:10.1016/S0013-7944(03)00018-3.
[122] Korsunsky AM, Wells KE, Withers PJ. Mapping two-dimensional state of strain using synchroton X-ray diffraction. Scr Mater 1998;39:1705–12. doi:10.1016/S1359-6462(98)00385-6.
[123] Britton TB, Wilkinson AJ. High resolution electron backscatter diffraction measurements of elastic strain variations in the presence of larger lattice rotations. Ultramicroscopy 2012;114:82–95. doi:10.1016/j.ultramic.2012.01.004.
[124] Wilkinson AJ, Meaden G, Dingley DJ. High-resolution elastic strain measurement from electron backscatter diffraction patterns: New levels of sensitivity. Ultramicroscopy 2006;106:307–13. doi:10.1016/j.ultramic.2005.10.001.
[125] Britton TB, Wilkinson AJ. Measurement of residual elastic strain and lattice rotations with high resolution electron backscatter diffraction. Ultramicroscopy 2011;111:1395–404. doi:10.1016/j.ultramic.2011.05.007.
[126] Zhang T, Collins DM, Dunne FPE, Shollock BA. Crystal plasticity and high-resolution electron backscatter diffraction analysis of full-field polycrystal Ni superalloy strains and rotations under thermal loading. Acta Mater 2014;80:25–38. doi:10.1016/j.actamat.2014.07.036.
[127] Crecraft DI. The measurement of applied and residual stresses in metals using ultrasonic waves. J Sound Vib 1967;5:173–92. doi:10.1016/0022-460X(67)90186-1.
[128] Suresh S, Giannakopoulos AE. A new method for estimating residual stresses by instrumented sharp indentation. Acta Mater 1998;46:5755–67. doi:10.1016/S1359-6454(98)00226-2.
[129] Zhu L, Xu B, Wang H, Wang C. Measurement of residual stress in quenched 1045 steel by the nanoindentation method. Mater Charact 2010;61:1359–62. doi:10.1016/j.matchar.2010.09.006.
[130] Abe T, Mitsunaga Y, Koga H. Photoelastic computer tomography: a novel measurement method for axial residual stress profile in optical fibers. JOSA A 1986;3:133–8. doi:10.1364/JOSAA.3.000133.
[131] Prevéy P. The Effect of Cold Work on the Thermal Stability of Residual Compression in Surface Enhanced IN718. Proc. 20th ASM Mater. Solut. Conf. Expo., St. Louis, MO: 2000.
[132] Wilkens M. The determination of density and distribution of dislocations in deformed single crystals from broadened X-ray diffraction profiles. Phys Status Solidi A 1970;2:359–70. doi:10.1002/pssa.19700020224.
[133] Groma I, Ungár T, Wilkens M. Asymmetric X-ray line broadening of plastically deformed crystals. I. Theory. J Appl Crystallogr 1988;21:47–54. doi:10.1107/S0021889887009178.
[134] Ayers JE. The measurement of threading dislocation densities in semiconductor crystals by X-ray diffraction. J Cryst Growth 1994;135:71–7. doi:10.1016/0022-0248(94)90727-7.
[135] Heinke H, Kirchner V, Einfeldt S, Hommel D. X-ray diffraction analysis of the defect structure in epitaxial GaN. Appl Phys Lett 2000;77:2145–7. doi:10.1063/1.1314877.
[136] Fathallah R, Laamouri A, Sidhom H, Braham C. High cycle fatigue behavior prediction of shot-peened parts. Int J Fatigue 2004;26:1053–67. doi:10.1016/j.ijfatigue.2004.03.007.

[137] Li Y, Kanouté P, François M. Disturbance induced by surface preparation on instrumented indentation test. Mater Sci Eng A 2015;642:381–90. doi:10.1016/j.msea.2015.06.099.
[138] Ji V, Zhang Y-G, Chen C-Q. The non-destructive estimation of the superficial mechanical properties of components in the INCONEL 600 alloy by X-ray diffraction peak width. Surf Coat Technol 2000;130:95–9. doi:10.1016/S0257-8972(00)00683-6.
[139] Prevéy P. The Measurement of Subsurface Residual Stress and Cold Work Distributions in Nickel Base Alloys, 1987.
[140] Bouraoui C, Ben Sghaier R, Fathallah R. An engineering predictive design approach of high cycle fatigue reliability of shot peened metallic parts. Mater Des 2009;30:475–86. doi:10.1016/j.matdes.2008.05.076.
[141] Kocks UF. A statistical theory of flow stress and work-hardening. Philos Mag J Theor Exp Appl Phys 1966;13:541–66. doi:10.1080/14786436608212647.
[142] Mott NF. CXVII. A theory of work-hardening of metal crystals. Lond Edinb Dublin Philos Mag J Sci 1952;43:1151–78. doi:10.1080/14786441108521024.
[143] Koehler JS. The Nature of Work-Hardening. Phys Rev 1952;86:52–9.
[144] Ashby MF. Work hardening of dispersion-hardened crystals. Philos Mag J Theor Exp Appl Phys 1966;14:1157–78. doi:10.1080/14786436608224282.
[145] Multiscale Phenomena in Plasticity: From Experiments to | Joël Lépinoux | Springer. n.d.
[146] Arsenlis A, Parks DM. Modeling the evolution of crystallographic dislocation density in crystal plasticity. J Mech Phys Solids 2002;50:1979–2009. doi:10.1016/S0022-5096(01)00134-X.
[147] Child DJ, West GD, Thomson RC. Assessment of surface hardening effects from shot peening on a Ni-based alloy using electron backscatter diffraction techniques. Acta Mater 2011;59:4825–34. doi:10.1016/j.actamat.2011.04.025.
[148] Barbier D, Gey N, Bozzolo N, Allain S, Humbert M. EBSD for analysing the twinning microstructure in fine-grained TWIP steels and its influence on work hardening. J Microsc 2009;235:67–78. doi:10.1111/j.1365-2818.2009.03182.x.
[149] Sun Z, Retraint D, Baudin T, Helbert AL, Brisset F, Chemkhi M, et al. Experimental study of microstructure changes due to low cycle fatigue of a steel nanocrystallised by Surface Mechanical Attrition Treatment (SMAT). Mater Charact 2017;124:117–21. doi:10.1016/j.matchar.2016.12.017.
[150] Coules HE, Smith DJ, Abburi Venkata K, Truman CE. A method for reconstruction of residual stress fields from measurements made in an incompatible region. Int J Solids Struct 2014;51:1980–90. doi:10.1016/j.ijsolstr.2014.02.008.
[151] Jun T-S, Korsunsky AM. Evaluation of residual stresses and strains using the Eigenstrain Reconstruction Method. Int J Solids Struct 2010;47:1678–86. doi:10.1016/j.ijsolstr.2010.03.002.
[152] Musinski WD, McDowell DL. On the eigenstrain application of shot-peened residual stresses within a crystal plasticity framework: Application to Ni-base superalloy specimens. Int J Mech Sci 2015;100:195–208. doi:10.1016/j.ijmecsci.2015.06.020.
[153] Xu S. Modelling residual stresses and deformation in metal at different scales. PhD Thesis. University of Oxford, 2010.
[154] Prasannavenkatesan R, Zhang J, McDowell DL, Olson GB, Jou H-J. 3D modeling of subsurface fatigue crack nucleation potency of primary inclusions in heat treated and shot peened martensitic gear steels. Int J Fatigue 2009;31:1176–89. doi:10.1016/j.ijfatigue.2008.12.001.
[155] Qian X, Yao Z, Cao Y, Lu J. An inverse approach for constructing residual stress using BEM. Eng Anal Bound Elem 2004;28:205–11. doi:10.1016/S0955-7997(03)00051-1.

[156] Korsunsky AM. On the modelling of residual stresses due to surface peening using eigenstrain distributions. J Strain Anal Eng Des 2005;40:817–24.
[157] Salvati E, Lunt AJG, Ying S, Sui T, Zhang HJ, Heason C, et al. Eigenstrain reconstruction of residual strains in an additively manufactured and shot peened nickel superalloy compressor blade. Comput Methods Appl Mech Eng 2017;320:335–51. doi:10.1016/j.cma.2017.03.005.
[158] Achintha M, Nowell D. Eigenstrain modelling of residual stresses generated by laser shock peening. J Mater Process Technol 2011;211:1091–101. doi:10.1016/j.jmatprotec.2011.01.011.
[159] Achintha M, Nowell D, Shapiro K, Withers PJ. Eigenstrain modelling of residual stress generated by arrays of laser shock peening shots and determination of the complete stress field using limited strain measurements. Surf Coat Technol 2013;216:68–77. doi:10.1016/j.surfcoat.2012.11.027.
[160] Song X, Liu WC, Belnoue JP, Dong J, Wu GH, Ding WJ, et al. An eigenstrain-based finite element model and the evolution of shot peening residual stresses during fatigue of GW103 magnesium alloy. Int J Fatigue 2012;42:284–95. doi:10.1016/j.ijfatigue.2012.01.019.
[161] Salvati E, Korsunsky AM. A simplified FEM eigenstrain residual stress reconstruction for surface treatments in arbitrary 3D geometries. Int J Mech Sci 2018;138–139:457–66. doi:10.1016/j.ijmecsci.2018.02.016.
[162] Benedetti M, Fontanari V, Winiarski B, Allahkarami M, Hanan JC. Residual stresses reconstruction in shot peened specimens containing sharp and blunt notches by experimental measurements and finite element analysis. Int J Fatigue 2016;87:102–11. doi:10.1016/j.ijfatigue.2016.01.020.
[163] Faghidian SA. A smoothed inverse eigenstrain method for reconstruction of the regularized residual fields. Int J Solids Struct 2014;51:4427–34. doi:10.1016/j.ijsolstr.2014.09.012.
[164] Korsunsky AM. Residual elastic strain due to laser shock peening: Modelling by eigenstrain distribution. J Strain Anal Eng Des 2006. doi:10.1243/03093247JSA141.
[165] DeWald AT, Hill MR. Eigenstrain-based model for prediction of laser peening residual stresses in arbitrary three-dimensional bodies Part 2: Model verification. J Strain Anal Eng Des 2008. doi:10.1243/03093247JSA420.
[166] Korsunsky AM, Regino GM, Nowell D. Variational eigenstrain analysis of residual stresses in a welded plate. Int J Solids Struct 2007;44:4574–91. doi:10.1016/j.ijsolstr.2006.11.037.
[167] Farrahi GH, Faghidian SA, Smith DJ. Reconstruction of residual stresses in autofrettaged thick-walled tubes from limited measurements. Int J Press Vessels Pip 2009;86:777–84. doi:10.1016/j.ijpvp.2009.03.010.
[168] Farrahi GH, Faghidian SA, Smith DJ. An Inverse Method for Reconstruction of the Residual Stress Field in Welded Plates. J Press Vessel Technol 2010;132:061205-061205–9. doi:10.1115/1.4001268.
[169] Korsunsky AM. Residual Elastic Strains in Autofrettaged Tubes: Elastic–Ideally Plastic Model Analysis. J Eng Mater Technol 2006;129:77–81. doi:10.1115/1.2400267.
[170] Chaboche JL, Jung O. Application of a kinematic hardening viscoplasticity model with thresholds to the residual stress relaxation. Int J Plast 1997;13:785–807. doi:10.1016/S0749-6419(97)00066-1.
[171] Armstrong PJ, Frederick CO. A mathematical representation of the multiaxial Bauschinger effect. Generating Board, Berkeley, UK.: CEGB, Central Electricity; 1966.
[172] Prager W. Recent Developments in the Mathematical Theory of Plasticity. J Appl Phys 1949;20:235–41. doi:10.1063/1.1698348.

[173] Chaboche JL, Rousselier G. On the Plastic and Viscoplastic Constitutive Equations—Part I: Rules Developed With Internal Variable Concept. J Press Vessel Technol 1983;105:153–8. doi:10.1115/1.3264257.
[174] Chaboche JL. On some modifications of kinematic hardening to improve the description of ratchetting effects. Int J Plast 1991;7:661–78. doi:10.1016/0749-6419(91)90050-9.
[175] Ohno N, Wang J-D. Kinematic hardening rules with critical state of dynamic recovery, part I: formulation and basic features for ratchetting behavior. Int J Plast 1993;9:375–90. doi:10.1016/0749-6419(93)90042-O.
[176] Kang G. Ratchetting: Recent progresses in phenomenon observation, constitutive modeling and application. Int J Fatigue 2008;30:1448–72. doi:10.1016/j.ijfatigue.2007.10.002.
[177] Chaboche J-L, Kanouté P, Azzouz F. Cyclic inelastic constitutive equations and their impact on the fatigue life predictions. Int J Plast 2012;35:44–66. doi:10.1016/j.ijplas.2012.01.010.
[178] Ohno N. Material models of cyclic plasticity with extended isotropic hardening: a review. Mech Eng Rev 2015;2:14–00425. doi:10.1299/mer.14-00425.
[179] Marnier, Keller C, Taleb L. Tensile prestrain memory effect on subsequent cyclic behavior of FCC metallic materials presenting different dislocations slip modes. Int J Plast 2016;78:64–83. doi:10.1016/j.ijplas.2015.11.001.
[180] Krishna S, Hassan T, Ben Naceur I, Saï K, Cailletaud G. Macro versus micro-scale constitutive models in simulating proportional and nonproportional cyclic and ratcheting responses of stainless steel 304. Int J Plast 2009;25:1910–49. doi:10.1016/j.ijplas.2008.12.009.
[181] Belattar A, Taleb L, Hauet A, Taheri S. Dependence of the cyclic stress–strain curve on loading history and its interaction with fatigue of 304L stainless steel. Mater Sci Eng A 2012;536:170–80. doi:10.1016/j.msea.2011.12.097.
[182] Belattar A, Keller C, Taleb L. Multiscale analysis of the pre-hardening effect on the cyclic behavior and fatigue life of 304L stainless steel. Mater Sci Eng A 2016;662:468–80. doi:10.1016/j.msea.2016.03.093.
[183] Xu L, Nie X, Fan J, Tao M, Ding R. Cyclic hardening and softening behavior of the low yield point steel BLY160: Experimental response and constitutive modeling. Int J Plast 2016;78:44–63. doi:10.1016/j.ijplas.2015.10.009.
[184] Zhang J, Jiang Y. Constitutive modeling of cyclic plasticity deformation of a pure polycrystalline copper. Int J Plast 2008;24:1890–915. doi:10.1016/j.ijplas.2008.02.008.
[185] Ohno N. A Constitutive Model of Cyclic Plasticity With a Nonhardening Strain Region. J Appl Mech 1982;49:721–7. doi:10.1115/1.3162603.
[186] Nouailhas D, Cailletaud G, Policella H, Marquis D, Dufailly J, Lieurade HP, et al. On the description of cyclic hardening and initial cold working. Eng Fract Mech 1985;21:887–95. doi:10.1016/0013-7944(85)90095-5.
[187] Chaboche J-L, Gaubert A, Kanouté P, Longuet A, Azzouz F, Mazière M. Viscoplastic constitutive equations of combustion chamber materials including cyclic hardening and dynamic strain aging. Microstruct-Based Models Plast Deform 2013;46:1–22. doi:10.1016/j.ijplas.2012.09.011.
[188] Taleb L, Cailletaud G, Saï K. Experimental and numerical analysis about the cyclic behavior of the 304L and 316L stainless steels at 350°C. Int J Plast 2014;61:32–48. doi:10.1016/j.ijplas.2014.05.006.
[189] Lee C-H, Do VNV, Chang K-H. Analysis of uniaxial ratcheting behavior and cyclic mean stress relaxation of a duplex stainless steel. Int J Plast 2014;62:17–33. doi:10.1016/j.ijplas.2014.06.008.

[190] Zhu Y, Kang G, Kan Q, Bruhns OT, Liu Y. Thermo-mechanically coupled cyclic elasto-viscoplastic constitutive model of metals: Theory and application. Int J Plast 2016;79:111–52. doi:10.1016/j.ijplas.2015.12.005.
[191] Zhang S-L, Xuan F-Z. Interaction of cyclic softening and stress relaxation of 9–12% Cr steel under strain-controlled fatigue-creep condition: Experimental and modeling. Int J Plast 2017;98:45–64. doi:10.1016/j.ijplas.2017.06.007.
[192] Kang G, Ohno N, Nebu A. Constitutive modeling of strain range dependent cyclic hardening. Int J Plast 2003;19:1801–19. doi:10.1016/S0749-6419(03)00016-0.
[193] Ahmed R, Barrett PR, Hassan T. Unified viscoplasticity modeling for isothermal low-cycle fatigue and fatigue-creep stress–strain responses of Haynes 230. Int J Solids Struct 2016;88–89:131–45. doi:10.1016/j.ijsolstr.2016.03.012.
[194] Zhu Y, Kang G, Yu C. A finite cyclic elasto-plastic constitutive model to improve the description of cyclic stress-strain hysteresis loops. Int J Plast 2017;95:191–215. doi:10.1016/j.ijplas.2017.04.009.
[195] Yaguchi M, Takahashi Y. Ratchetting of viscoplastic material with cyclic softening, part 2: application of constitutive models. Int J Plast 2005;21:835–60. doi:10.1016/j.ijplas.2004.05.012.
[196] Chaboche JL, Rousselier G. On the Plastic and Viscoplastic Constitutive Equations—Part II: Application of Internal Variable Concepts to the 316 Stainless Steel. J Press Vessel Technol 1983;105:159–64. doi:10.1115/1.3264258.
[197] Choteau M, Quaegebeur P, Degallaix S. Modelling of Bauschinger effect by various constitutive relations derived from thermodynamical formulation. Mech Mater 2005;37:1143–52. doi:10.1016/j.mechmat.2004.12.001.
[198] Voyiadjis GZ, Basuroychowdhury IN. A plasticity model for multiaxial cyclic loading and ratchetting. Acta Mech 1998;126:19–35. doi:10.1007/BF01172796.
[199] Calloch S, Marquis D. Triaxial tension–compression tests for multiaxial cyclic plasticity. Int J Plast 1999;15:521–49. doi:10.1016/S0749-6419(99)00005-4.
[200] Vincent L, Calloch S, Marquis D. A general cyclic plasticity model taking into account yield surface distortion for multiaxial ratchetting. Int J Plast 2004;20:1817–50. doi:10.1016/j.ijplas.2003.10.008.
[201] Wu H, Meggiolaro MA, de Castro JTP. Computational implementation of a non-linear kinematic hardening formulation for tension–torsion multiaxial fatigue calculations. Int J Fatigue 2016;91:304–12. doi:10.1016/j.ijfatigue.2016.01.005.
[202] Roy SC, Goyal S, Sandhya R, Ray SK. Low cycle fatigue life prediction of 316 L(N) stainless steel based on cyclic elasto-plastic response. Nucl Eng Des 2012;253:219–25. doi:10.1016/j.nucengdes.2012.08.024.
[203] Zhou J, Sun Z, Kanouté P, Retraint D. Effect of surface mechanical attrition treatment on low cycle fatigue properties of an austenitic stainless steel. Int J Fatigue 2017;103:309–17. doi:10.1016/j.ijfatigue.2017.06.011.
[204] Cottrell AH. Dislocations and Plastic Flow in Crystals. London: Oxford University Press; 1953.
[205] Feaugas X, Gaudin C. Different levels of plastic strain incompatibility during cyclic loading: in terms of dislocation density and distribution. Mater Sci Eng A 2001;309–310:382–5. doi:10.1016/S0921-5093(00)01730-5.
[206] Marnier, Keller C, Taleb L. Fatigue of OFHC pure copper and 316L stainless steel subjected to prior tensile and cyclic prestrains. Int J Fatigue 2016;91:204–19. doi:10.1016/j.ijfatigue.2016.06.009.
[207] Kocks UF, Mecking H. Physics and phenomenology of strain hardening: the FCC case. Prog Mater Sci 2003;48:171–273. doi:10.1016/S0079-6425(02)00003-8.
[208] Argon AS. Strengthening mechanisms in crystal plasticity. Oxford University Press; 2008.

[209] Rice JR. Inelastic constitutive relations for solids: An internal-variable theory and its application to metal plasticity. J Mech Phys Solids 1971;19:433–55. doi:10.1016/0022-5096(71)90010-X.
[210] Asaro RJ, Rice JR. Strain localization in ductile single crystals. J Mech Phys Solids 1977;25:309–38. doi:10.1016/0022-5096(77)90001-1.
[211] Grilli N, Janssens KGF, Nellessen J, Sandlöbes S, Raabe D. Multiple slip dislocation patterning in a dislocation-based crystal plasticity finite element method. Int J Plast 2018;100:104–21. doi:10.1016/j.ijplas.2017.09.015.
[212] Lu J, Sun W, Becker A. Material characterisation and finite element modelling of cyclic plasticity behaviour for 304 stainless steel using a crystal plasticity model. Int J Mech Sci 2016;105:315–29. doi:10.1016/j.ijmecsci.2015.11.024.
[213] Cruzado A, LLorca J, Segurado J. Modeling cyclic deformation of inconel 718 superalloy by means of crystal plasticity and computational homogenization. Int J Solids Struct 2017;122:148–61. doi:10.1016/j.ijsolstr.2017.06.014.
[214] Shenoy M, Tjiptowidjojo Y, McDowell D. Microstructure-sensitive modeling of polycrystalline IN 100. Int J Plast 2008;24:1694–730. doi:10.1016/j.ijplas.2008.01.001.
[215] Zhang M, Zhang J, McDowell DL. Microstructure-based crystal plasticity modeling of cyclic deformation of Ti–6Al–4V. Int J Plast 2007;23:1328–48. doi:10.1016/j.ijplas.2006.11.009.
[216] G S. Zur Ableitung einer Fließbedingung. Z Ver Dtsch Ing 1928;72:734–736.
[217] Taylor GI. Plastic strain in metals. Plast Strain Met 1938;62:307–24.
[218] Lin TH. Analysis of elastic and plastic strains of a face-centred cubic crystal. J Mech Phys Solids 1957;5:143–9. doi:10.1016/0022-5096(57)90058-3.
[219] Hill R. Continuum micro-mechanics of elastoplastic polycrystals. J Mech Phys Solids 1965;13:89–101. doi:10.1016/0022-5096(65)90023-2.
[220] Hill R. Continuum micro-mechanics of elastoplastic polycrystals. J Mech Phys Solids 1965;13:89–101. doi:10.1016/0022-5096(65)90023-2.
[221] Cailletaud G, Pilvin P. Utilisation de modèles polycristallins pour le calcul par éléments finis. Rev Eur Éléments Finis 1994;3:515–41. doi:10.1080/12506559.1994.10511147.
[222] Cailletaud G. A micromechanical approach to inelastic behaviour of metals. Int J Plast 1992;8:55–73. doi:10.1016/0749-6419(92)90038-E.
[223] Abdul-Latif A, Dingli JP, Saanouni K. Elastic-Inelastic Self-Consistent Model for Polycrystals. J Appl Mech 2002;69:309–16. doi:10.1115/1.1427693.
[224] Lipinski P, Naddari A, Berveiller M. Recent results concerning the modelling of polycrystalline plasticity at large strains. Int J Solids Struct 1992;29:1873–81. doi:10.1016/0020-7683(92)90178-V.
[225] Rougier Y, Stolz C, Zaoui A. Self consistent modelling of elastic-viscoplastic polycrystals. Comptes Rendus Acad Sci Ser II 1994;318:145–51.
[226] Molinari A, Ahzi S, Kouddane R. On the self-consistent modeling of elastic-plastic behavior of polycrystals. Mech Mater 1997;26:43–62. doi:10.1016/S0167-6636(97)00017-3.
[227] Cailletaud G, Sai K. A polycrystalline model for the description of ratchetting: Effect of intergranular and intragranular hardening. Mater Sci Eng A 2008;480:24–39. doi:10.1016/j.msea.2007.06.071.
[228] Guerchais R. Influence d'accidents géométriques et du mode de chargement sur le comportement en fatigue à grand nombre de cycles d'un acier inoxydable austénitique 316L. PhD Thesis. Ecole nationale supérieure d'arts et métiers - ENSAM, 2014.

[229] Evrard P, Alvarez-Armas I, Aubin V, Degallaix S. Polycrystalline modeling of the cyclic hardening/softening behavior of an austenitic–ferritic stainless steel. Mech Mater 2010;42:395–404. doi:10.1016/j.mechmat.2010.01.007.
[230] Kang G, Bruhns OT, Sai K. Cyclic polycrystalline visco-plastic model for ratchetting of 316L stainless steel. Comput Mater Sci 2011;50:1399–405. doi:10.1016/j.commatsci.2010.11.021.
[231] Liu G, Lu J, Lu K. Surface nanocrystallization of 316L stainless steel induced by ultrasonic shot peening. Mater Sci Eng A 2000;286:91–5. doi:10.1016/S0921-5093(00)00686-9.
[232] Roland T, Retraint D, Lu K, Lu J. Enhanced mechanical behavior of a nanocrystallised stainless steel and its thermal stability. Mater Sci Eng A 2007;445:281–8. doi:10.1016/j.msea.2006.09.041.
[233] Wright SI, Nowell MM, Field DP. A review of strain analysis using electron backscatter diffraction. Microsc Microanal 2011;17:316–29. doi:10.1017/S1431927611000055.
[234] Peyre P, Scherpereel X, Berthe L, Carboni C, Fabbro R, Béranger G, et al. Surface modifications induced in 316L steel by laser peening and shot-peening. Influence on pitting corrosion resistance. Mater Sci Eng A 2000;280:294–302. doi:10.1016/S0921-5093(99)00698-X.
[235] Bahl S, Suwas S, Ungàr T, Chatterjee K. Elucidating microstructural evolution and strengthening mechanisms in nanocrystalline surface induced by surface mechanical attrition treatment of stainless steel. Acta Mater 2017;122:138–51. doi:10.1016/j.actamat.2016.09.041.
[236] Samih Y, Beausir B, Bolle B, Grosdidier T. In-depth quantitative analysis of the microstructures produced by Surface Mechanical Attrition Treatment (SMAT). Mater Charact 2013;83:129–38. doi:10.1016/j.matchar.2013.06.006.
[237] Paul SK, Sivaprasad S, Dhar S, Tarafder S. Cyclic plastic deformation and cyclic hardening/softening behavior in 304LN stainless steel. Theor Appl Fract Mech 2010;54:63–70. doi:10.1016/j.tafmec.2010.06.016.
[238] Kalkhof D, Grosse M, Niffenegger M, Leber HJ. Monitoring fatigue degradation in austenitic stainless steels. Fatigue Fract Eng Mater Struct 2004;27:595–607. doi:10.1111/j.1460-2695.2004.00784.x.
[239] Basu K, Das M, Bhattacharjee D, Chakraborti PC. Effect of grain size on austenite stability and room temperature low cycle fatigue behaviour of solution annealed AISI 316LN austenitic stainless steel. Mater Sci Technol 2007;23:1278–84. doi:10.1179/174328407X179575.
[240] Smaga M, Walther F, Eifler D. Deformation-induced martensitic transformation in metastable austenitic steels. 14th Int Conf Strength Mater 2008;483–484:394–7. doi:10.1016/j.msea.2006.09.140.
[241] Jeon YC, Kim CS, Ki H, Kwun SI, Byeon JW. Strain-Induced Martensitic Phase Transformation by Low-Cycle Fatigue in AISI 316L Stainless Steel. Mater Sci Forum 2008;580–582:597–600. doi:10.4028/www.scientific.net/MSF.580-582.597.
[242] Man J, Obrtlík K, Petrenec M, Beran P, Smaga M, Weidner A, et al. Stability of austenitic 316L steel against martensite formation during cyclic straining. Procedia Eng 2011;10:1279–84. doi:10.1016/j.proeng.2011.04.213.
[243] Oddershede J, Wright JP, Beaudoin A, Winther G. Deformation-induced orientation spread in individual bulk grains of an interstitial-free steel. Acta Mater 2015;85:301–13. doi:10.1016/j.actamat.2014.11.038.
[244] Wei YJ, Anand L. Grain-boundary sliding and separation in polycrystalline metals: application to nanocrystalline fcc metals. J Mech Phys Solids 2004;52:2587–616. doi:10.1016/j.jmps.2004.04.006.

[245] Wei Y, Bower AF, Gao H. Enhanced strain-rate sensitivity in fcc nanocrystals due to grain-boundary diffusion and sliding. Acta Mater 2008;56:1741–52. doi:10.1016/j.actamat.2007.12.028.
[246] Meyers MA, Mishra A, Benson DJ. Mechanical properties of nanocrystalline materials. Prog Mater Sci 2006;51:427–556. doi:10.1016/j.pmatsci.2005.08.003.
[247] Hassani-Gangaraj SM, Cho KS, Voigt H-JL, Guagliano M, Schuh CA. Experimental assessment and simulation of surface nanocrystallization by severe shot peening. Acta Mater 2015;97:105–15. doi:10.1016/j.actamat.2015.06.054.
[248] Whitehouse DJ. Handbook of Surface Metrology. CRC Press; 1994.
[249] Ungár T. Microstructural parameters from X-ray diffraction peak broadening. Viewp Set No 35 Met Alloys Struct Scale Micrometer At Dimens 2004;51:777–81. doi:10.1016/j.scriptamat.2004.05.007.
[250] Clausner A, Richter F. Determination of yield stress from nano-indentation experiments. Eur J Mech - ASolids 2015;51:11–20. doi:10.1016/j.euromechsol.2014.11.008.
[251] Clausner A, Richter F. Usage of the concept of the effectively shaped indenter for the determination of yield stress from Berkovich nano-indentation experiments. Eur J Mech - ASolids 2015;53:294–302. doi:10.1016/j.euromechsol.2015.05.011.
[252] Oliver WC, Pharr GM. An improved technique for determining hardness and elastic modulus using load and displacement sensing indentation experiments. J Mater Res 1992;7:1564–83. doi:10.1557/JMR.1992.1564.
[253] Fischer-Cripps AC. Nanoindentation. 3rd ed. New York: Springer-Verlag; 2011.
[254] Pandey V, Rao GS, Chattopadhyay K, Santhi Srinivas NC, Singh V. Effect of surface Nanostructuring on LCF behavior of aluminum alloy 2014. Mater Sci Eng A 2015;647:201–11. doi:10.1016/j.msea.2015.09.021.
[255] Portier L, Calloch S, Marquis D, Geyer P. Ratchetting under tension–torsion loadings: experiments and modelling. Int J Plast 2000;16:303–35. doi:10.1016/S0749-6419(99)00056-X.
[256] Taleb L. About the cyclic accumulation of the inelastic strain observed in metals subjected to cyclic stress control. Int J Plast 2013;43:1–19. doi:10.1016/j.ijplas.2012.10.009.
[257] Feaugas X. On the origin of the tensile flow stress in the stainless steel AISI 316L at 300 K: back stress and effective stress. Acta Mater 1999;47:3617–32. doi:10.1016/S1359-6454(99)00222-0.
[258] Haddou H, Gaudin C, Feaugas X. Stacking fault energy (s.f.e.) and grain size effects (d) on the tensile behaviour of f.c.c. polycrystalline alloys at 300 K: Back stress and effective stress evolutions. J Phys IV 2001;11:283–91. doi:10.1051/jp4:2001435.
[259] Ohno N, Abdel-Karim M, Kobayashi M, Igari T. Ratchetting characteristics of 316FR steel at high temperature, part I: Strain-controlled ratchetting experiments and simulations. Int J Plast 1998;14:355–72. doi:10.1016/S0749-6419(98)00009-6.
[260] Taheri S, Hauet A, Taleb L, Kpodekon C. Micro–macro investigations about the fatigue behavior of pre-hardened 304L steel. Int J Plast 2011;27:1981–2004. doi:10.1016/j.ijplas.2011.06.004.
[261] Wang H, Jing H, Zhao L, Han Y, Lv X, Xu L. Uniaxial ratcheting behaviour of 304L stainless steel and ER308L weld joints. Mater Sci Eng A 2017;708:21–42. doi:10.1016/j.msea.2017.09.109.
[262] Mazánová V, Škorík V, Kruml T, Polák J. Cyclic response and early damage evolution in multiaxial cyclic loading of 316L austenitic steel. Int J Fatigue 2017;100:466–76. doi:10.1016/j.ijfatigue.2016.11.018.
[263] Marquis D. Etude théorique et vérification expérimentale d'un modèle de plasticité cyclique. Thèse de Doctorat. Université Pierre et Marie Curie, 1979.

[264] Chaboche JL. Constitutive equations for cyclic plasticity and cyclic viscoplasticity. Int J Plast 1989;5:247–302. doi:10.1016/0749-6419(89)90015-6.
[265] Jiang Y, Kurath P. Nonproportional cyclic deformation: critical experiments and analytical modeling. Int J Plast 1997;13:743–63. doi:10.1016/S0749-6419(97)00030-2.
[266] Taleb L, Cailletaud G. Cyclic accumulation of the inelastic strain in the 304L SS under stress control at room temperature: Ratcheting or creep? Int J Plast 2011;27:1936–58. doi:10.1016/j.ijplas.2011.02.001.
[267] Ohno N, Yamamoto R, Sasaki T, Okumura D. Resetting scheme for plastic strain surface in constitutive modeling of cyclic plasticity. ZAMM · Z Angew Math Mech 2017:1–14. doi:10.1002/zamm.201700298.
[268] Shetty MN. Dislocations and Mechanical Behaviour of Materials. PHI Learning Pvt. Ltd.; 2013.
[269] Ohno N, Kachi Y. A Constitutive Model of Cyclic Plasticity for Nonlinear Hardening Materials. J Appl Mech 1986;53:395–403. doi:10.1115/1.3171771.
[270] Taleb L, Cailletaud G. An updated version of the multimechanism model for cyclic plasticity. Int J Plast 2010;26:859–74. doi:10.1016/j.ijplas.2009.11.002.
[271] Méric L, Poubanne P, Cailletaud G. Single Crystal Modeling for Structural Calculations: Part 1—Model Presentation. J Eng Mater Technol 1991;113:162–70. doi:10.1115/1.2903374.
[272] Pilvin P. Approches multi-échelles pour la prévision du comportement anélastique des métaux. Thèse de Doctorat. Univ. Paris VI, 1990.
[273] Gallitelli D, Boyer V, Gelineau M, Colaitis Y, Rouhaud E, Retraint D, et al. Simulation of shot peening: From process parameters to residual stress fields in a structure. Comput Simul Manuf Process 2016;344:355–74. doi:10.1016/j.crme.2016.02.006.
[274] Dunne FPE, Wilkinson AJ, Allen R. Experimental and computational studies of low cycle fatigue crack nucleation in a polycrystal. Int J Plast 2007;23:273–95. doi:10.1016/j.ijplas.2006.07.001.
[275] Chan HL, Ruan HH, Chen AY, Lu J. Optimization of the strain rate to achieve exceptional mechanical properties of 304 stainless steel using high speed ultrasonic surface mechanical attrition treatment. Acta Mater 2010;58:5086–96. doi:10.1016/j.actamat.2010.05.044.
[276] Pham MS, Holdsworth SR, Janssens KGF, Mazza E. Cyclic deformation response of AISI 316L at room temperature: Mechanical behaviour, microstructural evolution, physically-based evolutionary constitutive modelling. Int J Plast 2013;47:143–64. doi:10.1016/j.ijplas.2013.01.017.
[277] Marnier G, Keller C, Taleb L. Tensile prestrain memory effect on subsequent cyclic behavior of FCC metallic materials presenting different dislocations slip modes. Int J Plast 2016;78:64–83. doi:10.1016/j.ijplas.2015.11.001.
[278] Labergere C, Saanouni K, Sun ZD, Dhifallah MA, Li Y, Duval JL. Prediction of Low Cycle Fatigue Life Using Cycles Jumping Integration Scheme. Appl Mech Mater 2015;784:308–16. doi:10.4028/www.scientific.net/AMM.784.308.

Jianqiang ZHOU

Doctorat : Matériaux, Mécanique, Optique et Nanotechnologie

Année 2018

Etude expérimentale et modélisation multi-échelle du comportement cyclique d'aciers 316L traités par SMAT

Ce travail de thèse est focalisé sur des caractérisations microstructurales, des essais de fatigue et une modélisation multi-échelle du comportement en fatigue oligocyclique d'aciers 316L nanocristallisés superficiellement par SMAT. Le gradient de taille de grains superficiel, les contraintes résiduelles et l'écrouissage générés sont évalués à l'aide de différentes techniques : EBSD, DRX et essais de dureté. Le durcissement/adoucissement cyclique des éprouvettes SMATées et l'évolution de la microstructure au cours du chargement cyclique sont ensuite étudiés grâce à des essais de fatigue et des observations par EBSD. Une comparaison entre le SMAT et le grenaillage conventionnel est réalisée en analysant la topographie de surface, les champs de contraintes résiduelles et les profils d'écrouissage générés. Les effets de ces deux traitements sur la durée de vie en fatigue oligocyclique sont également étudiés.

Une méthodologie de modélisation des contraintes résiduelles et de l'écrouissage est par ailleurs développée. Elle comporte une modélisation multi-échelle, la reconstruction des contraintes résiduelles et de l'écrouissage ainsi que la simulation du chargement cyclique. Une modélisation macroscopique de la plasticité cyclique de l'acier est d'abord réalisée. Une approche auto-cohérente du durcissement/adoucissement cyclique est ensuite développée. Enfin, une nouvelle méthode de reconstruction des contraintes résiduelles et de l'écrouissage est proposée et appliquée à une structure SMATée.

Mots clés : grenaillage de précontrainte - acier inoxydable austénitique - matériaux, fatigue - simulation par ordinateur - contraintes résiduelles - écrouissage.

Experimental Study and Multi-scale Modelling of LCF Behaviour of Austenitic Steels Treated by SMAT

This work focuses on experimental analysis and multiscale modelling of LCF behaviour of 316L steels treated by SMAT. The gradient microstructure features of a 316L steel treated by SMAT are characterized by EBSD, XRD and hardness tests. Grain size gradient, residual stress and plastic deformation are evaluated. The cyclic hardening/softening behaviour of the SMATed specimens and the evolution of the microstructures during cyclic loading are studied based on LCF tests and EBSD observations. A comparison between SMAT and conventional shot peening is performed by analysing the surface topography, residual stress fields, and work hardening profiles of the treated specimens as well as their effects on LCF life.

A modelling methodology of residual stress and work hardening is developed including constitutive modelling, reconstruction technique, and cyclic loading simulation. First, a macroscopic constitutive modelling of the cyclic plasticity behaviour of a 316L steel is performed. Then, a self-consistent modelling of the cyclic hardening/softening behaviour is developed. Afterwards, a new method for reconstructing residual stress and work hardening is proposed and applied to a SMATed structure. Both of the previous macroscopic and microscopic models are used to predict the cyclic behaviour of the SMATed material.

Keywords: shot peening - austenitic stainless steel - materials, fatigue - computer simulation - residual stresses – strain hardening.